High precision theoretical predictions for the production of top-quark pairs associated with additional heavy particles at the LHC

Von der Fakultät für Mathematik und Naturwissenschaften der RWTH Aachen University zur Erlangung des akademischen Grades eines Doktors der Naturwissenschaften genehmigte Dissertation

vorgelegt von

Nikolaos Dimitrakopoulos, M.Sc.

aus

Athen, Griechenland

Berichter: apl. Prof. Dr. rer. nat. Malgorzata Worek
University Professor Dr. rer. nat. Johannes Erdmann

Tag der mündlichen Prüfung: 04.09.2026

Diese Dissertation ist auf den Internetseiten der Universitätsbibliothek verfügbar.

Abstract

This thesis studies the rare Standard-Model $pp \to t\bar{t}t\bar{t}$ and $pp \to t\bar{t}W^+ +$ jets processes at the Large Hadron Collider (LHC). All results are obtained within the HELAC-NLO framework, which is extended in this work by an implementation of the `MiNLO` method and subsequently applied to full off-shell predictions for $pp \to t\bar{t}W^+ +$ jets.

For four-top-quark production at $\sqrt{s} = 13.6\,\text{TeV}$, predictions are presented for the 4ℓ and 3ℓ decay channels in the narrow-width approximation (NWA). Next-to-leading order (NLO) QCD corrections are incorporated consistently in both production and decay stages. This provides a matrix-element description of hard real radiation in the decays and retains spin correlations at NLO accuracy in perturbative QCD. Integrated and differential fiducial cross sections are reported for several NWA approaches. In particular, the impact of missing higher-order QCD corrections in the decays is quantified, and the effect of expanding the top-quark width in the computation is investigated.

The thesis further details the implementation of the `MiNLO` method into HELAC-NLO. `MiNLO` enables a dynamical extraction of renormalization and factorization scales by identifying a most probable sequence of parton branchings, and it improves fixed-order predictions through the inclusion of Sudakov form factors that resum large logarithms in the presence of strong scale hierarchies. Differences between the present implementation and the original `MiNLO` proposal are discussed, and the impact of the adopted prescriptions on phenomenological predictions is highlighted.

To improve predictions for the full off-shell $pp \to t\bar{t}W^+ +$ jets processes, `MiNLO` is applied using the actual event kinematics to determine the scales associated with additional jets relative to the $t\bar{t}W^+$ system. Results are presented for the fully leptonic channel $pp \to e^+\nu_e\,\mu^-\bar{\nu}_\mu\,\tau^+\nu_\tau\,b\bar{b} + \{0,1,2\}$ jets at the LHC with $\sqrt{s} = 13\,\text{TeV}$. A dedicated comparison of standard NLO and `MiNLO` predictions is performed at the integrated and differential fiducial cross-section level, including an assessment of systematic uncertainties inherent to the `MiNLO` procedure. Finally, merged predictions are constructed to improve the modeling of the $pp \to t\bar{t}W^+$ processes by combining samples with different jet multiplicities through the introduction of an explicit merging-scale parameter.

Zusammenfassung

Diese Dissertation untersucht die seltenen Prozesse des Standardmodells $pp \to t\bar{t}t\bar{t}$ und $pp \to t\bar{t}W^+ +$ jets am Large Hadron Collider (LHC). Alle Ergebnisse wurden mit Hilfe des HELAC-NLO-Frameworks erzielt, welches im Zuge dieser Arbeit durch eine Implementierung der `MiNLO` -Methode erweitert und anschließend auf vollständige Off-Shell-Vorhersagen für $pp \to t\bar{t}W^+ +$ jets angewandt wurde.

Vorhersagen für die Produktion von vier Top-Quarks bei $\sqrt{s} = 13.6\,\text{TeV}$ werden für die 4ℓ- und 3ℓ-Zerfallskanäle in der Narrow-Width-Approximation (NWA) präsentiert. Die nächsthöheren (NLO) QCD-Korrekturen werden sowohl in der Produktions- als auch im Zerfallsprozess konsistent berücksichtigt. Dies ermöglicht eine Matrixelement-Beschreibung harter reeller Strahlung in den Zerfällen und erhält Spin-Korrelationen mit NLO-Genauigkeit in QCD. Integrierte und differentielle fiduzielle Wirkungsquerschnitte werden für mehrere NWA-Ansätze angegeben. Insbesondere wird der Einfluss fehlender höherer QCD-Korrekturen in den Zerfällen quantifiziert sowie der Effekt der Entwicklung der Top-Quark-Breite in der Berechnung untersucht.

Die Dissertation beschreibt darüber hinaus die Implementierung der `MiNLO` -Methode in HELAC-NLO. `MiNLO` ermöglicht eine dynamische Bestimmung der Renormierungs und Faktorisierungsskalen durch die Identifikation der wahrscheinlichsten Sequenz von Partonaufspaltungen und verbessert Fixed-Order-Vorhersagen durch die Einbeziehung von Sudakov-Formfaktoren, welche große Logarithmen bei starken Skalenhierarchien resummieren. Unterschiede zwischen der vorliegenden Implementierung und der ursprünglichen `MiNLO` -Formulierung werden diskutiert, und der Einfluss der verwendeten Berechnungsvorschriften auf phänomenologische Vorhersagen wird hervorgehoben.

Zur Verbesserung der Vorhersagen für die Off-Shell-Prozesse $pp \to t\bar{t}W^+ +$ jets wird `MiNLO` unter Verwendung der tatsächlichen Ereigniskinematik angewandt, um die mit zusätzlichen Jets verbundenen Skalen relativ zum $t\bar{t}W^+$-System zu bestimmen. Ergebnisse werden für den vollständig leptonischen Zerfallskanal $pp \to e^+\nu_e\,\mu^-\bar{\nu}_\mu\,\tau^+\nu_\tau\,b\bar{b} + \{0,1,2\}$ jets am LHC bei $\sqrt{s} = 13\,\text{TeV}$ präsentiert. Ein Vergleich zwischen Standard-NLO- und `MiNLO` -Vorhersagen wird sowohl auf Ebene der integrierten als auch der differentiellen fiduziellen Wirkungsquerschnitte durchgeführt, einschließlich einer Bewertung systematischer Unsicherheiten, die dem `MiNLO` -Verfahren inhärent sind. Abschließend werden zusammengeführte Vorhersagen konstruiert, um die Modellierung der $pp \to t\bar{t}W^+$-Prozesse durch die Kombination von Datensätzen mit unterschiedlichen Jet-Multiplizitäten mittels Einführung eines expliziten Zusammenführungsskalenparameters zu verbessern.

Acknowledgments

First and foremost, I would like to express my sincere gratitude to my supervisor, Prof. Malgorzata Worek, for her invaluable support and outstanding guidance throughout my doctoral studies. Her mentorship and our many discussions profoundly shaped both my understanding of physics and my development as a young scientist. I would also like to thank my second supervisor, Prof. Johannes Erdmann, for his continuous support, his availability, and the many stimulating scientific discussions.

This dissertation would not have been possible without the invaluable contributions of my collaborators Manal Alsairafi, Leon Mans, Minos Reinartz and Johannes Welter, who carefully proofread substantial parts of this dissertation. In particular, I would like to thank Minos Reinartz, with whom I shared an office for four years, Leon Mans, for his remarkable help and genuine interest in scientific discussions, and Manal Alsairafi, for the excellent collaboration we had while writing a paper together. My interactions with them greatly contributed to my scientific development and provided me with valuable lessons that I will carry forward in my future career.

Furthermore, I would like to acknowledge the funding of my position by the Deutsche Forschungsgemeinschaft (DFG) under grant 396021762 - TRR 257: Particle Physics Phenomenology after the Higgs Discovery, and grant 400140256 - GRK 2497: The Physics of the Heaviest Particles at the LHC, as well as the computing time provided at the NHR Center NHR4CES at RWTH Aachen University (project number p0020216).

Finally, I would like to thank my family for their constant support and my girlfriend Manthoula for her patience and understanding whenever I was stressed and did not not have much time. To my family: Ευχαριστώ ιδιαιτέρως την οικογένειά μου, και συγκεκριμένα τη μητέρα μου Αλεξάνδρα, τον πατέρα μου Γιώργο και την αδερφή μου Θεανώ. Ευχαριστώ ιδιαίτερα τους γονείς μου για την αγάπη και την άνευ όρων στήριξή τους στην προσπάθειά μου να πραγματοποιήσω τα όνειρά μου.

Eidesstattliche Erklärung / Declaration of Authorship

I, Nikolaos Dimitrakopoulos, declare that this thesis and the work presented in it are my own and has been generated by me as the result of my own original research.

Hiermit erkläre ich an Eides statt / I do solemnly swear that:

1. This work was done wholly or mainly while in candidature for the doctoral degree at this faculty and university;
2. Where any part of this thesis has previously been submitted for a degree or any other qualification at this university or any other institution, this has been clearly stated;
3. Where I have consulted the published work of others or myself, this is always clearly attributed;
4. Where I have quoted from the work of others or myself, the source is always given. This thesis is entirely my own work, with the exception of such quotations;
5. I have acknowledged all major sources of assistance;
6. Where the thesis is based on work done by myself jointly with others, I have made clear exactly what was done by others and what I have contributed myself;
7. Parts of this work have been published before as:

   [1] *Four top final states with NLO accuracy in perturbative QCD: 4 lepton channel*
   Nikolaos Dimitrakopoulos and Malgorzata Worek, JHEP, 06:129, 2024

   [2] *Four top final states with NLO accuracy in perturbative QCD: 3 lepton channel*
   Nikolaos Dimitrakopoulos and Malgorzata Worek, JHEP, 03:025, 2025

   [3] *Multi-scale improved predictions for* $pp \to t\bar{t}W^+ + X$
   Nikolaos Dimitrakopoulos and Malgorzata Worek, arXiv:2607.11652

September 21, 2026

Declaration of AI usage

I, Nikolaos Dimitrakopoulos, hereby declare that the use of artificial intelligence (AI) tools in the preparation of this document was strictly limited to improving grammar, punctuation, wording clarity, and overall flow of the text. No AI tools were utilized for generating original scientific content, data interpretation, or conceptual development. All research results, analyses, and scientific conclusions presented are entirely my own work.

September 21, 2026

List of Publications

Parts of this thesis have already been published or presented during conferences.

Peer-reviewed publications

[1] *Four top final states with NLO accuracy in perturbative QCD: 4 lepton channel*
Nikolaos Dimitrakopoulos and Malgorzata Worek, JHEP, 06:129, 2024

[2] *Four top final states with NLO accuracy in perturbative QCD: 3 lepton channel*
Nikolaos Dimitrakopoulos and Malgorzata Worek, JHEP, 03:025, 2025

[3] *Modeling top-quark decays in $t\bar{t}t\bar{t}$ production at the LHC*
Manal Alsairafi, Nikolaos Dimitrakopoulos, and Malgorzata Worek, Phys. Rev. D, 112(11):114002, 2025

Accepted for publication in JHEP

[1] *Multi-scale improved predictions for $pp \to t\bar{t}W^+ + X$*
Nikolaos Dimitrakopoulos and Malgorzata Worek, arXiv:2607.11652

Conference proceedings

[1] *$t\bar{t}t\bar{t}$: NLO QCD corrections in production and decays for the 4ℓ channel*
Nikolaos Dimitrakopoulos, PoS ICHEP2024 (2025) 367. Presented at the 42nd International Conference on High Energy Physics (ICHEP2024).

[2] *$t\bar{t}t\bar{t}$: NLO QCD corrections in production and decays for the 3ℓ channel*
Nikolaos Dimitrakopoulos, SciPost Phys.Proc. 18 (2026) 015. Presented at the 17th International Workshop on Top Quark Physics (TOP2024).

Contents

1 Introduction **1**
- 1.1 A brief history of the top quark . . . 1
- 1.2 Top-quark properties . . . 3
  - 1.2.1 Top-quark mass . . . 3
  - 1.2.2 Top-quark decays . . . 6
- 1.3 Top-quark associated processes . . . 8
  - 1.3.1 Top-quark pair production . . . 8
  - 1.3.2 $t\bar{t}+$ jets . . . 10
  - 1.3.3 $t\bar{t}+$ photons . . . 13
  - 1.3.4 $t\bar{t}+Z$ . . . 14
  - 1.3.5 $t\bar{t}+H$ . . . 15
  - 1.3.6 $t\bar{t}+W^{\pm}$ . . . 17
  - 1.3.7 $t\bar{t}+t\bar{t}$ . . . 19

2 Theoretical framework **23**
- 2.1 Factorization and parton distribution functions . . . 24
- 2.2 Hard process . . . 25
- 2.3 Parton showers and Hadronization . . . 29
- 2.4 Top-quark modeling in perturbative calculations . . . 31
  - 2.4.1 Full off-shell approach . . . 31
  - 2.4.2 Narrow-width approximation . . . 33

3 Helac-Nlo **37**
- 3.1 Tree-level matrix element calculation . . . 38
- 3.2 Color flow decomposition . . . 41
- 3.3 Virtual corrections . . . 44
  - 3.3.1 The OPP method . . . 44
  - 3.3.2 Example: Determining the d coefficient of a four-point function with rank four . . . 46
  - 3.3.3 Reweighting mode . . . 49
- 3.4 Real corrections and subtraction schemes . . . 51
- 3.5 The final NLO cross-section formula . . . 54

4 The $pp \to t\bar{t}t\bar{t}$ process in QCD **57**
- 4.1 Description of the calculation . . . 57
- 4.2 4ℓ channel . . . 60
  - 4.2.1 Computational setup . . . 60
  - 4.2.2 Integrated fiducial results . . . 62
  - 4.2.3 Differential results . . . 66

4.2.4 Full off-shell vs NWA at Leading Order in QCD 74
4.3 3ℓ channel 76
4.3.1 Computational setup 77
4.3.2 Integrated fiducial results 78
4.3.3 Differential results 82

5 The MiNLO method 95
5.1 Implementation of MiNLO at LO - MiLO 96
5.2 Implementation of MiNLO at NLO - MiNLO 100
5.3 Scale variation 101
5.4 Sudakov form factors 102
5.5 Additional notes on the implementation 104
5.5.1 Clusterings with initial-state partons 105
5.5.2 Unordered clusterings 105

6 MiNLO predictions for $pp \to t\bar{t}W^+ +$ jets in QCD 107
6.1 Description of the calculation and computational setup 108
6.2 MiNLO vs NLO: Integrated fiducial results 111
6.2.1 Study of the systematic uncertainties in the MiNLO method . . 112
6.2.2 The MiNLO behavior with suboptimal scales and various transverse momentum thresholds 117
6.3 On the form of the Sudakov form factors 119
6.4 MiNLO vs NLO: Differential cross-section distributions 122
6.5 Merged predictions 127

7 Conclusions 137

A Appendix 141
A.1 The MiNLO input card 141
A.2 Cross checks for the MiNLO implementation 142

Chapter 1

Introduction

1.1 A brief history of the top quark

Long before the top quark was experimentally discovered, particle physicists had already predicted its existence. This prediction was essential for maintaining the internal coherence of the Standard Model (SM) of particle physics, as the absence of such a quark would lead to gauge anomalies and hence to a loss of gauge invariance. Since the early 1960s, the existence of the u, d, s quarks had been postulated to account for the large number of hadrons discovered at the time [1, 2]. These hadrons could be systematically organized into groups following an SU(3) flavor symmetry [3, 4], and the introduction of three distinct quark types provided a natural explanation for this symmetry structure. However, the picture of the quark model was not yet complete. The main problem at that time was to explain why certain kaon decays occurred much less frequently than predicted by the theory. The absence of flavor-changing neutral currents (FCNC) at the tree level could actually solve this problem, but this required the existence of a fourth type of quark. For this reason, the charm quark was theoretically postulated in 1970 along with the Glashow–Iliopoulos–Maiani (GIM) mechanism [5] that suppresses FCNC effects and could thus explain the aforementioned rare kaon decays. Four years later, the J/ψ ($c\bar{c}$) meson was experimentally discovered [6, 7], verifying the existence of the charm quark. The left-handed c and s quarks were grouped together into an $\mathrm{SU(2)_L}$ weak isospin doublet, forming, along with their right-handed singlet partners, the second quark generation. The classification of quarks into two families was appealing given that, at that time, leptons had also been classified into two families of electrons and muons, together with their corresponding neutrinos. However, the CP violation observed in 1964 [8] in kaon decays led physicists to hypothesize the existence of an additional third generation of quarks. This is because, the Cabibbo-Kobayashi-Maskawa (CKM) [9,10] matrix contains no physical CP-violating phase for only two quark generations. Therefore, a new weak isospin $\mathrm{SU(2)_L}$ doublet was proposed, consisting of the left-handed bottom and top quarks, with their right-handed components transforming as singlets under $\mathrm{SU(2)_L}$. The existence of the bottom quark was experimentally confirmed at Fermilab with the discovery of the Υ meson [11], a bound state of a b and $\bar{b}$ quarks, with a mass of about 10 GeV. Around the same period, the discovery of the τ lepton [12] completed the symmetrical pattern of the three generations of quarks and leptons, with the only piece missing from the puzzle being the experimental discovery of the top quark. It is important to highlight

here that the presence of the top quark is needed for the cancellation of the chiral anomalies [13, 14] in the SM. In fact, if there were only a bottom quark without a corresponding top-quark partner, these anomalies would violate gauge invariance, rendering the SM an invalid quantum field theory.

The discovery of the top quark, however, was accomplished after many years of effort, culminating in 1995. Below, we summarize some of the key steps leading to this discovery, primarily following Ref. [15]. Initially, significant efforts were made to detect the top quark using the electron-positron (e^+e^-) accelerators available at that time. Notable among these accelerators were PETRA at DESY, TRISTAN in Japan, as well as the Stanford Linear Accelerator (SLC) and the Large Electron–Positron Collider (LEP) at CERN. From these collider measurements, useful lower limits on the top-quark mass were obtained. For instance, SLC and LEP reported in 1990 a lower limit on m_t of about 45.8 GeV [16–19]. Nonetheless, these measurements were insufficient to establish whether the top quark is heavier or lighter than the W boson, making it difficult to ascertain whether the top quark could appear as a decay product of the W boson, or the other way around. Starting in the early 1980s, the construction of proton-antiproton colliders, such as the Super Proton-Antiproton Synchrotron ($Sp\bar{p}S$) at CERN and the Tevatron at Fermilab, allowed for further constraints on the top-quark mass due to their significantly higher energies. Searches for a top quark with $m_t < m_W$ were unsuccessful after investigating potential $W^+ \to t\bar{b}$ and $W^- \to \bar{t}b$ decays, which consequently suggested that the top quark is likely heavier than the W boson. The latter was experimentally confirmed by the Collider Detector at Fermilab (CDF) collaboration through a detailed analysis of the $\ell +$ jets channel. Specifically, after comparing with SM expectations, lower limits of 91 GeV were established in 1992, and two years later, the new D0 experiment extended this limit to 131 GeV [20]. The first evidence for the top-quark discovery was made in 1994 by the CDF collaboration, after reporting several events in the 2ℓ and $1\ell +$ jets channels [21]. While the possibility of background fluctuations that could produce similar event counts was not completely ruled out, it was deemed sufficiently small and motivated more precise measurements as additional data became available. Indeed, one year later, in 1995, both the CDF collaboration [22] and the D0 experiment [23] independently announced the discovery of the top quark, with statistical significances of $4.8\,\sigma$ and $4.6\,\sigma$, respectively. Taken together, the combined significance exceeded the $5\,\sigma$ threshold required to claim a discovery. The top-quark mass was reconstructed for the $1\ell +$ jets channel by utilizing the momenta of the final-state jets and charged leptons. The four-momentum associated with the presence of a neutrino in the final state was also determined using m_W as a constraint. The corresponding figure from the discovery paper of the CDF collaboration is displayed in Fig. 1.1. The observed events are represented by solid lines, the background by dotted lines, and the dashed lines illustrate the sum of the background along with a $t\bar{t}$ Monte-Carlo simulation using $m_t = 175$ GeV. From the likelihood fit, $m_t = 176 \pm 13$ GeV was obtained by CDF, while a similar analysis conducted by D0 yielded $m_t = 199 \pm 30$ GeV.

Since then, significantly more precise measurements of the top-quark's properties, including its mass and width, have been achieved. The Large Hadron Collider (LHC), which began operations in 2010, has opened a new avenue for such studies, allowing for high-precision investigations of the top quark. In fact, the LHC functions as a top-quark factory, producing an impressive rate of up to 30 top and antitop

quarks per second, given the instantaneous luminosity of $2.1 \times 10^{-2}\,\mathrm{pb}^{-1}\,\mathrm{s}^{-1}$ [24]. As the heaviest SM particle known to date, the top quark occupies a unique position among the realm of SM particles and plays a crucial role in many areas of particle physics, including the determination of the electroweak vacuum stability [25], searches for physics beyond the SM (BSM) and many others. Owing to its extremely short lifetime, however, it can not be directly observed in the LHC detectors. Instead, its properties are studied through its decay products. As predicted by the SM, these decay products consist of a $W^{\pm}$ boson and a bottom quark nearly 100% of the time. Since $W^{\pm}$ bosons are also heavy and unstable particles, they further decay to either a pair of leptons or hadrons. These final-state particles leave their characteristic mark in the detectors, allowing them to be reconstructed and interpreted as candidates for top-quark decays.

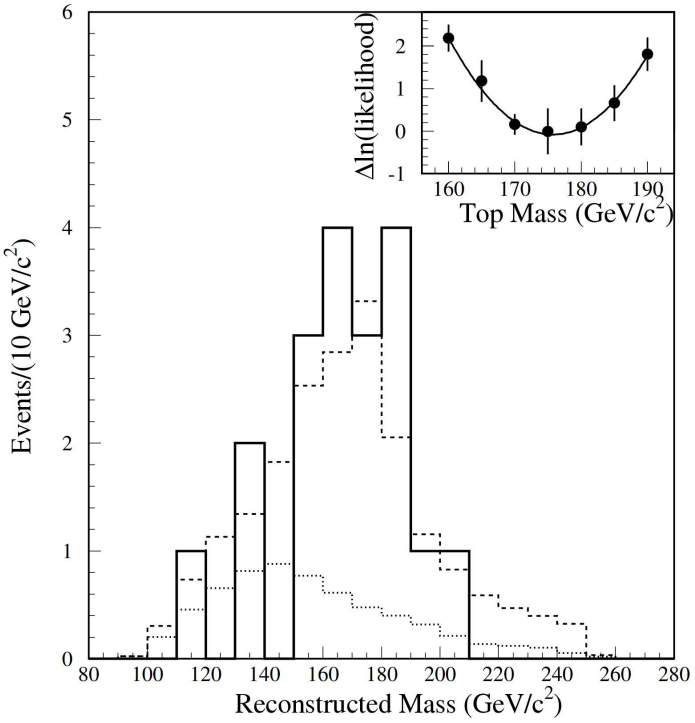

Figure 1.1: *Top-quark mass reconstruction by the CDF collaboration as included in the discovery paper [22]. The solid lines demonstrate the observed events, the dotted lines the background events, while the dashed lines illustrate the sum of the background events together with $t\bar{t}$ Monte-Carlo simulation using $m_t = 175\,\mathrm{GeV}$.*

1.2 Top-quark properties

In the following subsections, several important properties of the top quark are discussed in more detail, focusing on the mass and width of the top quark. The discussion presented in this section is largely based on Refs. [26, 27].

1.2.1 Top-quark mass

The mass of the top-quark is fundamental to several aspects of the Standard Model, and increasingly precise measurements of this parameter are vital for enhancing

the accuracy of electroweak precision tests. Specifically, the mass of the $W^{\pm}$ boson receives radiative corrections from one-loop diagrams that include a top quark in the loop, so that any uncertainty in the top-quark mass directly affects the theoretical prediction of the $W^{\pm}$ mass. Achieving a precise determination of the top-quark mass is therefore essential to reduce this uncertainty. In addition, precise measurements of the top-quark mass are important for assessing the stability of the electroweak vacuum [28]. As illustrated in Fig. 1.2, absolute stability, in which the electroweak vacuum corresponds to the global minimum of the Higgs potential, has not yet been fully excluded. Hence, an even more precise measurement of the top-quark mass is required to determine whether the electroweak vacuum can be definitively classified as metastable or not.

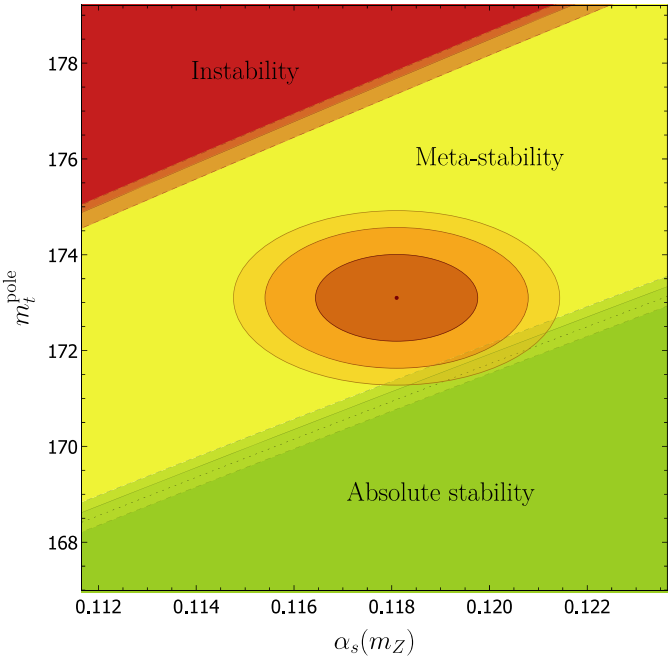

Figure 1.2: *Vacuum structure of the Higgs potential in the two-dimensional* $(m_t^{\rm pole}, \alpha_s(m_Z))$ *plot. The ellipses indicate the 68%, 95% and 99% confidence levels based on experimental measurements. Figure is taken from Ref. [29].*

Nonetheless, as already highlighted, the top quark is not observed as an asymptotic state. As a consequence, its properties, including the top-quark mass, are not inherently physical but rather scheme-dependent. One of the most common schemes employed for defining the top-quark mass is the *pole-mass scheme*, in which the mass is treated as a fixed parameter independent of the renormalization scale and is defined as the pole of the renormalized propagator. However, similar to the treatment of the strong coupling constant, which is scale dependent, one could also treat the top-quark mass as a renormalization-scale dependent parameter. In the most common scale-dependent scheme, called the $\overline{MS}$ *scheme*, the $1/\varepsilon$ ultraviolet (UV) pole along with the $\ln(4\pi e^{-\gamma_E})$ piece are absorbed inside the renormalized mass $\overline{m}_t(\mu)$, the dynamics of which are governed by the renormalization group equation:

$$\frac{d}{d\ln\mu}\overline{m}_t(\mu) = -\overline{m}_t(\mu)\left(\frac{\alpha_s(\mu)}{\pi}\right) + \dots . \tag{1.1}$$

In this scheme, μ can be interpreted as the scale above which self-energy corrections

are absorbed inside the mass. As a result, the $\overline{\text{MS}}$ scheme is largely insensitive to low-energy effects and is therefore commonly referred to as a short-distance mass, reflecting its sensitivity to physics at high energy scales. Even though this mass scheme is well-suited for describing inclusive observables that depend only indirectly on the top-quark mass, it is less appropriate for observables with direct kinematic sensitivity to the mass. Such observables typically involve the decay products of the top quark and exhibit resonance structures that depend on scales $R \ll m_t$. An example of such an observable discussed in Ref. [27] is the invariant mass of the jets originating from a hadronic top-quark decay. In this case, while the position of the resonance peak is determined by the high-energy scale set by the top-quark mass, the width of the resonance is governed by much smaller scales R. An appropriate short-distance mass scheme that also captures quantum effects above the scale R is the *MSR scheme*. Its evolution with the scale R is linear and can be expressed as:

$$\frac{d}{d\ln R} m_t^{\text{MSR}}(R) = -\frac{4}{3} R \left(\frac{\alpha_s(R)}{\pi} \right) + \dots . \tag{1.2}$$

Taking the limit $R \to 0$, one effectively recovers the pole mass that does not exhibit any scale dependence. In this sense, the pole mass can be viewed as capturing all quantum effects down to arbitrarily small energy scales. This regime is, however, dominated by non-perturbative effects, implying that the pole-mass scheme suffers from the renormalon ambiguity and therefore carries an intrinsic uncertainty of $110 - 250\,\text{MeV}$ [30, 31]. Thus, for top-quark mass extractions aiming for precision below these values, the pole-mass scheme should be avoided. On top of that, apart from the dominant QCD corrections, subleading electroweak effects must also be taken into account when determining the top-quark mass if uncertainties below 1 GeV are to be achieved [26].

From the experimental standpoint, the top-quark mass extraction is mostly performed at the LHC using *direct measurements*. In this approach, the top-quark decay products are directly reconstructed and used to build observables sensitive to the top-quark mass. Such observables include, among others, resonance peaks and/or sharp kinematic edges, which exhibit a strong dependence on the value of the top-quark mass. One advantage of these methods is that they are largely independent of the top-quark production mechanism, as they rely only on the reconstruction of the decay products. However, they depend strongly on the Monte Carlo (MC) mass parameter m_t^{MC} used in the event simulations. Although this mass should be numerically close to the pole mass, certain limitations arise from the accuracy of parton showers in the MC event generators as well as in the hadronization models, preventing such a precise statement to be made. *Indirect measurements* have also been widely used to determine the top-quark mass in well-defined schemes such as the pole-mass or the $\overline{\text{MS}}$ scheme. In this approach, the extracted mass is obtained by comparing the measured inclusive $t\bar{t}$ production cross section with theoretical predictions calculated at next-to-next-to-leading order (NNLO) in QCD [32–35]. Since this comparison is performed at the parton level using fixed-order NNLO calculations, the measured cross section must first be unfolded to the parton level. The accuracy of these predictions is at the level of 2 GeV [36], primarily due to the insufficient precision in the determination of the gluon parton distribution function (PDF), which significantly influences the results. Therefore, reducing these uncertainties will necessitate even more precise predictions that go beyond the currently

available NNLO calculations. In addition to comparisons at the inclusive level, differential measurements have also been employed by utilizing the $t\bar{t}j$ and the $M_{t\bar{t}}$ distributions, the shapes of which are very sensitive to the top-quark mass. The precision of these measurements is currently at the level of 1 to 2 GeV [37–43], but it can be improved with more accurate theoretical calculations. These include, for instance, predictions for $t\bar{t}j$ at NNLO and $t\bar{t}$ at next-to-next-to-next-to-leading order (N^3LO) in QCD, off-shell effects as well as more precise treatment of Coulomb effects [44–46] that become important near the threshold region.

The current status of the top-quark mass from the direct and indirect measurements of ATLAS and CMS is summarized in Fig. 1.3.

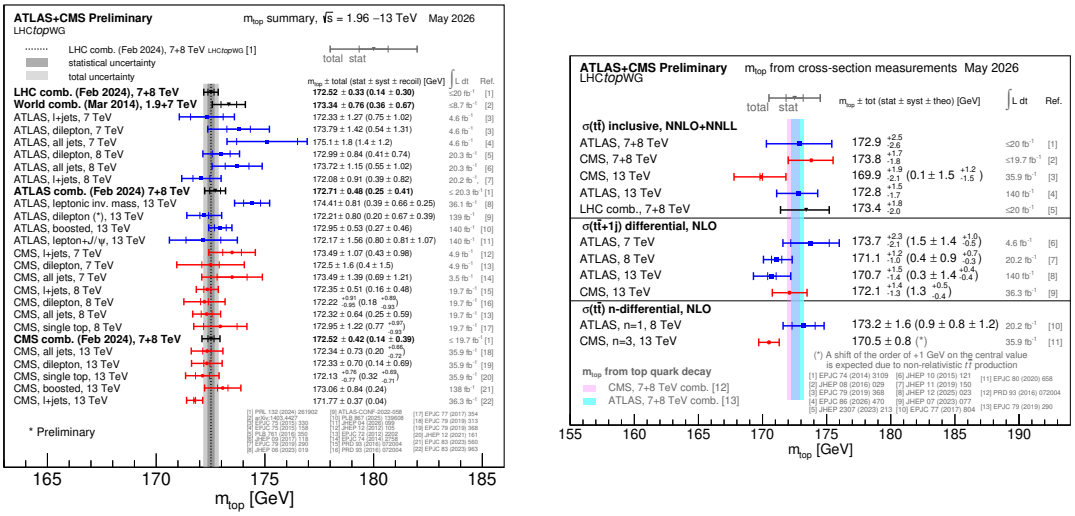

Figure 1.3: *Summary of the direct (left) and indirect (right) measurements of the top-quark mass by ATLAS and CMS. Figure is taken from the LHCTopWG Summary Plots [47].*

The combined results from ATLAS and CMS for direct measurements during LHC Run I at $\sqrt{s} = 7\,\text{TeV}$ and $\sqrt{s} = 8\,\text{TeV}$ yield $m_t = 172.52 \pm 0.33\,\text{GeV}$ [48]. A subsequent CMS measurement using a profile-likelihood approach in the lepton+jets final state at $\sqrt{s} = 13\,\text{TeV}$ achieved a comparable precision, obtaining $m_t = 171.77 \pm 0.37\,\text{GeV}$ [49]. In contrast, indirect determinations typically have larger uncertainties, as previously mentioned.

1.2.2 Top-quark decays

The very short lifetime of the top quark of about 0.5×10^{-24} s [50], allows it to decay before hadronization effects take place, a feature unique among SM quarks. Precise measurements of its decay width are essential for determining whether the observed value agrees with SM predictions as well as for probing possible new physics in its decays. From the theory side, the top-quark width Γ_t has been computed to $N^{(3)}LO$ in QCD [51], following previous calculations conducted to NNLO accuracy in QCD [52, 53]. The inclusion of next-to-leading order (NLO) electroweak corrections has also been studied in Refs. [53–55]. Although measurements of the top-quark mass have reached the remarkable accuracy of almost 0.2%, measurements of the top-quark width are far more challenging. From the experimental side, two approaches have been employed to measure the top-quark width. The first involves

direct measurements by analyzing the top-quark mass spectrum, with a particular emphasis on the resonance peak. Such efforts have been made at both the LHC and previously at the Tevatron, but with significant limitations. Specifically, the experimental resolutions are inadequate for accurately measuring Γ_t, as they are poorer than the value of the top-quark width predicted by the SM. The best value of Γ_t extracted from this method is $\Gamma_t = 1.9 \pm 0.5\,\text{GeV}$ [56] by the ATLAS collaboration. A more novel method that also utilizes events away from the resonance peak has yielded an improved value of $\Gamma_t = 1.28 \pm 0.30\,\text{GeV}$ [57]. The second approach involves indirect measurements of Γ_t from the single top-quark production in the t channel, under the assumption that no new physics influences the decay of the top quark. In this method, the top-quark width is extracted by assuming that the measured $\Gamma(t \to Wb)/\sigma(t - \text{channel})$ ratio is equal to the Standard Model prediction. Thus, the knowledge of the SM values $\Gamma(t \to Wb)_{\text{SM}}$ and $\sigma(t - \text{channel})_{\text{SM}}$, together with the observed t-channel cross section, is sufficient to determine $\Gamma(t \to Wb)$. The full top-quark width Γ_t is then computed by the following formula:

$$\Gamma_t = \frac{\Gamma(t \to Wb)}{\text{Br}(t \to Wb)} = \frac{\sigma(t - \text{channel})}{\sigma(t - \text{channel})_{\text{SM}}} \frac{\Gamma(t \to Wb)_{\text{SM}}}{\text{Br}(t \to Wb)}\,, \tag{1.3}$$

where $\text{Br}(t \to Wb)$ denotes the branching ratio of the top-quark decay to a $W^\pm$ boson and a bottom quark. The value of $\mathcal{R} = \dfrac{\text{Br}(t \to Wb)}{\sum_q \text{Br}(t \to Wq)}$, where $q = d, s, b$, has been measured by the CMS collaboration, resulting in $\mathcal{R} = 1.014 \pm 0.003\,(\text{stat}) \pm 0.032\,(\text{syst})$ [58]. In the same analysis, with the additional assumption of $\sum_q \text{Br}(t \to Wq) = 1$, indicating no new physics in the decays of top quarks, a value of $\Gamma_t = 1.36 \pm 0.02\,(\text{stat})^{+0.14}_{-0.11}\,(\text{syst})\,\text{GeV}$ was extracted, yielding the most accurate measurement of the top-quark width to date, with an uncertainty of roughly 10%. Although the top quark predominantly decays into a $W^\pm$ boson and a b quark, other decay modes such as $t \to W^\pm q$, with $q = d, s$, are also possible. These modes are, however, strongly suppressed due to the large hierarchy in the CKM mixing matrix, where $|V_{tb}| \gg |V_{ts}| > |V_{td}|$. Other SM decays of the top quark proceed through flavor-changing neutral currents, in which the top quark decays into a neutral particle (Z, γ, H, g) accompanied by an up-type quark $q = u, c$. Such decays are absent at tree level and can occur only through one-loop diagrams. The absence of tree-level contributions, combined with the additional suppression of the loop amplitudes due to the GIM mechanism [5], renders these decays extremely rare, with branching ratios of the order of $10^{-17} - 10^{-12}$ [50].

Furthermore, due to its very short lifetime, the spin of the top quark is transferred to its decay products, leading to observable spin correlations. These correlations can be probed through the angular distributions of the decay products, which provide the highest sensitivity to such effects. Measurements of spin correlations have been carried out by both the ATLAS [59] and CMS [60] collaborations. The results from both experiments are generally consistent with the SM predictions, although some deviations have been reported in the ATLAS analysis. Further details are discussed in Sec. 1.3.1. Finally, it is worth noting that top-quark entanglement has recently been observed for the first time at the LHC [61, 62], marking a unique achievement in high-energy measurements.

1.3 Top-quark associated processes

The study of production processes involving the top quark is of paramount importance, as it enables rigorous testing of the SM and searches for new physics beyond it. Indeed, measurements of the top-quark's mass and width, as previously described, along with those related to spin correlations and SM couplings, are fundamentally based on these top-quark production processes. In addition to providing stringent tests of QCD, measurements of top-quark interactions with other SM particles, such as electroweak gauge bosons and the Higgs boson, are essential for constraining anomalous top-quark couplings and discovering potential signals of new physics. In the following subsections, we give a brief overview of the current theoretical and experimental status of $t\bar{t}$ production, as well as of the associated production of $t\bar{t}$ with additional SM particles. A significant portion of the following discussion is based on Refs. [26, 50, 63], to which the reader is referred for further details.

1.3.1 Top-quark pair production

Top-quark pair production at the LHC predominantly occurs through gluon fusion, where two gluons from the colliding protons interact to create the $t\bar{t}$ pair. Specifically, nearly 90% of the total leading-order (LO) $pp \to t\bar{t}$ cross section at the LHC with $\sqrt{s} = 13\,\text{TeV}$ is attributed to gluon fusion ($gg \to t\bar{t}$), while the remaining contribution arises from quark-antiquark annihilation ($q\bar{q} \to t\bar{t}$). At NLO in QCD, new channels open up because of the emission of the additional radiation. These new channels comprise a quark/antiquark and a gluon in the initial state. As the top quarks are unstable particles with a very short lifetime, they decay before hadronization and leave their mark at the detectors through their decay products. As predicted by the SM, top quarks decay almost exclusively to a $W^{\pm}$ boson and a bottom quark, while $W^{\pm}$ bosons subsequently decay leptonically with a branching ratio of roughly 33% or hadronically with about 67%. Therefore, three decay channels can be distinguished in $t\bar{t}$ production and decays:

- *Di-lepton channel*: Both top and antitop quarks decay leptonically,
- *Lepton+jets channel*: One top/antitop quark decays leptonically and the other hadronically,
- *All-hadronic channel*: Both top and antitop quarks decay hadronically.

Due to the cleaner final-state signatures involving charged leptons, the di-lepton and lepton+jets channels are experimentally easier to identify. Although the fully hadronic channel has the largest branching fraction, it suffers from large QCD multijet backgrounds, making it more challenging to measure experimentally.

As the most widely studied process at hadron colliders, numerous theoretical predictions for $pp \to t\bar{t}$ have been developed over the years. Early calculations focused on NLO QCD corrections for stable top-quark production [64–67], which were subsequently enhanced by NLO electroweak (EW) corrections [68–72]. The matching of NLO QCD calculations to parton-shower (PS) programs was achieved in Refs. [73,74] and Refs. [75,76] through the development of the MC@NLO [73] and POWHEG [75–77] matching frameworks, respectively. The treatment of the heavy resonances using the narrow-width approximation (NWA) was studied in Ref. [78],

in which NLO+PS results were obtained for the di-lepton channel. The impact of full off-shell effects for this channel is known at NLO in QCD [79–84] and NLO EW [85]. For the lepton+jets channel, full off-shell NLO QCD calculations are available [86], while complete NLO corrections have recently been published [87]. The matching of NLO QCD calculations to PS programs that retain all off-shell and non-resonant effects was first presented in Ref. [88] for the di-lepton channel and subsequently extended to the lepton+jets channel in Ref. [89]. Furthermore, fixed-order predictions at higher orders in the perturbative expansion have also been achieved, including NNLO QCD corrections at both inclusive [32–35] and differential levels [90–92], along with the inclusion of NLO EW corrections [93]. Additionally, incorporating top-quark decays into NNLO QCD calculations has been accomplished in Refs. [94, 95] using the NWA framework, while approximate NNLO QCD predictions that include exact NNLO corrections in top-quark decays were published in Ref. [96]. The NNLO QCD results have also been matched to PS algorithms [97, 98] via the development of the $\texttt{MiNNLO}_{\text{PS}}$ method [99, 100]. Soft-gluon resummation effects were first included at next-to-leading logarithmic (NLL) accuracy [101, 102] and later improved to next-to-next-to-leading logarithmic (NNLL) accuracy [103–106]. Finally, although progress towards the $\text{N}^{(3)}\text{LO}$ direction has been made [107–110], the exact predictions at this perturbative order are still pending.

Following the discovery of the top quark through the $pp \to t\bar{t}$ production process at the Tevatron [22, 23], numerous measurements of this process have been conducted at both the Tevatron and the LHC. A summary of these measurements at the level of the inclusive cross section is displayed in Fig. 1.4, showcasing results for $\sqrt{s} = 1.96\,\text{TeV}$ at the Tevatron and $\sqrt{s} = 5.02, 7, 8, 13, 13.6\,\text{TeV}$ at the LHC. The observed cross sections are compared with the NNLO + NNLL theoretical predictions of Ref. [35] and are found to be consistent with them within the uncertainties. The theoretical uncertainties originate from missing higher-order corrections, parton distribution functions and the strong coupling constant α_s, amounting to roughly 3%. The recent ATLAS measurement at $\sqrt{s} = 13\,\text{TeV}$ [40] reached a remarkable 1.3% precision, with systematic uncertainties as the dominant source of the experimental error. It is worth pointing out that experimental uncertainties are expected to be reduced at the high-luminosity phase of the LHC (HL-LHC) [111], highlighting the importance of even more precise theoretical predictions for improving the comparison with experimental data. As also shown in Fig. 1.4, dilepton and lepton+jets channels involving electrons and/or muons have been studied by both collaborations. For a more comprehensive overview of these studies, the reader is referred to Ref. [50]. In addition to inclusive measurements, the analysis of differential distributions is important because it provides, among others, more rigorous tests of perturbative QCD in different regions of phase space and contributes to the determination of PDFs in global fits. Such measurements have also been performed for a variety of observables at the LHC and generally demonstrate good agreement with theoretical predictions. However, for certain distributions, the inclusion of NNLO QCD corrections is essential to achieve better agreement with the experimental data. A notable example is the transverse momentum of the reconstructed top quark that has been analyzed by both the CMS [113] and ATLAS [114] collaborations in the lepton+jets channel. In this case, as shown on the left plot of Fig. 1.5, the NLO+PS predictions tend to overestimate the data, leading to significant deviations, while comparisons with the NNLO theoretical predictions show better

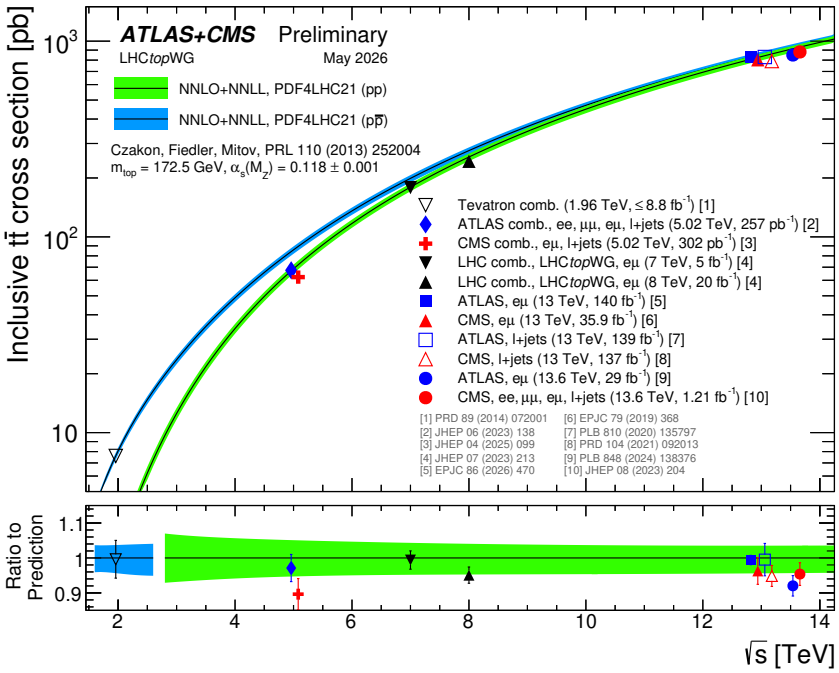

Figure 1.4: *Summary of the LHC and Tevatron inclusive measurements of the top-quark pair production compared to the NNLO+NNLL theoretical predictions [35], for different center-of-mass energies. Figure is taken from the LHCTopWG Summary Plots [112].*

agreement. In the ATLAS collaboration, the NLO+PS predictions were reweighted to the NNLO+NNLL total cross section, while a direct comparison with the NNLO QCD corrections [115, 116] was conducted by CMS, reaching the same conclusions. This highlights the need for higher-order QCD corrections in order to accurately account for the experimental observations. Nonetheless, particularly in studies of the di-lepton channel, a slight tension between the data and theoretical predictions is observed for certain classes of observables sensitive to spin correlations, even after accounting for NNLO corrections. This is illustrated in the right plot of Fig. 1.5, which depicts the angular separation between the two oppositely charged leptons, $\Delta\phi(l^+, l^-)$, arising from the decay products of the top quarks. The comparison with the NNLO predictions [94] improves slightly the agreement with the experimental data [59, 60] compared to the NLO+PS predictions, but significant discrepancies remain.

1.3.2 $t\bar{t}$ + jets

After the production of a $t\bar{t}$ pair, the process with the largest cross section at the LHC is $pp \to t\bar{t}j$, where j represents a light jet. It is therefore not surprising that this process has also been extensively studied both experimentally and theoretically. We already discussed before that this process has been used experimentally for the precise determination of the top-quark mass [37–39]. Beyond that, $pp \to t\bar{t}j$ serves as an important background in SM processes involving high jet multiplicities. For instance, it represents the primary background in Higgs boson production, particularly in the $H \to W^+W^-$ channel [118, 119]. In addition, it is an important

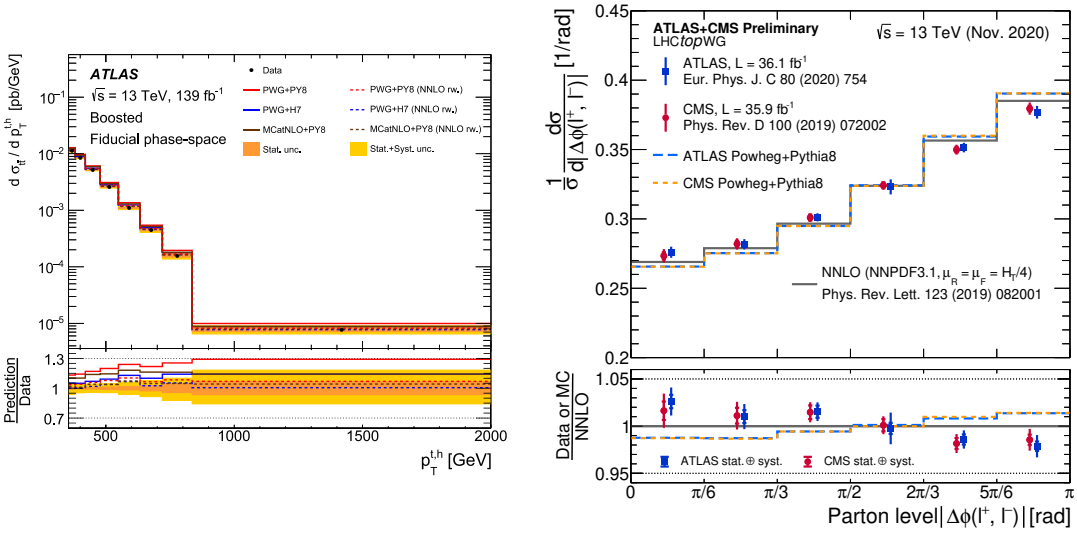

Figure 1.5: *Differential cross-section distributions for top-quark pair production and decay, showing the transverse momentum of the hadronically decaying top quark $p_T^{t,h}$ (left) and the azimuthal separation between oppositely charged leptons, $\Delta\phi(l^+, l^-)$ (right), from top-quark decays. In the left panel, the data are compared to NLO+PS predictions, including results reweighted to the NNLO+NNLL $pp \to t\bar{t}$ cross section. The right panel presents the measured distributions by ATLAS and CMS at the parton level compared with NLO+PS and NNLO predictions. The left figure is taken from the ATLAS analysis in Ref. [114], while the right plot is taken from the LHCTopWG Summary Plots [117].*

background to searches for new physics in W^+W^- production in association with jets.

From the theory side, NLO QCD corrections to stable $t\bar{t}j$ production were computed in Refs. [120, 121], while the inclusion of NLO EW corrections was achieved almost a decade later in Ref. [122]. The matching of the NLO fixed-order calculations with parton-shower algorithms was performed in Refs. [123, 124] and further improved in Ref. [125] to preserve spin correlations between the production and decay of top quarks at LO accuracy. To enhance the overall modeling of $t\bar{t}$, merging $pp \to t\bar{t}+$ jets samples with different jet multiplicities was presented in Ref. [126], and later supplemented by the inclusion of EW corrections into the merging of $t\bar{t}$ and $t\bar{t}j$ samples in Ref. [122]. The incorporation of top-quark decays at the matrix-element level was initially described at LO accuracy [127] and subsequently improved to NLO accuracy in perturbative QCD via the use of the NWA [128]. The impact of full off-shell effects, which effectively include all resonant and non-resonant contributions, is also known for the di-lepton channel [129, 130]. Recently, building on the advances reported in Refs. [131–134], NNLO QCD corrections to the on-shell $t\bar{t}j$ process were presented in the leading-color approximation, neglecting contributions from heavy quarks in the finite part of the two-loop amplitude [135]. The impact of NNLO QCD corrections has been shown to be important as it substantially reduces the theoretical uncertainties associated with missing higher-order effects.

The production of a $t\bar{t}$ pair together with more than one jet is even more challenging to study theoretically due to the higher-parton multiplicity that further complicates the computation. Nevertheless, NLO QCD corrections have been known for

many years for the $pp \to t\bar{t}jj$ [136, 137] and $pp \to t\bar{t}jjj$ [126] processes. In the latter study, results were provided using the `MiNLO` framework [138] in addition to the standard NLO calculations. The `MiNLO` method comprises a considerable part of this thesis and is thoroughly discussed in Chapter 5. Moreover, fixed-order predictions matched to parton showers are available for top-quark-pair production in association with only up to two jets [139]. In this work, top-quark decays were described by the parton shower and spin correlations were only retained at LO accuracy. In a later study [140], NLO QCD corrections for the $pp \to t\bar{t}jj$ process were properly included in both production and decay stages of the top quarks using the NWA, extending the accuracy of spin correlations to NLO.

Another process closely related to $pp \to t\bar{t}jj$ is $pp \to t\bar{t}b\bar{b}$. In fact, the former constitutes an important background to $pp \to t\bar{t}b\bar{b}$ due to the finite mis-tagging probability in experiments, which may result in a light-flavor jet being misidentified as a b-jet. Apart from that, $pp \to t\bar{t}b\bar{b}$ serves as the dominant QCD background to $t\bar{t}H$ production in the $H \to b\bar{b}$ decay channel and represents one of the main backgrounds to four-top-quark production. It therefore follows that precise measurements of this process are crucial for better control of $t\bar{t}H$ and $t\bar{t}t\bar{t}$, which have both been utilized to constrain the top-Yukawa coupling. Finally, the $pp \to t\bar{t}b\bar{b}$ process is very interesting on its own because of the multiple scales involved in its description. Its study can therefore deepen our understanding of top-quark dynamics across different energy scales. For this process, NLO QCD corrections for the on-shell $t\bar{t}b\bar{b}$ production have been known for quite some time [141–146], while NLO QCD predictions matched to parton showers have also been calculated. Specifically, results are available for stable top quarks using either massless [147] or massive b quarks [148, 149], as well as including top-quark decays for both massless [150] and massive b quarks [149, 151]. Recently, NLO QCD predictions were matched to parton shower with b-quark mass effects using a variable flavor number scheme [152]. In another study [153], NLO QCD results were also matched to parton shower in the five-flavor scheme by proposing a novel method to enhance the b-jet selection efficiency. In these calculations, whenever top-quark decays were included, spin correlations were retained at most at LO accuracy, while higher-order QCD effects in the top-quark decays were omitted. In Refs. [154, 155], full off-shell effects for the di-lepton channel were reported, and in a subsequent study, the calculation was additionally performed using the NWA [156]. In both cases, spin correlations are fully preserved at NLO. It was found that the NWA performs well and agrees with the full off-shell predictions at both the integrated and differential cross-section levels. Finally, predictions for the $pp \to t\bar{t}b\bar{b}j$ process have also been computed in Ref. [157], improving the overall description of the jet activity in the $t\bar{t}b\bar{b}$ process.

The top-quark pair production process in association with jets has been extensively studied and many analyses from ATLAS [158–167] and CMS [168–172] have been conducted at $\sqrt{s} = 7, 8, 13\,\text{TeV}$. Dedicated CMS analyses [173, 174] have simultaneously measured $t\bar{t}b\bar{b}$ and $t\bar{t}jj$ production and their cross-section ratio $R_b = \sigma_{t\bar{t}b\bar{b}}/\sigma_{t\bar{t}jj}$. This ratio is particularly useful for testing and improving the modeling of both processes, as several systematic uncertainties partially cancel in the ratio compared to the individual cross sections. Finally, both ATLAS and CMS have also performed measurements sensitive to $pp \to t\bar{t}c\bar{c}$ production [167, 171]. These studies provide important constraints on heavy-flavor modeling and thereby contribute to a better control of the $t\bar{t}b\bar{b}$ and $t\bar{t}c\bar{c}$ backgrounds in $t\bar{t}H$ searches.

1.3.3 $t\bar{t}$ + photons

Among the top-quark pair production processes in association with an electroweak gauge boson at the LHC, $pp \to t\bar{t}\gamma$ has the largest cross section. Studying this process provides a direct probe of the top-quark electric charge [175] and offers valuable insight into the structure of the $t\bar{t}\gamma$ vertex. Knowledge of these properties is of paramount importance, as it can be used to constrain new physics effects within the framework of the Standard Model Effective Field Theory (SMEFT) [176], as well as anomalous electric dipole moments of the top quark predicted in many BSM scenarios [177–184]. Nonetheless, the accurate description of $pp \to t\bar{t}\gamma$ poses many challenges both theoretically and experimentally, primarily owing to the large contributions from photon emission in top-quark decays, which can account for up to 50% of the total signal [185, 186] under certain fiducial phase-space cuts. From an experimental perspective, these emissions introduce additional difficulties in reconstructing the top-quark momenta [187].

From the theoretical side, the first higher-order predictions for the on-shell $pp \to t\bar{t}\gamma$ production process were obtained at NLO QCD [188–190] and NLO EW [191], and they were recently supplemented by the inclusion of all subleading contributions in Ref. [192], yielding complete NLO results. The treatment of top-quark decays was initially addressed through matching to parton showers in Ref. [193], and later incorporated at the matrix-element level using the NWA in Ref. [185], effectively capturing NLO QCD corrections in the top-quark decays. Furthermore, the impact of all resonant and non-resonant contributions was investigated in Refs. [194,195] by computing full off-shell effects at NLO in QCD for the di-lepton channel. In a complementary study [186], these effects were further compared to various NWA approaches, where photon emission occurs either during the production stage alone or during both production and decay stages. Recently, complete NLO predictions have become available in Ref. [196] for the di-lepton channel using the NWA for the modeling of the unstable particles, revealing that subleading contributions have a significant impact in the tails of certain dimensionful distributions. For the same channel, Ref. [197] assessed the impact of different photon-isolation prescriptions, including the fixed-cone criterion used in ATLAS and CMS, thereby allowing for a direct comparison with experimental measurements. For this purpose, predictions were provided at NLO in QCD, retaining all full off-shell effects. A significant effort has also been taken towards the NNLO QCD corrections to the stable $pp \to t\bar{t}\gamma$ production process. In that direction, the authors of Ref. [198] computed approximate NNLO (aNNLO) calculations based on soft-gluon resummation, and combined the results with the complete NLO corrections. Additionally, analytic expressions for the one-loop virtual QCD amplitudes up to $\mathcal{O}(\varepsilon^2)$ have been derived in Ref. [199], while many relevant studies on $t\bar{t}\gamma$ have contributed towards the evaluation of the two-loop amplitudes [131,132,200,201]. Recently, approximate two-loop amplitudes for $t\bar{t}\gamma$ production were reported in Ref. [202]. However, exact NNLO QCD results are not yet fully available.

The top-quark pair production in association with two photons is also of particular interest since it is the main background to $t\bar{t}H$ production in the $H \to \gamma\gamma$ decay channel. For this process, NLO QCD corrections as well as matching to parton shower have been known for some time for on-shell $t\bar{t}\gamma\gamma$ production [190, 203–205], while NLO EW corrections have also been recently computed [192]. Beyond that, Ref. [206] reported NLO QCD corrections in both the production and decay of top

quarks for the di-lepton and lepton+jets channels, employing the NWA and consistently incorporating photon emission in both the production and decay stages. Finally, complete NLO corrections are available for $pp \to t\bar{t}\gamma\gamma$ in the di-lepton channel within the context of the NWA [196].

Both $pp \to t\bar{t}\gamma$ and $pp \to t\bar{t}\gamma\gamma$ production processes have been observed at the LHC. In particular, the $pp \to t\bar{t}\gamma$ process was first observed by the ATLAS collaboration with $\sqrt{s} = 7\,\text{TeV}$ [207], while ATLAS recently reported the observation of $pp \to t\bar{t}\gamma\gamma$ with $\sqrt{s} = 13\,\text{TeV}$ [208]. Apart from the discovery papers, many other analyses of $t\bar{t}\gamma$ production have been conducted by both the ATLAS and CMS collaborations [209–216], focusing on the di-lepton and lepton+jets channels. Some of these analyses [213–215] also derive constraints on Wilson coefficients associated with the $t\gamma$ and tZ interactions within the SMEFT framework.

1.3.4 $t\bar{t} + Z$

The production of a Z boson in association with a $t\bar{t}$ pair is a relatively rare process at the LHC. Nevertheless, it is of particular interest for several reasons. First, it provides direct access to the coupling between the top quark and the Z boson already at the tree level. Any deviation from the corresponding SM prediction could thus indicate signs of new physics. For this reason, this process is highly relevant for searches involving exotic particles, such as heavy Z' resonances or vector-like leptons [217–223], and has been widely used to constrain effective field theory (EFT) operators [176, 177, 184, 217–226]. Furthermore, $pp \to t\bar{t}Z$ constitutes an important background to several SM processes, particularly $pp \to t\bar{t}H$, $pp \to tZ$, and $pp \to t\bar{t}t\bar{t}$. The unstable nature of the Z boson leads to decays that occur either hadronically or leptonically. However, its leptonic decay channels are typically preferred in experimental analyses due to their cleaner signatures and reduced QCD backgrounds. In addition, the invisible decay channel $Z \to \nu_\ell\bar{\nu}_\ell$ represents an irreducible background in dark matter searches, as it leads to missing transverse energy signatures similar to those expected from dark matter particles. Therefore, the role of $pp \to t\bar{t}Z$ as a background in these searches [227–229] is also fundamental.

The first predictions for the inclusive $pp \to t\bar{t}Z$ process were obtained in Ref. [230] at NLO in QCD and later revisited in Refs. [190, 231]. The inclusion of NLO EW corrections to the dominant LO contributions was also reported in Ref. [232]. Also known are soft-gluon resummation effects at NNLL accuracy [233–235]. Recently, the NLO QCD predictions were further improved by computing approximate NNLO and N$^{(3)}$LO contributions obtained by adding soft-gluon corrections to the exact NLO QCD result [236]. The top-quark decays were initially incorporated by matching fixed-order NLO QCD calculations to parton-shower simulations [237,238]. To preserve spin correlations between the production and decay stages of the top quarks, in Ref. [239], the $Z \to \ell^+\ell^-$ decay was included at the matrix-element level while also considering interference contributions with the $pp \to t\bar{t}\gamma^{(*)} \to t\bar{t}\ \ell^+\ell^-$ process. These results were subsequently also matched to parton-shower algorithms using the POWHEG-BOX [77] framework. Furthermore, full off-shell predictions at NLO in QCD have also been computed, first for the $Z \to \nu_\ell\bar{\nu}_\ell$ decay channel [228], and later also for the $Z \to \ell^+\ell^-$ decay channel [240]. In both cases, predictions have also been obtained using the NWA [226, 229]. The latter was found to perform poorly for many dimensionful and dimensionless observables in the $Z \to \ell^+\ell^-$

decay channel [240], underscoring the importance of full off-shell effects for a more accurate description of the underlying process. Finally, the full off-shell description of the $Z \to \ell^+\ell^-$ decay channel was further extended in Ref. [241], where complete NLO corrections were computed for the first time.

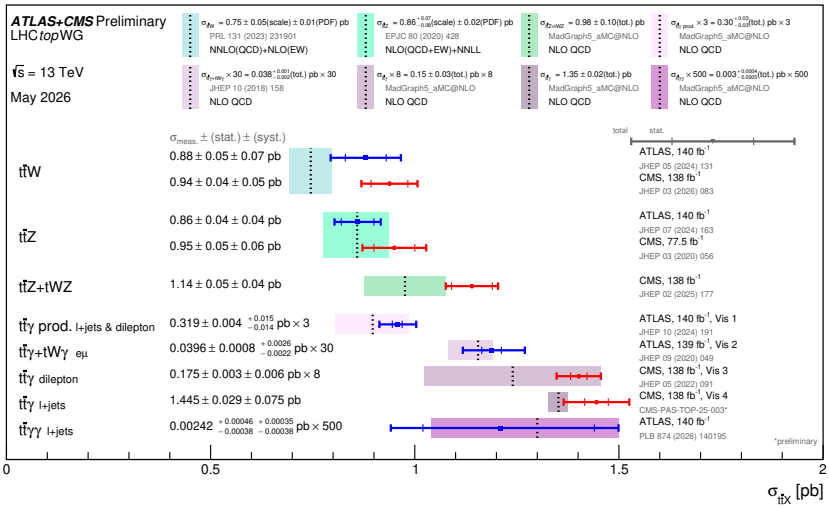

Figure 1.6: *Overview of the $pp \to t\bar{t} + X$ $(X = W, Z, \gamma)$ production processes at the LHC. The measured cross sections from ATLAS and CMS at $\sqrt{s} = 13\,\text{TeV}$ are compared with the corresponding theoretical predictions. Figure is taken from the LHCTopWG Summary Plots [242].*

Despite its small cross section, $pp \to t\bar{t}Z$ production has been measured by both the ATLAS and CMS collaborations [243–251], yielding results that are in good agreement with the SM predictions. In addition, both collaborations have reported constraints on SMEFT Wilson coefficients in their recent analyses [250, 251]. Nonetheless, as illustrated in Fig. 1.6, the experimental uncertainties are already comparable to those of the NLO (QCD+EW) + NNLL theoretical predictions [235]. Given the anticipated reduction of experimental uncertainties at the HL-LHC [252], further enhancements in theoretical predictions through higher-order QCD calculations will be essential in the coming years, aiming to minimize the uncertainties associated with missing higher-order contributions.

1.3.5 $t\bar{t} + H$

Undoubtedly, the Higgs boson plays a pivotal role in particle physics, as it is responsible for giving mass to SM particles through the electroweak symmetry breaking (EWSB) mechanism. Accurate calculations of its properties are crucial for testing the consistency of the SM, probing potential new-physics effects, and assessing the stability of the electroweak vacuum. The discovery of the Higgs boson at the LHC [253, 254] completed the final missing piece of the SM puzzle, while at the same time opened up avenues for further exploration of its properties with higher precision. Similar to the top quark, the Higgs boson is a heavy unstable particle that can only be detected through its decay products. Although the $H \to b\bar{b}$ channel has the largest branching ratio of about 58% [255], the discovery of the Higgs boson was primarily driven by the observation of a significant excess of events in the $H \to \gamma\gamma$ and $H \to ZZ^{(*)} \to 4\ell$ channels, both of which have branching ratios well below

1%, amounting to roughly 0.2% and 0.03% [255]. This is due to the much cleaner experimental signatures of these channels, which do not suffer from large QCD backgrounds. The production of a Higgs boson occurs predominantly via gluon fusion through a top-quark loop. While other quarks that couple to the Higgs boson also contribute, their effects are significantly suppressed due to their smaller masses. In contrast, the top Yukawa coupling, $y_t = \sqrt{2}m_t/v$, is of order unity as a consequence of the large top-quark mass. Therefore, Higgs boson production provides indirect access to y_t through these loop-induced contributions. The production of a Higgs boson in association with a $t\bar{t}$ pair is special because, unlike $gg \to H$, it offers direct sensitivity to y_t, which enters already at tree level. Despite representing only 1% of the total Higgs boson production cross section [255], $pp \to t\bar{t}H$ production has been remarkably observed by both the ATLAS [256] and CMS [257] collaborations, following earlier searches in several channels [258–267]. After the discovery, $t\bar{t}H$ has also been used to constrain BSM models related to extended Higgs sectors that could give rise to CP-odd Higgs-like particles [268–270]. A current summary of the observed signal strengths, $\mu = \sigma_{t\bar{t}H}/\sigma^{\mathrm{SM}}_{t\bar{t}H}$, for multiple decay channels is shown in Fig. 1.7. In contrast to the 4ℓ, $\gamma\gamma$ and multilepton channels, which are dominated by

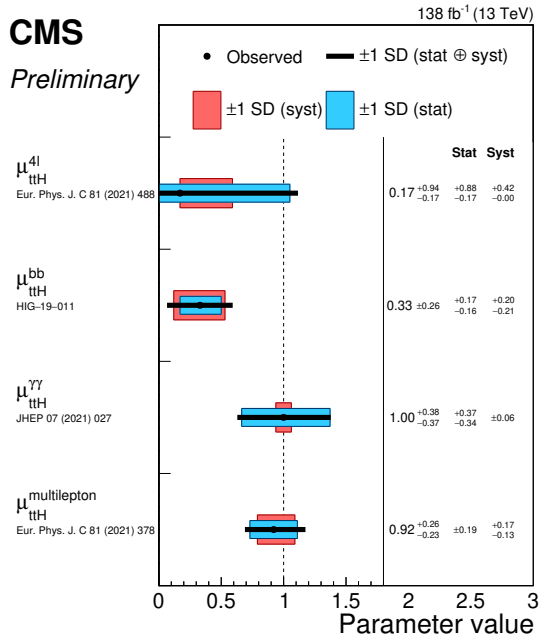

Figure 1.7: *Observed signal strengths $\mu_{t\bar{t}H}$ for different Higgs-boson decay channels in the $pp \to t\bar{t}H$ process. Figure is taken from the Higgs PAG Summary Plots [271].*

statistical uncertainties, the present experimental limitations in the $H \to b\bar{b}$ decay channel arise primarily from systematic uncertainties [272–274]. These are related to the treatment of the large QCD backgrounds affecting this channel, such as $t\bar{t}jj, t\bar{t}b\bar{b}$ and $t\bar{t}Z$ ($Z \to b\bar{b}$). Finally, a recent analysis of the $t\bar{t}H$ process in the $H \to c\bar{c}$ decay channel [275], when combined with previous studies on WH/ZH ($H \to c\bar{c}$) [276], established the most stringent limit on the Higgs-charm Yukawa coupling modifier κ_c, yielding $|\kappa_c| < 3.5$.

A significant effort has also been made by the theoretical community to accurately describe the $pp \to t\bar{t}H$ process. The first predictions at NLO in QCD [277–281] for stable $t\bar{t}H$ production were developed in the early 2000s and were

subsequently enhanced with the inclusion of NLO EW corrections [232, 282, 283]. Soft-gluon resummation effects, which are crucial for accurately capturing the dynamics near the $t\bar{t}H$ threshold, are known up to NNLL accuracy [284–289]. More realistic phenomenological analyses that include top-quark and Higgs-boson decays were initially performed in the context of matching the NLO QCD calculations to parton-shower simulations [190, 290–292]. Later, the impact of NLO EW Sudakov logarithms (EWSL) was also investigated by combining EWSL with the NLO (QCD) + PS results in Ref. [293]. Higher-order QCD effects in top-quark decays, not described by the parton shower but already incorporated at the matrix-element level, were first computed at NLO in QCD in Ref. [294], where the Higgs boson was treated as stable while off-shell effects were retained. This analysis was subsequently extended to include NLO electroweak corrections [295]. In a complementary study [296], the impact of CP-violating Higgs couplings was explored by treating the Higgs boson as stable and consistently including full off-shell effects in the dilepton channel. Various decay channels of the Higgs boson have also been described at the matrix element level using the NWA [297] and retaining all full off-shell effects associated with the decay products of $t\bar{t}$. The calculation of NNLO QCD corrections to the $pp \to t\bar{t}H$ process has been conducted at both the inclusive [298, 299] and differential [300] levels, where the treatment of the two-loop amplitude was performed in a soft Higgs boson approximation. These results were recently combined with NNLL soft-gluon resummation and EW corrections in Ref. [301], yielding the most accurate NNLO+NNLL+EW predictions for this process to date. Nonetheless, a complete NNLO QCD description of $pp \to t\bar{t}H$ remains challenging. Towards that direction, significant progress has been achieved through the calculation of one-loop amplitudes up to $\mathcal{O}(\varepsilon^2)$ in Refs. [302, 303], as well as in the computation of full two-loop virtual amplitudes [304–306]. Finally, very recently, Ref. [307] presented the first NNLO QCD calculation for $pp \to t\bar{t}H$ matched to parton showers using the $\texttt{MiNNLO}_{\text{PS}}$ method [99, 100]. The calculation is exact except for the two-loop amplitude, which is approximated through a pointwise combination of the soft Higgs-boson and high-energy limits across the full phase space.

1.3.6 $t\bar{t} + W^{\pm}$

Unlike other associated top-quark production processes, $t\bar{t}W^{\pm}$ production proceeds through the $q\bar{q}'$ channels at LO, while the gluon-initiated gq and gg subprocesses enter only at NLO and NNLO, respectively. This underscores the importance of higher-order corrections for a precise description of $pp \to t\bar{t}W^{\pm}$, given the sizable contribution from gluon PDFs. Due to its strong sensitivity to quark–antiquark initial states, $pp \to t\bar{t}W^{\pm}$ plays a special role in global SMEFT fits [308], particularly in probing four-quark operators, and also allows for precise measurements of the top-quark charge asymmetry and asymmetries in its decay products [190,309,310]. Since the $W^{\pm}$ boson decays either into a charged lepton and its corresponding neutrino or into a quark-antiquark pair, combined with the decays from the $t\bar{t}$ system, this leads to a variety of final-state channels ranging from purely hadronic to multilepton signatures. From this perspective, $t\bar{t}W^{\pm}$ is one of the rare processes capable of producing same-sign lepton signatures. Notably, these signatures are present in many BSM scenarios that predict an enhancement in its production cross-section, highlighting its sensitivity to a wide range of new-physics models involving, among

others, new heavy top-quark resonances [311, 312], heavy Majorana neutrinos [313] and extended Higgs sectors [314–317]. Furthermore, owing to the diversity of these final-state signatures, $pp \to t\bar{t}W^{\pm}$ is a background to many SM processes featuring leptons and b jets in the final state, with particular significance for processes such as $pp \to t\bar{t}H$ and $pp \to t\bar{t}t\bar{t}$.

The $pp \to t\bar{t}W^{\pm}$ process has been extensively studied in the literature. In particular, theoretical predictions at NLO in QCD with stable top quarks and $W^{\pm}$ boson were provided in Refs. [190, 309, 318] and they were further supplemented by the inclusion of electroweak corrections in Refs. [232, 319] and subleading contributions in Refs. [320, 321]. Results matched to parton-shower algorithms using either the POHWEG method or the MC@NLO framework were obtained in Refs. [190, 237, 309, 318, 322] at NLO in QCD, while the impact of subleading electroweak corrections was also studied in Refs. [322, 323]. In addition, soft-gluon resummation effects were incorporated in Refs. [234, 235, 324–326] at the NNLL accuracy. To improve the accuracy and modeling of the $pp \to t\bar{t}W^{\pm} + X$ process, merged predictions with up to 2 jets at NLO in QCD were assessed in Ref. [327], while electroweak and subleading contributions were also incorporated in Ref. [328], by utilizing the FXFX [329] framework. In this study, the decays of the top quarks and the $W^{\pm}$ boson were modeled at LO accuracy using MADSPIN [330] that retains LO spin correlations. The impact of higher-order QCD corrections in the decays of the $t\bar{t}W^{\pm}$ system within the NWA was first studied in Ref. [331], keeping full NLO spin correlations, while full off-shell effects at NLO in QCD were later computed for the multilepton channel in Ref. [332]. Two additional studies reproduced [333] and extended [334] the full off-shell calculation of Ref. [332] for the same multi-lepton channel by accounting also for electroweak corrections and subleading contributions. The overall impact of full off-shell effects compared to matched-to-parton shower predictions was further investigated in Ref. [335], while special emphasis on the effect of top-quark modeling on charge asymmetries was given in Ref. [310]. Finally, the impact of matrix-element corrections (MEC) during the showering of the $pp \to t\bar{t}W^{\pm}$ system, to compensate for the lack of hard emissions in the decays, was studied in Ref. [336]. However, for the $pp \to t\bar{t}W^{\pm} + X$ process, the important gq and gg channels open up only at NLO and NNLO accuracy in QCD, respectively, while the LO contributions involve solely channels with quarks in the initial state. For this reason, in Ref. [337], full off-shell predictions for the $pp \to t\bar{t}W^{+}j + X$ process were provided for the first time, effectively describing the kinematics of the leading jet at NLO accuracy. In this process, the gq channel is properly included at LO, while the gg initiated subprocess is incorporated at NLO. One of the key findings from Ref. [337] was the observation of significant shape distortions between the fully off-shell $pp \to t\bar{t}W^{+}j + X$ and $pp \to t\bar{t}W^{+} + X$ processes at the differential level, indicating that the behavior of the extra jet in $pp \to t\bar{t}W^{+}j + X$ is quite important. Finally, in Ref. [338], the `MiNLO` method [138] was applied to the fully off-shell $pp \to t\bar{t}W^{+} + X$ process in the multilepton channel, together with a merging procedure for samples of different jet multiplicities. A detailed discussion of these results is presented in Chapter 6 of this thesis. Significant progress has also been made beyond NLO corrections to $pp \to t\bar{t}W^{\pm}$, particularly towards NNLO QCD corrections. Specifically, NNLO QCD corrections combined with NLO QCD + EW results are known up to the finite part of the two-loop amplitudes [339], where certain approximations were employed [340–343]. Furthermore, recent advances toward exact

NNLO QCD corrections have been reported in Refs. [344, 345], including one-loop QCD corrections to $\bar{u}d \to t\bar{t}W$ at $\mathcal{O}(\varepsilon^2)$ and a complete set of two-loop Feynman integrals at NNLO QCD within the leading-color approximation. Finally, soft-gluon corrections at aNNLO and aN$^{(3)}$LO, including also NLO QCD + EW contributions, were provided in Ref. [346].

From the experimental side, ATLAS and CMS collaborations have measured $pp \to t\bar{t}W^{\pm}$ using data collected with $\sqrt{s} = 8\,\text{TeV}$ [243, 244] and $\sqrt{s} = 13\,\text{TeV}$ [245–247, 347–350]. As illustrated in Fig. 1.6, a tension between the observed and theoretical cross sections is evident, despite the use of approximate NNLO predictions [339] for the $t\bar{t}W^{\pm}$ production process, unlike other associated processes shown. Discrepancies between theoretical predictions and data also persist at the differential cross-section level for certain observables. An illustrative example is presented in Fig. 1.8, taken from an ATLAS analysis [349], showing the angular separation between the leading b jet and charged lepton $\Delta R_{\text{lb, lead}}$, across multiple decay channels. The left plot displays absolute predictions, while the right plot shows normalized differential results. Notably, the observed results were also compared with the full off-shell predictions of Ref. [332] for the multilepton channels. Nonetheless, none of the theoretical predictions fully reproduces the experimental data. Given that deviations were expected for absolute predictions due to the tension observed at the integrated level, normalized distributions provided a more robust comparison and improved the agreement with the experimental data. However, even in this case, significant discrepancies remained. Finally, the leptonic charge asymmetry has also

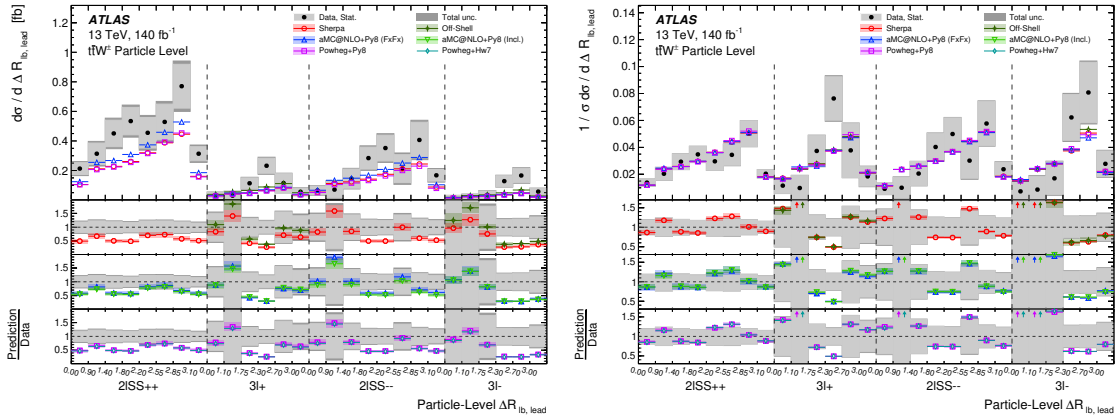

Figure 1.8: *Absolute (left) and normalized (right) differential distributions for the angular separation between the leading b-tagged jet and charged lepton, $\Delta R_{lb,lead}$, in the $pp \to t\bar{t}W^{\pm}$ process. The ATLAS experimental data are compared with the theoretical NLO+PS predictions, as well as the full off-shell results from Ref. [332]. Figures are taken from Ref. [349].*

been measured by both the ATLAS [348] and CMS [350] collaborations, with the results found to be consistent with SM expectations.

1.3.7 $t\bar{t} + t\bar{t}$

The simultaneous production of four top quarks is among the rarest processes observed at the LHC. Despite its very small SM cross section, the $pp \to t\bar{t}t\bar{t}$ process is

particularly interesting, as it provides a sensitive probe of various new-physics scenarios and direct access to the top Yukawa coupling y_t, already at the Born level. In the SM, the top Yukawa coupling is given by $y_t = \sqrt{2}m_t/v$, and is therefore directly related to the top-quark mass and the Higgs vacuum expectation value. Precise experimental constraints on y_t are thus of great importance, since any deviation from the SM prediction could be a hint for potential new physics. For this purpose, the four-top quark production process has been widely used by both the ATLAS and CMS collaborations to provide exclusion limits on y_t [351–353]. The current experimental constraints on the top-Yukawa coupling strength modifier $\kappa_t = y_t/y_t^{\text{SM}}$ are $|\kappa_t| < 1.9$ and $|\kappa_t| < 1.7$ at 95% confidence level, as reported by the ATLAS [353] and CMS [351] analyses, respectively [1]. After constraining the top Yukawa coupling, the four-top quark production process can also be used together with $pp \to t\bar{t}H$ to constrain other SM parameters, such as the decay width of the Higgs boson and its branching ratio to other SM particles [355]. In addition, the $pp \to t\bar{t}t\bar{t}$ process is extremely sensitive to a plethora of BSM models that predict an enhancement in its cross section. Such models include top-philic scenarios [220, 356], where new heavy resonances decay into a pair of top quarks, extended Higgs sectors, where additional scalar or pseudoscalar bosons can be produced in association with a top-quark pair [357–360], composite top-quark models, featuring a composite right-handed top quark [361–364], extra-dimensional frameworks with heavy Kaluza–Klein gluons or quarks [365], and supersymmetric scenarios predicting scalar gluons produced in pairs [366, 367]. On top of that, it can also be studied to constrain Wilson coefficients within the SMEFT framework [368–370]. Several of these SMEFT operators induce contact interactions among four top quarks and can therefore directly be probed by the $pp \to t\bar{t}t\bar{t}$ process.

Due to the large number of top quarks produced, four-top production leads to a variety of possible final states, ranging from purely hadronic events to signatures containing up to four charged leptons. Recently, following numerous analyses [351,371–377], both the ATLAS [353] and CMS collaborations [378] reported the discovery of the four-top quark production, by analyzing the 2ℓ same-sign (SS), 3ℓ and 4ℓ channels. The observed cross sections were found to be consistent with the SM predictions, but the total experimental uncertainties remain large, of the order of $25\% - 30\%$. Experimental uncertainties are expected to be significantly reduced at the HL-LHC, highlighting the importance of achieving higher-precision calculations in the near future. Since NNLO QCD computations for $pp \to t\bar{t}t\bar{t}$ are not anticipated soon, improving the modeling of this process through a better description of top-quark decays, including NLO corrections, could be highly beneficial. Overall, opportunities for discovering new physics remain open, making precise theoretical predictions more crucial than ever for meaningful comparisons with forthcoming experimental data.

From the theory side, the first predictions for the $pp \to t\bar{t}t\bar{t}$ process at NLO in QCD were obtained more than a decade ago in Ref. [379] and were recomputed a few years later in Ref. [190]. Complete NLO predictions including QCD and electroweak (EW) corrections to all LO contributions were also provided in Ref. [320], estimating for the first time the impact of the subleading contributions to

[1] It is worth noting that more precise constraints on κ_t are obtained from measurements of $t\bar{t}H$ and tH production, yielding $0.86 < \kappa_t < 1.26$ at 95% confidence level by CMS [270] and $\kappa_t = 1.11^{+0.11}_{-0.11}$ by ATLAS [354].

this process. More recently, threshold resummation for the production of four top quarks accurate to NLO (QCD + EW) + NLL′ has also become available in Refs. [380, 381], providing the most accurate predictions to date for stable four-top quark production. Nonetheless, in all the aforementioned studies, the top-quark decays were not included in the calculations. Incorporating top-quark decays is, however, crucial for a more realistic description of the fiducial phase-space regions. Towards that direction, in Ref. [382], the theoretical predictions for the $pp \to t\bar{t}t\bar{t}$ process were matched to parton shower, using the POWHEG framework [75, 77] interfaced with the PYTHIA 8 Monte Carlo (MC) program [383]. However, results were obtained only for the 1ℓ + jets channel and the top-quark decays were considered only at LO accuracy via MADSPIN [330], thereby preserving spin correlations only at LO [384]. Also, higher-order QCD corrections to the top-quark decays were solely described by the parton shower. Since parton showers are designed to be accurate only in the soft and collinear regions, any hard QCD radiation produced by the shower in the decays is not expected to be reliably modeled. In Refs. [385, 386], NLO QCD corrections were computed for production and decay of the $t\bar{t}t\bar{t}$ system using the NWA for the 4ℓ and 3ℓ channels, preserving spin correlations to NLO accuracy. The results of these studies are thoroughly discussed in Chapter 4. In a later study [387], the fixed-order results for the 4ℓ channel were compared to those obtained by matching to parton-shower algorithms using the POWHEG and MC@NLO frameworks. The impact of MEC in the parton shower was also investigated and shown to improve the agreement with the fixed-order predictions in which NLO QCD corrections to top-quark decays are consistently included.

In this thesis, the main focus lies on the $pp \to t\bar{t}t\bar{t}$ and $pp \to t\bar{t}W^+$ processes, which have the smallest cross sections among the other associated $pp \to t\bar{t} + X$ processes described above. Our goal is to provide precision calculations for processes in which a top-quark pair is produced in association with additional heavy particles at the LHC, specifically, the W^+ boson and another $t\bar{t}$ pair. The main focus on the latter lies in providing a more accurate description of the top-quark decays already at the matrix element level by considering NLO QCD corrections in both the production and decay stages, which is essential for improving its overall modeling, as previously highlighted. Alongside employing traditional perturbative QCD methods at NLO accuracy, we also explore the impact of the `MiNLO` method [138] on the fully off-shell $pp \to t\bar{t}W^+$ + jets processes. This approach provides an alternative prescription for assigning renormalization and factorization scales and enhances the overall NLO accuracy through the incorporation of Sudakov form factors. The structure of the thesis is as follows: in Chapter 2 we give a brief overview of the theoretical framework for hadron-hadron collisions, while in Chapter 3 we present the computational HELAC-NLO software package [388] used to generate all results. The NLO QCD corrections to the $pp \to t\bar{t}t\bar{t}$ process for the 4ℓ and 3ℓ channels are discussed in Chapter 4, while in Chapter 5 the focus shifts to describing the `MiNLO` method, which serves as an alternative approach for performing perturbative QCD calculations. Technical details on how the `MiNLO` method can be enabled within the HELAC-NLO framework are provided in the Appendix A. Finally, in Chapter 6 the `MiNLO` method is applied to the $pp \to t\bar{t}W^+$ + jets samples and results are presented at both the integrated and differential cross-section levels.

Chapter 2

Theoretical framework

The ultimate goal of high-energy proton-proton (pp) collisions at the LHC is to investigate the fundamental structure of matter. The colliding hadrons are protons consisting of three valence quarks (uud), gluons and additional pairs of quarks and antiquarks, usually referred to as sea quarks. The valence quarks differ from the sea ones in that they determine the quantum numbers of the proton, such as its charge and spin. The sea quarks, on the other hand, correspond to non-valence partonic components that arise from gluon splittings and can subsequently recombine into gluons. The high energy of the pp collisions allows us to probe the proton's structure at very short distances, and therefore, to study the fundamental interactions of its constituents. This implies that in this high-energy regime, quarks and gluons from the colliding proton beams can be treated perturbatively as quasi-free partons, the interactions of which lead to the production of many final-state particles. This stage represents the hard process, where these interactions can be described perturbatively, as both the strong and electroweak couplings become sufficiently small at high energies. The dependence of the strong coupling constant α_s on the energy scale is displayed in Fig. 2.1.

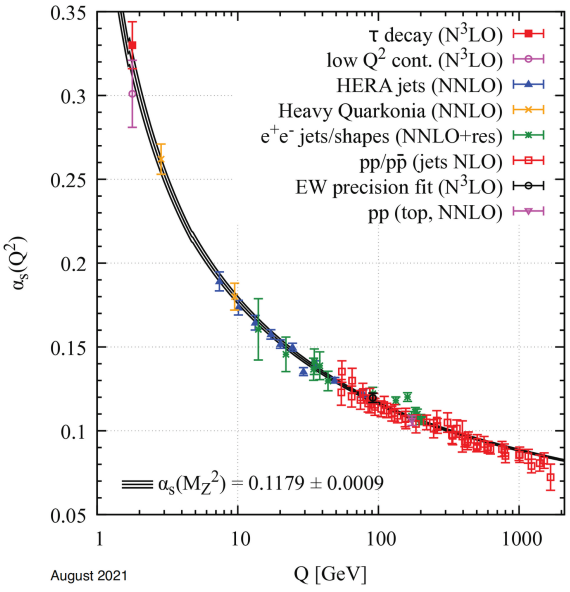

Figure 2.1: *The energy scale dependence of the strong coupling constant α_s. Figure is taken from Ref. [389].*

It is clear that at high energies, α_s is sufficiently small for the perturbative treatment to be applied. However, the partons produced from the hard process are not the ones directly measured by the LHC detectors. Instead, they are subjected to further emissions mainly through QCD interactions, since the electroweak coupling constant α is much smaller than α_s. This stage is theoretically modeled by parton-shower algorithms, where, as we will discuss later, soft and collinear emissions are favored. As the shower evolution scale decreases and approaches the critical value of $\Lambda_{\text{QCD}} \approx 200$ MeV, the strong coupling constant becomes very large and the perturbative treatment breaks down. At this stage, these non-perturbative effects can be described by various hadronization models, where color confinement forces the final-state QCD partons to form color-neutral bound states known as hadrons. Finally, these hadrons decay further, resulting in stable or long-lived particles that leave their mark in the LHC detectors. In the following sections, the different stages mentioned above will be described in a bit more detail.

2.1 Factorization and parton distribution functions

The starting point in a hadron-hadron collision is the factorization theorem that allows us to separate the perturbative and the non-perturbative parts of the calculation. Although this theorem has only been proven for deep-inelastic scattering (DIS) and Drell-Yan processes [390–393], it serves as a basis for a broad class of sufficiently inclusive or infrared-safe processes in hadron-hadron collisions. In a hard scattering, the non-perturbative part is encoded inside the parton-distribution functions (PDFs) $f_i(x, \mu^2)$. At leading-order (LO), PDFs represent the probability of finding a parton i carrying a momentum fraction x of the proton, when probed at the energy scale μ. Although this simple picture provides a physical intuition of PDFs, it no longer holds at higher orders, as $f_i(x, \mu^2)$ can take negative values, breaking the above probabilistic interpretation. The formula for the hadronic cross section σ_h is given below:

$$\sigma_h = \sum_{a,b} \int_0^1 dx_a dx_b f_a(x_a, \mu_F^2) f_b(x_b, \mu_F^2) \hat{\sigma}_{ab}(\mu_R, \mu_F) \,, \tag{2.1}$$

where $\hat{\sigma}_{ab}$ represents the partonic cross section of initial state partons a, b to a given final state. To obtain the full hadronic cross section σ_h, one has to sum over all possible initial state partons a, b whose interactions can produce the given final-state system. The heart of the factorization theorem lies in the fact that partonic cross sections can be calculated using perturbation theory, independent of the PDFs. The PDFs are universal functions whose values are extracted from global fits to experimental data, and are thus independent of the particular processes under consideration. These data have been collected from various sources, including fixed-target experiments, Tevatron, HERA and the LHC. Most of the processes included in global PDF fits are known at NLO accuracy, while an increasing number of them have recently become available at NNLO [394]. This progress enables the use of these data in PDF extractions at NNLO, leading to PDF sets available at LO, NLO, and in many cases, NNLO accuracy. Returning to the factorization formula of Eq. (2.1), we stress that the factorization scale μ_F is an arbitrary but characteristic scale that separates the long-distance physics from the short-distance physics. Hence, the long-distance information below this scale is absorbed into the definition of the parton

distribution functions $f_i(x, \mu_F^2)$, while hard emissions above μ_F are described by the matrix element. The renormalization scale μ_R is also an arbitrary scale that arises during the renormalization procedure, which removes the ultraviolet (UV) divergences appearing in loop calculations at NLO and beyond. Although PDFs are non-perturbative objects, the framework of perturbative QCD can be used to determine their scale evolution via the Dokshitzer-Gribov-Lipatov-Altarelli-Parisi (DGLAP) equation [390, 395, 396]. The knowledge of the scaling behavior is crucial as it enables the evolution of the PDFs extracted from data at an energy scale Q to any arbitrary μ_F scale used in perturbative calculations. The DGLAP equation is given by:

$$\begin{aligned} &\frac{\partial}{\partial \log Q^2} \begin{pmatrix} f_{q_i}(x, Q^2) \\ f_g(x, Q^2) \end{pmatrix} \\ &\qquad = \frac{\alpha_s(Q^2)}{2\pi} \sum_{q_j, \bar{q}_j} \int_x^1 \frac{d\xi}{\xi} \begin{pmatrix} P_{q_i q_j}(\frac{x}{\xi}) & P_{q_i g}(\frac{x}{\xi}) \\ P_{g q_j}(\frac{x}{\xi}) & P_{gg}(\frac{x}{\xi}) \end{pmatrix} \begin{pmatrix} f_{q_j}(\xi, Q^2) \\ f_g(\xi, Q^2) \end{pmatrix} , \end{aligned} \tag{2.2}$$

where $P_{ab}(z)$ are the $b \to ac$ splitting functions, describing the collinear splitting of the parton b to parton a with momentum fraction z. At LO, they read:

$$\begin{aligned} P_{q_i q_j}(z) =& P_{\bar{q}_i \bar{q}_j}(z) = \delta_{ij}\, C_F \left[\frac{1+z^2}{(1-z)_+} + \frac{3}{2}\,\delta(1-z) \right] , \\ P_{q_i g}(z) =& P_{\bar{q}_i g}(z) = T_R \left[z^2 + (1-z)^2 \right] , \\ P_{g q_i}(z) =& P_{g \bar{q}_i}(z) = C_F \left[\frac{1+(1-z)^2}{z} \right] , \\ P_{gg}(z) =& 2\, C_A \left[\frac{z}{(1-z)_+} + \frac{1-z}{z} + z(1-z) \right] \\ &+ \delta(1-z) \frac{11 C_A - 4 n_f T_R}{6} , \end{aligned} \tag{2.3}$$

where $C_F = 4/3, C_A = 3, T_R = 1/2$ and n_f is the number of active flavors inside the proton. Finally, the 'plus' distribution has been introduced to regulate the singular parts of the splitting functions, such that their integrals with any smooth function are finite.

2.2 Hard process

In this section, we focus on the perturbative part of the factorization formula, namely the calculation of the partonic cross sections. These cross sections are calculated from first principles using perturbation theory, where an expansion in terms of the small couplings takes place. As discussed earlier, in the high-energy regime, the strong and weak coupling constants are sufficiently small for a perturbative treatment to be valid. Since the main focus of this thesis is on QCD corrections to processes involving top-quarks, we will present here the perturbative expansion of $\hat{\sigma}_{ab}$ only in terms of the strong coupling constant α_s. In principle, one could also perform an expansion in the weak coupling constant α, which would yield electroweak corrections to the process under consideration. Nonetheless, as the electroweak coupling constant is smaller than α_s, such corrections are typically subdominant

compared to the QCD ones, and can thus be neglected as a first approximation. The QCD expansion of $\hat{\sigma}_{ab}$ is the following:

$$\hat{\sigma}_{ab} = \alpha_s^p \alpha^q [\hat{\sigma}_{ab}^{(0)} + \alpha_s \hat{\sigma}_{ab}^{(1)} + \mathcal{O}(\alpha_s^2)] \,, \tag{2.4}$$

where p and q denote the powers of α_s and α, respectively, associated with the Born term. In addition, $\hat{\sigma}_{ab}^{(0)}$ represents the leading-order (LO) contribution, $\alpha_s \hat{\sigma}_{ab}^{(1)}$ the next-to-leading order (NLO) contribution and $\mathcal{O}(\alpha_s^2)$ are higher-order terms from next-to-next-to-leading order (NNLO) and beyond. For any final-state system comprising n partons, prior to evaluating the partonic cross section, the complete knowledge of the matrix element is needed. Then, the partonic cross section for the two colliding partons a, b yielding the n-parton final state is given by:

$$\hat{\sigma}_{ab} = \frac{1}{2\hat{s}} \int d\Phi_n |\mathcal{M}_{ab\to n}|^2(\Phi_n; \mu_F, \mu_R) \,, \tag{2.5}$$

where $\sqrt{\hat{s}}$ is the center-of-mass energy of the two colliding partons and $d\Phi_n$ is the n-parton phase-space element defined as follows:

$$d\Phi_n = \prod_{i=1}^{n} \left[\frac{d^4 p_i}{(2\pi)^4} (2\pi) \delta(p_i^2 - m_i^2) \Theta(p_i^{(0)}) \right] (2\pi)^4 \delta^{(4)}(p_a + p_b - \sum_{i=1}^{n} p_i) \,. \tag{2.6}$$

The first delta function inside the brackets ensures that final-state particles are on-shell, while the four-dimensional delta function is needed for four-momentum conservation. The integration over the phase space $d\Phi_n$ can, in principle, be performed analytically once the matrix element of the process is known. However, as the number of final-state partons increases, one has to deal with high-dimensional integrals, and their analytical evaluation becomes increasingly cumbersome. For this reason, alternative numerical techniques based on Monte Carlo integration are widely employed, as they are far more efficient in practice. In such methods, the n-parton phase space is sampled to optimize event generation, after which phase-space points are generated accordingly. In the HELAC-NLO framework [388] that we utilized to generate all results for this thesis, the phase-space integration and optimization are performed with the help of PARNI [397] and KALEU [398].

For the NLO contribution to the partonic cross section, QCD corrections to the Born process $\mathcal{B}$ are taken into account. These corrections are divided into two categories: real-emission contributions $\mathcal{R}$, which describe the emission of additional radiation, and virtual contributions $\mathcal{V}$ defined as the interference between one-loop diagrams and the Born amplitude. We denote the Born matrix element as $\mathcal{M}_n^{(0)}$, the matrix element for the real emission as $\mathcal{M}_{n+1}^{(1)}$ and the one-loop matrix element as $\mathcal{M}_n^{(1)}$. The superscripts (0) and (1) indicate the perturbative order in the strong coupling g_s, corresponding to the LO and NLO contributions, respectively. The perturbative expansion of the squared matrix element cannot be written as a single squared sum, since contributions with different final-state multiplicities correspond to distinct phase spaces and must be treated separately. For the n-particle final state, one obtains:

$$\begin{aligned} |\mathcal{M}_n|^2 &= |\mathcal{M}_n^{(0)} + \mathcal{M}_n^{(1)} + ...|^2 \\ &= \mathcal{B}(\Phi_n) + \mathcal{V}(\Phi_n) + ... \,, \end{aligned} \tag{2.7}$$

where $\mathcal{B}(\Phi_n) = |\mathcal{M}_n^{(0)}|^2$, $\mathcal{V}(\Phi_n) = 2\mathrm{Re}(\mathcal{M}_n^{(0)}\mathcal{M}_n^{(1)})$ and higher-order terms with two extra α_s couplings relative to the Born cross section are not explicitly shown. Similarly, for the $(n+1)$-particle final state, one obtains the real emission term $\mathcal{R}(\Phi_{n+1}) = |\mathcal{M}_{n+1}^{(1)}|^2$. The inclusion of the real and virtual contributions, however, introduces further complications in the calculation, as they both contain divergences that cancel only after the different pieces are combined. These divergences have two different origins: ultraviolet (UV) and infrared (IR) singularities. The UV divergences emerge only from loop diagrams and are regulated by dimensional regularization, where one works in $d = 4 - 2\varepsilon$ rather than $d = 4$ dimensions. In this framework, a renormalization scale μ_R is introduced to compensate for the mass dimension of the couplings in $d \neq 4$ dimensions. Using dimensional regularization, the divergences manifest as poles in $1/\varepsilon$ and are removed by adding new terms to the Lagrangian, called counterterms. As a consequence, the coupling constants acquire a dependence on the renormalization scale μ_R, governed by the renormalization group equation (RGE). The specific form of this dependence depends on the chosen renormalization scheme. In contrast to UV divergences, IR singularities arise both in the real emission contribution $\mathcal{R}$ and in the virtual corrections $\mathcal{V}$. Although both pieces are separately divergent, the cancellation of the IR divergences is guaranteed by the Kinoshita–Lee–Nauenberg (KLN) theorem [399, 400]. In the real-emission terms, IR divergences occur when an emitted parton becomes soft or collinear with another massless parton. If massive quarks are involved instead, collinear divergences are naturally regulated by their finite mass, which acts as a cut-off. Soft divergences are, on the other hand, always present because of the massless gluons. Similarly, in the virtual contributions, soft and collinear singularities arise when the momentum of a virtual particle in the loop becomes soft or collinear with that of an external parton. We highlight here, however, that the KLN theorem ensures the cancellation of soft and collinear IR divergences only when one sums over all degenerate initial and final states for sufficiently inclusive observables. In hadron collisions, the initial state is a non-perturbative hadron described by the PDFs, so initial-state collinear singularities remain uncancelled even after combining the real and virtual pieces together. These divergences are absorbed into the redefinition of the PDFs through the factorization procedure. In practice, this implies that renormalized PDFs are introduced in place of the bare ones, which leads to an explicit dependence on the factorization scale μ_F. Because of that, proper collinear counterterms need to be introduced in the partonic cross-section formula to ensure that the NLO cross section is finite. In the $\overline{\mathrm{MS}}$ scheme and in $d = 4 - 2\varepsilon$ dimensions, these counterterms are given by:

$$\int_0^1 dx \int_n d\Phi_n(x)\mathcal{A}^C(x) = \tag{2.8}$$

$$= \frac{\alpha_s}{2\pi}\frac{1}{\Gamma(1-\varepsilon)}\sum_k \int_0^1 dx \int_n d\Phi_n(x)\mathcal{B}_{kb}(xp_a, p_b)\frac{1}{\varepsilon}\left(\frac{4\pi\mu_R^2}{\mu_F^2}\right)^{\varepsilon} P_{ka}(x) \tag{2.9}$$

$$+ \frac{\alpha_s}{2\pi}\frac{1}{\Gamma(1-\varepsilon)}\sum_k \int_0^1 dx \int_n d\Phi_n(x)\mathcal{B}_{ak}(p_a, xp_b)\frac{1}{\varepsilon}\left(\frac{4\pi\mu_R^2}{\mu_F^2}\right)^{\varepsilon} P_{kb}(x)\,, \tag{2.10}$$

where p_a, p_b denote the momenta of the initial-state partons and the DGLAP splitting functions describe the collinear $a \to kc$ and $b \to kc$ splittings in the second and third lines, respectively. With that in mind, the full finite NLO cross section can be

written as follows:

$$\begin{aligned}\hat{\sigma}^{\rm NLO} = &\int d\Phi_n \mathcal{B}(\Phi_n) + \int d\Phi_n \mathcal{V}(\Phi_n) \\ &+ \int d\Phi_{n+1} \mathcal{R}(\Phi_{n+1}) + \int_0^1 dx \int_n d\Phi_n(x) \mathcal{A}^C(x)\,.\end{aligned} \tag{2.11}$$

Although the above NLO cross section is finite after including all counterterms, special methods are required to properly handle the intermediate IR singularities in numerical simulations. The IR singularities from the virtual contributions are regulated in dimensional regularization and are expressed in terms of $1/\varepsilon$ and $1/\varepsilon^2$ poles after computing the one-loop integrals in $d = 4 - 2\varepsilon$ dimensions. Once these poles are extracted analytically, the phase-space integration can be safely performed in $d = 4$ dimensions without any problems. The situation is not the same though for the real emission contributions. In this case, the soft and collinear singularities appear when the integration is carried out in $d = 4 - 2\varepsilon$ dimensions, and therefore the phase-space integration cannot be directly performed in four dimensions. To overcome this obstacle, subtraction terms $\mathcal{S}(\Phi_{n+1})$ are introduced to cancel the divergences from the real-emission graphs locally already at the integrand level. These subtraction terms are constructed to mimic the behavior of the real-emission matrix element in the soft and collinear limits. By adding and subtracting them, one obtains a finite subtracted-real contribution $(\mathcal{R} - \mathcal{S})$ that can be safely integrated numerically in $d = 4$ dimensions. At the same time, the subtraction terms are integrated over the phase-space of the unresolved parton, yielding explicit poles that cancel the corresponding divergences in the virtual and collinear counterterm parts. This schematically reads:

$$\begin{aligned}\hat{\sigma}^{\rm NLO} = &\int d\Phi_n \mathcal{B}(\Phi_n) + \int d\Phi_{n+1} [\mathcal{R}(\Phi_{n+1}) - \mathcal{S}(\Phi_{n+1})] \\ &+ \int d\Phi_n [\mathcal{V}(\Phi_n) + \mathcal{I}^{(S)}(\Phi_n)] + \int_0^1 dx \int_n d\Phi_n(x) \mathcal{A}^C(x)\,,\end{aligned} \tag{2.12}$$

where $\mathcal{I}^{(S)}$ denotes the integrated subtraction terms. The form of the subtraction terms is not unique, and therefore, different subtraction schemes could be employed. In Sec. 3.4, we discuss in more detail two of them: the Catani-Seymour [401,402] and Nagy-Soper subtraction schemes [403]. Both of them have been implemented into the HELAC-NLO code and have been extensively used to validate the independence of the results with respect to the chosen subtraction scheme. An alternative method for handling IR divergences is phase-space slicing [404, 405], although it is used less frequently. In this approach, a cut-off parameter κ is introduced to divide the real-emission phase space into a region containing the soft and collinear singular limits and a region that is finite. The parameter κ is unphysical, and the final result should be independent of its specific value. In practice, κ must be chosen small enough for the approximations to be valid, but not so small as to introduce large logarithms and numerical instabilities. The ambiguity in selecting the optimal value of κ has led to phase-space slicing methods being used less frequently, while subtraction techniques have become the standard approach.

2.3 Parton showers and Hadronization

Although the hard process effectively describes the production of particles at a given order in perturbation theory, higher-order corrections must be included to obtain a more complete picture of the underlying dynamics. This is achieved through parton-shower algorithms, which approximately incorporate enhanced contributions to all orders. These enhanced terms correspond to soft and collinear emissions that dominate the radiation pattern, as the cross section increases in these kinematic limits. In particular, fixed-order calculations are reliable away from such singular regions, whereas parton-shower algorithms can properly resum the corresponding soft and collinear enhancements through Sudakov form factors. The starting point in a parton-shower algorithm is the realization that in the collinear limit, the cross section can be written as:

$$d\sigma \approx \sigma_0 \sum_{partons,i} \frac{\alpha_s}{2\pi} \frac{d\theta^2}{\theta^2} dz P_{ji}(z,\phi) d\phi \,, \tag{2.13}$$

where σ_0 is the cross section for producing partons of any flavor i and P_{ji} describes the splitting of the parton i into a parton j that carries a fraction z of the momentum and azimuthal angle ϕ. The variable θ parameterizes the collinear emission angle, though other evolution variables, such as the virtuality or the transverse momentum of the branching, can also be used. The key feature of this factorization is that the collinear emission probability is universal and independent of the hard process under consideration. This universality enables the construction of a probabilistic algorithm that generates successive emissions recursively, ensuring unitarity through the use of Sudakov form factors. The Sudakov form factors represent the probability of not emitting any resolvable branching between two scales Q_1, Q_2, given by [406]:

$$\Delta_i(Q_1^2, Q_2^2) = \exp\left\{ - \int_{Q_1^2}^{Q_2^2} \frac{dk^2}{k^2} \frac{\alpha_s}{2\pi} \int_{\delta}^{1-\delta} dz P_{ji}(z) \right\}, \tag{2.14}$$

where δ is an infrared cut-off that regulates the singular regions when $z \to 0$ and $z \to 1$. However, before building such an algorithm, a resolution scale Q_0 must be introduced to regulate the infrared singular regions of the phase space. This scale is chosen small enough to capture the dominant soft and collinear dynamics, but also large enough for the perturbative treatment to still be applicable. Thus, values of the order of 1 GeV are commonly used, which are well above the Λ_{QCD}. With the above considerations, the basic workflow of a parton shower algorithm proceeds as follows: first, a random number ρ between 0 and 1 is generated, and the branching scale q^2 is evaluated by solving the equation $\Delta_i(Q^2, q^2) = \rho$, where Q^2 is the starting energy scale of the shower. If the obtained q^2 is larger than Q_0^2, a resolvable branching is generated at that scale, and the momentum fraction z of the emitted parton is calculated using $P_{ji}(z)$ as the probability density function. The process is then repeated recursively for each of the outgoing partons, using q^2 as the new starting scale. If, on the other hand, q^2 is smaller than the cut-off Q_0^2 scale, then no resolvable branching is found and the algorithm terminates. The above prescription is repeated until all partons have been evolved down to the cut-off scale. It should be highlighted at this point that the discussion so far accounts only for collinear emissions. Soft emissions are more complicated because the factorization is valid already at the

amplitude level, in contrast to the collinear case, where such a factorization holds at the cross-section level. As a result, Feynman diagrams where soft gluons are emitted from different partons interfere with each other, breaking the simple picture of the independent evolution of the individual partons. Nevertheless, the effects of soft-gluon coherence can be effectively incorporated within collinear-based parton-shower frameworks by choosing an appropriate evolution variable. Modern Monte Carlo event generators such as HERWIG [407, 408], PYTHIA [383, 409] and SHERPA [410–413] implement different strategies for parton showers, which differ both in their evolution variable and in their formulation. The most common choices of evolution variable include angular ordering and transverse-momentum ordering. Alternatively, dipole showers offer a different formulation in which emissions are generated from color-connected parton pairs, using dipole splitting kernels derived from subtraction formalisms.

The additional emissions in the parton shower are generated on top of a fixed-order calculation. To enhance the accuracy of the predictions and reduce overall uncertainties, it is essential to match fixed-order calculations at least at NLO accuracy to parton showers. This ensures that the first emission, which is typically the hardest, is generated at the amplitude level, while subsequent emissions are handled by the parton shower. The matching described above must be carried out carefully to avoid double counting of contributions. Indeed, naively applying a parton shower to an NLO sample can lead to the same emission being generated both by the fixed-order calculation and by the parton shower. Two widely used matching frameworks that address this issue and perform the matching consistently are the MC@NLO [73] and POWHEG [75–77] frameworks. In the former matching scheme, the parton-shower approximation is subtracted from the fixed-order weight, which can lead to events with negative weights. In the latter, the first emission is corrected to reproduce the real-emission matrix element and is ensured to be the hardest in the event. Processes with different jet multiplicities can also be combined using merging techniques, which allows additional emissions to be described at the matrix-element level. This approach has the advantage of providing a more accurate description of hard real emissions, which are typically not well modeled by parton showers that perform best in the soft and collinear regions. These merging techniques typically require the introduction of a merging scale to avoid double counting of contributions. The most widely established merging methods that fall in this category are the FXFX [329] and MEPS@NLO [414,415]. In contrast, the `MiNLO` method [138,416] avoids the need for an unphysical merging scale by employing a dynamical merging procedure designed to maintain NLO accuracy for observables both inclusive and exclusive to the additional radiation.

To enable a direct comparison with experimental data, hadronization effects must also be taken into account. In processes where collinear factorization applies, the non-perturbative transition of final-state partons into hadrons is described by *fragmentation functions*, which are analogous to parton distribution functions. In practice, however, a single parton can produce multiple hadrons, and this simple picture is refined by hadronization models such as the string [417, 418] and cluster [419, 420] models.

2.4 Top-quark modeling in perturbative calculations

As highlighted in the previous chapter, processes involving the production of top and antitop quarks are abundant at the LHC. Therefore, a cautious treatment of their dynamics is crucial for a correct modeling of their properties. As top quarks are short-lived particles, they decay before hadronization, resulting in leptonic or hadronic signatures depending on their decay modes. The decay products are then observed in the LHC detectors, enabling the origin of these signatures to be identified as most likely coming from top quarks. For instance, for the $pp \to t\bar{t}$ production and decay process, the fully leptonic signatures comprise two opposite-charged leptons, two b jets and missing transverse energy. Nonetheless, identical signatures can also be produced from processes not involving two intermediate top-quark resonances. Some illustrative examples are presented in Fig. 2.2, for the $pp \to e^+\nu_e\,\mu^-\bar{\nu}_\mu\,b\bar{b}$ process.

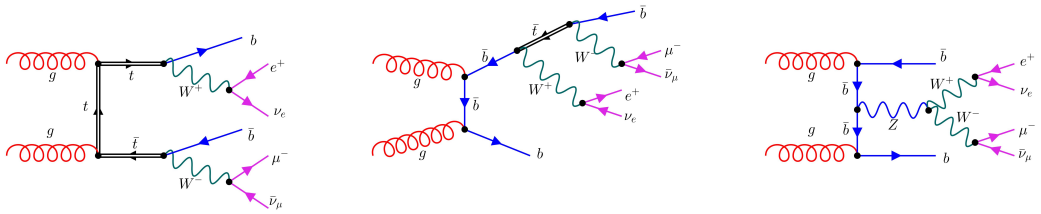

Figure 2.2: *Representative Feynman diagrams for the $pp \to e^+\nu_e\,\mu^-\bar{\nu}_\mu\,b\bar{b}$ process at the LHC, featuring two colliding gluons. The left diagram contains two top-quark resonances, the middle diagram shows a single top-quark resonance, and the right diagram does not include any intermediate top-quark resonances. Diagrams were generated with FeynGame [421–423].*

Experimental measurements usually associate the $\ell\nu_\ell\,\ell'\bar{\nu}_{\ell'}\,b\bar{b}$ signature as the production of a $t\bar{t}$ pair, relying on the on-shell approximation, while diagrams with one or zero top-quark resonances are treated as a background. As top quarks are never observed in the LHC detectors, it is natural to describe processes involving the production of a $t\bar{t}$ pair in terms of their decay products. This idea can of course be extended to any process involving top quarks and is not limited only to the $pp \to t\bar{t}$ process. Below, we discuss two theoretical methods for modeling such processes: the *full off-shell* approach and the *narrow-width approximation* (NWA).

2.4.1 Full off-shell approach

In the full off-shell approach, all potential diagrams that lead to a specific final state are incorporated into the calculations. For instance, in the $pp \to e^+\nu_e\,\mu^-\bar{\nu}_\mu\,b\bar{b}$ process, this includes diagrams featuring double, single, and no top-quark resonances, as displayed in Fig. 2.2. Denoting with $\mathcal{M}_{2t}, \mathcal{M}_{1t}$ and $\mathcal{M}_{0t}$ the matrix elements with two, one and no top-quark resonances, the full matrix element squared is expressed

as:

$$|\mathcal{M}|^2_{\text{full off}-\text{shell}} = |\mathcal{M}_{2t} + \mathcal{M}_{1t} + \mathcal{M}_{0t}|^2 \\ = |\mathcal{M}_{2t}|^2 + |\mathcal{M}_{1t}|^2 + |\mathcal{M}_{0t}|^2 + 2\text{Re}(\mathcal{M}_{2t}\mathcal{M}^*_{1t} + \mathcal{M}_{2t}\mathcal{M}^*_{0t} + \mathcal{M}_{1t}\mathcal{M}^*_{0t}) \,. \tag{2.15}$$

This formulation indicates that all interference effects between diagrams with different number of top-quark resonances are systematically included in the calculations. In more complicated processes, such as the simultaneous production and decay of four top quarks, one would encounter diagrams featuring four, three, two, one, and zero top-quark resonances. The Eq. 2.15 would then have to be extended by the additional introduction of the M_{3t} and M_{4t} amplitudes, but the analogy would remain the same. Hence, the full off-shell approach also captures the processes which are usually treated as background in the experimental analyses. For instance, one of the most significant backgrounds for top-quark pair production and decay is the $pp \to tW$ process. At LO in the perturbative expansion, this process involves diagrams with a single top-quark resonance. At NLO in QCD, however, the presence of an additional b quark in the final state leads to extra contributions from diagrams with two top-quark resonances. As this process is analyzed separately in experimental studies, special care must be taken to prevent the overlapping contributions with the signal process. These contributions are associated with the double-resonant diagrams, which are properly subtracted from the $pp \to tWb$ process using the diagram removal (DR) or diagram subtraction (DS) approaches [424, 425]. In the former method, the double resonant contributions are directly removed at the amplitude level, while in the latter, subtraction terms are introduced to cancel the double-resonant contribution locally. However, it has been shown that even such approaches are inadequate in accurately describing the data in phase-space regions of certain observables which are sensitive to off-shell effects [426]. This underscores the necessity of incorporating full off-shell effects for a more realistic description of the process under consideration.

As intermediate unstable particles are allowed to be off-shell in full off-shell calculations, special care must be taken to avoid the singular region when $p^2 \to m^2$ in the propagator. To address this, the finite width Γ of the unstable particle is incorporated into the propagator as follows:

$$\frac{1}{p^2 - m^2 + im\Gamma} \,, \tag{2.16}$$

which results in the well-known Breit-Wigner distribution in the squared matrix element:

$$\frac{1}{(p^2 - m^2)^2 + m^2\Gamma^2} \,. \tag{2.17}$$

Nevertheless, by naively inserting the Γ width in the propagator, a procedure commonly referred to as the *fixed-width scheme* [427, 428], violates gauge invariance. An alternative scheme that overcomes this issue is the *complex-mass scheme*, which was first proposed in Ref. [429]. More technical details arising at the one-loop level are also discussed in Refs. [430, 431]. In this scheme, the real bare mass in the Lagrangian is replaced by a complex mass along with a complex counterterm simply by adding and subtracting the imaginary $im\Gamma$ part. As a consequence, the imaginary component of the renormalized mass is included in the propagator, while the

imaginary part of the counterterm becomes associated with a counterterm vertex. Since the bare Lagrangian is left unchanged by the above rearrangements, gauge invariance is preserved. Therefore, all unstable particles, including the top quark and electroweak gauge bosons, can be handled within this scheme, which means their masses are treated as complex parameters through the following replacement:

$$m^2 \to \mu^2 = m^2 - im\Gamma\,. \tag{2.18}$$

As a result, other Standard Model parameters that depend on the masses of the unstable particles also become complex. This includes the top-Yukawa coupling and the weak mixing angle, which are then expressed as:

$$y_t = \sqrt{2}\frac{\mu_t}{v}, \quad \sin^2\theta_W = 1 - \frac{\mu_W^2}{\mu_Z^2}\,. \tag{2.19}$$

Finally, we note that in the complex-mass scheme, the presence of complex masses implies that unitarity can not be proven order-by-order [430, 431]. Nonetheless, the effect of unitarity violations is of higher-order.

2.4.2 Narrow-width approximation

Incorporating full off-shell calculations is not always a trivial task. Particularly for processes with many final-state particles, the complexity of the computation increases significantly due to the substantial number of Feynman diagrams that need to be computed. In these cases, alternative methods of handling top-quark decays are often employed, which effectively speed up the required calculation time. One such method is the NWA, which is valid for inclusive observables when the decay width of the unstable particle is much smaller than its mass. More precisely, in this approximation, the Γ/m ratio is sent to zero, resulting in the unstable particle being exactly on-shell, and the Breit-Wigner propagator becomes proportional to a delta function:

$$\frac{1}{(p^2-m^2)^2+m^2\Gamma^2} \xrightarrow{\Gamma/m\to 0} \frac{\pi}{m\Gamma}\delta(p^2-m^2)\,. \tag{2.20}$$

As a consequence, only Feynman diagrams with the maximum number of top-quark resonances contribute to a given process, while less-resonant and non-resonant contributions completely drop out. For instance, applying the NWA to the $pp \to e^+\nu_e\,\mu^-\bar{\nu}_\mu\,b\bar{b}$ process implies that only double-resonant diagrams will contribute to the calculation. The physical interpretation of this is that top quarks are first produced on-shell and subsequently decay either leptonically or hadronically, resulting in a specific configuration of final-state objects. Nevertheless, as its name suggests, the NWA is just an approximation and the impact of missing certain resonant and non-resonant contributions is of the order of $\mathcal{O}(\Gamma/m)$ [432]. As long as the Γ/m ratio is sufficiently small, the NWA offers an accurate description of inclusive observables, yielding results that agree with the full off-shell predictions, typically within the theoretical uncertainties. The advantage of using the NWA is then the much smaller number of diagrams that need to be calculated, and therefore, the smaller number of computational resources required. On top of that, it can also be employed for processes where full off-shell calculations are currently out of reach because of the enormous number of diagrams entering the calculation. Typically, this number increases factorially with the number of external final-state partons. An example of

such a process is the production and decay of four top quarks, which is discussed in detail in Chapter 4. This process involves the production of 12 final-state particles at LO and up to 13 at NLO. It is important to highlight, however, that at the differential cross-section level, off-shell effects can become especially important for some observables in certain phase-space regions. There are multiple studies where these phenomena have been thoroughly discussed, see e.g. [156, 186, 240].

As the NWA factorizes the production and decay of the top quarks, there is no cross-talk between these two stages nor between the different top-quark decays. For the simple $pp \to t\bar{t}$ process with subsequent decays, following the notation of Refs. [94, 95], the differential cross section is then given by:

$$d\sigma = d\sigma_{t\bar{t}} \times \frac{d\Gamma_t}{\Gamma_t} \times \frac{d\Gamma_{\bar{t}}}{\Gamma_t}\,, \tag{2.21}$$

where $d\sigma_{t\bar{t}}$ is the differential cross section for the on-shell $pp \to t\bar{t}$ production, $d\Gamma_t$ ($d\Gamma_{\bar{t}}$) is the differential decay rate for the top (antitop) quark, and the $\times$ symbol represents the fully preserved spin correlations. The NWA can also be applied to other heavy resonances, such as the $W^{\pm}$ bosons, which together with the $b/\bar{b}$ quarks comprise the decay products of the $t/\bar{t}$ quarks. In this case, the differential top and antitop-quark decay rates are written as:

$$d\Gamma_t = d\Gamma_{t\to W^+b}\frac{d\Gamma_{W^+}}{\Gamma_W}, \quad d\Gamma_{\bar{t}} = d\Gamma_{\bar{t}\to W^-\bar{b}}\frac{d\Gamma_{W^-}}{\Gamma_W}\,, \tag{2.22}$$

where in a full analogy, $d\Gamma_{W^{\pm}}$ represents the $W^{\pm}$ decay rate. When higher-order corrections in the perturbative expansion of the strong coupling are included within the NWA, they are applied separately to the production and decay stages. Non-factorizable contributions, such as loop diagrams connecting production and decay stages as well as real-emission interferences, are neglected since they are suppressed by powers of $\mathcal{O}(\Gamma/m)$ [433]. As a consequence, at NLO in QCD within the NWA framework, the cross section for the production and decay of a $t\bar{t}$ pair is expressed as follows:

$$\begin{aligned} d\sigma^{\mathrm{NLO}} = {} & d\sigma_{t\bar{t}}^{\mathrm{NLO}} \times \frac{d\Gamma_t^{(0)}}{\Gamma_t} \times \frac{d\Gamma_{\bar{t}}^{(0)}}{\Gamma_t} \\ & + d\sigma_{t\bar{t}}^{\mathrm{LO}} \times \frac{d\Gamma_t^{(1)}}{\Gamma_t} \times \frac{d\Gamma_{\bar{t}}^{(0)}}{\Gamma_t} \\ & + d\sigma_{t\bar{t}}^{\mathrm{LO}} \times \frac{d\Gamma_t^{(0)}}{\Gamma_t} \times \frac{d\Gamma_{\bar{t}}^{(1)}}{\Gamma_t}\,, \end{aligned} \tag{2.23}$$

where $d\sigma_{t\bar{t}}^{(\mathrm{N})\mathrm{LO}}$ describes the (N)LO cross section for the production of the $t\bar{t}$ pair, and the top-quark decay rate is perturbatively expanded according to:

$$d\Gamma_t = d\Gamma_t^{(0)} + \alpha_s d\Gamma_t^{(1)} + \mathcal{O}(\alpha_s^2)\,. \tag{2.24}$$

Hence, $d\Gamma_t^{(0)}$ and $d\Gamma_t^{(1)}$ denote the LO and NLO contributions to the top-quark decay rate. The first line of Eq. (2.23) accounts for real emission contributions and virtual corrections during the production stage of top quarks, whereas the remaining two lines describe QCD corrections in the top- and antitop-quark decays. From Eq. (2.23), it is clear that incorporating only the first line in the calculation provides

an estimate of the missing higher-order effects in the decays, a method commonly referred to in this thesis as $\text{NLO}_{\text{LO}_{\text{dec}}}$. Another important aspect to consider is the treatment of the decay width Γ_t, which can also be treated as a perturbative parameter:

$$\Gamma_t = \Gamma_t^{(0)} + \alpha_s \Gamma_t^{(1)} + \mathcal{O}(\alpha_s^2)\,. \tag{2.25}$$

Substituting this formula into Eq. (2.23), expanding in terms of the strong coupling constant, and retaining the relevant NLO terms, yields:

$$d\sigma_{\text{exp}}^{\text{NLO}} = d\sigma^{\text{NLO}} \times \left(\frac{\Gamma_t^{\text{NLO}}}{\Gamma_t^{\text{LO}}}\right)^2 - d\sigma^{\text{LO}} \times \frac{2(\Gamma_t^{\text{NLO}} - \Gamma_t^{\text{LO}})}{\Gamma_t^{\text{LO}}}\,, \tag{2.26}$$

where $\Gamma_t^{\text{LO}} = \Gamma_t^{(0)}$, and $\Gamma_t^{\text{NLO}} = \Gamma_t^{(0)} + \alpha_s \Gamma_t^{(1)}$. Additionally,

$$d\sigma^{\text{LO}} = d\sigma_{t\bar{t}}^{\text{LO}} \times \frac{d\Gamma_t^{(0)}}{\Gamma_t^{\text{LO}}} \times \frac{d\Gamma_{\bar{t}}^{(0)}}{\Gamma_t^{\text{LO}}}\,. \tag{2.27}$$

This methodology is commonly referred to as NLO_{exp}, and has been explored in various studies, see e.g. Refs. [94, 95, 156, 434, 435]. The impact of employing these different approaches is extensively studied in this thesis, especially concerning the $pp \to t\bar{t}t\bar{t}$ process in QCD, as discussed in Chapter 4.

Chapter 3

HELAC-NLO

From the previous chapter, it has become clear that simulating the pp collisions at the LHC requires software programs with substantial computational capabilities. In this chapter, we discuss the Monte Carlo HELAC-NLO computational software package [388], which provides theoretical predictions at NLO in QCD for a given scattering process, thus capturing an essential part of the hard partonic interaction. HELAC-NLO can, in principle, deal with processes involving an arbitrary number of particles in the final state, with the only limitations arising from the available computational and time resources. As the number of external legs increases, traditional methods based on the explicit evaluation of the Feynman diagrams become highly inefficient, due to the rapid growth in the number of contributing diagrams. In particular, the computational complexity of diagrammatic approaches typically grows factorially with the number of external particles. In contrast, HELAC-NLO employs numerical Dyson–Schwinger recursive algorithms [436] to construct scattering amplitudes, leading to a much milder growth in the computation cost, typically of the order of $\sim 3^n$, where n denotes the number of external legs. To obtain the full NLO results, the calculation is split into different pieces that involve the evaluation of the real emission contributions along with the integrated subtraction terms, and the computation of the one-loop corrections to the Born amplitudes. The former are carried out by HELAC-DIPOLES [437] while the latter with HELAC-1LOOP [438]. These two frameworks comprise the building blocks of HELAC-NLO and are discussed in more detail in this chapter.

All results obtained with HELAC-NLO are stored in modified LES HOUCHES FILES [439] and are subsequently converted to ROOT NTUPLE FILES [440, 441]. This step is crucial as it enables the usage of different renormalization and factorization scales, alternative PDF sets, more stringent cuts on the final-state objects, and also rebinning of the differential distributions. All the above can be performed simply by reweighting techniques without the need to rerun the entire process under consideration from scratch. These steps are handled by the internal HEPLOT program [442], which is designed to be compatible with HELAC-NLO. For completeness, it is worth mentioning that the main components of HELAC-NLO were derived from its predecessor, HELAC-PHEGAS [443], an event generator for LO Standard Model processes. The original workflow combined the HELAC algorithm [436], based on Dyson-Schwinger equations, with the phase-space generator PHEGAS [444]. However, in the current version of HELAC-NLO, phase-space integration and optimization are primarily handled by KALEU [398] and PARNI [397].

3.1 Tree-level matrix element calculation

Before discussing the NLO contributions to the scattering amplitude, it is essential to describe the HELAC algorithm used for the numerical evaluation of tree-level amplitudes. As mentioned previously, this algorithm is based on Dyson–Schwinger equations and constitutes a fundamental building block for the numerical computation of the scattering matrix elements. In particular, the tree-level amplitudes obtained in this way enter both the Born contributions and the real-emission parts of NLO calculations, and therefore provide the basis upon which the higher-order corrections are constructed. The Dyson–Schwinger equations provide a recursive framework in which n-point Green's functions are expressed in terms of $(n-1)-, (n-2)-, ..., 1$ point functions. In the following, we present the algorithm by closely following Ref. [436], where the QED case is discussed. This example already contains all the essential ingredients needed to understand the algorithm. The treatment of color degrees of freedom for quarks and gluons is addressed in the next section. Let us start by considering a scattering amplitude with n external legs such that:

$$\sum_{i=1}^{n} p_i = 0\,, \tag{3.1}$$

where p_i denote the momenta of the external particles, assuming that they are all incoming. Then, the subamplitudes from which fermions or photons can be constructed are represented by:

$\psi(P) =$ 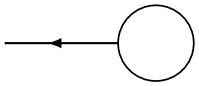

$\bar{\psi}(P) =$ 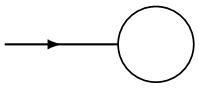 (3.2)

$A_\mu(P) =$ 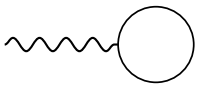

where ψ, $\bar{\psi}$ and A_μ denote spinors, antispinors and vector bosons, respectively. The Dyson-Schwinger equations can then be schematically written as follows:

$\psi(P) =$ 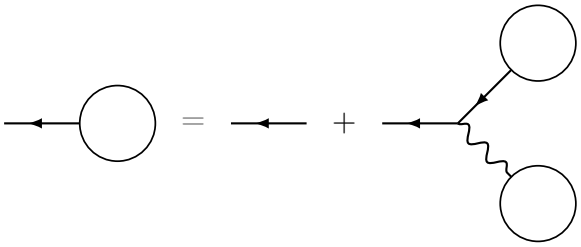 (3.3)

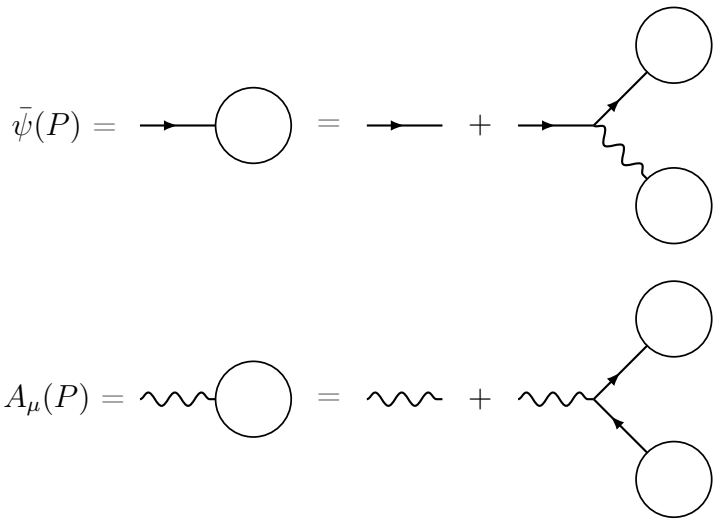

(3.4)

where the first two lines correspond to fermions and antifermions, respectively, and the third line to photons. This schematic representation indicates that fermionic (antifermionic) subamplitudes are obtained either from an external fermion (antifermion) line or from the combination of a fermion (antifermion) and a photon into a fermion (antifermion) propagator. Similarly, photon subamplitudes are constructed either from an external photon or from the combination of a fermion-antifermion pair into a photon propagator. The momentum P is given by

$$P = \sum_{i=1}^{n} n_i \, p_i \,, \tag{3.5}$$

where n_i is either 0 or 1, depending on whether the external particle with momentum p_i contributes to P or not. To keep track of all the possible combinations of particles, it is convenient to introduce a binary representation by assigning to each external particle with momentum p_i the integer 2^{i-1}. By doing so, the identity number of any subamplitude with momentum P is defined as

$$m = \sum_{i=1}^{n} n_i 2^{i-1}, \tag{3.6}$$

which encodes the set of external particles entering the subamplitude. Therefore, there exists a one-to-one correspondence between the momentum P of a subamplitude and its associated integer label m, as given by Eq. (3.6). More generally, any subamplitude characterized by momentum P_k is represented by the corresponding integer m_k. For instance, if a subamplitude with momentum P is obtained by combining two subamplitudes with momenta P_1 and P_2, then $m = m_1 + m_2$. With these

definitions, the recursive relations of Eqs. (3.3) and (3.4) take the explicit form [1]:

$$\begin{aligned}
\psi(m) &= \sum_{i=1}^{n} \delta_{m,2^{i-1}}\, \psi(2^{i-1}) \;+\; \sum_{m=m_1+m_2} (ig)\, \mathcal{P}\, \not{A}_{\mu}(m_2)\, \psi(m_1)\, \varepsilon(m_1,m_2)\,, \\
\bar{\psi}(m) &= \sum_{i=1}^{n} \delta_{m,2^{i-1}}\, \bar{\psi}(2^{i-1}) \;+\; \sum_{m=m_1+m_2} (ig)\, \bar{\psi}(m_1)\, \not{A}_{\mu}(m_2)\, \bar{\mathcal{P}}\, \varepsilon(m_1,m_2)\,, \\
A_{\mu}(m) &= \sum_{i=1}^{n} \delta_{m,2^{i-1}}\, A_{\mu}(2^{i-1}) \;+\; \sum_{m=m_1+m_2} (ig)\, \Pi_{\mu}^{\nu}\, \bar{\psi}(m_2)\, \gamma_{\nu}\, \psi(m_1)\, \varepsilon(m_1,m_2),
\end{aligned} \tag{3.7}$$

where g is the QED coupling constant and $\mathcal{P}$, $\bar{\mathcal{P}}$ and Π_{ν}^{μ} are the fermionic, antifermionic and photon propagators given by:

$$\mathcal{P} = \frac{i}{\not{P} - m}, \quad \bar{\mathcal{P}} = \frac{i}{-\not{P} - m} \quad \text{and} \quad \Pi_{\nu}^{\mu} = \frac{i}{P^2}\left[-g_{\nu}^{\mu} + \frac{P^{\mu}P_{\nu}}{P^2}(1-\xi)\right]. \tag{3.8}$$

In the above formulas, ξ is a number that defines the gauge choice and $\varepsilon(m_1,m_2) = \pm 1$, ensuring the correct fermionic sign in the recursive construction. For each blob of Eqs. (3.3) and (3.4), the procedure outlined in Eq. (3.7) is iterated until the recursion is complete. This is achieved by treating one external particle as a reference and excluding it from the recursion. At the end, the constructed subamplitude with rank $(n-1)$ is contracted with the spinor or polarization vector of the reference particle. Assuming the reference particle is represented by the integer number 2^{k-1}, the $(n-1)$ subamplitude has the identity number:

$$m = \sum_{i=1, i\neq k}^{n} 2^{i-1} = 2^n - 1 - 2^{k-1}\,, \tag{3.9}$$

as all the external legs $i \neq k$ have been used to construct it. As a consequence, the total scattering amplitude is given by:

$$\mathcal{M}(p_1,p_2,...,p_n) = \begin{cases} A_0^{\mu}(2^n - 1 - 2^{k-1})\, A_{\mu}(2^{k-1})\,, & \text{if the reference particle is a photon} \\ \bar{\psi}_0(2^n - 1 - 2^{k-1})\, \psi(2^{k-1})\,, & \text{if the reference particle is an incoming} \\ & \text{fermion or an outgoing antifermion}\,, \\ \bar{\psi}(2^n - 1 - 2^{k-1})\, \psi_0(2^{k-1})\,, & \text{if the reference particle is an incoming} \\ & \text{antifermion or an outgoing fermion} \end{cases} \tag{3.10}$$

where the subscript "0" indicates that the spinors and polarization vectors are taken from Eq. (3.7) with the propagators removed, since k is an external on-shell particle. The external spinors and polarization vectors are given by:

$$\begin{aligned}
A^{\mu}(p_k) &= \varepsilon_{\lambda}^{\mu}(p_k),\ \lambda = \pm 1 \\
\psi(p_i) &= \begin{cases} u_{\lambda}(p_i)\,, & \text{if } p_i^0 \geq 0 \\ v_{\lambda}(-p_i)\,, & \text{if } p_i^0 \leq 0 \end{cases} \\
\bar{\psi}(p_i) &= \begin{cases} \bar{u}_{\lambda}(p_i)\,, & \text{if } p_i^0 \geq 0 \\ \bar{v}_{\lambda}(-p_i)\,, & \text{if } p_i^0 \leq 0 \end{cases}
\end{aligned} \tag{3.11}$$

[1] We adopt the notation used in Ref. [445] to express the spinors and the fields as functions of m.

where $\varepsilon^{\mu}_{\lambda}, u_{\lambda}, v_{\lambda}, \bar{u}_{\lambda}$ and $\bar{v}_{\lambda}$ represent the helicity states for photons and fermions. The squared matrix element is then obtained by summing over all possible helicity configurations. As the phase-scape integration for calculating the cross section is performed using Monte Carlo techniques, a similar strategy can be adopted for the helicity degrees of freedom. In particular, Monte Carlo sampling over helicity configurations can be used instead of an explicit helicity sum, thereby significantly reducing the computational cost. However, naive uniform sampling over helicity configurations often leads to large statistical fluctuations, since different helicity contributions may differ by many orders of magnitude. One method designed to address this issue is the so-called random polarization method [437,446,447]. In this approach, the discrete sum over helicities is replaced by an integral over a phase ϕ and helicity states become phase-dependent. For instance, the photon polarization vector is expressed as

$$\varepsilon^{\mu}(p,\phi) = e^{i\phi}\varepsilon^{\mu}_{+}(p) + e^{-i\phi}\varepsilon^{\mu}_{-}(p)\,, \tag{3.12}$$

with analogous expressions holding for fermionic spinors. As a result, the sum over helicity configurations can be replaced by:

$$\sum_{s} |\mathcal{M}_s|^2 = \frac{1}{2\pi}\int_0^{2\pi} d\phi\, |\mathcal{M}_{\phi}|^2\,. \tag{3.13}$$

As both helicity states contribute for a given value of ϕ, there are no large variations between different $\mathcal{M}_{\phi}$ values, and thus a uniform sampling of the phase ϕ can be used effectively. Then, for a sufficiently large number of sampled ϕ values, the integral on the right-hand side of Eq. (3.13) converges to the exact helicity sum.

3.2 Color flow decomposition

So far, we have restricted the discussion to the QED case, where only colorless particles are involved. Scattering amplitudes containing quarks and gluons can also be constructed using the Dyson-Schwinger recursion algorithm discussed in the previous section. In this case, however, the color degrees of freedom entering the calculation require a separate and dedicated treatment.

In HELAC-NLO, the color degrees of freedom are handled using the so-called color-flow decomposition [443, 448–451]. This decomposition has been shown to be very efficient compared to other traditional approaches that require the computation of traces that involve the generators of the $SU(N_c)$ gauge group. For instance, considering an $n-$gluon scattering amplitude, the matrix element can be decomposed as:

$$\mathcal{M}^{a_1 a_2 \ldots a_n} = \sum_{\sigma} \mathrm{Tr}[t^{a_{\sigma_1}} t^{a_{\sigma_2}} \ldots t^{a_{\sigma_n}}]\mathcal{M}_{\sigma}\,, \tag{3.14}$$

where t^a are the generators of the $SU(N_c)$ gauge group in the fundamental representation, the sum $\sigma = (\sigma_1, \sigma_2, ..., \sigma_n)$ runs over all possible permutations of $(1, 2, ..., n)$ and $\mathcal{M}_{\sigma}$ is the color-ordered partial amplitude corresponding to a given permutation. Although the structure of the amplitude is in general more complicated when quarks are involved, a similar decomposition can also be derived in this case [452]. The core idea of the color-flow decomposition is to treat quarks and gluons in a unified way

by expressing the gluon fields as matrices in the fundamental representation. This can be achieved by defining:

$$(A_\mu)_{ij} = \sum_{a=1}^{N_c^2-1} A_\mu^a (t^a)_{ij} \,, \quad i,j = 1,...,N_c \,. \tag{3.15}$$

With this representation, gluons naturally acquire a color-anticolor structure and can be interpreted as pairs of color lines, in a direct analogy with quark fields. Then, any matrix element involving n_g external gluons and n_q external quark-antiquark pairs can be written as

$$\mathcal{M}^{i_1' i_2' ... i_{n_q}' \, i_1 i_2 ... i_{n_g}}_{j_1' j_2' ... j_{n_q}' \, j_1 j_2 ... j_{n_g}} = \sum_{a_1,a_2,...,a_{n_g}} \mathcal{M}^{i_1' i_2' ... i_{n_q}' \, a_1 a_2 ... a_{n_g}}_{j_1' j_2' ... j_{n_q}'} \prod_{k=1}^{n_g} (t^{a_k})_{i_k j_k} \,, \tag{3.16}$$

where the adjoint color indices a_k of the external gluons have been converted into pairs of fundamental indices (i_k, j_k) through the direct application of Eq. (3.15) to all external gluons. As a result, the color structure of the amplitude can be expressed entirely in terms of fundamental representation indices. In addition, after the use of some standard $SU(N_c)$ group-theoretical identities, the color part of the Feynman rules can be expressed in terms of products of Kronecker deltas. For instance, the Feynman rule for the triple-gluon vertex in the color space is given by:

$$\sum_{a_1,a_2,a_3} f^{a_1 a_2 a_3} (t^{a_1})_{i_1 j_1} (t^{a_2})_{i_2 j_2} (t^{a_3})_{i_3 j_3} = -\frac{i}{4} (\delta_{i_1 j_2} \delta_{i_2 j_3} \delta_{i_3 j_1} - \delta_{i_1 j_3} \delta_{i_2 j_1} \delta_{i_3 j_2}) \,, \tag{3.17}$$

which schematically corresponds to the following color-flow graphs:

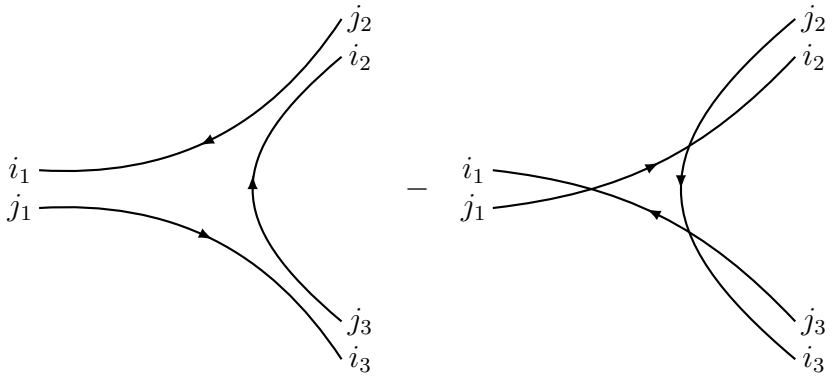

Similarly, the color-structure of the $q\bar{q}g$ vertex is given by:

$$\sum_a (t^a)_{i_1 j_1} (t^a)_{i_2 j_2} = \frac{1}{2} \left(\delta_{i_1 j_2} \delta_{i_2 j_1} - \frac{1}{N_c} \delta_{i_1 j_1} \delta_{i_2 j_2} \right) \,, \tag{3.18}$$

and is schematically represented by the two diagrams shown below:

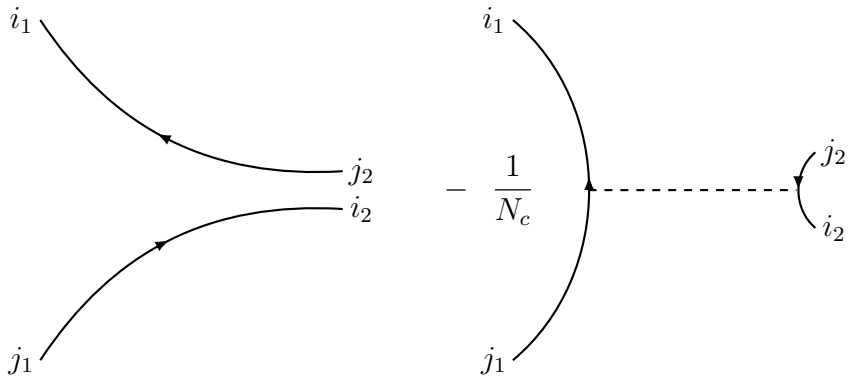

The dashed line represents a $U(1)$ unphysical gluon that couples only with quarks but not gluons. Its presence is reflected in the fact that the gluon field $(A_\mu)_{ij}$ written in the fundamental representation, contains $N_c \times N_c$ components, whereas the physical gluon degrees of freedom are only $N_c^2 - 1$. Indeed, the gluon fields defined in Eq. (3.15) are traceless,

$$\sum_i (A_\mu)_{ii} = 0\,, \tag{3.19}$$

which follows directly from $\mathrm{Tr}(t^a) = 0$. This condition leads to linear relations among color-flow amplitudes, and in particular between contributions that involve the unphysical $U(1)$ gluon and those that do not, ensuring that physical amplitudes depend only on the $SU(N_c)$ degrees of freedom. For more details, the reader is referred to e.g. Ref. [453]. With all the above, it becomes clear that any matrix element involving n_g gluons and n_q quark-antiquark pairs can be written as:

$$\mathcal{M}^{i_1 i_2 \ldots i_n}_{j_1 j_2 \ldots j_n} = \sum_\sigma \delta_{i_{\sigma_1} j_1} \delta_{i_{\sigma_2} j_2} \ldots \delta_{i_{\sigma_n} j_n} \mathcal{M}_\sigma\,, \tag{3.20}$$

where $n = n_q + n_g$. Squaring the amplitude yields:

$$|\mathcal{M}|^2 = \sum_{\sigma,\bar{\sigma}} \sum_{i_1,i_2,\ldots,i_n} \sum_{j_1,j_2,\ldots,j_n} \delta_{i_{\sigma_1} j_1} \delta_{i_{\sigma_2} j_2} \ldots \delta_{i_{\sigma_n} j_n}\, \delta_{i_{\bar{\sigma}_1} j_1} \delta_{i_{\bar{\sigma}_2} j_2} \ldots \delta_{i_{\bar{\sigma}_n} j_n} \mathcal{M}_\sigma \mathcal{M}^*_{\bar{\sigma}}\,. \tag{3.21}$$

The correlated color-matrix is then defined to be:

$$\mathcal{C}_{\sigma,\bar{\sigma}} = \sum_{i_1,i_2,\ldots,i_n} \sum_{j_1,j_2,\ldots,j_n} \delta_{i_{\sigma_1} j_1} \delta_{i_{\sigma_2} j_2} \ldots \delta_{i_{\sigma_n} j_n}\, \delta_{i_{\bar{\sigma}_1} j_1} \delta_{i_{\bar{\sigma}_2} j_2} \ldots \delta_{i_{\bar{\sigma}_n} j_n}\,. \tag{3.22}$$

In practice, the color structure of the squared matrix element can be expressed as a sum of products of Kronecker deltas, which provides a straightforward way to handle the color degrees of freedom. However, for processes with many external colored states, the explicit evaluation of this sum could become cumbersome and computationally expensive. In such cases, alternative approaches, such as Monte Carlo sampling over color configurations, can also be employed [450].

3.3 Virtual corrections

3.3.1 The OPP method

An essential component of an NLO calculation is the evaluation of virtual contributions, defined as the interference between the one-loop amplitudes and the Born amplitude. This task requires computing one-loop amplitudes, which can be highly challenging due to the complexity of the associated Feynman diagrams. Another major difficulty lies in the reduction of n-point one-loop integrals to lower-point functions, which can be more conveniently computed using analytical techniques in dimensional regularization. The method implemented in HELAC-NLO to address these kinds of problems is the OPP method, initially proposed in 2006 by Ossola, Papadopoulos and Pittau [454]. This method is implemented in CUTTOOLS [455], which, together with ONELOOP [456], the program responsible for evaluating scalar integrals, constitutes the essential building blocks of HELAC-1LOOP. The starting point of the OPP method is the observation that any m-point one-loop integral can be written in the following form:

$$\overline{A}(\bar{\ell}) = \int \frac{d^D\bar{\ell}}{(2\pi)^4} \frac{\overline{N}(\bar{\ell})}{\overline{D}_0\overline{D}_1...\overline{D}_{m-1}}, \quad \overline{D}_i = (\bar{\ell}+q_i)^2 - m_i^2, \quad q_i = \sum_{j=1}^{i} p_j, \quad q_0 = 0\,. \tag{3.23}$$

In the above expressions, the use of the bar symbol indicates that these objects live in $D = 4 + \varepsilon$ dimensions. The p_i are the external momenta satisfying momentum conservation $p_1 + p_2 + ... + p_m = 0$, and are hence 4-dimensional objects. It has been shown [457] that when attempting to reconstruct the numerator in a form that includes some of the propagators from the denominator, the numerator takes the following form:

$$\begin{aligned}
\overline{N}(\bar{\ell}) = & \sum_{i_0<i_1<i_2<i_3}^{m-1} \Big[d(i_0i_1i_2i_3) + \tilde{d}(\bar{\ell};i_0i_1i_2i_3)\Big] \prod_{i\neq i_0,i_1,i_2,i_3}^{m-1} \overline{D}_i \\
& + \sum_{i_0<i_1<i_2}^{m-1} \big[c(i_0i_1i_2) + \tilde{c}(\bar{\ell};i_0i_1i_2)\big] \prod_{i\neq i_0,i_1,i_2}^{m-1} \overline{D}_i \\
& + \sum_{i_0<i_1}^{m-1} \Big[b(i_0i_1) + \tilde{b}(\bar{\ell};i_0i_1)\Big] \prod_{i\neq i_0,i_1}^{m-1} \overline{D}_i \\
& + \sum_{i_0}^{m-1} \big[a(i_0) + \tilde{a}(\bar{\ell};i_0)\big] \prod_{i\neq i_0}^{m-1} \overline{D}_i \\
& + \tilde{P}(\bar{\ell}) \prod_{i}^{m-1} \overline{D}_i\,,
\end{aligned} \tag{3.24}$$

where d, c, b, a are the coefficients of the 4,3,2,1- point integrals respectively. Indeed, for instance, from the first line of Eq. (3.24) all propagators inside the product will cancel with the corresponding ones from the denominator of Eq. (3.23), resulting in only 4 propagators in the denominator and thus a 4-point function. The $\tilde{d}, \tilde{c}, \tilde{b}, \tilde{a}$ and $\tilde{P}$ coefficients depend on the loop-momentum $\bar{\ell}$ and are called spurious terms because they vanish upon integration. An explanation of this phenomenon for the 4-point

spurious term $\tilde{d}$ is presented in the next section. From all the above, it becomes clear that *any* m-point integral can be written in terms of 4,3,2,1-point functions, meaning that even loop integrals with more than four propagators inside the loop can be systematically reduced to a linear combination of lower-point functions with at most 4 propagators in the denominator. A proof demonstrating how one-loop N-point functions with $N \geq 5$ can be reduced to 4-point functions in four dimensions has long been established in Ref. [458]. This allows us to write the whole one-loop amplitude as

$$\mathcal{M}_{1-loop} = \sum_i d_i \text{ Box}_i + \sum_i c_i \text{ Triangle}_i + \sum_i b_i \text{ Bubble}_i + \sum_i a_i \text{ Tadpole}_i + \text{R}\,. \tag{3.25}$$

The R term corresponds to the rational part that will be discussed below and is the result of working in $D = 4 + \varepsilon$ instead of exactly $D = 4$ dimensions. Leaving this aside for now, it is clear that the essence of the OPP method is to simply determine the coefficients d_i, c_i, b_i, a_i, as the scalar integrals can be easily calculated. In HELAC-NLO, this is done with the help of ONELOOP [456]. Therefore, in the following, we focus on the idea underlying the extraction of these coefficients.

As a first comment, we highlight that it is convenient to perform the reduction of the one-loop integrals by splitting the D-dimensional numerator into a pure 4-dimensional piece plus an ε-dimensional part, as follows:

$$\overline{N}(\overline{\ell}) = N(\ell) + \tilde{N}(\tilde{\ell}^2, \ell, \varepsilon)\,, \tag{3.26}$$

where $\tilde{\ell}^2 = \overline{\ell}^2 - \ell^2$ and ℓ is the 4-dimensional loop momentum. The contribution of the $\tilde{N}(\tilde{\ell}^2, \ell, \varepsilon)$ term gives rise to the rational part of the second kind R_2 defined as:

$$\text{R}_2 = \int \frac{d^D\overline{\ell}}{(2\pi)^4} \frac{\tilde{N}(\tilde{\ell}^2, \ell, \varepsilon)}{\overline{D}_0 \overline{D}_1 ... \overline{D}_{m-1}}\,. \tag{3.27}$$

It has been shown [459] that the calculation of the R_2 terms is reduced to a tree-level computation by introducing some new Feynman rules for the theory at hand. Thus, we will rather focus on the 4-dimensional part of the numerator $N(\ell)$. The determination of the coefficients d, c, b, a begins with the evaluation of the 4-point coefficients d_i. To do this, it is sufficient to find a loop momentum ℓ_c such that all except $D_{i_0}, D_{i_1}, D_{i_2}, D_{i_3}$ are zero. In this way, all terms related to the 3,2,1-point functions in the numerator will disappear, as they are multiplied by at least one of the following propagators $D_{i_0}, D_{i_1}, D_{i_2}, D_{i_3}$. Therefore, only the 4-point coefficients will survive and can be calculated given that the numerator is known for this particular loop momentum ℓ_c. Once the d_i coefficients have been determined, the same logic is applied recursively to determine the remaining c_i, b_i, a_i coefficients.

However, when working with the 4-dimensional numerator, the four-dimensional propagators D_i appear in Eq. (3.24) instead of the $\overline{D}_i$ ones. As a consequence, the cancellation between the propagators in the numerator and those in the denominator of Eq. (3.23) is not exact, since $\overline{D}_i \neq D_i$. Specifically, they are related by $\overline{D}_i = D_i + \tilde{\ell}^2$. This forbids us from writing the one-loop amplitude in the form of the expression (3.25). The dimensional mismatch between the numerator and the denominator gives birth to the rational term of the first kind, denoted as R_1. One method to tackle this problem is to rewrite the $N(\ell)$ numerator after applying the following shift [459]:

$$m_i^2 \to m_i^2 - \tilde{\ell}^2. \tag{3.28}$$

By doing so, the D_i in $N(\ell)$ are replaced by $\overline{D}_i$, at the cost of introducing an $\tilde{\ell}^2$ dependence in the coefficients. These coefficients can then be expanded in powers of $\tilde{\ell}^2$ giving rise to the R_1 term. Once the 4-dimensional coefficients are determined by the method described above, these $\tilde{\ell}^2$-dependent coefficients can also be computed by calculating $N(\ell)$ for different $\tilde{\ell}^2$ values.

We conclude this section by emphasizing that the reduction method described above can be applied directly at the amplitude level for one-loop integrals sharing the same set of denominators. This offers the clear advantage of avoiding the need to repeat the procedure for each individual Feynman diagram, making the method particularly suitable for numerical implementation.

3.3.2 Example: Determining the d coefficient of a four-point function with rank four

To better understand how the OPP method works and how the reduction is performed at the integrand level, we present below the reduction of a 4-point one-loop integral with rank 4, by closely following the methodology of Ref. [460]. This is the most complicated structure of a box diagram with four loop momenta appearing in the numerator:

$$\mathcal{I}_4 = \frac{\overline{\mathcal{N}}_4(\bar{\ell})}{\overline{D}_0\overline{D}_1\overline{D}_2\overline{D}_3} = \frac{\prod_{i=1}^{4}(u_i\cdot\bar{\ell})}{\overline{D}_0\overline{D}_1\overline{D}_2\overline{D}_3}\,, \tag{3.29}$$

where u_i are some 4-dimensional external vectors.

In particular, our main goal is to extract the 4-point $d(0123)$ coefficient, along with the spurious term $\tilde{d}(\bar{\ell};0123)$ that vanishes upon integration. Even though in the original OPP paper [454] this was done by working in the spinorial representation, here we follow a slightly different approach by working in the more convenient van Neerven - Vermaseren basis [458]. This basis is constructed by introducing the following $\mathcal{V}_i$ $(i=1,2,3)$ vectors:

$$\mathcal{V}_1^\mu = \frac{\delta^{\mu q_2 q_3}_{q_1 q_2 q_3}}{\delta^{q_1 q_2 q_3}_{q_1 q_2 q_3}}, \quad \mathcal{V}_2^\mu = \frac{\delta^{q_1 \mu q_3}_{q_1 q_2 q_3}}{\delta^{q_1 q_2 q_3}_{q_1 q_2 q_3}}, \quad \mathcal{V}_3^\mu = \frac{\delta^{q_1 q_2 \mu}_{q_1 q_2 q_3}}{\delta^{q_1 q_2 q_3}_{q_1 q_2 q_3}}\,, \tag{3.30}$$

where:

$$\delta^{\mu q_1 q_2}_{q_1 q_2 q_3} = \varepsilon^{\mu\nu\lambda} q_{2,\nu} q_{3,\lambda} \varepsilon^{\kappa\rho\sigma} q_{1,\kappa} q_{2,\rho} q_{3,\sigma}, \quad \delta^{q_1 q_2 q_3}_{q_1 q_2 q_3} = \left(\varepsilon^{\mu\nu\lambda} q_{1,\mu} q_{2,\nu} q_{3,\lambda}\right)^2 . \tag{3.31}$$

Similar definitions also hold for $\delta^{q_1\mu q_3}_{q_1 q_2 q_3}$ and $\delta^{q_1 q_2 \mu}_{q_1 q_2 q_3}$. From the above definitions it follows that $\mathcal{V}_i \cdot q_j = \delta_{ij}$. Then, any loop momenta in $D = 4+\varepsilon$ dimensions can be expressed as follows:

$$\bar{\ell}^\mu = \sum_{i=1}^{3} (\bar{\ell}\cdot q_i)\mathcal{V}_i^\mu + (\bar{\ell}\cdot\eta_4)\eta_4^\mu + (\bar{\ell}\cdot\eta_\varepsilon)\eta_\varepsilon^\mu\,, \tag{3.32}$$

where the vectors η_4, η_ε lie in the transverse space satisfying

$$\mathcal{V}_i\cdot\eta_4 = \mathcal{V}_i\cdot\eta_\varepsilon = \eta_4\cdot q_i = \eta_\varepsilon\cdot q_i = \eta_4\cdot\eta_\varepsilon = u_i\cdot\eta_\varepsilon = 0\,, \tag{3.33}$$

and they have been included for completeness. In this way, the $\bar{\ell}^\mu$ vector has been written as a linear combination of 5 independent vectors, the last one of which

is the result of working in $D = 4 + \varepsilon$ instead of four dimensions. We note here that any loop momenta could in principle be written as a linear combination of the $q_i, \eta_4, \eta_\varepsilon$ vectors without the need to introduce the van Neerven - Vermaseren basis. In this case, however, determining the q_i coefficients would not be so simple as the q_i vectors are non-orthogonal. The use of the van Neerven-Vermaseren basis is then useful, since by exploiting the relation $\mathcal{V}_i \cdot q_j = \delta_{ij}$, which holds by definition, the determination of the $\mathcal{V}_i$ coefficients becomes a trivial task. The reduction of the integral in the expression (3.29) works as follows [2] Using Eq. 3.32, we can write

$$\begin{aligned}\overline{\mathcal{N}}_4(\bar{\ell}) &= \prod_{i=1}^{4}(u_i \cdot \bar{\ell}) = \prod_{i=1}^{3}(u_i \cdot \bar{\ell}) \left[\sum_{j=1}^{3}(\bar{\ell} \cdot q_j)(u_4 \cdot \mathcal{V}_j) + (\bar{\ell} \cdot \eta_4)(u_4 \cdot \eta_4)\right] \\ &= \prod_{i=1}^{3}(u_i \cdot \bar{\ell}) \left\{\frac{1}{2}\sum_{j=1}^{3}\left[(\overline{D}_j - \overline{D}_0) - (q_j^2 - m_j^2 + m_0^2)\right](u_4 \cdot \mathcal{V}_j) + (\bar{\ell} \cdot \eta_4)(u_4 \cdot \eta_4)\right\},\end{aligned} \tag{3.34}$$

where the identity $\bar{\ell} \cdot q_j = \frac{1}{2}\left[(\overline{D}_j - \overline{D}_0) - (q_j^2 - m_j^2 + m_0^2)\right]$ has been used in the second line. From the above equation, we notice that the terms inside the summation have been "reduced"; they belong to either lower-point or lower-rank integrals. Another important observation is that every $u_i \cdot \bar{\ell}$ product that we pull out yields a constant term with respect to the loop momentum and another term which is linear in $\bar{\ell}$. In particular:

$$u_i \cdot \bar{\ell} \to \text{constant} + (u_i \cdot \eta_4)(\bar{\ell} \cdot \eta_4)\,. \tag{3.35}$$

By repeating the above procedure for all $u_i \cdot \bar{\ell}$ products, we will therefore end up with

$$\overline{\mathcal{N}}_4(\bar{\ell}) = d_0 + d_1(\bar{\ell}\cdot\eta_4) + d_2(\bar{\ell}\cdot\eta_4)^2 + d_3(\bar{\ell}\cdot\eta_4)^3 + d_4(\bar{\ell}\cdot\eta_4)^4 + \text{lower-point terms}\,. \tag{3.36}$$

The lower-point terms are those that carry at least one denominator $\overline{D}_i$ and therefore will contribute to lower-point integrals. Since our goal is to extract the coefficient of the 4-point function, we are interested in deriving the constant coefficient and, at the same time, understanding the role of the remaining terms that carry an $\bar{\ell}$ dependence. Before doing that, we note that Eq. 3.36 can be further simplified. In particular, by squaring Eq. (3.32) and using $\overline{D}_0 = \bar{\ell}^2 - m_0^2$ we can write:

$$\begin{aligned}\bar{\ell}^2 &= \sum_{i,j=1}^{3}(\bar{\ell} \cdot q_i)(\bar{\ell} \cdot q_j)(\mathcal{V}_i \cdot \mathcal{V}_j) + (\bar{\ell} \cdot \eta_4)^2 + (\bar{\ell} \cdot \eta_\varepsilon)^2\,, \\ \overline{D}_0 + m_0^2 &= \frac{1}{4}\sum_{i,j=1}^{3}(\overline{D}_i - \overline{D}_0 - q_i^2 + m_i^2 - m_0^2)(\overline{D}_j - \overline{D}_0 - q_j^2 + m_j^2 - m_0^2)(\mathcal{V}_i \cdot \mathcal{V}_j) \\ &\quad + (\bar{\ell} \cdot \eta_4)^2 + (\bar{\ell} \cdot \eta_\varepsilon)^2\,, \\ (\bar{\ell} \cdot \eta_4)^2 &= -(\bar{\ell} \cdot \eta_\varepsilon)^2 + \text{constants} + \mathcal{O}(\overline{D}_0, \overline{D}_1, \overline{D}_2, \overline{D}_3)\,.\end{aligned} \tag{3.37}$$

[2] We perform the reduction directly using D-dimensional objects without splitting the numerator into a 4-dimensional piece plus an ε dimensional part as described in the previous section. The reduction mechanism described here is, however, the same as if it were carried out in 4 dimensions.

Therefore, Eq. (3.36) can be rewritten as:

$$\overline{\mathcal{N}}_4(\bar{\ell}) = \tilde{d}_0 + \tilde{d}_1(\bar{\ell}\cdot\eta_4) + \tilde{d}_2(\bar{\ell}\cdot\eta_\varepsilon)^2 + \tilde{d}_3(\bar{\ell}\cdot\eta_\varepsilon)^2(\bar{\ell}\cdot\eta_4) + \tilde{d}_4(\bar{\ell}\cdot\eta_\varepsilon)^4 + \text{lower-point terms}\,. \tag{3.38}$$

From the above formula, it is clear that terms with η_ε dependence are a result of the fact that we are working in $D = 4+\varepsilon$ dimensions and will contribute to the R_2 part, which is beyond the scope of this section. Using the language from the previous section, $\tilde{\ell}^2 = (\bar{\ell}\cdot\eta_\varepsilon)^2$ and hence the 4-dimensional part of the numerator is:

$$\mathcal{N}_4(\ell) = \tilde{d}_0 + \tilde{d}_1(\bar{\ell}\cdot\eta_4) + \text{lower-point terms}\,. \tag{3.39}$$

We also notice that since the 4-point coefficients $\tilde{d}_0$ and $\tilde{d}_1(\ell\cdot\eta_4)$ are not multiplied by any propagator, there is no dimensional mismatch between propagators appearing in the numerator and the ones from the denominator of the one-loop integral in Eq. (3.29). Thus, the part of the R_1 term associated with the 4-point coefficients is zero in this case, and any contribution to it will come from the lower-point terms of Eq. (3.39). Moving on, from the above expression, we also recognize the spurious term with the ℓ dependence as $\tilde{d}_1(\ell\cdot\eta_4)$. It is easy to verify that this term vanishes upon integration as:

$$\tilde{d}_1\int\frac{d^D\bar{\ell}}{(2\pi)^D}\frac{\bar{\ell}_\mu}{\overline{D}_0\overline{D}_1\overline{D}_2\overline{D}_3}\eta_4^\mu = \sum_{i=1}^{3} c_i q_{i,\mu}\eta_4^\mu = 0\,, \tag{3.40}$$

for some coefficients c_i. Indeed, the above integral without η_4^μ can only depend on the q_i^μ momenta that appear in the denominators, and it can therefore be written as a linear combination of all these momenta. Then, since $q_i\cdot\eta_4 = 0$, the spurious term vanishes. We conclude that:

$$\begin{aligned} d(0123) &= \tilde{d}_0\,,\\ \tilde{d}(\ell;0123) &= \tilde{d}_1(\ell\cdot\eta_4)\,. \end{aligned} \tag{3.41}$$

Our final goal now is to determine these two coefficients. By setting $\overline{D}_0(\bar{\ell}_c) = \overline{D}_1(\bar{\ell}_c) = \overline{D}_2(\bar{\ell}_c) = \overline{D}_3(\bar{\ell}_c) = 0$ for some momentum $\bar{\ell}_c$ as described in the previous section, we get:

$$\bar{\ell}_c\cdot q_j = \frac{1}{2}\left(\overline{D}_j(\bar{\ell}_c) - \overline{D}_0(\bar{\ell}_c) - q_j^2 + m_j^2 - m_0^2\right) = -\frac{1}{2}(q_j^2 - m_j^2 + m_0^2)\,, \tag{3.42}$$

and

$$\bar{\ell}_c^2 = \overline{D}_0(\bar{\ell}_c) + m_0^2 = m_0^2\,. \tag{3.43}$$

The above two equations constrain the form that the $\bar{\ell}_c$ momenta can have. Writing $\bar{\ell}_c^\mu$ in our working basis:

$$\bar{\ell}_c^\mu = V^\mu + (\bar{\ell}_c\cdot\eta_4)\eta_4^\mu + (\bar{\ell}_c\cdot\eta_\varepsilon)\eta_\varepsilon^\mu\,, \tag{3.44}$$

where:

$$V^\mu = -\frac{1}{2}\sum_{j=1}^{3}(q_j^2 - m_j^2 + m_0^2)\mathcal{V}_j^\mu\,. \tag{3.45}$$

Then, squaring Eq. (3.44) we get:

$$m_0^2 = V^2 + (\bar{\ell}_c\cdot\eta_4)^2 + (\bar{\ell}_c\cdot\eta_\varepsilon)^2\,. \tag{3.46}$$

Since we want to determine some momentum $\overline{\ell}_c^\mu$ for which all denominators are zero, we have the freedom to choose $\overline{\ell}_c \cdot \eta_\varepsilon = 0$. Then:

$$\overline{\ell}_c \cdot \eta_4 = \pm\sqrt{m_0^2 - V^2}\,. \tag{3.47}$$

Therefore, we get two loop momenta ℓ_+, ℓ_- both satisfying $\overline{D}_0(\ell_\pm) = \overline{D}_1(\ell_\pm) = \overline{D}_2(\ell_\pm) = \overline{D}_3(\ell_\pm) = 0$:

$$\ell_\pm^\mu = V^\mu \pm \sqrt{m_0^2 - V^2}\eta_4^\mu\,. \tag{3.48}$$

For the $\ell_\pm$, all lower-point terms of Eq. (3.39) vanish and we get:

$$\begin{aligned} \mathcal{N}_4(\ell_+) &= \tilde{d}_0 + \tilde{d}_1(\ell_+ \cdot \eta_4) = \tilde{d}_0 + \sqrt{m_0^2 - V^2}\tilde{d}_1\,, \\ \mathcal{N}_4(\ell_-) &= \tilde{d}_0 + \tilde{d}_1(\ell_- \cdot \eta_4) = \tilde{d}_0 - \sqrt{m_0^2 - V^2}\tilde{d}_1\,. \end{aligned} \tag{3.49}$$

From the above system of equations, we can finally determine the desired coefficients:

$$\begin{aligned} d(0123) = \tilde{d}_0 &= \frac{\mathcal{N}_4(\ell_+) + \mathcal{N}_4(\ell_-)}{2}\,, \\ \tilde{d}(\ell_\pm; 0123) = \pm\sqrt{m_0^2 - V^2}\tilde{d}_1, \quad &\text{where} \quad \tilde{d}_1 = \frac{\mathcal{N}_4(\ell_+) - \mathcal{N}_4(\ell_-)}{2\sqrt{m_0^2 - V^2}}\,. \end{aligned} \tag{3.50}$$

3.3.3 Reweighting mode

In this section, we report on the computation of the virtual contributions based on the reweighting technique described in Refs. [388, 461, 462]. As the evaluation of one-loop diagrams is, in general, a complicated task, it is desirable to minimize the number of times they are computed. Indeed, without reweighting techniques, one-loop amplitudes would have to be calculated several times during the event generation and phase-space optimization stages, which would require a significant amount of computational resources. To address this issue, a reweighting technique is employed that allows tree-level unweighted events to be reused for the computation of the virtual contribution, thereby substantially increasing the efficiency of the calculation. In practice, the tree-level events are generated through the HELAC-TREES program, and are subsequently used for reweighting in HELAC-1LOOP. The starting point of the method is the observation that the LO and the virtual cross section to a given process with a, b being the colliding partons can be written as:

$$\begin{aligned} \sigma_{ab}^{LO+V} &= \int dx_1 dx_2 d\Phi_m\; f_a(x_a) f_b(x_b)(|\mathcal{M}|^2 + \mathcal{M}^*\mathcal{L} + \mathcal{M}\mathcal{L}^*) \\ &= \int dx_1 dx_2 d\Phi_m\; f_a(x_a) f_b(x_b)|\mathcal{M}|^2 \left(1 + \frac{\mathcal{M}^*\mathcal{L} + \mathcal{M}\mathcal{L}^*}{|\mathcal{M}|^2}\right)\,, \end{aligned} \tag{3.51}$$

where $\mathcal{M}$ and $\mathcal{L}$ denote the LO and one-loop matrix elements, respectively. Note also that the factor of $1/2\hat{s}$ appearing in Eq. (2.5) is assumed to be absorbed in the definition of $d\Phi_m$ and the explicit dependence on μ_F and μ_R is not shown for simplicity. By further defining:

$$g(\vec{X}) = g(x_1, x_2, \Phi_m) = \frac{1}{\sigma_{ab}^{LO}} \frac{d\sigma_{ab}^{LO}}{dx_1 dx_2 d\Phi_m}\,, \tag{3.52}$$

we notice that, by construction, $g(\vec{X})$ can serve as a probability density function as it satisfies

$$\int d\vec{X}\, g(\vec{X}) = 1\,. \tag{3.53}$$

Hence, for any observable $\mathcal{O}(\vec{X})$ it holds that:

$$\int d\vec{X}\, g(\vec{X})\, \mathcal{O}(\vec{X}) = \frac{1}{N}\sum_{i=1}^{N} \mathcal{O}(\vec{X}_i)\,, \tag{3.54}$$

where N denotes the number of unweighted events generated according to $g(\vec{X})$. As evident from Eq. (3.52), these events are associated with the calculation of the LO cross section, but they can be reused for the evaluation of the virtual contribution, provided they are stored appropriately in modified LES HOUCHES FILES [439] for further reweighting. This is possible because LO unweighted events populate the same phase space as the virtual contributions and therefore share identical kinematics, although they carry different weights. To better illustrate how the reweighting works, by choosing

$$\mathcal{O}(\vec{X}) = \left(1 + \frac{\mathcal{M}^*\mathcal{L} + \mathcal{M}\mathcal{L}^*}{|\mathcal{M}|^2}\right)\,, \tag{3.55}$$

it becomes clear that

$$\sigma_{ab}^{LO+V} = \sigma_{ab}^{LO} \int d\vec{X}\, g(\vec{X})\, \mathcal{O}(\vec{X}) = \sigma_{ab}^{LO}\, \frac{1}{N}\sum_{i=1}^{N} \mathcal{O}(\vec{X}_i)\,, \tag{3.56}$$

or equivalently:

$$\frac{1}{N}\sum_{i=1}^{N} \mathcal{O}(\vec{X}_i) = \frac{\sigma_{ab}^{LO+V}}{\sigma_{ab}^{LO}}\,. \tag{3.57}$$

As a consequence, the virtual cross section can be expressed as a product of the LO cross section with the average reweighting factor $\langle w\rangle$:

$$\sigma_{ab}^{V} = \langle w\rangle \sigma_{ab}^{LO}\,, \quad w = \frac{\mathcal{M}^*\mathcal{L} + \mathcal{M}\mathcal{L}^*}{|\mathcal{M}|^2}\,. \tag{3.58}$$

In practice, the LO unweighted events are utilized for the calculation of the virtual contribution once the one-loop contribution $\mathcal{L}$ is determined for a given phase-space point, by multiplying each event weight with the reweighting factor w. We finally note that in HELAC-1LOOP several consistency checks [463] are performed in order to control numerical instabilities that may arise from the calculation of one-loop amplitudes. Such instabilities are more frequent in processes with external gluons. For this reason, a gauge-invariance test based on Ward identities is applied on an event-by-event basis by replacing the polarization vector of an external gluon with its corresponding four-momentum. If this test fails, the amplitude is recomputed using higher numerical precision. Albeit less frequent, instabilities may also arise from external quarks. As in the case of gluon-induced instabilities, a scale test [464] based on momentum rescaling is performed to verify the Ward identity, and higher numerical precision is employed if the test fails.

3.4 Real corrections and subtraction schemes

The full computation of the NLO corrections also requires the calculation of the real emission contributions to the Born process. When NLO QCD corrections are taken into account, the real emission contributions correspond to the emission of an extra light quark or gluon relative to the Born process. As already discussed in Sec. 2.2, such emissions lead to infrared singularities in the soft and collinear regions, and subtraction techniques are required to properly handle these divergences in numerical calculations. In HELAC-DIPOLES, two such subtraction methods have been implemented: the Catani-Seymour (CS) [401, 402] and the Nagy-Soper (NS) [403] subtraction schemes. As the final NLO cross section does not depend on the choice of the subtraction scheme, employing two distinct subtraction methods has been proven very useful for verifying the validity of the results. However, before discussing the differences between the two schemes, it is important to report on the basics of any subtraction method aiming to handle the infrared divergences in Monte Carlo numerical simulations. We begin by highlighting that in the soft and collinear regions, the squared-matrix element with $m+1$ particles is factorized into a Born piece and a universal factor that contains the singularities. By following Ref. [401] we discuss how this factorization looks like in the soft and collinear limits. First, to parametrize the soft divergence, we introduce a parameter λ such that the momentum of the extra gluon can be written as $p_j^\mu = \lambda q^\mu$, and the soft limit is effectively described by taking $\lambda \to 0$. In that limit, the squared-matrix element behaves as follows:

$$\begin{aligned} &\langle 1,2,...,m+1|1,2,...,m+1\rangle_{m+1} \to \\ &-\frac{1}{\lambda^2} 4\pi\mu^{2\varepsilon}\alpha_s \langle 1,2,...,m+1|[\mathbf{J}^\mu(q)]^\dagger \mathbf{J}_\mu(q)|1,2,...,m+1\rangle_m \,, \end{aligned} \tag{3.59}$$

where m is the number of external particles at the Born configuration. In the second line of the above formula, the matrix element involves m external particles, with the extra soft gluon having been removed. In addition, the $\mathbf{J}^\mu(q)$ term is the eikonal current of a soft gluon, which is given by:

$$\mathbf{J}^\mu(q) = \sum_{i=1}^{m+1} \mathbf{T}_i \frac{p_i^\mu}{p_i\, q} \,, \tag{3.60}$$

where $\mathbf{T}_i$ is the color-charge operator, defined in the adjoint representation when the emitting particle i is a gluon and in the fundamental representation when i is a quark. A similar factorization formula can also be obtained in the collinear limit. Below, we restrict the discussion to the case where only two final-state partons i, j can become collinear, but a similar factorization formula also holds in the case where a final-state parton becomes collinear with an initial-state parton. For the case of our interest, the momenta of the final-state partons i, j that become collinear can be parametrized as follows:

$$p_i^\mu = z p^\mu + k_\perp^\mu - \frac{k_\perp^2}{z}\frac{n^\mu}{2\,p\,n} \,, \quad p_j^\mu = (1-z) p^\mu - k_\perp^\mu - \frac{k_\perp^2}{1-z}\frac{n^\mu}{2\,p\,n} \,, \tag{3.61}$$

and the collinear limit is taken by $k_\perp \to 0$. In the above expressions, p^μ and n^μ are light-like vectors satisfying $p^2 = n^2 = 0$, while the transverse momentum $k_\perp^\mu$ obeys

$k_\perp p = k_\perp n = 0$. Then, in the collinear limit, the squared matrix element behaves as:

$$\begin{aligned}&\langle 1,2,...,m+1|1,2,...,m+1\rangle_{m+1} \to \\ &\frac{1}{p_i p_j} 4\pi\mu^{2\varepsilon}\alpha_s \langle 1,2,...,m+1|\hat{P}_{i,(ij)}(z,k_\perp;\varepsilon)|1,2,...,m+1\rangle_m \,,\end{aligned} \tag{3.62}$$

where in the squared-matrix element of the second line, the collinear partons i, j have been replaced by a single parton, labeled as ij. The $\hat{P}_{i,(ij)}$ kernels are universal, d-dimensional operators acting on the spin states of partons i, j with an additional dependence on the transverse momentum $k_\perp$. Upon summing over helicities and integrating over the transverse momentum of the unresolved radiation, these kernels reduce to the usual DGLAP splitting functions [390, 395, 396] discussed in Sec. 2.1. Their explicit formulas are given below:

$$\begin{aligned}\langle s|\hat{P}_{qq}(z,k_\perp;\varepsilon)|s'\rangle &= \delta_{ss'}C_F\left[\frac{1+z^2}{1-z} - \varepsilon(1-z)\right] \,, \\ \langle s|\hat{P}_{gq}(z,k_\perp;\varepsilon)|s'\rangle &= \delta_{ss'}C_F\left[\frac{1+(1-z)^2}{z} - \varepsilon z\right] \,, \\ \langle \mu|\hat{P}_{qg}(z,k_\perp;\varepsilon)|\nu\rangle &= T_R\left[-g^{\mu\nu} + 4z(1-z)\frac{k_\perp^\mu k_\perp^\nu}{k_\perp^2}\right] \,, \\ \langle \mu|\hat{P}_{gg}(z,k_\perp;\varepsilon)|\nu\rangle &= 2C_A\left[-g^{\mu\nu}\left(\frac{z}{1-z}+\frac{1-z}{z}\right) - 2(1-\varepsilon)z(1-z)\frac{k_\perp^\mu k_\perp^\nu}{k_\perp^2}\right] \,.\end{aligned} \tag{3.63}$$

The core idea of any subtraction method is to exploit the universal factorization properties described above in the soft and collinear limits, and to construct local subtraction terms that reproduce the behavior of the real-emission matrix element as given in Eqs. (3.59) and (3.62) in the corresponding singular regions. These expressions cannot be used directly for this purpose, since they are strictly valid only in the soft and collinear limits. Subtraction terms are, however, constructed to reproduce these singular behaviors locally, while being defined over the entire $d\Phi_{m+1}$ phase space so that their difference with the real-emission contribution is finite everywhere. This requires the introduction of appropriate phase-space mappings from the $(m+1)-$ to $m-$particle kinematics that restore momentum conservation also outside the singular limits:

$$\{p\}_{m+1} \to \{\tilde{p}\}_m \,, \tag{3.64}$$

where $\{\tilde{p}\}_m$ denote the momenta of the particles after the mapping. Denoting by i the emitting and j the emitted parton, the mapping produces a new parton $\tilde{ij}$, whose kinematics are determined by the corresponding mapping. The mapping must respect momentum conservation and the on-shell conditions of all particles, with the recoil absorbed by one or more spectator partons, typically labeled as k. Such phase-space mappings are not unique, and therefore different subtraction methods can be constructed with distinct mappings as long as the mapping preserves momentum conservation, on-shell conditions, and reproduces the correct soft and collinear limits. For instance, in the CS subtraction scheme, each parton in the event can act as a spectator, while in the NS subtraction scheme, the recoil is shared among

all particles, effectively defining a single collective spectator. By closely following the notation of Ref. [403], the subtraction term for the CS scheme is given by:

$$|\mathcal{M}^S_{CS}(\{p\}_{m+1})|^2 = \sum_{\substack{i,j=1 \\ i\neq j}}^{m+1} \sum_{\substack{k=1 \\ k\neq i,j}}^{m+1} |\mathcal{M}(\{\tilde{p}\}^{(ijk)}_m)|^2 \otimes \mathcal{D}^{(ijk)}_{CS}(\{\tilde{p}^{(ijk)}_m, \{p\}_{m+1}), \tag{3.65}$$

where (ijk) characterizes the individual mapping that depends on the kinematics of the emitter, the emitted and the spectator. As a consequence, the number of distinct mappings can scale as $\mathcal{O}(m_p^3)$, where m_p is the number of final-state QCD partons, since one must sum over all possible (i, j, k) pairs. By contrast, in the NS scheme, there is a single mapping associated with each (ij) pair, so the total number of mappings is much smaller, scaling only as $\mathcal{O}(m_p^2)$. Hence, for processes with high jet multiplicities, employing the NS scheme can lead to a substantial reduction in the computational time required for the calculation, even though the phase-space integration over the unresolved radiation is more demanding because of the more involved $\{\tilde{p}_m\}$ kinematics. The subtraction term in this scheme is expressed as:

$$|\mathcal{M}^S_{NS}(\{p\}_{m+1})|^2 = \sum_{i,j=1}^{m+1} |\mathcal{M}(\{\tilde{p}\}^{(ij)}_m)|^2 \otimes \left(\sum_{k=1}^{m+1} \mathcal{D}^{(ijk)}_{NS}(\{\tilde{p}^{(ij)}_m, \{p\}_{m+1}) \right). \tag{3.66}$$

In both Eqs. (3.65) and (3.66), the $\mathcal{D}^{(ijk)}_{CS/NS}$ terms are splitting functions constructed in such a way to reproduce the exact behavior of the real squared matrix element in the singular regions. Their explicit form as well as the corresponding mappings can be found in Ref. [401] for the CS and Ref. [403] for the NS scheme. Finally, the $\otimes$ symbol represents all possible color and spin correlations.

Overall, the subtraction term at the cross-section level can be written as:

$$d\sigma^S = \sum_{\text{dipoles}} d\sigma^B \otimes (dV_{\text{dipole}} + dV'_{\text{dipole}}), \tag{3.67}$$

where the notation of the original CS subtraction scheme [401,402] has been adopted. In other subtraction schemes, including the NS scheme, the explicit form and organization of the local counterterms differ, but the same underlying principle, namely the construction of local counterterms that reproduce the soft and collinear limits of the real-emission contribution, remains the same. Sticking to the CS scheme, dV_{dipole} denotes the dipole terms that correctly reproduce the soft singularities as well as the collinear divergences associated with final-state partons. The dV'_{dipole} terms, on the other hand, account for configurations in which a final-state parton becomes collinear with an initial-state one. As already discussed in Sec. 2.2, such singularities do not cancel against the infrared poles of the virtual corrections, but are instead absorbed into the parton distribution functions through the factorization procedure.

After constructing the subtracted terms, the numerical integration of the subtracted real contribution can be carried out in $d = 4$ dimensions. To enhance the efficiency of this integration, one can restrict the region of the phase space in which the dipole subtraction terms are applied by ensuring that the singular regions are captured. This strategy is effective because the purpose of the subtraction scheme is to address these singular regions where divergences occur. In the CS scheme,

this can be achieved by introducing the parameter a_{max} [437, 465, 466], which acts as a cut-off on the dipole phase-space variables and determines the region in which the dipole subtraction terms are applied. The dipole phase-space variables differ depending on whether the emitter (i) and the spectator (k) partons are in the final or initial state. For instance, when both the emitter and the spectator are in the final state, the following restriction is applied:

$$y_{ij,k} < a_{max}, \quad y_{ij,k} = \frac{p_i p_j}{p_i p_j + p_i p_k + p_j p_k} \,. \tag{3.68}$$

The a_{max} parameter typically ranges from $(0, 1]$ as the singular behavior is associated with $y_{ij,k} \to 0$. By incorporating such a parameter, the integration over the subtracted term takes the following form [465]:

$$\begin{aligned} &\int d\Phi_{m+1}\, d\sigma^S(a_{max}) = \\ &\sum_{\substack{k=1 \\ k\neq i,j}}^{m+1} \int d\Phi_m(\{\tilde{p}\}_m^{(ijk)}) dp_i(\{\tilde{p}\}_m^{(ijk)}) \mathcal{D}_{CS}^{(ijk)} \theta(y_{ij,k} < a_{max}) \mathcal{F}_J(\{\tilde{p}\}_m^{(ijk)}) \,, \end{aligned} \tag{3.69}$$

where $dp_i(\{\tilde{p}\}_m^{(ijk)})$ represents the phase space of the unresolved parton arising from the factorization of the $(m+1)$-particle phase space for each individual dipole, according to:

$$d\Phi_{m+1}(\{p\}_{m+1}) = d\Phi_m(\{\tilde{p}\}_m^{(ijk)}) dp_i(\{\tilde{p}\}_m^{(ijk)}) \,, \tag{3.70}$$

and F_J is the m-parton jet function which depends on the mapped momenta $\{\tilde{p}\}_m^{(ijk)}$ from the individual mapping. Finally, it is important to note that the introduction of the a_{max} parameter is unphysical and should not influence the value of the NLO cross section. Therefore, in this thesis, varying the a_{max} values during computations has been utilized as a cross-check to confirm the validity of the results. For the NS subtraction scheme, alternative phase-space restrictions are used [124, 467], but the goal remains the same, i.e., optimizing the integration by constraining the phase space of the dipoles in the non-singular regions.

3.5 The final NLO cross-section formula

Upon integration of Eq. (3.67) over the phase space of the unresolved emission, two distinct contributions arise:

1. The **I** operator, defined as $\mathbf{I} = \sum_{\text{dipoles}} \int_1 dV_{\text{dipole}}$, which contains the $1/\varepsilon$ and $1/\varepsilon^2$ poles that cancel the corresponding singularities present in the virtual contributions, together with a finite remainder.

2. Additional terms stemming from the integration of the dV'_{dipole} contributions. These generate initial-state collinear singularities that exactly cancel the corresponding poles introduced by the collinear counterterms in Eq. (2.8). The remaining finite terms comprise the so-called **K** and **P** operators, commonly referred to collectively as the **KP** operator. We recall that the collinear counterterms in Eq. (2.8) are included in the definition of the partonic cross section to ensure that after convolution with renormalized parton distribution functions, the NLO cross section is finite.

To fully obtain the NLO cross section for a given process, HELAC-1LOOP is employed to generate the Born and virtual contributions, while HELAC-DIPOLES is utilized for calculating the real-subtracted contributions, the **KP** operator and the finite remainders of the **I** operator. The NLO cross-section formula is then expressed as follows:

$$\begin{aligned}\sigma^{\rm NLO} = &\int d\Phi_{m+1}\left[d\sigma^R - d\sigma^S\right] \\ &+ \int d\Phi_m\left[d\sigma^{B+V} + d\sigma^B \otimes \mathbf{I}\right] + \int_0^1 dx \int d\Phi_m\, d\sigma^B \otimes \left[\mathbf{K} + \mathbf{P}\right] .\end{aligned} \tag{3.71}$$

For all results presented in this thesis, multiple cross-checks have been conducted to ensure the validity of the computations. This includes verifying the cancellation of the $1/\varepsilon$ and $1/\varepsilon^2$ poles between the virtual contributions and the $d\sigma^B \otimes \mathbf{I}$ term for various phase-space points. Additionally, both the CS and NS subtraction schemes were employed to confirm that the final NLO cross section remains independent of the chosen subtraction scheme. Indeed, while different subtraction schemes yield distinct expressions for the $[d\sigma^R - d\sigma^S]$, $d\sigma^B \otimes \mathbf{I}$ and $d\sigma^B \otimes [\mathbf{K} + \mathbf{P}]$ pieces, their combined effect alongside $d\sigma^{B+V}$ should consistently produce the same NLO cross section.

Chapter 4

The $pp \to t\bar{t}t\bar{t}$ process in QCD

In this chapter, we analyze the results of Refs. [385, 386]. These works provide the first exact NLO QCD predictions for the $pp \to t\bar{t}t\bar{t}$ process in the 4ℓ and 3ℓ channels, including NLO QCD corrections both in the production and the decays of the top quarks within the Narrow-Width Approximation (NWA) framework. As a result, hard real emissions are consistently incorporated in the decays, and spin correlations are preserved at NLO accuracy without any approximation. We emphasize that results are provided only for the dominant LO contributions and their corresponding NLO QCD corrections, while neglecting all subleading effects. This is because of two reasons: first, the main goal of Refs. [385, 386] is to fill the gap in the literature concerning the missing higher-order QCD corrections in the top-quark decays at the matrix element level, which are absent in previous studies. Second, although subleading effects can become important, especially at the differential cross-section level, at the level of the integrated cross section they are known to undergo accidental cancellations [320]. As a result, the dominant QCD corrections to the leading QCD contributions remain the primary effect. The structure of this chapter is as follows: In Sec. 4.1 we give the process description and present in detail the framework of the calculation and the various NWA treatments employed. Separate emphasis on the 4ℓ and 3ℓ channels is given in Sec. 4.2 and 4.3 respectively. For both channels we present the computational setup and the input parameters used in Sec. 4.2.1 and 4.3.1, while results at the integrated and differential cross-section level are discussed in Sec. 4.2.2, 4.2.3 and 4.3.2, 4.3.3 for the 4ℓ and 3ℓ channels, respectively.

4.1 Description of the calculation

We provide results for the

$$pp \to t\bar{t}t\bar{t} + X \to W^+W^+W^-W^-\, b\bar{b}\, b\bar{b} + X \to \ell^+\nu_\ell\, \ell^+\nu_\ell\, \ell^-\bar{\nu}_\ell\, \ell^-\bar{\nu}_\ell\, b\bar{b}\, b\bar{b} + X\ , \quad (4.1)$$

and

$$\begin{aligned} pp \to t\bar{t}t\bar{t} + X \to W^+W^+W^-W^-\, b\bar{b}\, b\bar{b} + X \to \ell^+\nu_\ell\, \ell^+\nu_\ell\, \ell^-\bar{\nu}_\ell\, q\bar{q}'\, b\bar{b}\, b\bar{b} + X\ , \\ pp \to t\bar{t}t\bar{t} + X \to W^+W^+W^-W^-\, b\bar{b}\, b\bar{b} + X \to \ell^+\nu_\ell\, \ell^-\bar{\nu}_\ell\, \ell^-\bar{\nu}_\ell\, q\bar{q}'\, b\bar{b}\, b\bar{b} + X \end{aligned} \quad (4.2)$$

processes at NLO in QCD, which we refer to as the 4ℓ and 3ℓ channels. In the above expressions, $\ell^\pm$ denotes $e^\pm$ or $\mu^\pm$, and the quark pairs are given by $q\bar{q}' = d\bar{u}, s\bar{c}$ for W^- decays and $q\bar{q}' = u\bar{d}, c\bar{s}$ for W^+ decays. We do not consider $\tau^\pm$ leptons

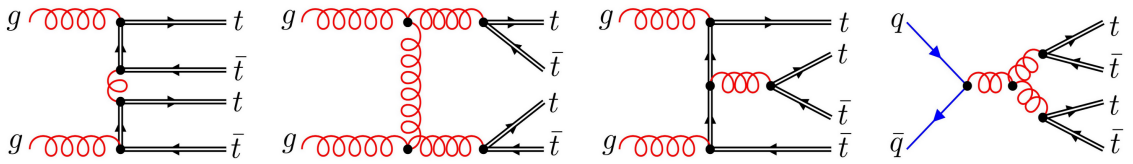

Figure 4.1: *Representative LO Feynman diagrams for the processes defined in Eq. (4.1) and (4.2) at the $\mathcal{O}(\alpha_s^4\alpha^8)$ order, where the decays of the top quarks are not shown for simplicity. The double lines correspond to top quarks, red curly lines to gluons and blue solid lines to light quarks. All graphs were generated with the help of the FeynGame package [421–423].*

in the final state, since they are often analyzed separately due to their rich and complex decay pattern. However, all results can be rescaled by the $3^4/2^4 = 81/16$ and $3^3/2^3 = 27/8$ lepton factors for the 4ℓ and 3ℓ channels, respectively, if the $\tau^\pm$ leptons are to be included. For both channels, we employ the NWA, in which the top quarks are produced on shell and subsequently decay into on-shell $W^\pm$ bosons and bottom quarks. In the 4ℓ channel, all four $W^\pm$ bosons decay leptonically, while in the 3ℓ channel, three decay leptonically and one hadronically. The processes under consideration involve up to 13 particles in the final state at NLO in QCD. As a result, full off-shell computations are currently beyond reach due to their complexity and the substantially larger number of Feynman diagrams that need to be computed. Nevertheless, for the 4ℓ channel, we were able to obtain full off-shell predictions at LO in QCD. In Sec. 4.2.4, we also assess the impact of full off-shell effects in the 4ℓ channel at both the integrated and differential fiducial cross-section level, by focusing on observables particularly sensitive to these effects. Nonetheless, the NWA is expected to be a good approximation, as the associated error is of order $\mathcal{O}(\Gamma_t/m_t)$ for sufficiently inclusive observables [433].

At LO in QCD, we include all contributions of order $\mathcal{O}(\alpha_s^4\alpha^8)$, where only the gg and $q\bar{q}/\bar{q}q$ subprocesses contribute, with $q = u, d, c, s, b$, as shown in Fig. 4.1. At NLO in QCD, we compute all QCD corrections to the LO contributions in both the production and decay stages of the top quarks, of the order of $\mathcal{O}(\alpha_s^5\alpha^8)$. Real emission contributions and virtual corrections are consistently incorporated. All results are generated within the Helac-Nlo framework [388], comprising Helac-1Loop [438] and Helac-Dipoles [437]. The cancellation of the $1/\varepsilon$ and $1/\varepsilon^2$ poles between the real emission contributions and the virtual corrections has been explicitly verified for multiple phase-space points. To further check the validity of our results, for both the 4ℓ and 3ℓ channels, we employed both the Catani-Seymour and the Nagy-Soper subtraction schemes and found perfect agreement. In addition, for both schemes, we varied the phase-space restriction parameters, confirming the independence of the final results from these choices. The finite virtual contributions, as well as the cancellation of the $1/\varepsilon$ and $1/\varepsilon^2$ infrared poles, were cross-checked using both the MadGraph_aMC@NLO [203] and Recola MC [468] program for multiple phase-space points and for all relevant partonic channels, namely the gg and $q\bar{q}/\bar{q}q$ initial states. For MadGraph_aMC@NLO, the comparison was carried out independently for production and decay, by evaluating the finite virtual parts and the infrared pole structure for the $pp \to t\bar{t}t\bar{t}$, $t \to \ell^+\nu_l b$ and $\bar{t} \to \ell^-\bar{\nu}_\ell\bar{b}$ processes. For the 3ℓ channel, analogous checks were performed for the hadronic top and antitop decays. For the comparison with Recola, we exploited its existing

interface within the HELAC-NLO framework, previously used in NWA studies of $pp \to t\bar{t}jj$ [140] and $pp \to t\bar{t}\gamma\gamma$ [206]. In this setup, the validation could be carried out without separating the production and decay stages, owing to the double-pole approximation [85, 469, 470] implemented in RECOLA, which interfaces smoothly with the HELAC-NLO framework for use within the NWA.

In what follows, we describe the various NWA treatments employed to obtain all results presented in this chapter. In particular, we consider scenarios where QCD corrections are included both in the production and in the decays of the top quarks, as well as a setup where QCD corrections are only applied in the production stage of the $pp \to t\bar{t}t\bar{t}$ system. By doing so, we are able to estimate the impact of higher-order QCD corrections in the top-quark decays. Such effects are usually not taken into account in the literature, or they are only modeled by parton-shower programs, see e.g. Ref. [382]. Their inclusion is, therefore, essential for a better description of the underlying dynamics. In the first approach, denoted as NLO_{full}, QCD corrections are applied in both stages of the calculation, and the NLO cross section is given by the formula below:

$$\begin{aligned}
d\sigma^{\text{NLO}}_{\text{full}} &= d\sigma^{\text{NLO}}_{t\bar{t}t\bar{t}} \times \frac{d\Gamma^{(0)}_t}{\Gamma^{\text{NLO}}_t} \times \frac{d\Gamma^{(0)}_{\bar{t}}}{\Gamma^{\text{NLO}}_t} \times \frac{d\Gamma^{(0)}_t}{\Gamma^{\text{NLO}}_t} \times \frac{d\Gamma^{(0)}_{\bar{t}}}{\Gamma^{\text{NLO}}_t} \\
&+ d\sigma^{\text{LO}}_{t\bar{t}t\bar{t}} \times \frac{d\Gamma^{(1)}_t}{\Gamma^{\text{NLO}}_t} \times \frac{d\Gamma^{(0)}_{\bar{t}}}{\Gamma^{\text{NLO}}_t} \times \frac{d\Gamma^{(0)}_t}{\Gamma^{\text{NLO}}_t} \times \frac{d\Gamma^{(0)}_{\bar{t}}}{\Gamma^{\text{NLO}}_t} \\
&+ d\sigma^{\text{LO}}_{t\bar{t}t\bar{t}} \times \frac{d\Gamma^{(0)}_t}{\Gamma^{\text{NLO}}_t} \times \frac{d\Gamma^{(1)}_{\bar{t}}}{\Gamma^{\text{NLO}}_t} \times \frac{d\Gamma^{(0)}_t}{\Gamma^{\text{NLO}}_t} \times \frac{d\Gamma^{(0)}_{\bar{t}}}{\Gamma^{\text{NLO}}_t} \\
&+ d\sigma^{\text{LO}}_{t\bar{t}t\bar{t}} \times \frac{d\Gamma^{(0)}_t}{\Gamma^{\text{NLO}}_t} \times \frac{d\Gamma^{(0)}_{\bar{t}}}{\Gamma^{\text{NLO}}_t} \times \frac{d\Gamma^{(1)}_t}{\Gamma^{\text{NLO}}_t} \times \frac{d\Gamma^{(0)}_{\bar{t}}}{\Gamma^{\text{NLO}}_t} \\
&+ d\sigma^{\text{LO}}_{t\bar{t}t\bar{t}} \times \frac{d\Gamma^{(0)}_t}{\Gamma^{\text{NLO}}_t} \times \frac{d\Gamma^{(0)}_{\bar{t}}}{\Gamma^{\text{NLO}}_t} \times \frac{d\Gamma^{(0)}_t}{\Gamma^{\text{NLO}}_t} \times \frac{d\Gamma^{(1)}_{\bar{t}}}{\Gamma^{\text{NLO}}_t} \,,
\end{aligned} \tag{4.3}$$

where $d\sigma^{(\text{N})\text{LO}}_{t\bar{t}t\bar{t}}$ represents the (N)LO cross section at the production stage of the four tops, $d\Gamma^{(0)}$ and $d\Gamma^{(1)}$ denote LO and NLO contributions to the decay processes, and Γ^{NLO}_t is the NLO decay width of the top quark. In the first line of the above formula, QCD corrections are applied in the production stage, while in the remaining lines QCD corrections are included in the decays of the t and $\bar{t}$ quarks. In addition, the symbol $\times$ represents spin correlations, which are NLO accurate, as QCD corrections are consistently included in both production and decays. Moreover, the individual terms in Eq. (4.3) do not interfere with one another, and there is no cross-talk between production and decay, nor among the different top-quark decays. In the second approach, referred to as $\text{NLO}_{\text{LO}_{\text{dec}}}$, only the first line of Eq. (4.3) is retained, and higher-order QCD effects are included solely at the production stage. In this case, all top quarks decay with LO accuracy, and thus the LO top-quark width Γ^{LO}_t is used consistently:

$$d\sigma^{\text{NLO}}_{\text{LO}_{\text{dec}}} = d\sigma^{\text{NLO}}_{t\bar{t}t\bar{t}} \times \frac{d\Gamma^{0}_t}{\Gamma^{\text{LO}}_t} \times \frac{d\Gamma^{0}_{\bar{t}}}{\Gamma^{\text{LO}}_t} \times \frac{d\Gamma^{0}_t}{\Gamma^{\text{LO}}_t} \times \frac{d\Gamma^{0}_{\bar{t}}}{\Gamma^{\text{LO}}_t} \,. \tag{4.4}$$

The top-quark width is, however, also a perturbative parameter that can be expanded in terms of the strong coupling constant α_s. Its expansion at NLO in QCD

is given by:

$$\Gamma_t^{\mathrm{NLO}} = \Gamma_t^{(0)} + \alpha_s \Gamma_t^{(1)} \,. \tag{4.5}$$

Therefore, in a third approach, which we denote as $\mathrm{NLO}_{\mathrm{exp}}$, the decay width of the top quark is also expanded in Eq. (4.3), yielding:

$$d\sigma_{\mathrm{exp}}^{\mathrm{NLO}} = d\sigma^{\mathrm{NLO}} = d\sigma_{\mathrm{full}}^{\mathrm{NLO}} \times \left(\frac{\Gamma_t^{\mathrm{NLO}}}{\Gamma_t^{\mathrm{LO}}}\right)^4 - d\sigma^{\mathrm{LO}} \times \frac{4(\Gamma_t^{\mathrm{NLO}} - \Gamma_t^{\mathrm{LO}})}{\Gamma_t^{\mathrm{LO}}} \,, \tag{4.6}$$

where $d\sigma^{\mathrm{LO}}$ indicates the LO cross section, given by:

$$d\sigma^{\mathrm{LO}} = \; d\sigma_{t\bar{t}t\bar{t}}^{\mathrm{LO}} \times \frac{d\Gamma_t^0}{\Gamma_t^{\mathrm{LO}}} \times \frac{d\Gamma_{\bar{t}}^0}{\Gamma_t^{\mathrm{LO}}} \times \frac{d\Gamma_t^0}{\Gamma_t^{\mathrm{LO}}} \times \frac{d\Gamma_{\bar{t}}^0}{\Gamma_t^{\mathrm{LO}}} \,. \tag{4.7}$$

The advantage of this approach is that it consistently removes higher-order terms arising from the usage of the NLO top-quark width everywhere in Eq. 4.3, even in cases where QCD corrections are only applied at the production stage. This prescription comprises our default setup, which we denote as $\mathrm{NLO}_{\mathrm{exp}}$ or simply NLO.

4.2 4ℓ channel

In this section, we focus on the 4ℓ channel of the $pp \to t\bar{t}t\bar{t}$ process, as defined in Eq. (4.1). We first present the computational setup used and then proceed to the cross-section results, both at the integrated and the differential level.

4.2.1 Computational setup

We perform the calculations for the LHC Run III using the $\sqrt{s} = 13.6$ TeV center-of-mass energy and employ the following SM input parameters:

$$\begin{aligned} &G_\mu = 1.1663787 \cdot 10^{-5}\ \mathrm{GeV}^{-2} \,, && m_t = 172.5\ \mathrm{GeV} \,, \\ &m_W = 80.379\ \mathrm{GeV} \,, && \Gamma_W^{\mathrm{NLO}} = 2.0972\ \mathrm{GeV} \,, \\ &m_Z = 91.1876\ \mathrm{GeV} \,, && m_b = 0\ \mathrm{GeV} \,. \end{aligned} \tag{4.8}$$

For the top-quark decay width, we use

$$\Gamma_t^{\mathrm{LO}} = 1.4806842\ \mathrm{GeV}, \quad \Gamma_{\mathrm{t}}^{\mathrm{NLO}} = 1.3535983\ \mathrm{GeV} \,, \tag{4.9}$$

for the LO and NLO calculations, respectively. These values have been obtained using the formulas from Ref. [81], assuming the $W^\pm$ boson to be exactly on shell. For the calculation of Γ_t^{NLO}, we employed the two-loop running of the strong coupling constant α_s with five active flavors, at the $\mu_R = m_t$ scale. However, alternative NLO top-quark widths computed with $\alpha_s(\mu_R = m_t/2)$ and $\alpha_s(\mu_R = 2m_t)$ have also been employed, yielding the values of $\Gamma_t^{\mathrm{NLO}} = 1.3402268$ GeV and $\Gamma_t^{\mathrm{NLO}} = 1.3646054$ GeV. We have explicitly verified that the results obtained using these values differ by at most $3\% - 4\%$, which lies well within the theoretical uncertainty of the process, as discussed in Sec. 4.2.2. The scale dependence of Γ_t^{NLO} is therefore included as part of the systematic uncertainty. For the $W^\pm$ boson decay width, we

employ the NLO QCD value evaluated at $\mu_R = m_W$ even though all $W^\pm$ bosons decay leptonically and thus do not receive NLO QCD corrections. This choice incorporates the known higher-order QCD corrections to the total $W^\pm$ decay width and hence to the normalization of the leptonic decay in the NWA. In addition, we keep the Cabibbo-Kobayashi-Maskawa mixing matrix [9, 10] diagonal and keep all light partons massless. The running of the strong coupling constant α_s is provided by the LHAPDF library [471], assuming five active flavors, while the electromagnetic coupling α is evaluated in the G_μ scheme:

$$\alpha_{G_\mu} = \frac{\sqrt{2}}{\pi} G_F \, m_W^2 \, \sin^2\theta_W, \quad \text{where} \quad \sin^2\theta_W = 1 - \frac{m_W^2}{m_Z^2}\,. \tag{4.10}$$

Results are provided for the following fixed and dynamical renormalization and factorization scales:

$$\mu_R = \mu_F = \mu_0 = 2m_t\,, \quad \mu_R = \mu_F = \mu_0 = E_T/4\,, \tag{4.11}$$

where E_T is defined as the transverse energy of the reconstructed top and antitop quarks:

$$E_T = \sum_{i\in\{t,\bar{t},t,\bar{t}\}} \sqrt{p_{T,i}^2 + m_i^2}\,. \tag{4.12}$$

The top and antitop quarks are reconstructed from their decay products without taking into account the existence of the potential extra light jet. However, we have checked that its inclusion does not have any significant impact on the results. To estimate the impact of missing higher-order corrections in our calculation, we employ the standard seven-point scale variation. In practice, this means that we consider the minimum and maximum cross-section values obtained after using the following μ_R, μ_F pairs:

$$\left(\frac{\mu_R}{\mu_0}\,,\frac{\mu_F}{\mu_0}\right) = \Big\{\,(2,1)\,,(0.5,1)\,,(1,2)\,,(1,1),(1,0.5),(2,2),(0.5,0.5)\Big\}\,. \tag{4.13}$$

Apart from the uncertainty associated with the scale choice, an additional source of theoretical error arises from the choice of PDFs. For this purpose, even though our default PDF is MSHT20 [472], in accordance with what is recommended from the PDF4LHC working group [473], we also provide results for two alternative PDF sets: NNPDF3.1 [474] and CT18 [475]. For the (N)LO computations, we utilize the corresponding (N)LO PDFs, where the α_s running is performed with (two-loop) one-loop accuracy and provided by the LHAPDF library [476] with $N_f = 5$. Since no LO PDF set is available for CT18, the CT14llo [471] PDF set with $\alpha_s(m_Z) = 0.130$ is used instead for the LO calculations.

Jets are constructed from all final state partons with $|\eta| < 5$, using the anti$-k_T$ clustering algorithm [477] with a resolution parameter $R = 0.4$. In addition, we require at least 4 b-jets and exactly 4 charged leptons in the final state that must satisfy the following selection criteria:

$$\begin{aligned} &p_{T,\ell} > 25\ \text{GeV}\,, && |y_\ell| < 2.5\,, && \Delta R_{\ell\ell} > 0.4\,,\\ &p_{T,b} > 25\ \text{GeV}\,, && |y_b| < 2.5\,, && \Delta R_{bb} > 0.4\,. \end{aligned} \tag{4.14}$$

PDF	$\sigma^{\rm LO}$ [ab]	δ_{scale}	$\sigma^{\rm NLO}$ [ab]	δ_{scale}	$\mathcal{K} = \sigma^{\rm NLO}/\sigma^{\rm LO}$
$\mu_R = \mu_F = \mu_0 = 2m_t$					
MSHT20	4.3868(3)	$^{+3.2237\ (73\%)}_{-1.7332\ (40\%)}$	4.895(2)	$^{+0.624\ (13\%)}_{-1.002\ (20\%)}$	1.12
NNPDF3.1	3.7389(2)	$^{+2.6811\ (72\%)}_{-1.4545\ (39\%)}$	4.846(2)	$^{+0.632\ (13\%)}_{-1.002\ (21\%)}$	1.30
CT18	4.6757(3)	$^{+3.3754\ (72\%)}_{-1.8311\ (39\%)}$	4.857(2)	$^{+0.620\ (13\%)}_{-0.992\ (20\%)}$	1.04
$\mu_R = \mu_F = \mu_0 = E_T/4$					
MSHT20	4.7479(3)	$^{+3.5156\ (74\%)}_{-1.8855\ (40\%)}$	5.170(3)	$^{+0.638\ (12\%)}_{-1.056\ (20\%)}$	1.09
NNPDF3.1	4.0930(3)	$^{+2.9792\ (73\%)}_{-1.6063\ (39\%)}$	5.126(3)	$^{+0.634\ (12\%)}_{-1.055\ (21\%)}$	1.25
CT18	5.0003(3)	$^{+3.6151\ (72\%)}_{-1.9623\ (39\%)}$	5.127(3)	$^{+0.636\ (12\%)}_{-1.045\ (20\%)}$	1.03

Table 4.1: *Integrated fiducial cross sections for the* $pp \to \ell^+\nu_\ell\,\ell^+\nu_\ell\,\ell^-\bar{\nu}_\ell\,\ell^-\bar{\nu}_\ell\,b\bar{b}\,b\bar{b}+X$ *process at the LHC using a center-of-mass energy of* $\sqrt{s} = 13.6$ TeV. *Results are presented for various (N)LO PDF sets at (N)LO in QCD, using the fixed* $\mu_0 = 2m_t$ *and the dynamical* $\mu_0 = E_T/4$ *scale choices, including the theoretical uncertainties obtained under the standard seven-point scale variation. In the last column,* $\mathcal{K}$ *factors, defined as* $\mathcal{K} = \sigma^{\rm NLO}/\sigma^{\rm LO}$, *are displayed. The numbers inside the parentheses for the central predictions correspond to Monte Carlo integration errors.*

These requirements mimic the typical ATLAS and CMS detector acceptance. We use the charge blind scheme [155] for clustering b quarks, which in practice implies the following recombination rules:

$$b\bar{b} \to g\,, \quad bb \to g\,, \quad \bar{b}\bar{b} \to g\,, \quad bg \to b\,, \quad \bar{b}g \to \bar{b}\,. \tag{4.15}$$

We set no cut on the missing transverse energy associated with neutrinos in the final state, nor on the kinematics of any additional light jet stemming from the real emission.

4.2.2 Integrated fiducial results

The integrated fiducial cross-section results for the $pp \to \ell^+\nu_\ell\,\ell^+\nu_\ell\,\ell^-\bar{\nu}_\ell\,\ell^-\bar{\nu}_\ell\,b\bar{b}\,b\bar{b}+X$ process at the LHC with $\sqrt{s} = 13.6$ TeV, using the NWA framework, are given in Table 4.1 both at LO and NLO in QCD. We present the results obtained using the MSHT20, NNPDF3.1 and CT18 PDF sets as well as the fixed and dynamical scale choices from Eq. (4.11), (4.12). Also shown are scale uncertainties obtained from the standard seven-point scale variation and $\mathcal{K}$ factors, to estimate the impact of the NLO QCD corrections to the LO contributions. First, we notice that the size of the LO scale uncertainties is sizable for both scale choices, reaching values up to 74%.

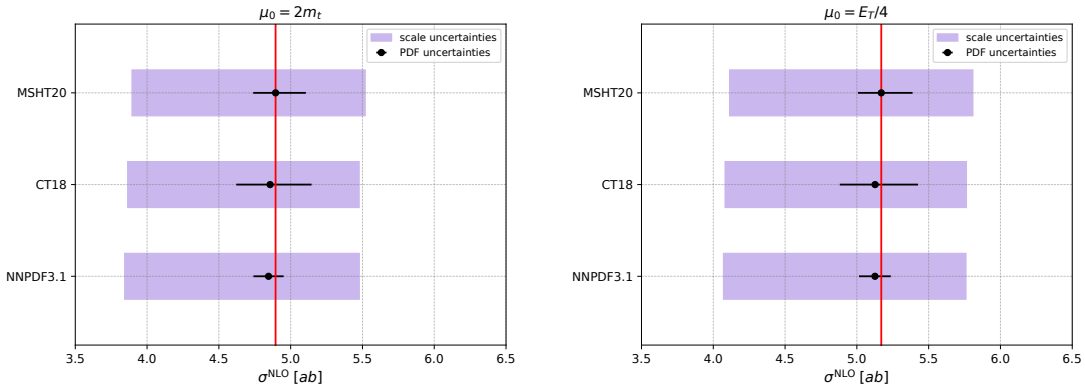

Figure 4.2: *Integrated fiducial cross sections at NLO in QCD for the* $pp \to \ell^+\nu_\ell\,\ell^+\nu_\ell\,\ell^-\bar{\nu}_\ell\,\ell^-\bar{\nu}_\ell\,b\bar{b}\,b\bar{b} + X$ *process at the LHC with* $\sqrt{s} = 13.6$ TeV*. Results are displayed for the fixed* $\mu_0 = 2m_t$ *(left) and dynamical* $\mu_0 = E_T/4$ *(right) scale choices and for the MSHT20, CT18 and NNPDF3.1 PDF sets. The purple bands illustrate the scale uncertainties, while the PDF uncertainties are demonstrated with the black error bands. The red vertical lines represent the central predictions of our default setup.*

The inclusion of higher-order QCD corrections substantially reduces the theoretical uncertainty to the level of $20\% - 21\%$. Furthermore, the central LO predictions among the different PDF sets can differ by as much as 20%, which is large but still compatible within the sizable LO scale uncertainties. In contrast, the central NLO predictions are highly consistent across the various PDF sets, varying by at most 1%. This highlights the importance of incorporating higher-order corrections for achieving more stable and reliable predictions for this process. The NLO results for the fixed and dynamical scale choices differ by roughly 5%, which is compatible within the theoretical errors. Turning our focus to the $\mathcal{K} = \sigma^{\mathrm{NLO}}/\sigma^{\mathrm{LO}}$ factors, we observe a wide range of values depending on the chosen PDF set. On the one hand, the CT18 PDF set exhibits the smallest $\mathcal{K}$ factors, yielding 1.04 for the fixed and 1.03 for the dynamical scale. On the other hand, for the NNPDF3.1 PDF set, the QCD corrections are significantly larger, reaching values up to 25%-30%. These variations originate from the substantial differences in the LO cross sections among the different PDF sets. This can be attributed to the significant discrepancies in the gluon and quark PDFs between LO and NLO. Indeed, the quark to gluon splittings start to appear only at NLO, causing large differences between the LO and NLO gluon PDFs, especially in the small-x region [474]. Additionally, global PDF fits rely heavily on deep-inelastic scattering (DIS) and Drell–Yan data, where the gluon PDF does not enter at LO. For the quark PDFs, the quality of the fit at LO is known to be rather poor, and notable shifts in their distributions appear when moving to NLO.

A visual representation of the theoretical uncertainties is further provided in Fig. 4.2, where we show the NLO cross sections obtained with three different PDF sets, together with their corresponding scale and PDF uncertainty bands. Results are presented for both the fixed and dynamical scale choices. We observe that scale uncertainties dominate the total theoretical error, while the PDF uncertainties are significantly smaller, reaching at most 6%. Among the three PDF sets, CT18

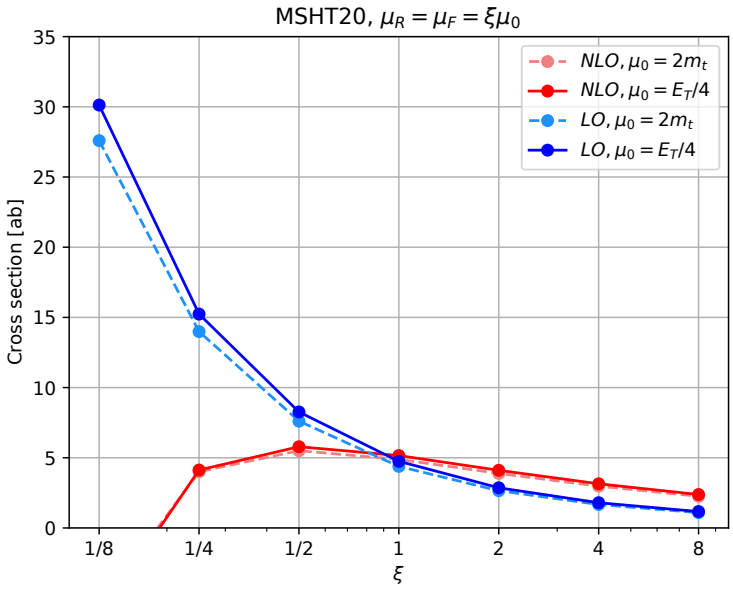

Figure 4.3: *Integrated fiducial cross section for the* $pp \to t\bar{t}t\bar{t} + X$ *process in the* 4ℓ *channel at the LHC with* $\sqrt{s} = 13.6$ TeV*, as a function of the scale-variation factor* ξ*, defined according to* $\mu_R = \mu_F = \xi\mu_0$*. Results are displayed at LO and NLO in QCD for the* $\mu_0 = 2m_t$ *(dashed) and* $\mu_0 = E_T/4$ *(solid) scale choices, using the default setup which employs the MSHT20 PDF set.*

exhibits the largest PDF uncertainty (6%), whereas the NNPDF3.1 uncertainties remain at the level of only 2%. Thus, after combining the PDF and scale uncertainties according to:

$$\delta\sigma = \sqrt{\delta^2_{scale} + \delta^2_{pdf}}\,, \tag{4.16}$$

we find that the total theoretical uncertainty $\delta\sigma$ increases only marginally relative to δ_{scale}, by at most 1%.

Another direction worth exploring is to examine how the LO and NLO cross sections behave when the renormalization and factorization scales are varied outside the conventional seven-point scale variation. For this purpose, in Fig. 4.3 we present the cross section as a function of the scale-variation factor ξ, defined according to $\mu_R = \mu_F = \xi\mu_0$. We plot our LO and NLO results in the $\xi \in (1/8, 8)$ range for $\mu_0 = 2m_t$ and $\mu_0 = E_T/4$ using the default MSHT20 PDF set. First, we note that Fig. 4.3 justifies the usage of $\mu_0 = 2m_t$ and $\mu_0 = E_T/4$ as our default central scales. This is because, near $\xi = 1$, the $\mathcal{K}$ factors become modest, indicating a stable perturbative expansion. Second, we observe that the LO cross sections vary significantly with ξ, becoming excessively large in the low-ξ regime. In contrast, the NLO scale dependence is much milder, yielding

$$\frac{\sigma^{\rm NLO}(\mu_R = \mu_F = \xi\mu_0)}{\sigma^{\rm NLO}(\mu_R = \mu_F = \mu_0)} \in [0.46, 1.24]\,. \tag{4.17}$$

We note here that only positive cross sections are displayed, since for very small ξ values close to 1/8 the NLO cross section becomes negative, leading to unphysical results. Hence, the NLO cross section for $\xi = 1/8$ has not been taken into account in determining the values for the above ratio. Finally, we remark that both at

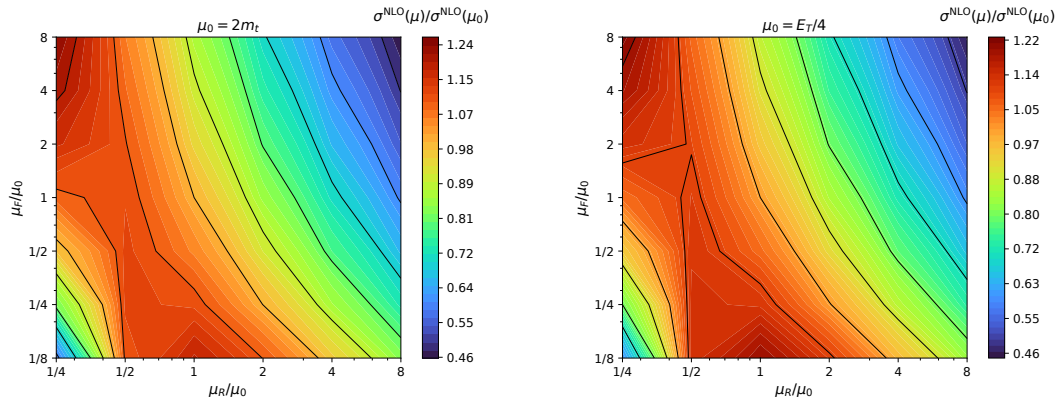

Figure 4.4: *Two-dimensional contour plots of the NLO QCD cross sections obtained after varying μ_R, μ_F independently, normalized to the central NLO prediction. Results are shown for the $\mu_0 = 2m_t$ (left) and $\mu_0 = E_T/4$ (right) scales for the $pp \to t\bar{t}t\bar{t} + X$ process in the 4ℓ channel at the LHC with $\sqrt{s} = 13.6$ TeV, using the default MSHT20 PDF set.*

LO and NLO, the fixed and dynamical scale choices display a qualitatively similar behavior. To further investigate the sensitivity of the predictions to the renormalization and factorization scales, Fig. 4.4 presents two-dimensional contour plots in which μ_R, μ_F are varied independently. The plots show the ratio of the resulting NLO cross sections to the central prediction for our default setup. Values of the renormalization scale μ_R smaller than 1/4 are not displayed because of the negative unphysical cross sections, which would obscure the readability of the plots. We find that the dominant contribution to the overall scale uncertainty arises from variations of the renormalization scale. In contrast, variations of the factorization scale have a comparatively mild impact and become relevant only when extreme values of μ_R are employed. Indeed, for $\mu_R = \mu_0$, changing the factorization scale modifies the NLO cross section at the level of only $13\% - 20\%$. Conversely, varying μ_R while keeping $\mu_F = \mu_0$ induces singificantly larger effects of about $11\% - 54\%$. Overall, when μ_R and μ_F are varied independently, the resulting NLO scale uncertainties lie in the range of approximately -54% to $+22\%$ or $+24\%$, depending on the scale choice. We finally notice that the largest scale variations arise when μ_R and μ_F acquire nearly identical values, coinciding with the behavior already encountered in Fig. 4.3 (see also Eq. (4.17)). Therefore, for this process, allowing μ_R and μ_F to vary independently does not introduce larger theoretical uncertainties than the case where $\mu_R = \mu_F = \xi\mu_0$.

We now proceed to discuss the differences among the various NWA treatments employed by presenting their NLO cross sections in Table 4.2. Our aim is to quantify the impact of higher-order QCD corrections in the decays of the top quarks, as well as the effects of not expanding the top-quark width in the calculation. The inclusion of higher-order effects in the latter case, where the NLO top-quark width is used everywhere, is of the order of $11\% - 12\%$ relative to the expanded case. Also, the magnitude of the theoretical error when the NLO_{full} scenario is employed reduces from 20% to roughly $15\% - 16\%$. The impact of QCD corrections to the decays of the $pp \to t\bar{t}t\bar{t}$ system is also at a similar level, accounting for $8\% - 9\%$, depending on the scale choice. In this case, however, the size of the scale uncertainties increases,

Decay treatment	$\sigma_i^{\rm NLO}$ [ab]	$+\delta_{scale}$ [ab]	$-\delta_{scale}$ [ab]	$\sigma_i^{\rm NLO}/\sigma_{\rm exp}^{\rm NLO} - 1$
$\mu_R = \mu_F = \mu_0 = 2m_t$				
full	5.462(3)	+0.156 (3%)	−0.853 (16%)	+11.6%
$\rm LO_{dec}$	5.295(3)	+1.123 (21%)	−1.224 (23%)	+8.2%
exp	4.895(2)	+0.624 (13%)	−1.002 (20%)	−
$\mu_R = \mu_F = \mu_0 = E_T/4$				
full	5.735(3)	+0.139 (2%)	−0.882 (15%)	+10.9%
$\rm LO_{dec}$	5.646(3)	+1.225 (22%)	−1.317 (23%)	+9.2%
exp	5.170(3)	+0.638 (12%)	−1.056 (20%)	−

Table 4.2: *Integrated fiducial cross sections at NLO in QCD for the* $pp \to t\bar{t}t\bar{t} + X$ *process in the* 4ℓ *channel at the LHC with* $\sqrt{s} = 13.6$ TeV*, using the following NWA treatments:* $\rm NLO_{full}, NLO_{LO_{dec}}$ *and* $\rm NLO_{exp}$*. Results are shown for the* $\mu_R = \mu_F = \mu_0 = 2m_t$ *and* $\mu_R = \mu_F = \mu_0 = E_T/4$ *scales and the MSHT20 PDF set. Also shown are theoretical uncertainties obtained via the standard seven-point scale variation, and the percentage differences with respect to our default* $\rm NLO_{exp}$ *setup.*

reaching values up to 23%. This highlights the significance of incorporating higher-order QCD effects in both production and decays for the $pp \to t\bar{t}t\bar{t}$ process in the 4ℓ channel. Overall, all the various NWA approaches are in quite good agreement with each other since their differences are well within the size of the theoretical errors.

4.2.3 Differential results

In this section, we show differential results for the $pp \to \ell^+\nu_\ell\,\ell^+\nu_\ell\,\ell^-\bar{\nu}_\ell\,\ell^-\bar{\nu}_\ell\,b\bar{b}\,b\bar{b} + X$ process at the LHC with $\sqrt{s} = 13.6$ TeV. We start by discussing the impact of higher-order QCD corrections at the differential level, and then we also report on the differences among the various NWA treatments employed. In Sec. 4.2.2, for our default setup, we found that QCD corrections at the integrated fiducial cross-section level are of the order of $9\% - 12\%$. Assessing the impact of higher-order QCD effects on differential observables is equally important, as it allows us to find fiducial phase-space regions potentially sensitive to these effects. For this purpose, we present results using the dynamical scale choice $\mu_0 = E_T/4$, which generally performs better compared to the fixed one, especially at the high-p_T tails of certain differential distributions. More specifically, with fixed scales, one may encounter situations where the NLO scale uncertainties exceed the LO ones or even cases where the central NLO predictions become negative. These effects have already been observed and discussed in various studies, see e.g. Refs. [81,129,130,155,194,228,240, 297,332]. We stress, however, that for this process the large production threshold of $4m_t$ shifts these effects to much higher transverse-momentum values, which are not

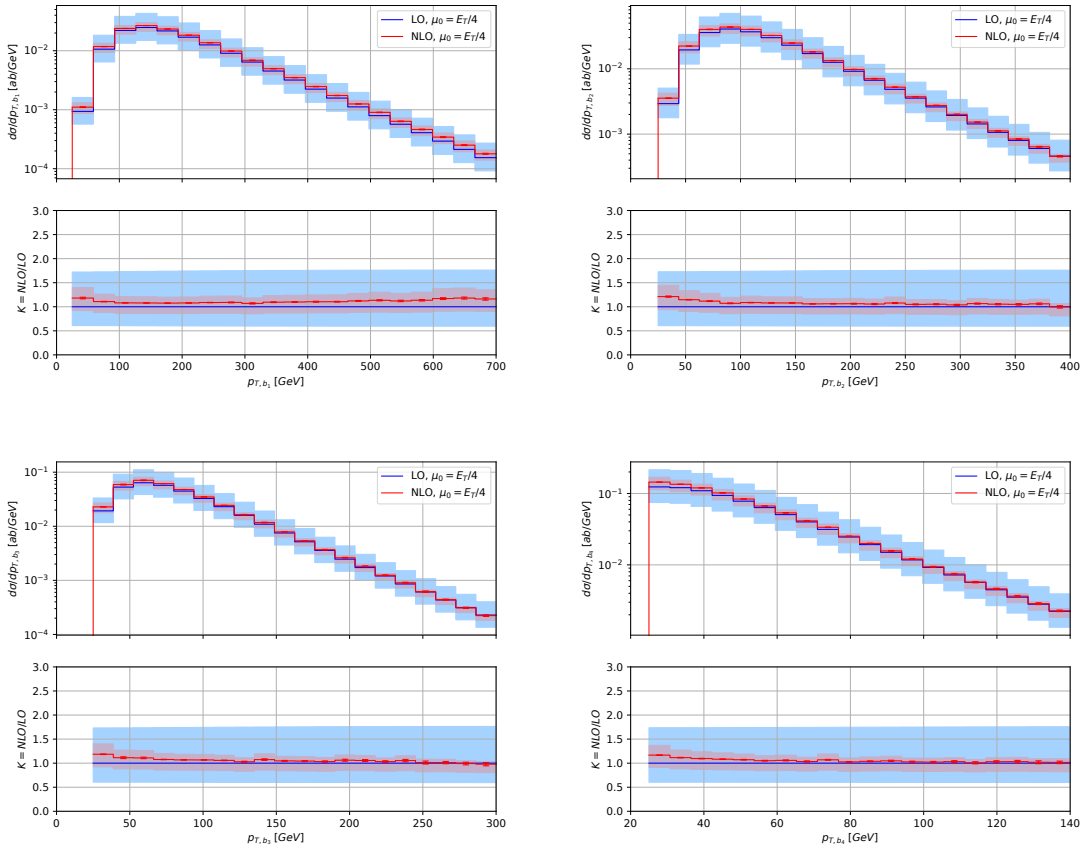

Figure 4.5: *Differential cross-section distributions for the* $pp \to \ell^+\nu_\ell\,\ell^+\nu_\ell\,\ell^-\bar{\nu}_\ell\,\ell^-\bar{\nu}_\ell\,b\bar{b}\,b\bar{b} + X$ *process at the LHC with* $\sqrt{s} = 13.6$ TeV*, for the following observables:* $p_{T,b_1}, p_{T,b_2}, p_{T,b_3}$ *and* p_{T,b_4}*. The b jets are ordered according to their transverse momentum i.e.* p_{T,b_1} *and* p_{T,b_4} *denote the b jets with the highest and lowest* p_T*, respectively. The upper panels display the absolute predictions at LO (blue) and NLO (red) in QCD, while in the bottom panels, the differential* $\mathcal{K}$ *factor is also depicted. The results have been obtained for our default setup, utilizing the (N)LO MSHT20 PDF set for the (N)LO calculations and the dynamical scale choice* $\mu_0 = \mu_R = \mu_F = E_T/4$*. Also shown are uncertainty bands obtained after varying the renormalization and factorization scales using the standard seven-point scale variation.*

phenomenologically relevant. We begin by presenting the transverse momenta of the b jets according to their hardness in Fig. 4.5. The absolute predictions at LO and NLO in QCD are shown in the upper panels, while the bottom panels display the differential $\mathcal{K}$ factor, defined as the (N)LO over the LO cross section for each bin. For the scale uncertainties in the bottom panels, the minimum and maximum NLO and LO bin-values are rescaled by the corresponding central LO predictions. From Fig. 4.5, we find that for all the aforementioned observables, the QCD corrections are generally modest, ranging between -2% to 21%. In particular, for the transverse momentum of the hardest b jet, QCD corrections remain relatively flat for the whole plotted range, being slightly smaller near the bulk of the events, where they amount to $7\% - 10\%$. In contrast, for the remaining observables, the higher-order QCD

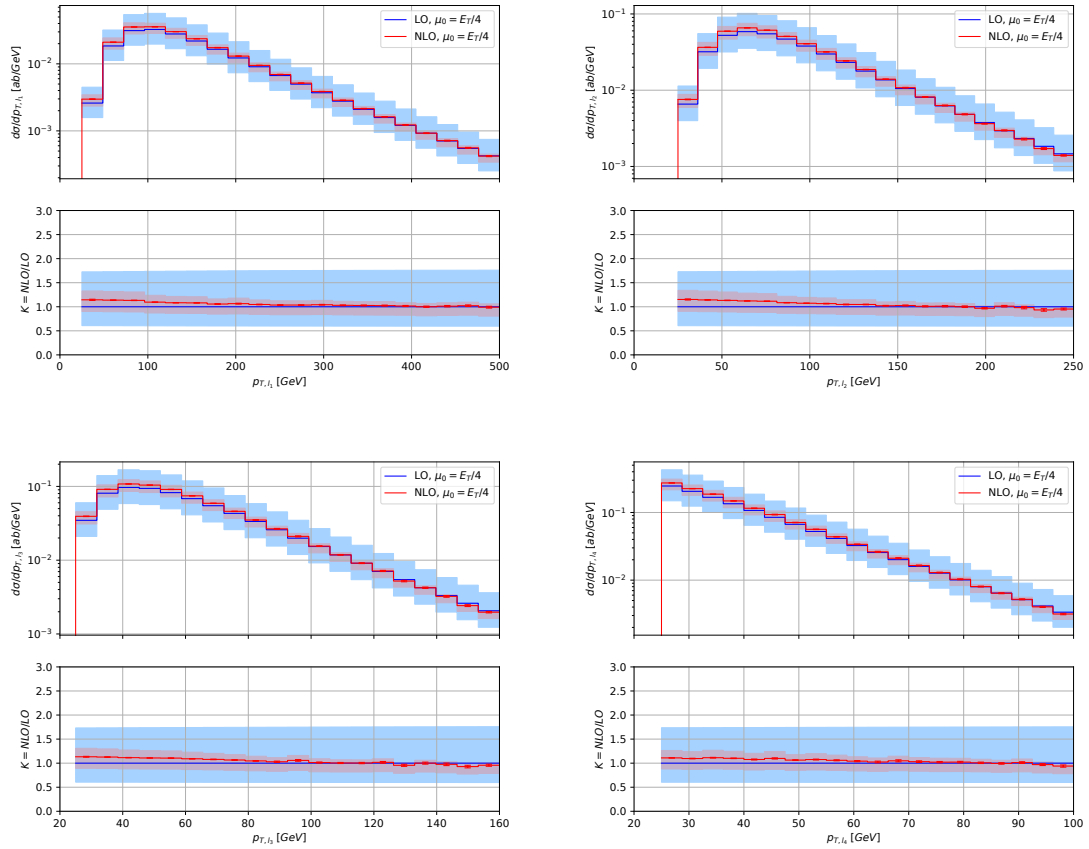

Figure 4.6: *Same as Fig. 4.5 but for the charged leptons ordered in hardness, i.e.* p_{T,l_1} *(*p_{T,l_4}*) corresponds to the charged lepton with the largest (smallest) transverse momentum.*

effects tend to reduce in the high-p_T tails, yielding $\mathcal{K}$ factors near unity. For all observables, the scale uncertainties at LO are consistently large, reaching up to 76%, whereas once QCD corrections are applied, they are significantly reduced, being at the level of 20%. A similar pattern is observed for the transverse momenta of the charged leptons according to their p_T, as shown in Fig. 4.6. In particular, the $\mathcal{K}$ factor follows a downward trend as the transverse momentum increases, with QCD corrections ranging from -7% to 15%. Regarding the size of the theoretical errors, the LO scale uncertainties are substantial in size, accounting for roughly 75%, while the NLO ones lie at the level of 20% for all displayed observables.

We now shift our focus to some dimensionless observables by examining the angular separations of various final-state objects in Fig. 4.7. More specifically, we show the angular separation between the two hardest b jets $\Delta R_{b_1 b_2}$, between the hardest and the third hardest b jets $\Delta R_{b_1 b_3}$, between the two softest b jets $\Delta R_{b_3 b_4}$ and between the hardest b jet and the leading charged lepton $\Delta R_{b_1 l_1}$. For the angular separation between b_1 and b_2, we observe a single, narrow peak around the value of π, indicating that the two hardest b jets are predominantly produced in a back-to-back configuration. In contrast, for the $\Delta R_{b_1 b_3}$ and $\Delta R_{b_3 b_4}$ distributions, peaks appear at similar values but are noticeably broader, and a significant number of events is observed also for ΔR values smaller than π. For all the aforementioned observables,

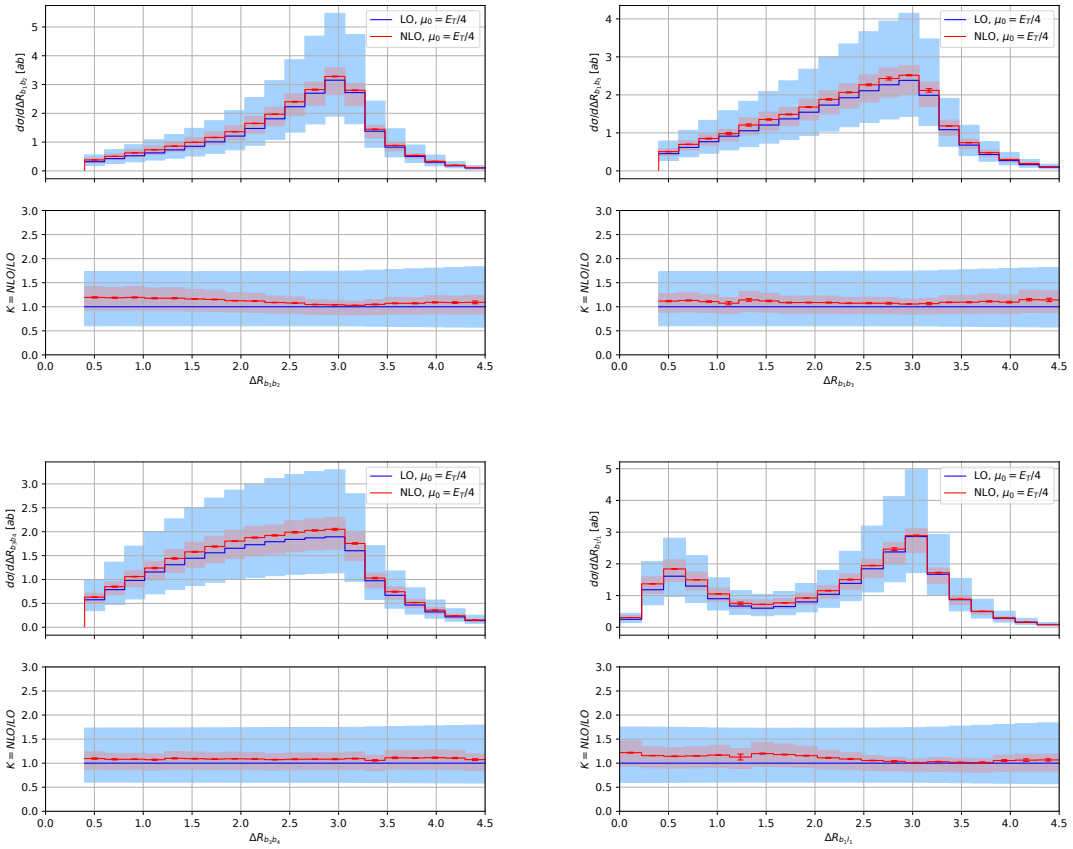

Figure 4.7: *Differential cross-section distributions for the* $pp \to \ell^+\nu_\ell\,\ell^+\nu_\ell\,\ell^-\bar{\nu}_\ell\,\ell^-\bar{\nu}_\ell\,b\bar{b}\,b\bar{b} + X$ *process at the LHC with* $\sqrt{s} = 13.6$ TeV, *for the following dimensionless observables:* $\Delta R_{b_1 b_2}$, $\Delta R_{b_1 b_3}$, $\Delta R_{b_3 b_4}$ *and* $\Delta R_{b_1 l_1}$. *The upper panels display the absolute predictions at LO (blue) and NLO (red) in QCD, while in the bottom panels, the differential* $\mathcal{K}$ *factor is also depicted. The results have been obtained for our default setup, utilizing the (N)LO MSHT20 PDF set for the (N)LO calculations and the dynamical scale choice* $\mu_0 = \mu_R = \mu_F = E_T/4$. *Also shown are uncertainty bands obtained after varying the renormalization and factorization scales using the standard seven-point scale variation.*

the QCD corrections remain moderate and never exceed 22%, and the NLO scale uncertainties are consistently at the level of 20%. For the angular separation between the hardest b jet and the hardest charged lepton, apart from the back-to-back emissions, there is a second notable peak around the value of $\Delta R_{b_1 l_1} \approx 0.5$. This structure reflects events in which a top or antitop quark is highly energetic, causing its decay products to be emitted with small angular separations.

All observables presented so far share a common characteristic: the QCD corrections are always within the large LO uncertainty bands. This is, nonetheless, not always guaranteed. For example, there might be cases where the NLO scale uncertainties become of similar size to the LO ones in certain phase-space regions, or the central NLO predictions are outside of the LO uncertainty bands. This is what is illustrated in Fig. 4.8, where the transverse momenta of the system of the two hardest b jets $p_{T,b_1 b_2}$, as well as the transverse momenta of the system comprising all

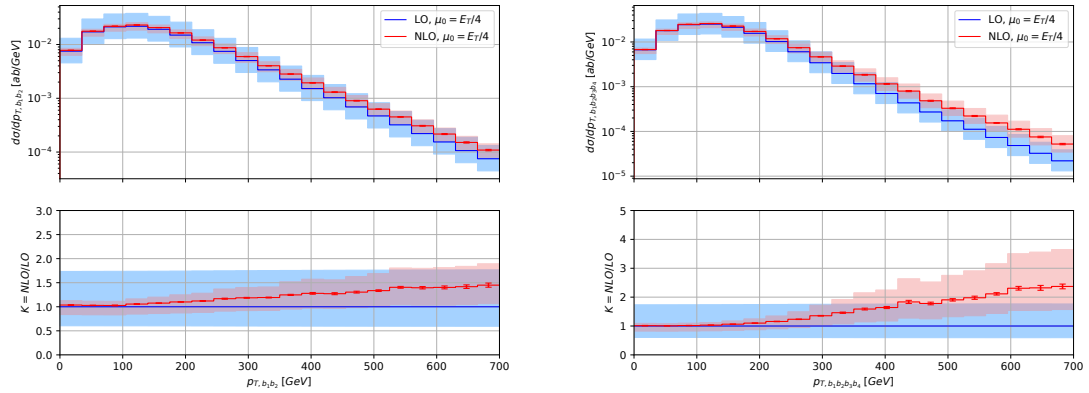

Figure 4.8: *Differential cross-section distributions for the* $pp \to \ell^+\nu_\ell\,\ell^+\nu_\ell\,\ell^-\bar{\nu}_\ell\,\ell^-\bar{\nu}_\ell\,b\bar{b}\,b\bar{b} + X$ *process at the LHC with* $\sqrt{s} = 13.6$ TeV, *shown for the transverse momentum of the system of the two hardest b jets,* p_{T,b_1b_2}, *and of the four hardest b jets,* $p_{T,b_1b_2b_3b_4}$. *The upper panels display the absolute predictions at LO (blue) and NLO (red) in QCD, while in the bottom panels, the differential* $\mathcal{K}$ *factor is also depicted. The results have been obtained for our default setup, utilizing the (N)LO MSHT20 PDF set for the (N)LO calculations and the dynamical scale choice* $\mu_0 = \mu_R = \mu_F = E_T/4$. *Also shown are uncertainty bands obtained after varying the renormalization and factorization scales using the standard seven-point scale variation.*

four b jets $p_{T,b_1b_2b_3b_4}$ are displayed. For both plots, we notice that higher-order QCD effects become particularly important in the high-p_T tails, with QCD corrections up to 45% for p_{T,b_1b_2} and 137% for $p_{T,b_1b_2b_3b_4}$. Accordingly, the size of the NLO scale uncertainties in these regions reaches 30% and 55%. Especially for the $p_{T,b_1b_2b_3b_4}$ observable, the central NLO predictions are outside the substantial LO scale uncertainties in the tail of the distribution. Although a similar trend is also visible in the p_{T,b_1b_2} observable, in this case, the central NLO predictions are covered by the LO scale uncertainties. In general, this behavior originates from the presence of a highly energetic light jet, emitted in the production stage at NLO, that recoils against the $pp \to t\bar{t}t\bar{t}$ system. As a consequence, top quarks and their decay products acquire large transverse momenta. At LO, such configurations are absent, and b quarks can only gain large transverse momenta via boosts of their parent particle. This is, however, kinematically disfavored at LO, as pure kinematics imply that in the rest frame of the top quark:

$$p_{T,b} \leq \frac{m_t^2 - m_W^2}{2m_t} \approx 67.5 \text{ GeV} \,. \tag{4.18}$$

This explains why sizable QCD corrections start to appear around $p_{T,b_1b_2b_3b_4} \approx 270$ GeV at NLO, as displayed in the figure. To verify that this behavior is indeed caused by the presence of high-p_T light jets at NLO, in Fig. 4.9 we present the same observables after applying a veto on the transverse momentum of the extra radiation. In particular, we consider several values: $p_{T,veto} = 25, 50, 100, 200, 300, 500$ GeV and plot the normalized distributions in the upper panels and the normalized ratios to the LO predictions in the bottom panels. Using normalized quantities avoids the large differences in the NLO cross sections from the various $p_{T,veto}$ values, which

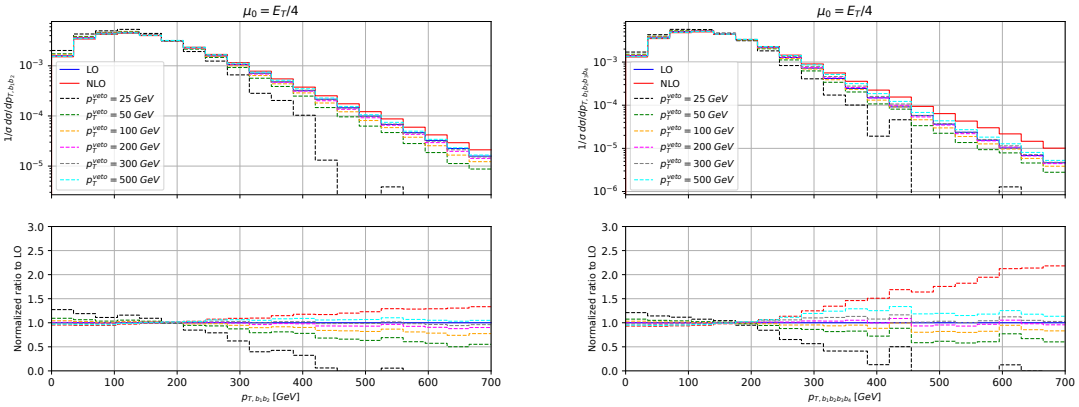

Figure 4.9: *Normalized differential cross-section distributions for the* $pp \to \ell^+\nu_\ell\,\ell^+\nu_\ell\,\ell^-\bar{\nu}_\ell\,\ell^-\bar{\nu}_\ell\,b\bar{b}\,b\bar{b} + X$ *process at the LHC with* $\sqrt{s} = 13.6$ TeV*, for the* p_{T,b_1b_2} *(left) and* $p_{T,b_1b_2b_3b_4}$ *(right) observables. The results are shown at (N)LO in QCD using the (N)LO MSHT20 PDF set and the dynamical scale choice* $\mu_R = \mu_F = \mu_0 = E_T/4$*, including cases with a jet veto* $p_{T,veto} \in [25, 50, 100, 200, 300, 500]$ GeV *imposed on the extra radiation at NLO. The bottom panels demonstrate the normalized ratios to the LO contributions.*

would otherwise make a direct comparison cumbersome. By applying a $p_{T,veto}$, any QCD emission above this value is not permitted, allowing us to test whether the effects described above can be suppressed. As shown in Fig. 4.9, $p_{T,veto}$ values between 50 and 500 GeV significantly suppress the large NLO enhancements discussed above, as for both observables, the NLO-to-LO ratios stay close to unity, reaching 0.5 only for $p_{T,veto} = 50$ GeV. These effects are particularly pronounced on the $p_{T,b_1b_2b_3b_4}$ observable, where the NLO results without the veto yield enhancements above a factor of 2. We also note that for the low veto choice of $p_{T,veto} = 25$ GeV, the normalized ratios can turn negative in the tails of the distributions. This reflects a well-known limitation of fixed-order perturbation theory. In practice, such issues are alleviated once shower effects or analytic resummation are included. Finally, we highlight that whenever a $p_{T,veto}$ is applied, the size of the NLO scale uncertainties drastically increases. For instance, choosing $p_{T,veto} = 50$ GeV, results in an enhancement on the theoretical uncertainties by factors of $3-7$ depending on the observable. Therefore, in these regions, reducing the theoretical uncertainties and improving the perturbative convergence would require adopting methods such as those discussed in Refs. [478–484].

Next, we assess the impact of using alternative PDF sets also at the differential cross-section level. Although the PDF uncertainties were found to be relatively small for the integrated fiducial cross section, it is essential to investigate their effect across various regions of the phase space. In Fig. 4.10, we present the NLO differential results for two dimensionful and two dimensionless observables. In particular, we focus on the transverse momenta of the hardest b jet b_1, and the hardest charged lepton l_1, as well as on the angular separation between the two hardest and two softest b jets, denoted as $\Delta R_{b_1b_2}$ and $\Delta R_{b_3b_4}$. In the upper panels, we show predictions obtained with the MSHT20, CT18, and NNPDF3.1 PDF sets. The middle panels display ratios to our default setup, including the corresponding scale-variation bands for the

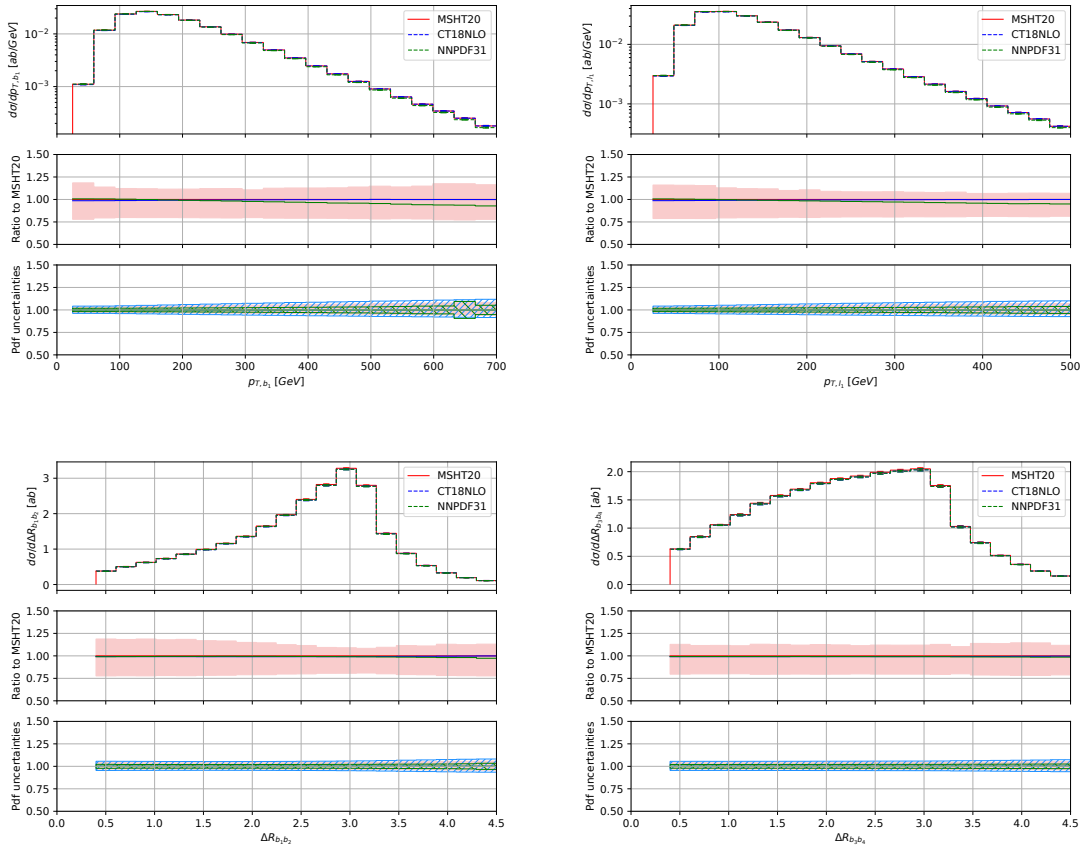

Figure 4.10: *Differential NLO in QCD cross-section distributions for the* $pp \to \ell^+\nu_\ell\,\ell^+\nu_\ell\,\ell^-\bar{\nu}_\ell\,\ell^-\bar{\nu}_\ell\,b\bar{b}\,b\bar{b} + X$ *process at the LHC with* $\sqrt{s} = 13.6$ TeV*, using the MSHT20 (red), CT18 (blue) and NNPDF3.1 (green) PDF sets, for the* $p_{T,b_1}, p_{T,l_1}, \Delta R_{b_1b_2}$ *and* $\Delta R_{b_3b_4}$ *observables. The upper panels display the absolute predictions, the middle panels the ratio to the MSHT20 PDF set, including the scale uncertainties for our default setup, while in the bottom panels, the internal PDF uncertainties are also shown. All results have been obtained using* $\mu_R = \mu_F = \mu_0 = E_T/4$.

MSHT20 PDF. Finally, the bottom panels illustrate the size of the internal PDF uncertainties for each PDF set. For the dimensionful observables, the differences among the various PDF sets are relatively small, at most 7%, and always covered by the large scale-uncertainty bands. The PDF uncertainties themselves are smaller than the scale uncertainties across the entire plotted ranges but grow gradually in the high-p_T tails of the p_{T,b_1} and p_{T,l_1} distributions, reaching up to about 10%. For the dimensionless observables, the differences between the PDFs are negligible, and the PDF uncertainties remain consistently below 10%.

For all figures depicted so far, the expanded NWA approach has been employed as a default option for presenting the NLO results. In what follows, we compare the alternative NLO_{full} and $\text{NLO}_{\text{LO}_{\text{dec}}}$ prescriptions with our default setup at the differential level. This is particularly important for assessing the impact of higher-order QCD corrections in the decays of the top quarks and of NLO spin correlations. In Figs. 4.11 and 4.12 we present the following observables: $M_{b_1b_2}, p_{T,l_1}, p_{T,b_1}, p_{T,b_1b_2}, \Delta\phi_{l_1l_2}$ and $\Delta\phi_{b_1b_2}$. For all the dimensionful observables,

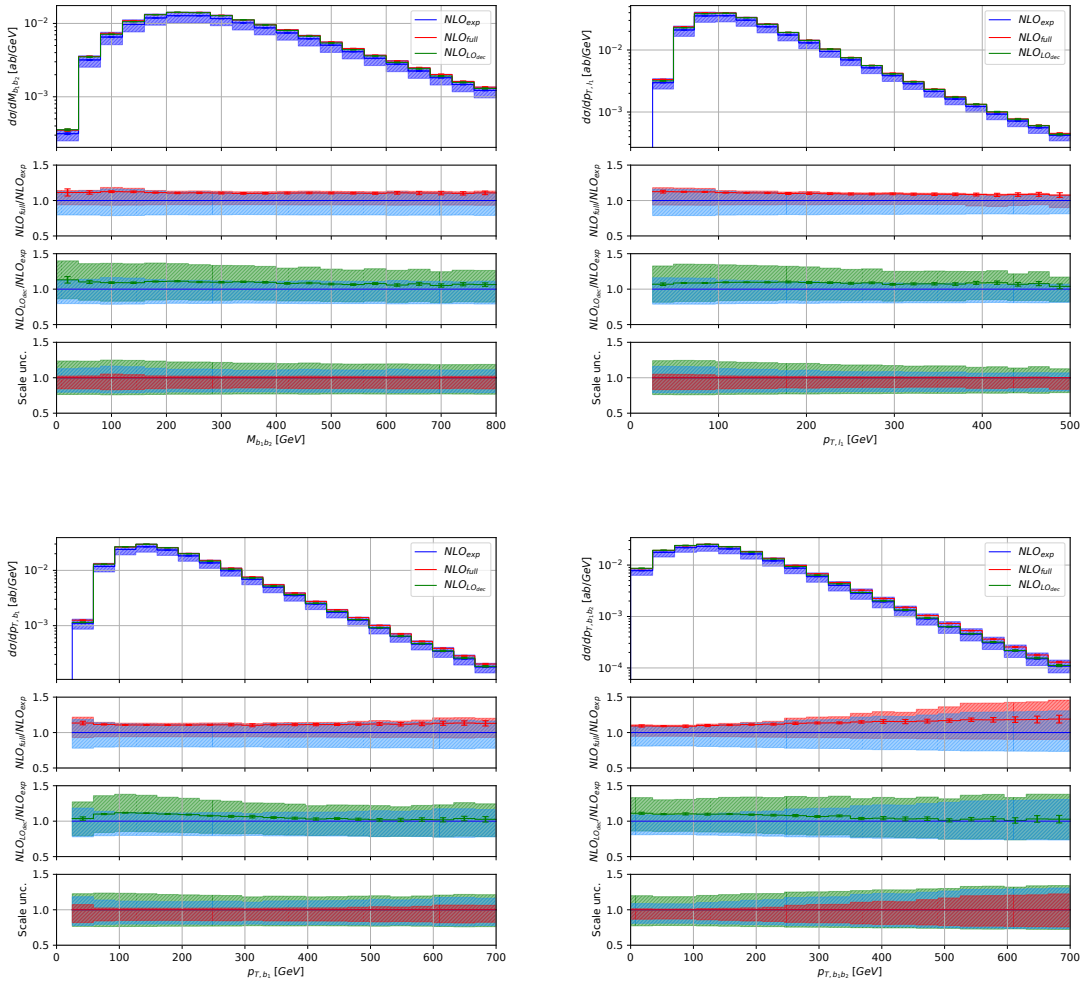

Figure 4.11: *Differential cross-section distributions for the* $pp \to \ell^+\nu_\ell\,\ell^+\nu_\ell\,\ell^-\bar{\nu}_\ell\,\ell^-\bar{\nu}_\ell\,b\bar{b}\,b\bar{b} + X$ *process at the LHC with* $\sqrt{s} = 13.6$ TeV*, for the following observables:* $M_{b_1b_2}, p_{T,l_1}, p_{T,b_1}$ *and* p_{T,b_1b_2}*. Results are displayed for the following* NWA *setups:* $\mathrm{NLO}_{\mathrm{exp}}$ *(blue),* $\mathrm{NLO}_{\mathrm{full}}$ *(red) and* $\mathrm{NLO}_{\mathrm{LO_{dec}}}$ *(green) for the dynamical scale choice* $\mu_0 = \mu_R = \mu_F = E_T/4$ *and the default MSHT20 PDF set. The upper panels present the absolute predictions, while in the middle panels, the ratio to our default setup is displayed, including the relative uncertainties obtained using the seven-point scale variation bin-by-bin. Also shown in the bottom panels is the size of the scale uncertainties for each setup, normalized to their corresponding NLO results.*

the impact of higher-order effects in the $\mathrm{NLO}_{\mathrm{full}}$ setup remains approximately flat at around 10%, reaching up to 20% only in the high-p_T tail of p_{T,b_1b_2}. The absence of QCD corrections in the decay stage of the top quarks also leads to differences of roughly 10%, becoming less important in the tails of the p_{T,b_1} and p_{T,b_1b_2} distributions. Similar to what has been observed at the integrated level, the scale uncertainties are significantly reduced once higher-order QCD corrections are applied consistently in both production and decays, across all regions of the phase space. Despite the differences between the various NWA treatments, all predictions remain compatible at the differential level, as all deviations are contained within

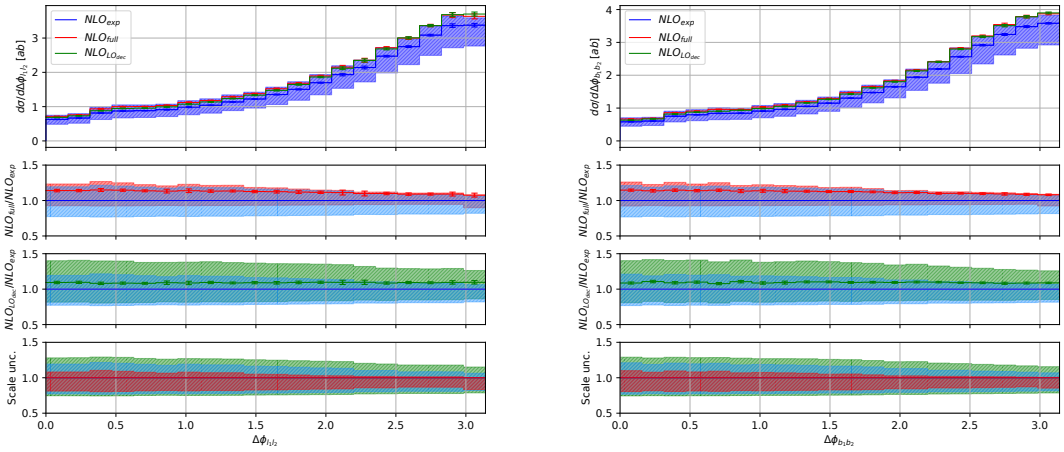

Figure 4.12: *Same as Fig. 4.11 but for the* $\Delta\phi_{l_1 l_2}$ *and* $\Delta\phi_{b_1 b_2}$ *distributions.*

the theoretical uncertainty bands of roughly $15\% - 25\%$ for $M_{b_1 b_2}, p_{T,l_1}, p_{T,b_1}$ and $25\% - 35\%$ for $p_{T,b_1 b_2}$. Moving on, angular separations as the ones demonstrated in Fig. 4.12 are known to be especially relevant to the study of spin correlations, see e.g. Refs [485–488]. For instance, the $\Delta\phi_{l^+l^-}$ distribution was used by both the ATLAS [489] and the CMS [490] collaborations for the measurement of spin correlations in the $t\bar{t}$ production at the LHC. By comparing the $\text{NLO}_{\text{LO}_{\text{dec}}}$ with our default setup, we find that NLO spin-correlation effects for this process amount to roughly 10%, and are fully contained within the sizable theoretical-uncertainty bands. Finally, the NLO_{full} predictions differ by up to 15% with the NLO_{exp} setup. Among all scenarios, the NLO_{full} setup yields the smallest theoretical uncertainties, while for our default setup, they remain in the 15%–25% range.

4.2.4 Full off-shell vs NWA at Leading Order in QCD

So far, we have presented results using the NWA framework in which only diagrams with four-top quark resonances contribute. We argued that this approximation is valid for inclusive observables up to $\mathcal{O}(\Gamma_t/m_t)$ [433], but full off-shell effects can become relevant, especially for some observables at the differential level. A complete NLO calculation including full off-shell effects is, however, currently out of reach due to the high complexity of the computation and the enormous number of Feynman diagrams involved. Nevertheless, in this section, we present full off-shell results at LO in QCD for the following process:

$$pp \to e^-\bar{\nu}_e\, e^-\bar{\nu}_e\, \mu^+\nu_\mu\, \tau^+\nu_\tau\, b\bar{b}\, b\bar{b}, \text{ at } \mathcal{O}(\alpha_s^4\alpha^8)\,. \tag{4.19}$$

The above channel is a subset of the full $pp \to \ell^+\nu_\ell\, \ell^+\nu_\ell\, \ell^-\bar{\nu}_\ell\, \ell^-\bar{\nu}_\ell\, b\bar{b}\, b\bar{b}$ process. However, obtaining the full off-shell results for the whole process would require computing several separate channels, since one cannot simply evaluate a single fixed-flavor configuration and multiply by a lepton–flavor factor. This is because, in contrast to the NWA case, the number and topology of diagrams differ among the various channels. For instance, whenever opposite-charge lepton pairs appear in the final state, additional contributions such as $\gamma/Z \to \ell^+\ell^-$ open up, which are

Subprocess	Full off-shell	NWA
gg	2592512	72
$q\bar{q}/\bar{q}q$	658416	14

Table 4.3: *Number of full off-shell and NWA Feynman diagrams for the* $pp \to e^-\bar{\nu}_e\, e^-\bar{\nu}_e\, \mu^+\nu_\mu\, \tau^+\nu_\tau\, b\bar{b}\, b\bar{b}$ *process at* $\mathcal{O}(\alpha_s^4\alpha^8)$*, for the* gg *and* $q\bar{q}/\bar{q}q$ *initiated subprocesses, where* $q = u, d, c, s$*. The bottom-induced initiated subprocesses* $b\bar{b}/\bar{b}b$ *as well as Higgs contributions in the intermediate state have not been considered to simplify the computation.*

absent in Eq. (4.19). A single representative channel, such as the one given in Eq. (4.19), is, nonetheless, sufficient for assessing the impact of full off-shell effects while avoiding unnecessary computational complexity. To get an idea of the level of complexity involved in the calculation, in Table 4.3, we present the number of Feynman diagrams at LO for the process under consideration, both in the full off-shell and in the NWA case. To increase the efficiency of the computation, we impose the following fiducial cuts in the final-state objects:

$$\begin{aligned} &p_{T,\ell} > 30 \text{ GeV}\,, && |y_\ell| < 2.5\,, && \Delta R_{\ell\ell} > 0.4\,, \\ &p_{T,b} > 40 \text{ GeV}\,, && |y_b| < 2.5\,, && \Delta R_{bb} > 0.4\,, \\ &p_{T,miss} > 50 \text{ GeV}\,, && \Delta R_{\ell b} > 0.4\,, \end{aligned} \tag{4.20}$$

where ℓ stands for e^-, μ^+, τ^+. We also employed the following input parameters:

$$\begin{aligned} &G_\mu = 1.1663787 \cdot 10^{-5} \text{ GeV}^{-2}\,, && m_t = 172.5 \text{ GeV}\,, \\ &m_W = 80.3850 \text{ GeV}\,, && \Gamma_W = 2.0840 \text{ GeV}\,, \\ &m_Z = 91.1535 \text{ GeV}\,, && \Gamma_Z = 2.4943 \text{ GeV}\,. \end{aligned} \tag{4.21}$$

The masses and the widths of the $W^\pm$ and Z bosons correspond to the pole values computed via the following relations [491]:

$$M_V = \frac{M_V^{OS}}{\sqrt{1 + (\Gamma_V^{OS}/M_V^{OS})^2}}\,, \quad \Gamma_V = \frac{\Gamma_V^{OS}}{\sqrt{1 + (\Gamma_V^{OS}/M_V^{OS})^2}}\,, \tag{4.22}$$

where V stands for $W^\pm, Z$ and the on-shell (OS) values were taken from Ref. [389]. For the top quark, we used:

$$\Gamma_{t,\text{off-shell}} = 1.4576608 \text{ GeV}, \quad \Gamma_{t,\text{NWA}} = 1.4806842 \text{ GeV}, \tag{4.23}$$

for the full off-shell and the NWA computations, respectively. All intermediate massive particles for the full off-shell calculation are treated in the complex-mass scheme [80, 81, 429, 430, 492], in which the decay widths appearing in the propagator of the unstable particles are absorbed into a redefinition of complex masses according to $\mu^2 = m^2 - im\Gamma$. Finally, we employed $\mu_0 = 2m_t$ for the choice of the renormalization and factorization scales, utilized the MSHT20 LO PDF set and performed the calculation using a center-of-mass energy of $\sqrt{s} = 13.6$ TeV at the LHC. The integrated fiducial results are given below:

$$\sigma^{\text{LO}}_{\text{full off-shell}} = 0.1314(4) \text{ ab}\,, \quad \sigma^{\text{LO}}_{\text{NWA}} = 0.1313(2) \text{ ab}\,. \tag{4.24}$$

We find a perfect agreement between the full off-shell and the NWA cross sections as the two approaches differ only by 0.1%. This difference is well within the NWA uncertainty $\mathcal{O}(\Gamma_t/m_t) \approx 0.9\%$. We also remark that the above results can be multiplied by a lepton factor of 3 to account for the remaining equivalent channels to Eq. (4.19), namely $pp \to \mu^-\bar{\nu}_\mu\,\mu^-\bar{\nu}_\mu\,e^+\nu_e\,\tau^+\nu_\tau\,b\bar{b}\,b\bar{b}$ and $pp \to \tau^-\bar{\nu}_\tau\,\tau^-\bar{\nu}_\tau\,\mu^+\nu_\mu\,e^+\nu_e\,b\bar{b}\,b\bar{b}$. At the differential cross-section level, certain types of observables are known to be sensitive to full off-shell effects. Among those, is the minimum invariant mass of the system of charged lepton and bottom quark $M(\ell b)_{min}$ that has been widely used by both the ATLAS [493] and CMS [494] collaborations in top-quark mass measurements from $t\bar{t}$ production, and the stransverse mass M_{T2}, first introduced in Refs. [495, 496]. For more details on their definition, the reader is also referred to Ref. [156]. Here, we focus only on the $M(\ell b)_{min}$ observable, and in particular, we present in Fig. 4.13 the $M(\tau^+ b)_{min}$ defined as:

$$M(\tau^+ b)_{min} = \min\{M(\tau^+ b_1), M(\tau^+ b_2), M(\tau^+ \bar{b}_1), M(\tau^+ \bar{b}_2)\}\,. \tag{4.25}$$

At LO in the NWA, the above observable exhibits a kinematical edge at exactly $\sqrt{m_t^2 - m_W^2} \approx 153$ GeV, as demonstrated in Fig. 4.13. This is because, for the following decay chain $t \to W^+ b \to \tau^+\nu_\tau b$, and assuming that top quarks and $W^\pm$ bosons are on shell and all leptons, neutrinos and b quarks are massless, the $M(\tau^+ b)$ is given by:

$$M(\tau^+ b) = \sqrt{m_t^2 - m_W^2 - 2|\vec{p}_{\nu_\tau}||\vec{p}_b|[1 - \cos(\theta_{\nu_\tau b})]} \leq \sqrt{m_t^2 - m_W^2}\,, \tag{4.26}$$

where $\vec{p}_{\nu_\tau}$ and $\vec{p}_b$ denote the three-vector momenta of the tau-neutrino and the bottom quark, respectively, and $\theta_{\nu_\tau b}$ is the angle between ν_τ and the b quark. Therefore, even if any other $\tau^+ b_i$ combination yields a larger invariant mass, taking the minimum according to Eq. (4.25), guarantees that the value does not exceed the $\sqrt{m_t^2 - m_W^2}$ threshold. For the full off-shell calculation, however, as displayed in Fig. 4.13, this kinematical edge is absent as there are diagrams with off-shell top quarks and $W^\pm$ bosons and even diagrams with no top-quark resonances at all. We also note that the very small number of events observed in the first bin is due to the $\Delta R_{\ell b}$ cut applied, forbidding the two particles to be collinear and thus the invariant mass $M(\tau^+ b)$ to be zero. We conclude this section by highlighting that for the types of observables presented in Sec. 4.2.3, full off-shell effects are expected to be significant in the high-p_T tails of some dimensionful observables, see e.g. Refs. [240, 332]. Nevertheless, these regions are far beyond the scope of the High-Luminosity phase of the LHC (HL-LHC) because of the very small cross section of the 4ℓ channel. Thus, even in the HL-LHC context, modeling this process within the NWA is well justified, as it provides a very reliable approximation.

4.3 3ℓ channel

In this section, the focus lies on the 3ℓ channel. Analogously to the 4ℓ channel, we first give a brief overview of the computation setup, and then present the integrated and differential fiducial results.

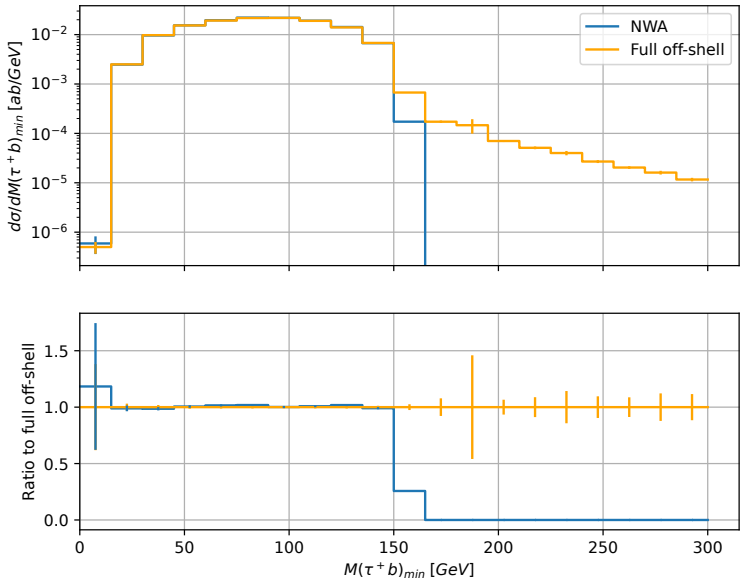

Figure 4.13: *Differential cross-section distribution for the $M(\tau^+b)$ observable defined in Eq. (4.25), using the NWA framework (blue) and the full off-shell (orange) predictions. The results are shown for the $pp \to e^-\bar{\nu}_e\, e^-\bar{\nu}_e\, \mu^+\nu_\mu\, \tau^+\nu_\tau\, b\bar{b}\, b\bar{b}$ process at LO in QCD and an LHC center-of-mass energy of $\sqrt{s} = 13.6$ TeV, utilizing $\mu_0 = \mu_R = \mu_F = 2m_t$ and the MSHT20 LO PDF set. The error bands correspond to Monte Carlo integration uncertainties.*

4.3.1 Computational setup

For the 3ℓ channel, the computational setup closely follows that of the 4ℓ channel described in Sec. 4.2.1. This implies that all input parameters, as well as the scale choices employed, are the same as in the 4ℓ channel. For the dynamical scale given in Eq. (4.12), the top and antitop quarks are again reconstructed from their decay products, but this time considering the potential extra light jet emitted at the decay stage of the $pp \to t\bar{t}t\bar{t}$ system. Below, we only highlight the additional ingredients and the differences specific to the 3ℓ case, arising from the presence of at least two light jets in the final state. In particular, our events are characterized by the presence of at least 2 light jets, at least 4 b-jets and exactly 3 charged leptons. On top of the cuts given in Eq. (4.14), we require the final state light jets to fulfil the following selection criteria:

$$p_{T,j} > 25 \text{ GeV}\,, \qquad |y_j| < 2.5\,, \qquad \Delta R_{bj} > 0.4\,. \qquad \Delta R_{jj} > 0.4\,. \quad (4.27)$$

Below, we explain why additional considerations are required for the 3ℓ channel, contrary to the 4ℓ channel. More specifically, at NLO in QCD, real-emission contributions introduce an extra light parton in the final state. This additional parton can be recombined with one of the light quarks originating from the $W^\pm$ decay, forming a jet that passes the generation cuts. If the remaining light jet and all other final-state objects also satisfy the selection criteria, the event would be accepted, as it would contain two resolved light jets in the final state. Such configurations typically lead to large $\mathcal{K}$ factors [86, 185, 206], defined as $\mathcal{K} = \sigma^{\text{NLO}}/\sigma^{\text{LO}}$, thereby

spoiling the perturbative stability of the calculation. A similar issue arises when a hard light jet is emitted, for instance, from the production stage, and passes all generation cuts, while the two jets from the $W^{\pm}$ decay are clustered together to form a single jet. As long as all remaining objects pass the selection cuts, these events are also accepted. Both types of configurations generate large $\mathcal{K}$ factors because they first appear at NLO in QCD. Indeed, at LO in the NWA, the two resolved light jets always originate from the $W^{\pm}$ decay, are well separated, and have an invariant mass equal to the W-boson mass, m_W. At NLO, however, this property is no longer guaranteed due to the scenarios described above, and special care must be taken to suppress such effects. To address this issue, we impose an additional cut on the invariant mass of the two light jets, M_{jj}, by introducing the parameter Q_{cut}, defined according to the following formula:

$$|M_{jj} - m_W| < Q_{cut}\,. \tag{4.28}$$

Since at NLO in QCD, there might be up to 3 light jets in the final state, we require at least one light-jet pair to fulfill the above condition. Our default setup comprises $Q_{cut} = 25$ GeV, but various values of the Q_{cut} parameter are also assessed in the next sections. This includes the scenario where no restriction is applied on M_{jj}, effectively considering the limit $Q_{cut} \to \infty$, which we also refer to as "no Q_{cut}".

4.3.2 Integrated fiducial results

In this section, we present the integrated fiducial results for the $pp \to t\bar{t}t\bar{t}+X$ process in the 3ℓ channel at the LHC with $\sqrt{s} = 13.6$ TeV. In Table 4.4, results are shown at LO and NLO in QCD for our default setup that utilizes $Q_{cut} = 25$ GeV, for various PDF sets and the $\mu_0 = \mu_R = \mu_F = E_T/4$ and $\mu_0 = \mu_R = \mu_F = 2m_t$ scale choices. Also displayed are scale uncertainties obtained from the standard seven-point scale variation, the size of PDF uncertainties and the $\mathcal{K} = \sigma^{\text{NLO}}/\sigma^{\text{LO}}$ factors. First, we observe that the LO scale uncertainties are substantial, ranging from 71% to 74% depending on the PDF set, while a sharp decrease is observed when higher-order QCD effects are taken into account, with theoretical errors being 23% for all PDF sets and for both scale options. The internal PDF errors are smaller in magnitude, being 2% for the NNPDF, 4% for MSHT20 and 6% for CT18. Second, the impact of QCD corrections is highly sensitive to the PDF set, with $\mathcal{K}$ factors ranging between 1.08 and 1.37. The source of the wide range of $\mathcal{K}$ factors has already been discussed in Sec. 4.2.2 and can be attributed to the poor quality of the fit for extracting the LO PDF sets, which manifests itself in the large discrepancies of the LO cross sections. Finally, the NLO differences between the two scales are at most 7%, which is well within the NLO scale-uncertainty bands for this process.

Next, we shift our focus to the impact of the Q_{cut} parameter on the calculation, which was initially introduced to suppress certain kinematic configurations that could result in large $\mathcal{K}$ factors. To illustrate the necessity of imposing a cut on the invariant mass of the light-jet system, M_{jj}, in Fig. 4.14 we present LO and NLO cross sections for various values of Q_{cut}. In the upper panels, the absolute NLO and LO predictions along with their scale-uncertainty bands are shown in red and blue, respectively. The bottom panels depict the ratio to the LO cross sections and the magnitude of the scale uncertainties normalized to the corresponding LO values. The results are displayed for both scale choices, $\mu_0 = E_T/4$ and $\mu_0 = 2m_t$.

PDF	$\sigma^{\rm LO}$ [ab]	δ_{scale}	$\sigma^{\rm NLO}$ [ab]	δ_{scale}	δ_{PDF}	$\mathcal{K} = \sigma^{\rm NLO}/\sigma^{\rm LO}$
$\mu_R = \mu_F = \mu_0 = 2m_t$						
MSHT20	35.575(2)	$^{+25.883\ (73\%)}_{-13.982\ (39\%)}$	42.25(2)	$^{+8.27\ (20\%)}_{-9.72\ (23\%)}$	$^{+1.76\ (4\%)}_{-1.32\ (3\%)}$	1.19
NNPDF3.1	30.581(2)	$^{+21.781\ (71\%)}_{-11.853\ (39\%)}$	41.89(2)	$^{+8.28\ (20\%)}_{-9.71\ (23\%)}$	$^{+0.89\ (2\%)}_{-0.89\ (2\%)}$	1.37
CT18	37.675(3)	$^{+26.858\ (71\%)}_{-14.655\ (39\%)}$	41.89(2)	$^{+8.20\ (20\%)}_{-9.62\ (23\%)}$	$^{+2.42\ (6\%)}_{-2.00\ (5\%)}$	1.11
$\mu_R = \mu_F = \mu_0 = E_T/4$						
MSHT20	39.424(3)	$^{+29.111\ (74\%)}_{-15.632\ (40\%)}$	44.91(2)	$^{+7.91\ (18\%)}_{-10.16\ (23\%)}$	$^{+1.84\ (4\%)}_{-1.38\ (3\%)}$	1.14
NNPDF3.1	34.193(3)	$^{+24.868\ (73\%)}_{-13.413\ (39\%)}$	44.60(2)	$^{+7.87\ (18\%)}_{-10.16\ (23\%)}$	$^{+0.94\ (2\%)}_{-0.94\ (2\%)}$	1.30
CT18	41.306(3)	$^{+29.728\ (72\%)}_{-16.169\ (39\%)}$	44.50(2)	$^{+7.86\ (18\%)}_{-10.06\ (23\%)}$	$^{+2.51\ (6\%)}_{-2.08\ (5\%)}$	1.08

Table 4.4: *Integrated fiducial cross sections for the $pp \to t\bar{t}t\bar{t} + X$ process in the 3ℓ channel at the LHC using a center-of-mass energy of $\sqrt{s} = 13.6$ TeV. Results are presented for various (N)LO PDF sets at (N)LO in QCD, using the fixed $\mu_0 = 2m_t$ and the dynamical $\mu_0 = E_T/4$ scale choices, including the theoretical uncertainties obtained under the standard seven-point scale variation. At NLO in QCD, at least one light-jet pair needs to satisfy the relation of Eq. (4.28), with $Q_{cut} = 25\,\text{GeV}$. In the last column, $\mathcal{K}$ factors, defined as $\mathcal{K} = \sigma^{\rm NLO}/\sigma^{\rm LO}$, are also displayed. The numbers inside the parentheses for the central predictions correspond to Monte Carlo integration errors.*

We find that with increasing values of Q_{cut}, the NLO cross sections become larger, with $\mathcal{K}$ factors approaching 1.5 for both scale choices when $Q_{cut} = 100$ GeV. At the same time, the NLO scale uncertainties increase substantially. This indicates that, for large values of Q_{cut}, there are certain topologies which are governed by LO dynamics as they first appear at NLO, leading to NLO uncertainties that resemble those at LO. For instance, although not explicitly shown in the figure, in the absence of any cut on M_{jj}, the QCD corrections amount to 78% for $\mu_0 = E_T/4$ and 87% for $\mu_0 = 2m_t$. In addition, the magnitude of the theoretical errors in this scenario becomes almost twice as large compared to our default setup, reaching 42% for the dynamical scale and 44% for the fixed scale. This behavior highlights the importance of choosing an appropriate value of the Q_{cut} parameter in order to maintain the validity of the perturbative expansion and to adequately suppress the configurations discussed in Sec. 4.3.1. We also comment that the LO cross sections are completely independent of the choice of Q_{cut}, as in this case, the invariant mass of the two light jets is always equal to m_W. The motivation for adopting $Q_{cut} = 25$ GeV as the default choice is illustrated in Fig. 4.15, where the NLO cross section is shown as a function of Q_{cut} for the different NWA scenarios and for both the fixed and dynamical scale choices. The upper panels show the absolute results, while the bottom panels present the relative deviations with respect to the default NLO_{exp}

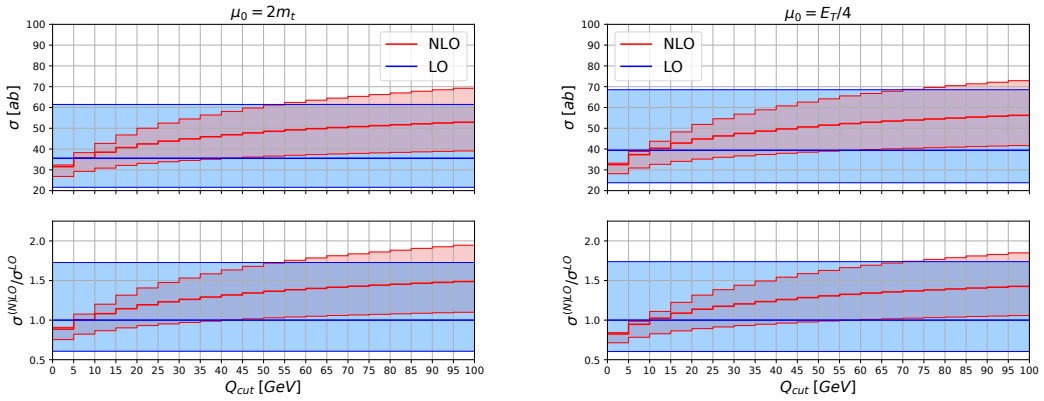

Figure 4.14: *Integrated fiducial cross section for the $pp \to t\bar{t}t\bar{t} + X$ process in the 3ℓ channel at the LHC with $\sqrt{s} = 13.6$ TeV, as a function of the Q_{cut} parameter defined in Eq. (4.28). The upper panels depict the absolute (N)LO QCD cross sections with (red) blue, while the bottom panels illustrate the relative ratio to the LO predictions, including the scale uncertainties relative to the LO results. Results are presented for the $\mu_0 = \mu_R = \mu_F = 2m_t$ (left) and $\mu_0 = \mu_R = \mu_F = E_T/4$ (right) scales and for our default setup, which utilizes the MSHT20 PDF set.*

setup. First, we notice that selecting $Q_{cut} = 25$ GeV helps to mitigate the large differences among the various NWA approaches, while simultaneously preventing the appearance of large $\mathcal{K}$ factors associated with larger Q_{cut} values. Moreover, the discrepancies between the NWA scenarios become particularly pronounced in the low-Q_{cut} regime, where the deviations between the $\text{NLO}_{\text{LO}_{\text{dec}}}$ and NLO_{exp} setups can reach up to 40% for both scale choices. Interestingly, these differences are not even covered by the NLO scale uncertainties. This suggests that the invariant mass of the light jets is strongly influenced by QCD corrections applied in the decays of the $pp \to t\bar{t}t\bar{t}$ system, as demonstrated in Fig. 4.16. In this figure, the invariant mass of the two hardest light jets is displayed when no Q_{cut} is applied, for both our default setup and the $\text{NLO}_{\text{LO}_{\text{dec}}}$ scenario. While a peak around the $W^{\pm}$-boson mass is present in both cases, it is noticeably narrower when QCD corrections are solely applied at the production stage. Compared to the LO prediction, where the M_{jj} distribution is a delta function at m_W, it becomes clear that the shape of M_{jj} is predominantly distorted when QCD corrections are included in both production and decays, leading to a significantly broadened peak around m_W for the NLO_{exp} case. Thus, imposing a very small Q_{cut} parameter removes a substantial fraction of the NLO_{exp} contributions, while having a much milder impact on the $\text{NLO}_{\text{LO}_{\text{dec}}}$ predictions, as the vast majority of the events are populated around $M_{jj} \approx m_W$. This explains the large differences between the two setups when small Q_{cut} values are chosen. Conversely, for large values of Q_{cut}, the differences between the $\text{NLO}_{\text{LO}_{\text{dec}}}$ and NLO_{exp} predictions become negligible, remaining below 5%. In this region, higher-order effects related to the treatment of the NLO top-quark width in the NLO_{full} setup are more important, leading to deviations of up to 20% with respect to the default configuration. Nevertheless, these effects are fully covered by the large NLO scale-uncertainty bands.

Finally, Table 4.5 summarizes the results for the different NWA scenarios, considering both the default setup with $Q_{cut} = 25$ GeV and the case without any

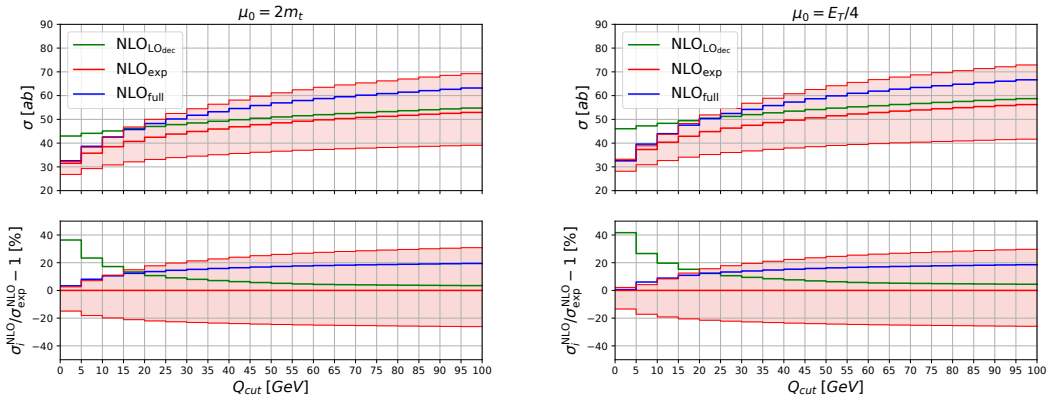

Figure 4.15: *Integrated fiducial cross sections at NLO in QCD for the* $pp \to t\bar{t}t\bar{t} + X$ *process in the* 3ℓ *channel with* $\sqrt{s} = 13.6$ TeV*, for three different NWA scenarios:* NLO_{exp} *(red),* $\text{NLO}_{\text{LO}_{\text{dec}}}$ *(green) and* NLO_{full} *(blue). Results are shown for several choices of the* Q_{cut} *parameter defined in Eq. (4.28), using the fixed scale* $\mu_0 = 2m_t$ *(left) and the dynamical scale* $\mu_0 = E_T/4$ *(right) together with the NLO MSHT20 PDF set. The upper panels show the absolute predictions, while the bottom panels present the percentage differences relative to the* NLO_{exp} *setup. In both panels, the NLO scale-uncertainty bands for our default setup are also displayed.*

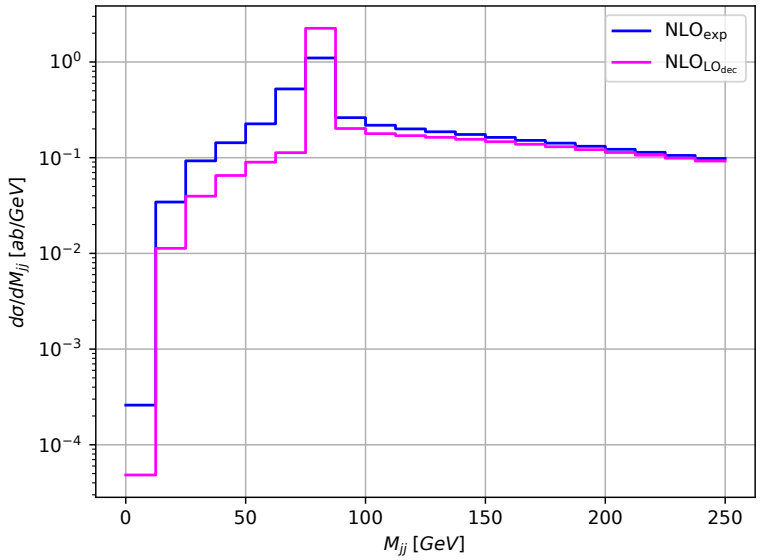

Figure 4.16: *Differential cross-section distribution for the the* $pp \to t\bar{t}t\bar{t} + X$ *process in the* 3ℓ *channel at the LHC with* $\sqrt{s} = 13.6$ TeV*, in terms of the invariant mass of the two hardest light jets in the final state,* M_{jj}*. Results are presented utilizing the dynamical scale choice* $\mu_0 = E_T/4$ *and the NLO MSHT20 PDF set for the* NLO_{exp} *(blue) and the* $\text{NLO}_{\text{LO}_{\text{dec}}}$ *(magenta) setups, without imposing any kinematic restriction on* M_{jj} *(*$Q_{cut} \to \infty$*).*

restriction on M_{jj}, corresponding to $Q_{cut} \to \infty$. Results are presented for the two scale choices $\mu_0 = 2m_t$ and $\mu_0 = E_T/4$, including theoretical uncertainties obtained from the seven-point scale variation, as well as deviations with respect to the default

NLO_{exp} setup. On the one hand, for $Q_{cut} = 25$ GeV, the impact of higher-order QCD effects in the decays is of the order of $11\% - 12\%$ depending on the scale choice, while the NLO_{full} cross sections exceed the NLO_{exp} results by about $12\% - 13\%$. In addition, once QCD corrections are consistently included in both the production and decay stages, the associated theoretical uncertainty is noticeably reduced, from 26% to 23%. At the same time, the NLO_{full} scenario exhibits the smallest scale dependence, with uncertainties at the level of 19%. On the other hand, when no Q_{cut} is applied on M_{jj}, the impact of higher-order QCD effects in the decays becomes negligible, at the level of $2\% - 3\%$, whereas the effects associated with using the NLO top-quark width everywhere in NLO_{full} increase substantially, reaching about 24%. Furthermore, the size of the scale uncertainties is substantial for all NWA scenarios, ranging between 42% and 45% for $\text{NLO}_{\text{LO}_{\text{dec}}}$ and NLO_{exp} and from 38% to 40% for NLO_{full}. Overall, in the absence of a Q_{cut}, the resulting QCD corrections are extremely large, yielding values between 80% and 130%, depending on whether the NLO_{exp} or NLO_{full} prescription is employed. This clearly demonstrates the necessity of imposing a finite Q_{cut} in order to maintain perturbative stability and ensure the reliability of the calculation.

4.3.3 Differential results

In this section, differential predictions for the $pp \to t\bar{t}t\bar{t}$ process in the 3ℓ channel at the LHC with $\sqrt{s} = 13.6$ TeV are presented. We focus on assessing the impact of higher-order QCD corrections in certain regions of the phase space, as well as on comparing the different treatments of the NWA at the differential level. On top of that, we examine the effects of not imposing any cut on the invariant mass of the light-jet system M_{jj}, and comment on the implications of this choice. We start by discussing the impact of the scale choice employed at the differential level. So far, integrated fiducial results have been presented using both a fixed, $\mu_0 = 2m_t$, and a dynamical scale, $\mu_0 = E_T/4$, for setting the renormalization and factorization scales. In Fig. 4.17, we show the behavior of these two scale choices at the differential cross-section level at LO and NLO in QCD, by presenting the sum of the transverse momenta of the four hardest b jets in the final state, $H_{T,b}$, and the sum of the transverse momenta of the charged leptons, $H_{T,l}$. In addition to the absolute predictions displayed in the upper panels, the ratios with respect to the fixed scale choice $\mu_0 = 2m_t$ are shown in the lower panels for both LO and NLO. For the NLO case, an additional panel illustrates the size of the theoretical uncertainties associated with the two scale choices, normalized to their corresponding predictions. From the LO ratio panels, sizable shape distortions between the two scale choices are observed for both observables, with deviations relative to the fixed scale ranging from -30% to $+30\%$. As shown by the NLO ratio panels, once higher-order QCD corrections are included, these discrepancies are significantly reduced and do not exceed 20%, indicating that the NLO predictions exhibit a reduced scale sensitivity. Concerning the size of the NLO theoretical errors, we notice that both scale choices lead to comparable scale uncertainties, even in the high-p_T regions, contrary to the naive expectations. As already mentioned for the 4ℓ channel, given that four-top production is characterized by a large production threshold, one may need to probe even higher-p_T regions in order to identify kinematic regimes where the dynamical scale yields smaller uncertainties compared to the fixed choice $\mu_0 = 2m_t$. Indeed, as

Decay treatment	σ_i^{NLO} [ab]	$+\delta_{scale}$ [ab]	$-\delta_{scale}$ [ab]	$\sigma_i^{\text{NLO}}/\sigma_{\text{exp}}^{\text{NLO}} - 1$
		$Q_{cut} = 25$ GeV		
		$\mu_R = \mu_F = \mu_0 = 2m_t$		
full	47.92(2)	+4.56 (10%)	−9.22 (19%)	+13.4%
LO_{dec}	46.76(2)	+12.33 (26%)	−11.51 (25%)	+10.7%
exp	42.25(2)	+8.27 (20%)	−9.72 (23%)	–
		$\mu_R = \mu_F = \mu_0 = E_T/4$		
full	50.45(3)	+3.47 (7%)	−9.32 (19%)	+12.3%
LO_{dec}	50.17(3)	+12.95 (26%)	−12.34 (25%)	+11.7%
exp	44.91(2)	+7.91 (18%)	−10.16 (23%)	–
		$Q_{cut} \to \infty$		
		$\mu_R = \mu_F = \mu_0 = 2m_t$		
full	82.45(7)	+33.16 (40%)	−24.17 (29%)	+24.2%
LO_{dec}	67.80(3)	+30.49 (45%)	−20.64 (30%)	+2.2%
exp	66.36(5)	+29.01 (44%)	−20.17 (30%)	–
		$\mu_R = \mu_F = \mu_0 = E_T/4$		
full	86.7(1)	+33.1 (38%)	−25.0 (29%)	+23.5%
LO_{dec}	72.05(3)	+31.83 (44%)	−21.83 (30%)	+2.6%
exp	70.19(7)	+29.69 (42%)	−21.12 (30%)	–

Table 4.5: *Integrated fiducial cross sections for the* $pp \to t\bar{t}t\bar{t} + X$ *process in the* 3ℓ *channel at the LHC with* $\sqrt{s} = 13.6$ TeV*, for the case where* $Q_{cut} = 25$ GeV *in Eq.* (4.28) *and the scenario where no restriction is applied on* M_{jj}*, denoted as* $Q_{cut} \to \infty$*. Results are presented for the following NWA treatments:* NLO_{exp}*,* NLO_{full} *and* $\text{NLO}_{\text{LO}_{\text{dec}}}$ *using* $\mu_0 = \mu_R = \mu_F = 2m_t$ *and* $\mu_0 = \mu_R = \mu_F = E_T/4$ *and the NLO MSHT20 PDF set. Also shown are scale uncertainties and the percentage differences to the* $\sigma_{\text{exp}}^{\text{NLO}}$ *cross sections.*

shown in Fig. 4.18 for the $H_{T,l}$ observable, the scale uncertainties associated with the $\mu_0 = 2m_t$ scale grow significantly above 1 TeV, reaching values near 100%. At the same time, the scale uncertainties obtained with the dynamical scale remain modest, never exceeding 25%. Although the same is not true for the $H_{T,b}$ distribution, this is an indication that employing the fixed scale could lead to substantial theoretical uncertainties in the high-energy tails of certain observables. These regions would, however, not be accessible at the LHC. Finally, we highlight that for

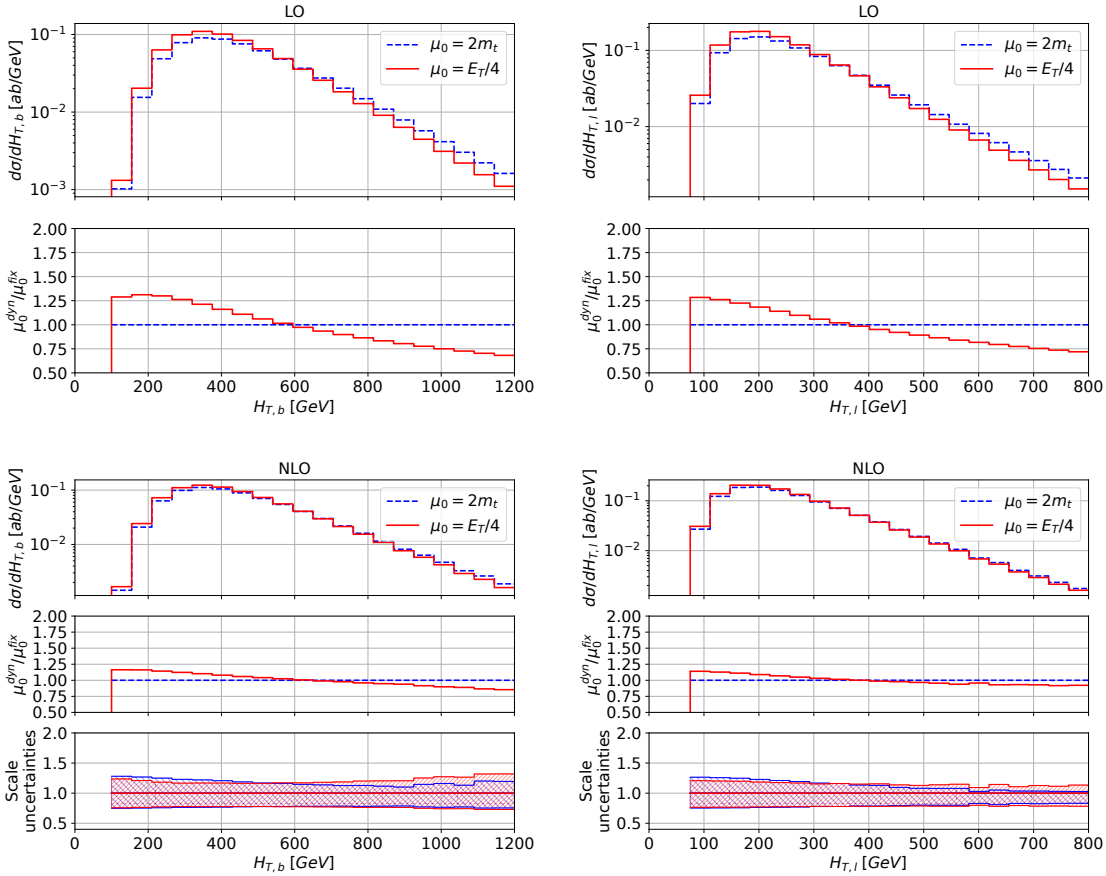

Figure 4.17: *Differential cross-section distributions for the* $pp \to t\bar{t}t\bar{t} + X$ *process in the* 3ℓ *channel at the LHC with* $\sqrt{s} = 13.6$ TeV*, for the* $H_{T,b}$ *(left) and* $H_{T,l}$ *(right) observables, using* $\mu_0 = 2m_t$ *and* $\mu_0 = E_T/4$*. The upper panels show the absolute results at LO (up) and NLO (bottom) accuracy in perturbative QCD, while in the lower panels the normalized ratio to the fixed scale choice* $\mu_0 = 2m_t$ *is also demonstrated. For the NLO results, a third panel is added to show the magnitude of the normalized scale uncertainties for both scale choices, relative to their corresponding predictions. For all results, the (N)LO MSHT20 PDF set was employed along with the* $|M_{jj} - m_W| < Q_{cut} = 25$ GeV *cut.*

all observables considered, the differential predictions obtained with the fixed and dynamical scale choices are consistent with each other within the NLO theoretical uncertainties. For this reason, in the remainder of this section, only results obtained using the dynamical scale choice $\mu_0 = E_T/4$ are shown.

In the following, we present a set of observables grouped into two categories. The first category, shown in Figs. 4.19- 4.21, includes observables related to the kinematics of b jets and leptons, while the second category, displayed in Figs. 4.22, 4.23, comprises observables that involve light-jet kinematics in their definition. All figures show LO and NLO differential predictions together with the corresponding scale uncertainties for our default setup with $|M_{jj} - m_W| < Q_{cut} = 25$ GeV. For both classes of observables, an additional panel is included to display the ratios to the LO predictions along with the associated relative uncertainties. In Fig. 4.22, however, such ratio panels are not shown because of the enormous QCD corrections that would

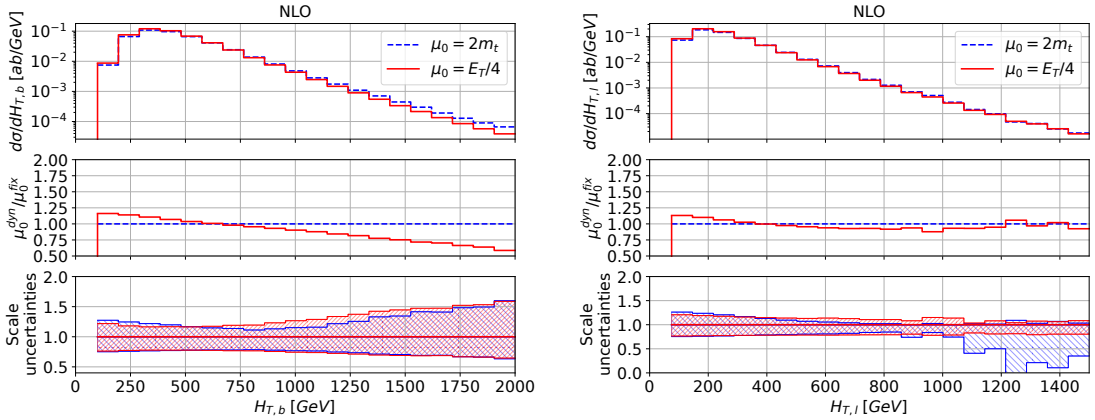

Figure 4.18: *Same as Fig. 4.17, but displaying only the NLO differential results and using extended kinematic ranges, reaching up to 2 TeV for $H_{T,b}$ and 1.5 TeV for $H_{T,l}$.*

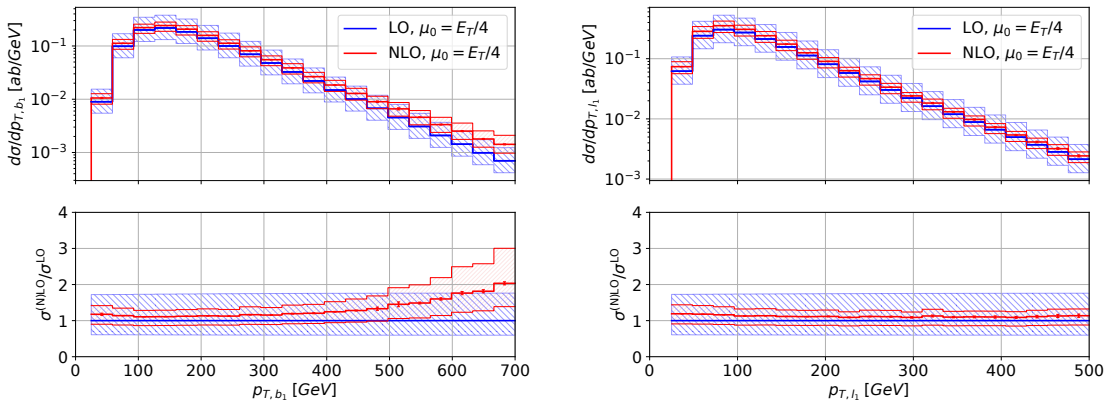

Figure 4.19: *Differential cross-section distributions for the $pp \to t\bar{t}t\bar{t} + X$ process in the 3ℓ channel at the LHC with $\sqrt{s} = 13.6$ TeV, for the p_{T,b_1} and p_{T,l_1} observables. Results are shown at LO (blue) and NLO (red) in QCD for the dynamical scale choice $\mu_0 = E_T/4$ and the (N)LO MSHT20 PDF set, including the scale uncertainties obtained under seven-point scale variation and utilizing the default setup with $|M_{jj} - m_W| < Q_{cut} = 25$ GeV. The upper panels depict the absolute predictions, while in the bottom panels, the ratio to the LO results is displayed along with the scale uncertainties normalized to the LO cross sections.*

obscure the readability of the plots. We begin our discussion from Fig. 4.19, where the transverse momenta of the hardest b jet, p_{T,b_1}, and the hardest charged lepton, p_{T,l_1}, are shown. For the p_{T,b_1} distribution, QCD corrections become particularly important in the high-p_T tail, reaching values up to 100% and lying slightly outside of the large LO uncertainty bands. In this regime, the absolute size of the NLO scale uncertainties becomes similar in size to that at LO, amounting to roughly 50%. On the contrary, the $\mathcal{K} = \sigma^{\text{NLO}}/\sigma^{\text{LO}}$ factor for the p_{T,l_1} distribution remains relatively flat, taking values in the $1.10 - 1.20$ range, while the NLO scale uncertainties are comparable in size to those observed at the integrated level.

In Fig. 4.20, we present some additional distributions related to b-jet and lepton

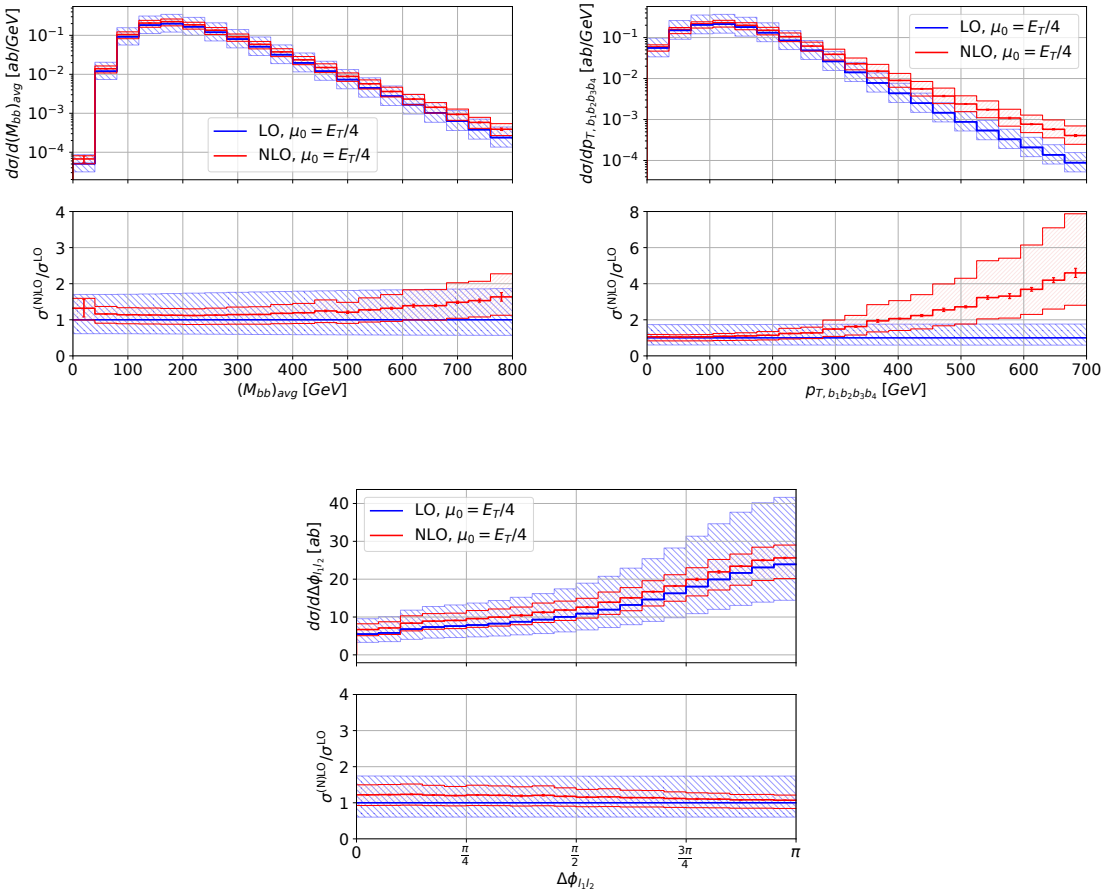

Figure 4.20: *Same as Fig. 4.19 but for the average invariant mass of the four hardest b jets, $(M_{bb})_{avg}$, the transverse momentum of the $b_1b_2b_3b_4$ system, $p_{T,b_1b_2b_3b_4}$, and the azimuthal angle between the two hardest charged leptons $\Delta\phi_{l_1l_2}$.*

kinematics. In particular, we show the average invariant mass of two b jets, $(M_{bb})_{avg}$, which we calculate after considering all possible invariant mass pairs between the 4 hardest b jets in the final state, the transverse momentum of the $b_1b_2b_3b_4$ system, $p_{T,b_1b_2b_3b_4}$, as well as the azimuthal angle between the two hardest charged leptons, $\Delta\phi_{l_1l_2}$. Several comments are in order now. In the $(M_{bb})_{avg}$ distribution, the QCD corrections tend to grow with increasing values of the invariant mass, and even though they reach values of up to roughly 65%, the central NLO predictions are always within the LO theoretical errors. In contrast, enormous QCD corrections are observed in the $p_{T,b_1b_2b_3b_4}$ distribution, with $\mathcal{K} = \sigma^{\rm NLO}/\sigma^{\rm LO}$ factors exceeding 4 in the high-p_T region. At the same time, the NLO uncertainties become very large, amounting to 70% in the tail of the $p_{T,b_1b_2b_3b_4}$ distribution. Similar effects have already been observed for the $pp \to t\bar{t}t\bar{t}$ process in the 4ℓ channel, but in this case they are significantly more pronounced. These large QCD corrections are attributed to the recoil of a highly energetic light jet against the $b_1b_2b_3b_4$ system, a configuration which is absent at LO. As a result, the NLO predictions in the high-p_T regime are governed by LO kinematics. Unlike $(M_{bb})_{avg}$ and $p_{T,b_1b_2b_3b_4}$, the impact of higher-order QCD effects in the $\Delta\phi_{l_1l_2}$ distribution is rather moderate, varying between $1\% - 20\%$. In general, for nearly all lepton-related observables we examined,

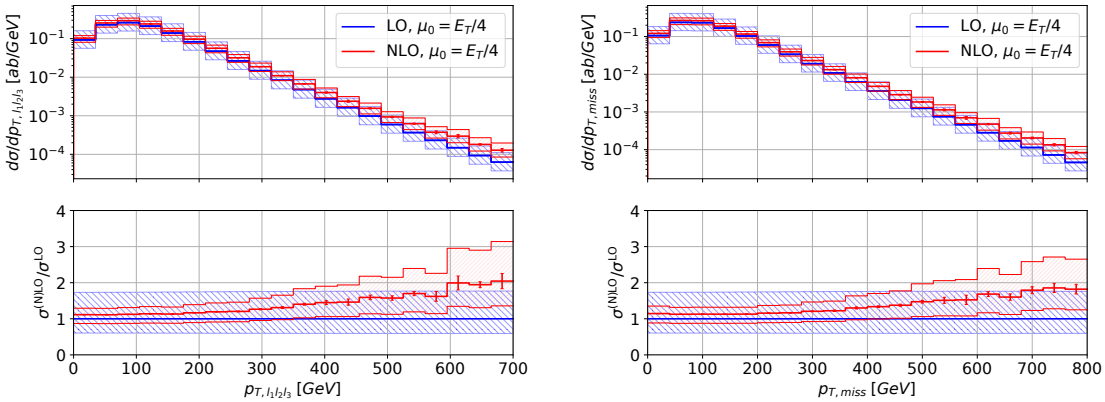

Figure 4.21: *Same as Fig. 4.19 but for the transverse momentum of the $l_1l_2l_3$ system (left) and the missing transverse momentum (right) associated with the presence of neutrinos in the final state.*

we found that QCD corrections were covered by the large LO uncertainty bands. The only exceptions are the $p_{T,l_1l_2l_3}$ and $p_{T,miss}$ observables shown in Fig. 4.21, for which QCD corrections are as high as $80\% - 100\%$ in the high-p_T tails. These sizable corrections are due to recoil effects, analogous to those discussed for the $p_{T,b_1b_2b_3b_4}$ observable. We can, therefore, conclude that lepton kinematics are generally less sensitive to higher-order QCD effects than those of the b jets.

We now shift our focus to observables that involve light jets in their definition. In Fig. 4.22, we present the transverse momenta of the two hardest light jets in the final state, p_{T,j_1} and p_{T,j_2}, together with their angular separation, $\Delta R_{j_1j_2}$. For these observables, in addition to large QCD corrections, significant shape distortions are observed. These effects are most pronounced in the p_{T,j_2} distribution, where the LO prediction exhibits a sharp cut-off at approximately $p_{T,j_2} \approx 200\,\text{GeV}$, while a substantial number of events populate the region above this value at NLO. This feature is a direct consequence of the LO kinematics in the NWA, which imply

$$(p_{T,j_2})_{max} \approx \frac{m_W}{(\Delta R_{j_1j_2})_{min}} \approx 200\ \text{GeV}\,. \tag{4.29}$$

The absence of such a kinematic restriction at NLO naturally explains the presence of events beyond this cut-off. For the p_{T,j_1} distribution, although enormous QCD corrections are observed in the high-p_T tail, a similar cut-off in the LO prediction is not visible within the plotted range. Nevertheless, as in the case of p_{T,j_2}, an upper bound on p_{T,j_1} can also be derived from LO kinematics. In particular, one finds

$$(p_{T,j_1})_{max} \approx \frac{m_W^2}{(p_{T,j_2})_{min}\,(\Delta R_{j_1j_2})^2_{min}} \approx 1615\ \text{GeV}\,, \tag{4.30}$$

but this value is in the TeV region, and thus, outside of the plotted range. Moreover, for both observables, the size of NLO uncertainties increases substantially in the high-p_T regime, becoming comparable to or even larger than that of LO, highlighting that these regions are effectively described only at LO accuracy. New structures also emerge in the $\Delta R_{j_1j_2}$ distribution. In particular, while at LO a single peak is present around $\Delta R_{j_1j_2} \approx 1.0$, at NLO a second, smaller yet still significant peak appears

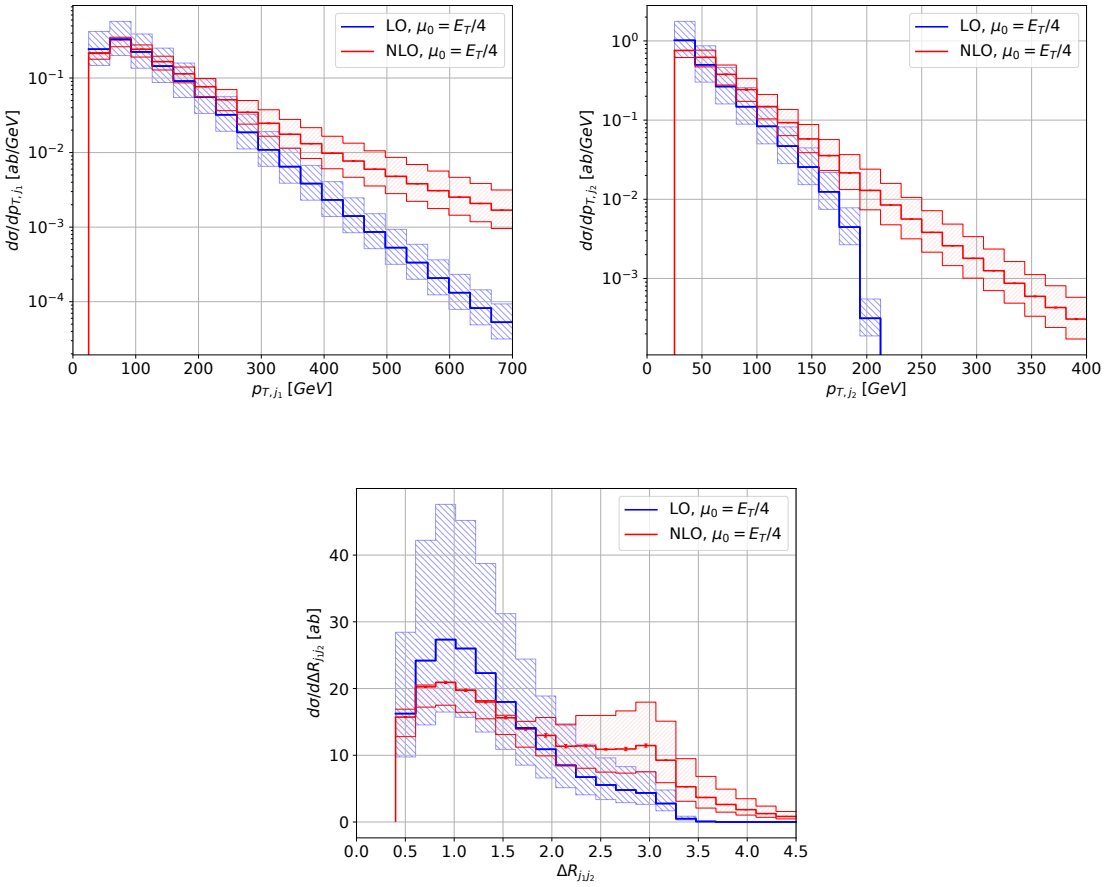

Figure 4.22: *Differential cross-section distributions for the* $pp \to t\bar{t}t\bar{t} + X$ *process in the* 3ℓ *channel at the LHC with* $\sqrt{s} = 13.6$ TeV*, for the* p_{T,j_1}*,* p_{T,j_2} *and* $\Delta R_{j_1j_2}$ *observables. The (N)LO in QCD predictions are illustrated with (red) blue for the (N)LO MSHT20 PDF set and the dynamical scale choice* $\mu_0 = E_T/4$*, utilizing the default setup with* $|M_{jj} - m_W| < Q_{cut} = 25$ GeV*. Also shown are scale uncertainties obtained after the standard seven-point scale variation in a bin-by-bin analysis.*

near $\Delta R_{j_1j_2} \approx \pi$, indicating configurations in which the two jets are produced back-to-back. Indeed, at NLO in QCD, the emission of an additional energetic light jet gives rise to kinematic configurations in which the two leading light jets recoil against each other, which are strongly suppressed at LO. In the back-to-back region, the NLO scale uncertainties reach values of up to 60%, once again indicating that this regime is dominated by LO dynamics.

Significant shape distortions and large $\mathcal{K}$ factors are also present in other observables related to light-jet kinematics. To illustrate this, in Fig. 4.23, we plot the invariant mass of the hardest light and b jet, $M_{j_1b_1}$, the azimuthal angle between the two hardest light jets $\Delta\phi_{j_1j_2}$, as well as the rapidity of the hardest light jet y_{j_1}. In the $M_{j_1b_1}$ distribution, the large NLO enhancements relative to the LO predictions observed in the tail are again a consequence of the LO kinematics that force $M_{j_1b_1}$ values above roughly $M_{j_1b_1} \approx 600$ GeV to be highly suppressed. Indeed, the LO

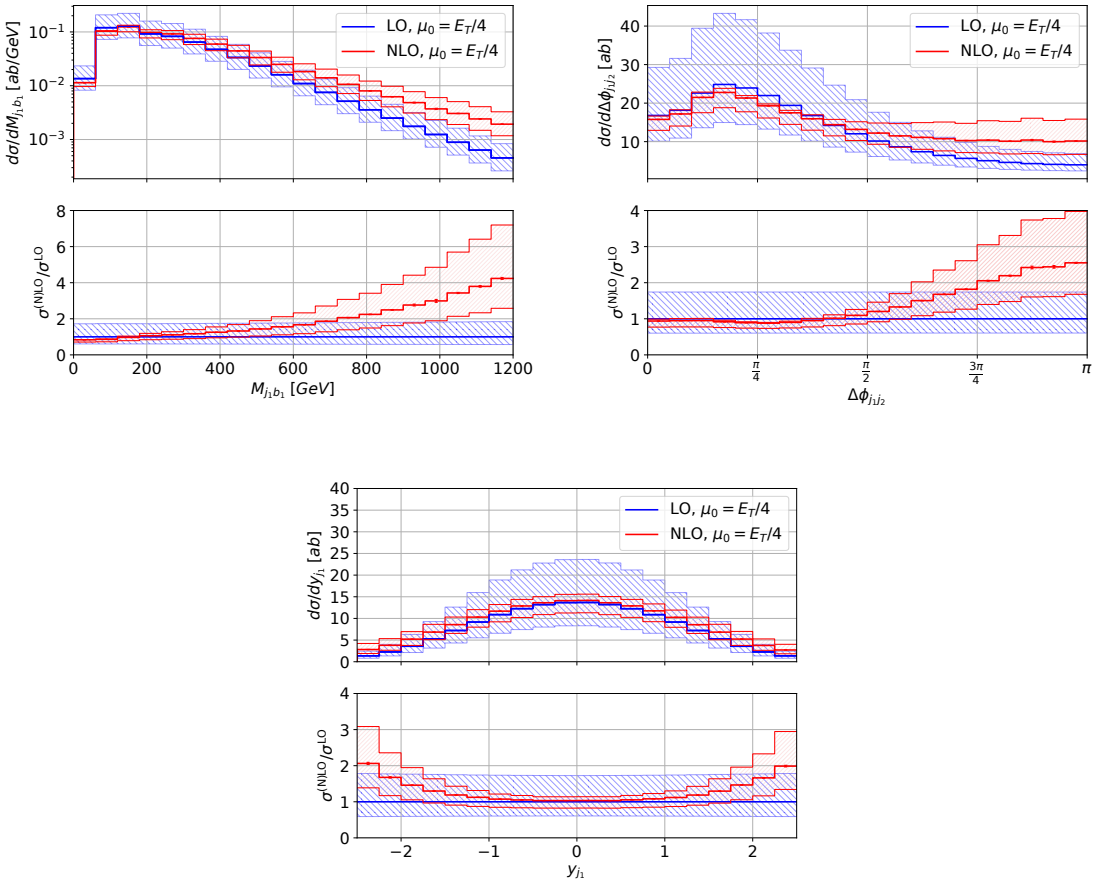

Figure 4.23: *Same as Fig. 4.19 but for the invariant mass of the hardest b jet and light jet, $M_{j_1b_1}$, the angular separation between the two hardest light jets $\Delta\phi_{j_1j_2}$ and the rapidity of the hardest light jet y_{j_1}.*

kinematics imply

$$(M_{j_1b_1})_{max} \approx 2\left((p_{T,b_1})_{max}\,(p_{T,j_1})_{max}\right)^{1/2} \approx 660\ \text{GeV}\,, \tag{4.31}$$

where Eqs. (4.30) and (4.18) have been used. Although the second equation was derived for the 4ℓ channel, it still holds for the 3ℓ channel, assuming again that most events are populated near the large $4m_t$ threshold. Therefore, as depicted in the plot, LO predictions for $M_{j_1b_1} \gtrsim 660$ GeV are strongly disfavored, leading to $\mathcal{K} = \sigma^{\text{NLO}}/\sigma^{\text{LO}}$ factors of up to 4 and to a substantial growth of the NLO scale uncertainties in the tail of the distribution. For the $\Delta\phi_{j_1j_2}$ distribution, QCD corrections reach almost 170% near $\Delta\phi_{j_1j_2} \approx \pi$ and are outside the LO uncertainty bands. Finally, the rapidity distribution of the hardest light jet also exhibits large $\mathcal{K}$ factors, approaching values of about 2 for $|y_{j_1}| \approx 2.5$. Such large rapidity values arise at NLO when a highly energetic light jet is emitted nearly collinearly with one of the incoming beams.

So far, all differential results presented in this section correspond to the value of $Q_{cut} = 25$ GeV for restricting M_{jj} in Eq. 4.28. As in the case of the integrated cross-sections, assessing the impact of the Q_{cut} parameter at the differential level is

also important. By doing so, we would be able to better understand the impact of the Q_{cut} parameter in various regions of the phase space and to identify potential regimes where differences between distinct Q_{cut} values may arise. For this purpose, in Figs. 4.24, 4.25 we plot several observables for the following three scenarios: $Q_{cut} = 15$ GeV, $Q_{cut} = 25$ GeV and the extreme case of $Q_{cut} \to \infty$. Since the integrated fiducial cross sections differ significantly among these setups, as also evident from Fig. 4.14, presenting the absolute predictions would not be very insightful, as normalization differences would make the plots very difficult to read. For this reason, we present the normalized predictions for each scenario and focus on identifying potential shape distortions between the differential predictions corresponding to the various Q_{cut} values. In all figures, the normalized predictions and the ratio to our default setup are displayed in the upper and middle panels, respectively, while the bottom panels present the size of the normalized scale uncertainties for each setup. In Fig. 4.24, we consider the observables previously examined, namely p_{T,b_1} and $(M_{bb})_{avg}$, together with the average transverse momentum of the charged leptons, $p_{T,l_{avg}}$, and the transverse momentum of the $b_1 b_2$ system, $p_{T,b_1 b_2}$. We observe that removing the restriction on the invariant mass of the light-jet pair, M_{jj}, has a pronounced impact on the high-energy tails of all distributions. Compared to the $Q_{cut} = 25$ GeV configuration, deviations reach approximately 80% for p_{T,b_1} and $p_{T,b_1 b_2}$, around 50% for $(M_{bb})_{avg}$, and about 35% for $p_{T,l_{avg}}$. Notably, these discrepancies in the tails lie well outside the NLO theoretical uncertainty bands of the default setup. Furthermore, across the entire kinematic ranges shown, the scale uncertainties associated with the $Q_{cut} \to \infty$ scenario are significantly larger. This behavior mirrors the sizable NLO uncertainties already observed at the inclusive level for this setup and highlights its reduced perturbative stability.

Additional normalized plots with emphasis on the light-jet kinematics are presented in Fig. 4.25. The observables considered are the transverse momenta of the first and second hardest light jets, p_{T,j_1} and p_{T,j_2}, as well as the angular separations $\Delta R_{j_1 j_2}$ and $\Delta\phi_{j_1 j_2}$. All these observables exhibit a common characteristic: the NLO scale uncertainties for all setups become of the same size in the tails of the distributions. This behavior is somehow expected, as these regions correspond to kinematic configurations where the NLO predictions effectively retain LO accuracy. In addition, contrary to the distributions shown in Fig. 4.24, the sizable shape distortions observed in the tails are covered by the substantial NLO theoretical bands, which are between $85\% - 90\%$ for p_{T,j_1}, p_{T,j_2} and $\Delta R_{j_1 j_2}$, and 55% for $\Delta\phi_{j_1 j_2}$. The only exception occurs in the last bin of the p_{T,j_2} distribution, where the discrepancy between the "no Q_{cut}" and the $Q_{cut} = 25$ GeV setups exceeds 100%. Furthermore, for all observables examined, the differences between the normalized differential predictions obtained with $Q_{cut} = 15$ GeV and $Q_{cut} = 25$ GeV are negligible, with no significant deviations observed in any region of the phase space. It is also worth emphasizing that, for all displayed observables, the magnitude of the theoretical errors is substantially smaller near the bulk of the events when either $Q_{cut} = 15$ GeV or $Q_{cut} = 25$ GeV is imposed, compared to the $Q_{cut} \to \infty$ scenario. This indicates that applying a restriction on the invariant mass of the light-jet system may be beneficial in improving the theoretical modeling relevant for experimental analyses that are targeting this channel. We stress, however, that the large theoretical uncertainties associated with setting $Q_{cut} \to \infty$ in $|M_{jj} - m_W| < Q_{cut}$ primarily reflect the limitations inherent to a fixed-order treatment. In realistic phenomenological studies,

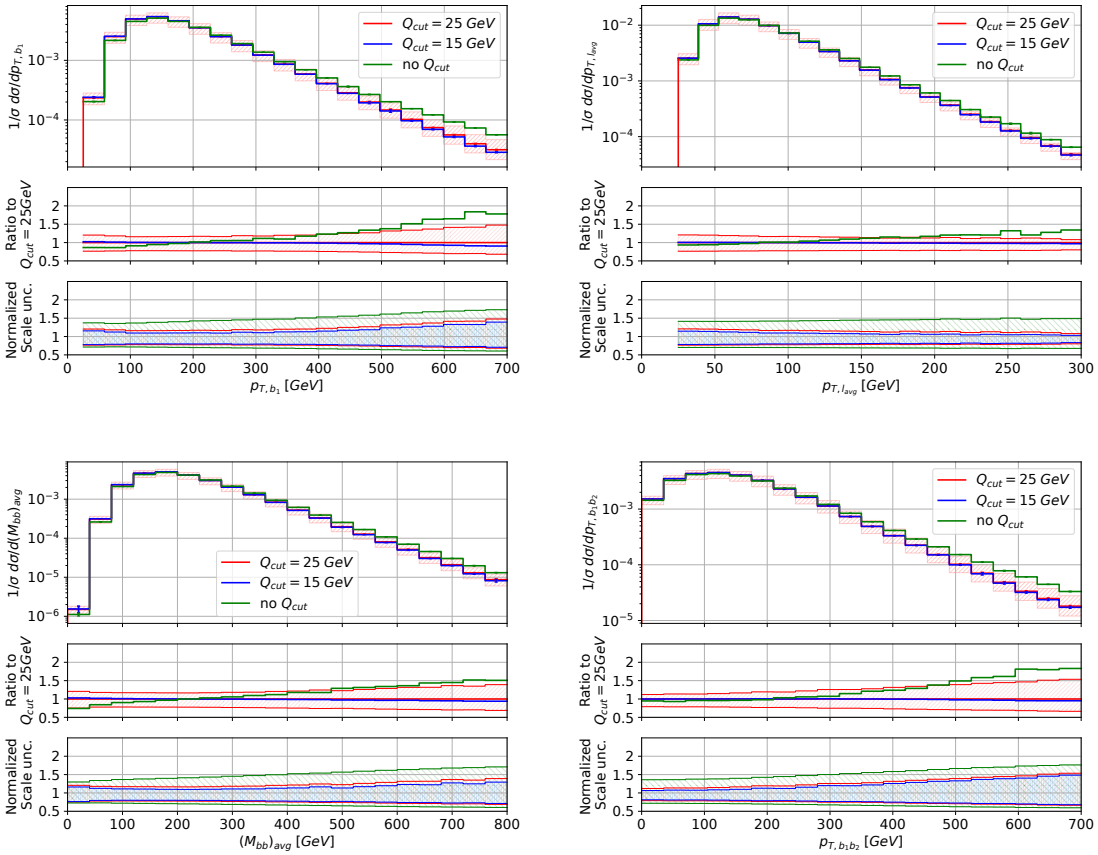

Figure 4.24: *Normalized NLO in QCD cross-section distributions for the* $pp \to t\bar{t}t\bar{t} + X$ *process in the* 3ℓ *channel at the LHC with* $\sqrt{s} = 13.6$ TeV*, for the* $p_{T,b_1}, p_{T,l_{avg}}, (M_{bb})_{avg}$ *and* p_{T,b_1b_2} *distributions. Results are shown for* $Q_{cut} = 25$ GeV *(red),* $Q_{cut} = 15$ GeV *(blue) and* $Q_{cut} \to \infty$ *(green) in Eq. (4.28), using* $\mu_0 = E_T/4$ *and the NLO MSHT20 PDF set. The middle panels display the normalized ratio to the default setup, while in the bottom panels, the normalized scale uncertainties for each setup are also demonstrated.*

where the $pp \to t\bar{t}t\bar{t}$ process is matched to parton-shower algorithms, not imposing any restriction on the invariant mass of the light-jet system is not expected to lead to large scale uncertainties.

Finally, we investigate the impact of higher-order QCD effects in the decays of the $pp \to t\bar{t}t\bar{t}$ system at the level of differential cross sections by comparing the default NLO_{exp} setup with the $\text{NLO}_{\text{LO}_{\text{dec}}}$ scenario. As discussed previously, this comparison is particularly relevant for assessing the effects of NLO spin correlations as well as hard QCD radiation in the decays of the top quarks. Among all the observables we examined, the most interesting ones are presented in Fig. 4.26. More specifically, the main emphasis is given on angular distributions, which are known to be most sensitive to spin correlations, by plotting the following observables: $\Delta R_{j_1 j_2}$, $\Delta R_{j_1 b_1}$, and $\Delta\phi_{l_1 l_2}$. In addition, we also present the invariant mass of the system comprising the hardest b and light jet, $M_{j_1 b_1}$. The absolute NLO predictions with $|M_{jj} - m_W| < Q_{cut} = 25$ GeV are demonstrated in the upper panels, while the middle panels display the ratios with respect to the default NLO_{exp} setup. Finally,

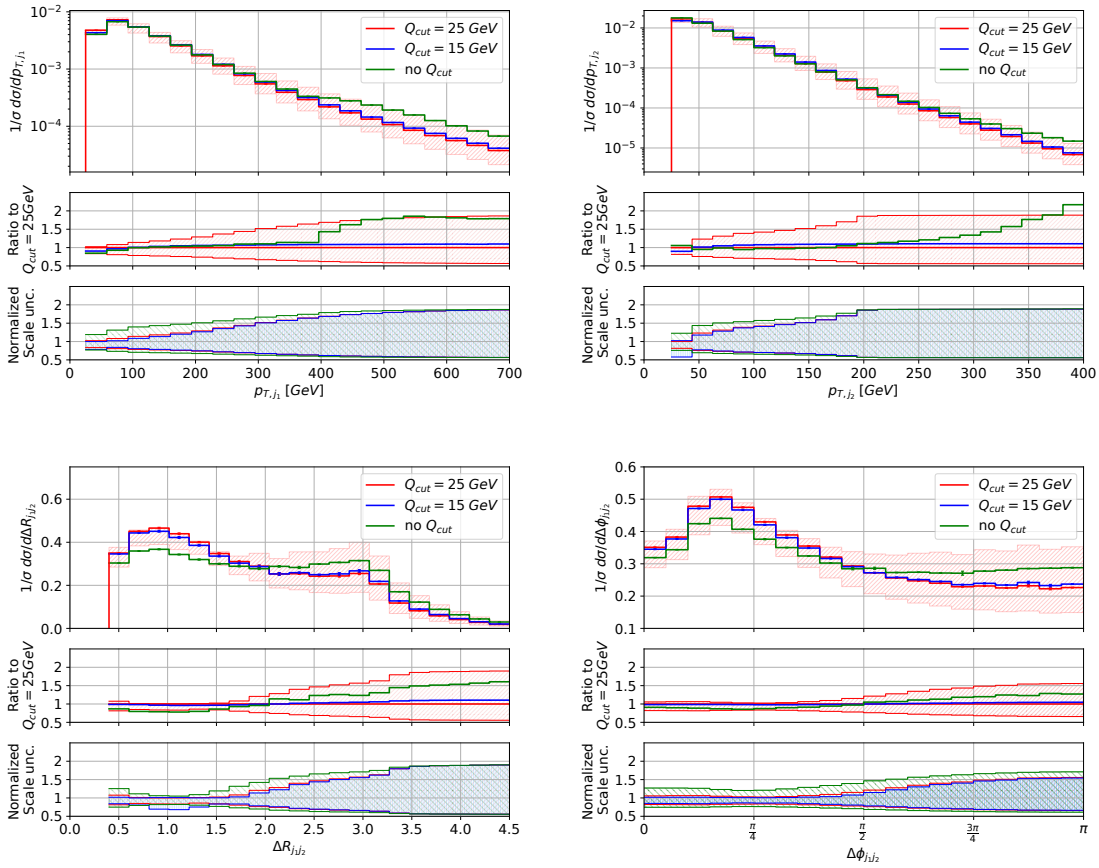

Figure 4.25: *Same as Fig. 4.24 but for the* $p_{T,j_1}, p_{T,j_2}, \Delta R_{j_1j_2}$ *and* $\Delta\phi_{j_1j_2}$ *observables.*

the lower panels illustrate the corresponding NLO scale uncertainties, normalized to the respective central predictions for the two setups. The main observation is that, in the region populated by the majority of events for $\Delta R_{j_1j_2}$ and $M_{j_1b_1}$, the impact of higher-order QCD effects in the decays is sizable. In particular, deviations of approximately 19%-22% are observed for $\Delta R_{j_1j_2}$, while effects of up to 15% are found for $M_{j_1b_1}$. Notably, as displayed in the middle panels, these differences lie outside the corresponding NLO theoretical uncertainty bands. For the $\Delta R_{j_1b_1}$ and $\Delta\phi_{l_1l_2}$ observables, the impact of QCD corrections in the decays is comparatively milder. In these cases, the $\text{NLO}_{\text{LOdec}}$-to-$\text{NLO}_{\text{exp}}$ ratios remain relatively flat, varying between 8% and 16% for $\Delta R_{j_1b_1}$ and between 10% and 12% for $\Delta\phi_{l_1l_2}$. Furthermore, for all observables considered, the inclusion of QCD corrections in the decays leads to a reduction of the scale uncertainties across the entire phase space. The only exception occurs in regions which are driven by LO dynamics, and the size of the scale uncertainties is the same for the two setups.

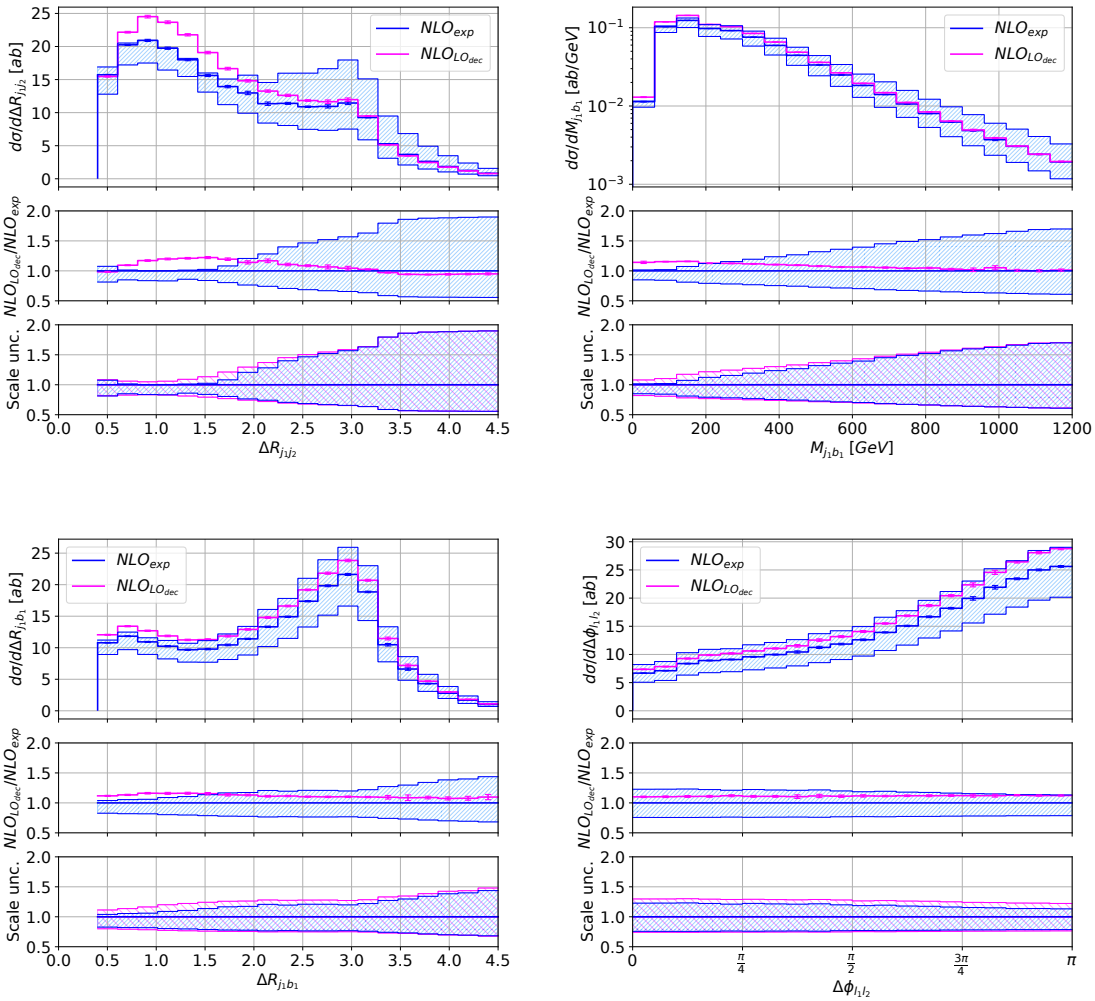

Figure 4.26: *Differential cross-section distributions for the* $pp \to t\bar{t}t\bar{t} + X$ *process in the* 3ℓ *channel at the LHC with* $\sqrt{s} = 13.6$ TeV*, for the following observables:* $\Delta R_{j_1 j_2}, M_{j_1 b_1}, \Delta R_{j_1 b_1}$ *and* $\Delta\phi_{l_1 l_2}$*. Results are displayed for the* $\mathrm{NLO}_{\mathrm{exp}}$ *(blue) and* $\mathrm{NLO}_{\mathrm{LO_{dec}}}$ *(magenta) setups with* $|M_{jj} - m_W| < Q_{cut} = 25$ GeV*, using the dynamical scale choice* $\mu_0 = E_T/4$ *and the default NLO MSHT20 PDF set. The upper panels present the absolute predictions, while in the middle panels the ratio to our default setup is displayed, including the* $\mathrm{NLO}_{\mathrm{exp}}$ *uncertainties obtained using the seven-point scale variation bin-by-bin. Also shown in the bottom panels is the size of the scale uncertainties for both setups, normalized to their corresponding NLO results.*

Chapter 5

The MiNLO method

In this section, we present the Multi-scale improved NLO (MiNLO) method focusing on its implementation at LO and then at NLO accuracy. The MiNLO method was first proposed in Ref. [138] and builds upon the CKKW procedure introduced in Refs. [497, 498]. The core idea of the method is to reduce the ambiguity in finding the optimal scale choice for performing calculations in perturbative QCD. Indeed, choosing appropriate renormalization and factorization scales is not always a trivial task, especially for processes where various scales are involved. This is very typical of fixed-order calculations with many external particles, in which the involvement of multiple hard partons introduces several kinematic scales, making the choice of renormalization and factorization scales more ambiguous. Although MiNLO was originally proposed as a framework for NLO calculations matched to parton-shower algorithms, it has also been employed in purely fixed-order calculations without the inclusion of a parton shower, see Ref. [126] for the $pp \to t\bar{t}$ + jets processes. One of the main objectives of this thesis is to apply and study the effect of the MiNLO method also in full off-shell calculations. This is done in Chapter 6, where MiNLO is applied to the fully off-shell $pp \to e^+\nu_e\,\mu^-\bar{\nu}_\mu\,\tau^+\nu_\tau\,b\bar{b}$ + jets processes. To address the ambiguity previously mentioned regarding the selection of optimal scales in perturbative calculations, the MiNLO framework establishes suitable scales for the strong coupling constants α_s associated with extra emissions based on the most likely branching history. This is achieved by recursively applying an inverse k_T-clustering algorithm [499] to identify the most likely sequence of branchings leading to a given assembly of particles that define the core process. At each clustering step, when two partons are combined, a pseudoparton is formed to represent the intermediate state. The scales for the α_s couplings are then set equal to the k_T measure obtained at each step of the clustering algorithm. This approach has the advantage of determining the scales that enter the calculation from the kinematics of the branchings, rather than relying on arbitrary user-defined scales. Furthermore, soft and collinear logarithms associated with the presence of large ratios of scales are also resummed in the MiNLO framework via appropriate Sudakov form factors that enter the calculation. These Sudakov form factors can be interpreted as no emission probabilities between two given scales, and they are incorporated in both external and intermediate lines, effectively resumming large logarithms emerging from events characterized by widely separated scales. In the following sections, the MiNLO method is discussed in greater detail, starting from its LO implementation and then proceeding to the NLO one. It has been fully integrated into the HELAC-NLO

framework [388] and can be applied generically to any process by straightforward reweighting facilitated by the HEPLOT program [442].

5.1 Implementation of MiNLO at LO - MiLO

Suppose that we are considering the following process:

$$pp \to X + \{N\}\,, \tag{5.1}$$

where X defines the core system and $\{N\}$ represents all the extra QCD partons with respect to it. We also define N as the number of additional α_s couplings beyond those of the core. Equivalently, N corresponds to the number of extra jets emitted relative to X. The goal is to dynamically extract all scales q_i, referred to as *nodal* scales, with $i = 1, ..., n$ and $n \leq N$, based on the most likely branching history via an inverse k_T-clustering algorithm. The reason why n is not necessarily equal to N is associated with the requirement of ordered clusterings to be discussed later. These nodal scales will serve as the arguments of the n additional powers of the strong coupling constants, while the remaining m powers of α_s will be associated with a core scale q_{core} which is user-defined and generally depends on the kinematics of X. The algorithm starts by recursively clustering back the $X + N$ parton event until one arrives at the primary system $pp \to X$. For each final-final (FF) branching, we consider:

$$d_{ij} = \frac{\min(p_{T,i}^2, p_{T,j}^2)\Delta R_{ij}^2}{R^2}\,, \tag{5.2}$$

while for final-initial (FI) we take:

$$d_i = p_{T,i}^2\,. \tag{5.3}$$

In the expressions above, the indices i, j represent the QCD partons that participate in the branching, and R is a freely adjustable resolution parameter. In the FI case, $p_{T,i}$ corresponds to the transverse momenta of the final-state parton. We note here that a branching is allowed only if it is compatible in flavor, which in practice implies that only the following QCD branchings are considered:

$$\text{FF:} \quad gg \to g, \quad gq \to q, \quad g\bar{q} \to \bar{q}, \quad q\bar{q} \to g \tag{5.4}$$

$$\text{FI:} \quad gg \to g, \quad gq \to q, \quad qg \to \bar{q}, \quad qq \to g \tag{5.5}$$

$$\text{FI:} \quad g\bar{q} \to \bar{q}, \quad \bar{q}g \to q, \quad \bar{q}\bar{q} \to g\,, \tag{5.6}$$

where $q = u, c, d, s, b$. Examples of such branchings are depicted in Fig. 5.1. From Eq. (5.3), it becomes clear that an ambiguity arises whenever a final-state parton can be clustered with both initial-state partons. In this case, the d_i measure would be the same regardless of the flavor and kinematics of the incoming beams. To resolve this issue, we allow clusterings with initial partons only if the final-state parton is produced in the same direction as the incoming one in the center-of-mass (CM) frame of the colliding beams. By doing so, for wide-angle emissions in the opposite direction of the incoming beam the clustering is not considered, thereby favoring the QCD emissions in the same direction. For more details on that topic, see Sec. 5.5.1. Among all possible clusterings, the one with the minimum $\min(\{d_{ij}\}, \{d_i\})$ value is performed. The pseudoparton $\tilde{ij}$ is then constructed with momentum $p_{\tilde{ij}} = p_i + p_j$

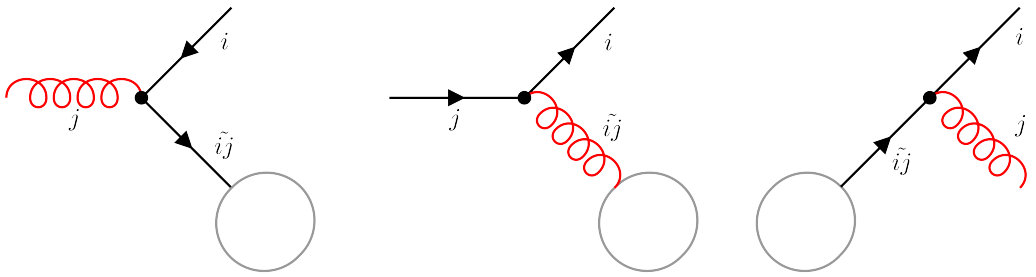

Figure 5.1: *Examples of FI (first two) and FF (third) $i+j \to \tilde{ij}$ branchings. The $\tilde{ij}$ represents the pseudoparton created after clustering the partons i and j. Quarks are depicted with black lines, gluons with red curly lines, and the grey blobs represent the rest of the process, capturing also the core interaction. The graphs were generated with the help of the FeynGame package [421–423].*

for FF branchings and $p_{\tilde{ij}} = p_i - p_j$ for FI branchings. The branching is subsequently associated with the following nodal scale:

$$q_k = \sqrt{\min(\{d_{ij}^{(k)}\}, \{d_i^{(k)}\})}\,, \tag{5.7}$$

where $d_{ij}^{(k)}$ and $d_i^{(k)}$ are the distance measures in the k-th clustering. Then, the resulting $\tilde{ij}$ pseudoparton participates in the next step of the algorithm, where a new pseudoparton is formed. The above procedure is iterated until no extra branching is available and the core process is reached. If at some point in the algorithm there is no available clustering to be performed, or the following condition is not fulfilled:

$$q_{k+1} > q_k\,, \tag{5.8}$$

we terminate the algorithm and all remaining partons are considered part of the core process. In this case, the core scale q_{core} needs to be reevaluated to account for the extra remaining partons that are now considered part of the primary system. This implies that only *ordered* clusterings are permitted, ensuring that at each step, the nodal scale q_{k+1} is greater than the previous one q_k. When the core process is reached, we additionally require the last nodal scale to be smaller than the core scale. If this is not true, the core scale is set equal to the last (largest) nodal scale, in line with the original proposal of Ref. [138]. In the end, we will end up with $n \leq N$ nodal scales that fulfill the following condition:

$$q_1 < \ldots < q_n \leq q_{core}\,. \tag{5.9}$$

The above ordering of clusterings is necessary because only ordered emissions can be consistently resummed with Sudakov form factors. Let us stress here that if $n = N$ all clusterings are ordered, while whenever n is smaller than N, an unordered clustering has taken place. More technical details about the treatment of unordered clusterings, also at the NLO case, are discussed in Sec. 5.5.2.

After extracting all nodal scales, the product of the strong α_s couplings in the matrix element has the following form:

$$[\alpha_s(q_{core})]^m \times \prod_{i=1}^{n} \alpha_s(q_i)\,, \tag{5.10}$$

where m represents the powers of α_s associated with the primary system. We emphasize here that when applying scale variation, this expression changes based on what is described in Sec. 5.3, where two alternative ways to perform scale variation are discussed.

Moving on, the entire calculation is dressed with appropriate Sudakov form factors. To understand how these factors are determined, we highlight that, beyond identifying the nodal scales q_i, we also retain the full branching history of the event. This includes information on all clustering steps, the particles involved in each branching, and the resulting pseudopartons. With this information, we construct the *skeleton* of the event, which consists of both external and internal lines, all ultimately connected to the core process. Following the prescription introduced in Ref. [126], for each external QCD parton connected with the scale q_j, we apply the following Sudakov form factor:

$$\Delta_{f_j}^{\text{ext}}(q_{res}^2; q_j^2) = \frac{\Delta_{f_j}(q_{res}^2, q_j^2)}{\Delta_{f_j}(q_{res}^2, q_1^2)}\,, \tag{5.11}$$

where f_j represents the flavor of the particle connected to the q_j scale and the resolution scale q_{res} is defined by:

$$q_{res} = \begin{cases} q_1, & \text{if the line is final} \\ \xi_F q_1, & \text{if the line is initial} \end{cases} \tag{5.12}$$

In the above equation, ξ_F represents the factorization scale-variation factor used in scale variation. For the central setup, we set $\xi_F = 1$. For internal lines that connect two successive branchings q_i and q_j, the following Sudakov form factor is applied:

$$\Delta_{f_{ij}}^{\text{int}}(q_{res}^2; q_i^2, q_j^2) = \frac{\Delta_{f_{ij}}(q_{res}^2, q_j^2)}{\Delta_{f_{ij}}(q_{res}^2, q_i^2)}\,, \tag{5.13}$$

where f_{ij} is the flavor of the internal line, and we have assumed that $q_j > q_i$. As explained in Ref. [126], the resolution scale q_{res} is varied according to Eq. (5.12) in order to match the PDF evolution up to the factorization scale, which we always set to $\mu_F = \xi_F q_1$. On the one hand, the q_1 scale can be thought of as the scale above which emissions are described by the matrix element, and below which any radiation is considered unresolved. On the other hand, varying this scale under factorization scale variation breaks its interpretation as the resolution scale of the process. One can therefore keep the q_1 scale fixed in the Sudakov form factors even under ξ_F variation or vary it according to Eq. (5.12). Although the latter approach comprises our default setup, the former case, originally proposed in the MiNLO paper [138], has also been implemented into our code and we refer to it as $\texttt{Mi(N)LO}_{\text{no}\xi_\text{F}}$. In our default setup, QCD radiation is resummed over the whole $(\xi_F q_1, q_{core})$ range with the help of Sudakov form factors, while any QCD emission below $\xi_F q_1$ is absorbed in the PDFs. The effects of using the $\texttt{MiNLO}_{\text{no}\xi_\text{F}}$ as an alternative approach are examined in this thesis and considered part of the systematic uncertainties.

The form of the Sudakov form factor that has been used in our implementation

follows Refs. [126, 500, 501]:

$$\Delta_f(t_0,t_1) = \exp\left\{-\int_{t_0}^{t_1} dt \frac{\alpha_s(t)}{2\pi t} \sum_{a=q,g} \int_0^{1-\sqrt{t/t_1}} dz \left(z P_{af}(z) + \delta_{af} \frac{2C_f}{1-z} \Lambda_2(t) \right) \right\}, \tag{5.14}$$

where f represents the flavor of the parton, $P_{af}(z)$ are the $f \to ab$ DGLAP splitting functions [390, 395, 396], $C_f = C_A$ for gluons and $C_f = C_F$ for quarks and $\Lambda_2(t)$ corresponds to the two-loop correction to the DGLAP splitting functions [502]. Its explicit form is given by:

$$\Lambda_2(t) = \frac{\alpha_s(t)}{2\pi} \left[\left(\frac{67}{18} - \frac{\pi^2}{6} \right) C_A - \frac{10}{9} T_R N_f(t) \right], \tag{5.15}$$

where $N_f(t)$ represents the number of active flavors at the scale t. In particular, for $t > m_t^2$ we consider 6 active flavors while for $t < m_t^2$ we set $N_f = 5$. The above definition of the Sudakov form factor respects unitarity, namely, it is interpreted as the probability of not emitting any resolved radiation between scales t_0 and t_1 and thus can not exceed unity. Also, it provides a next-to-leading-log (NLL) resummation of large double and single logarithms associated with soft, collinear and hard-collinear emissions. The exact formulas of the Sudakov form factors together with the differences compared to the Sudakov form factors used in the original MiNLO paper [138] are discussed in Sec. 5.4.

To summarize, after applying the MiLO method, the matrix element has the following form:

$$|\mathcal{M}_{\texttt{MiLO}}|^2 = |\mathcal{M}(\{q_i\}, q_{core}, \xi_R, \xi_F)|^2 \times \prod_i \Delta_{f_i}^{\text{ext}}(q_{res}^2; q_i^2) \times \prod_{ij} \Delta_{f_{ij}}^{\text{int}}(q_{res}^2; q_i^2, q_j^2)\,. \tag{5.16}$$

From the above expression, it is clear that the matrix element depends on the nodal scales $\{q_i\}$ determined from the inverse k_T-clustering algorithm, the user-defined q_{core} scale and the ξ_R, ξ_F factors used for scale variation. For the central setup, the α_s weight is explicitly given by Eq. (5.10). We also point out that the factorization scale is set equal to the smallest nodal scale, that is:

$$\mu_F = \xi_F q_1\,, \tag{5.17}$$

where the factorization scale factor is also included. For details on how scale variation is performed, the reader is referred to Sec. 5.3. Each event is further supplemented with Sudakov form factors applied to both internal and external lines. While these Sudakov factors remain unaffected for final-state lines under scale variation, they do exhibit a dependence on the factorization scale in the case of initial-state lines encoded in q_{res}, as defined in Eq. (5.12).

5.2 Implementation of MiNLO at NLO - MiNLO

The extension of the algorithm from LO to NLO is rather straightforward. In an NLO calculation, the cross section is given by the following formula:

$$\begin{aligned}\sigma^{\mathrm{NLO}} = &\int d\Phi_B \left[\mathcal{B}(\Phi_B;\mu_F,\mu_R) + \mathcal{V}(\Phi_B;\mu_F,\mu_R) + \mathcal{I}^{(S)}(\Phi_B;\mu_F,\mu_R)\right] \\ &+ \int d\Phi_R \left[\mathcal{R}(\Phi_R;\mu_F,\mu_R) - \mathcal{S}(\Phi_R;\mu_F,\mu_R)\right] ,\end{aligned} \tag{5.18}$$

where $\mathcal{B}$ stands for the Born contribution, $\mathcal{V}$ represents the virtual term and $\mathcal{R}$ denotes the real emission contribution. The $\mathcal{S}$ term accounts for the subtracted term that regulates the soft and collinear divergences, and $\mathcal{I}^{(S)}$ represents the integrated subtraction terms, which cancel the corresponding divergences in the virtual part. In the MiNLO method, all terms that live in the Born phase-space Φ_B, are treated in the same manner as the $\mathcal{B}$ term. Here we focus on the real emission contribution $\mathcal{R}$ that resides in the Φ_R phase-space comprising one extra parton at NLO. Let q_0 denote the first nodal scale obtained from the inverse k_T-clustering algorithm. Then, the following condition needs to be fulfilled:

$$q_0 < q_1 \, . \tag{5.19}$$

If this condition fails, the algorithm terminates, and the core scale q_{core} is used as the argument for all powers of the strong coupling α_s in the process. In this case, the kinematics of the real radiation are absorbed into the Born system and the core scale is then evaluated based on those kinematics. We stress here that the above condition is consistent with our requirement for ordered branchings given in Eq. (5.9), which is now extended to:

$$q_0 < q_1 < ... < q_n \leq q_{core} \, . \tag{5.20}$$

Once an ordered branching history satisfying Eq. (5.20) is constructed, the nodal scale q_0 is removed from the $\{q_i\}$ list, yielding a Born-like configuration. This is done to ensure proper cancellation of the infrared poles, as this clustering corresponds to the softest and thus potentially unresolved real radiation not present in the virtual part. As a result, q_0 does not contribute to the calculation, neither as an argument of the strong α_s coupling nor in the Sudakov form factors. The factorization scale is thus the same as in the MiLO case, namely $\mu_F = \xi_F q_1$. For the additional power of the strong coupling $\alpha_s^{(n+m+1)}$ appearing at NLO, two alternative prescriptions have been implemented into our code. This choice is formally a higher-order effect and does not spoil the NLO accuracy of the computation. Further details, including the choice of renormalization scale and the procedure for scale variation, are discussed in Sec. 5.3.

Another special care that must be taken in the NLO extension of the MiLO method concerns the absence of double-counting of terms. Indeed, Sudakov form factors incorporated into the Born term $\mathcal{B}$ effectively account for higher-order QCD corrections by representing the probability of no resolvable emission occurring between two energy scales. This becomes evident when expanding Eq. (5.14) in powers of the strong coupling constant α_s. However, some of these higher-order effects are already included in the one-loop corrections in the $\mathcal{V}$ term and in the unresolved

emission contributions $\mathcal{R}$. Therefore, to prevent double-counting, it is essential to properly subtract the overlapping contributions. This is achieved by applying the following replacement in the born term:

$$\begin{aligned}\mathcal{B} \to \mathcal{B} \times \Bigg(1 - \sum_i \left[\Delta^{(1)}_{f_i}(q^2_{res}, q^2_i) - \Delta^{(1)}_{f_i}(q^2_{res}, q^2_1)\right] \\ - \sum_{ij} \left[\Delta^{(1)}_{f_{ij}}(q^2_{res}, q^2_i) - \Delta^{(1)}_{f_{ij}}(q^2_{res}, q^2_j)\right]\Bigg),\end{aligned} \tag{5.21}$$

where the index i runs over all external lines associated with the nodal scales q_i, and the index ij runs over internal lines connecting nodes with scales q_i and q_j such that $q_i > q_j$. The $\Delta^{(1)}$ terms represent the first non-trivial contributions in the α_s expansion of the Sudakov form factor, thereby accounting for the NLO terms. The strong coupling encoded in these factors is the same as the $\alpha_s^{(n+m+1)}$ value used for the NLO calculation, see Sec. 5.3 for more details.

5.3 Scale variation

We have implemented two distinct methods to estimate the size of scale uncertainties:

- The first follows the original `MiNLO` prescription [138] and comprises our default setup. In this approach, all nodal scales q_i and the core scale q_{core} are uniformly rescaled via

$$q_i \to \xi_R q_i \quad \text{and} \quad q_{core} \to \xi_R q_{core}\,, \tag{5.22}$$

  where ξ_R is the renormalization scale-variation factor. In regions of the calculation with explicit dependence on the renormalization scale, μ_R is calculated according to:

$$\mu_R = \left((\xi_R q_{core})^m \times \prod_{i=1}^{n} (\xi_R q_i)\right)^{\frac{1}{m+n}}, \tag{5.23}$$

  where m defines the number of α_s couplings associated with the primary system and n is the number of nodal scales. The above geometric mean of scales ensures that, even when multiple q_i scales are involved, changing the renormalization scale in an NLO calculation is a higher-order effect. The additional power of α_s at NLO is given by the following arithmetic mean:

$$\alpha_s^{(n+m+1)} = \frac{1}{n+m}\left(\sum_{i=1}^{n} \alpha_s(\xi_R q_i) + m\alpha_s(\xi_R q_{core})\right). \tag{5.24}$$

- The second method follows the approach outlined in Refs. [126, 501] and we refer to it as $\texttt{MiNLO}_{\text{var}_2}$. In this case, an effective scale q_{eff} is determined from:

$$\alpha_s(q_{eff}) = \left([\alpha_s(q_{core})]^m \times \prod_{i=1}^{n} \alpha_s(q_i)\right)^{\frac{1}{m+n}}, \tag{5.25}$$

  and the renormalization scale is then set to

$$\mu_R = \xi_R q_{eff}\,. \tag{5.26}$$

For the extra α_s factor at NLO, the obtained renormalization scale is used and thus:

$$\alpha_s^{(n+m+1)} = \alpha_s(\mu_R)\,. \tag{5.27}$$

For the sake of completeness, we stress that, for both approaches, we set $\mu_F = \xi_F q_1$ and Sudakov form factors are varied only under factorization-scale variation according to Eq. (5.11), (5.12), (5.13). However, as already discussed in Sec. 5.1, an alternative approach labeled as $\texttt{MiNLO}_{\text{no}\xi_\text{F}}$, where no ξ_F variation is applied in the Sudakov form factors, is also examined throughout this thesis.

5.4 Sudakov form factors

In this section, we discuss the main steps leading to the derivation of the Sudakov form factor in Eq. (5.14), highlighting the differences with the form used in the original MiNLO paper [138]. We closely follow Ref. [501], from which the explicit expressions for the Sudakov form factors employed in our implementation are taken. As discussed in Chapter 2, in particular in Eq. (2.14), the Sudakov form factors for quarks and gluons are given by

$$\Delta_q(t_0,t_1) = \exp\left\{-\int_{t_0}^{t_1}\frac{dt}{t}\frac{\alpha_s(t)}{2\pi}\int_\delta^{1-\delta} dz\; P_{qq}(z)\right\}, \tag{5.28}$$

$$\Delta_g(t_0,t_1) = \exp\left\{-\int_{t_0}^{t_1}\frac{dt}{t}\frac{\alpha_s(t)}{2\pi}\int_\delta^{1-\delta} dz\;\left[\frac{1}{2}P_{gg}(z) + N_f(t)P_{qg}(z)\right]\right\}, \tag{5.29}$$

where δ is the infrared regulator and q denotes all possible quark flavors from the $g \to q\bar{q}$ splitting. The gluon Sudakov form factor receives contributions from both $g \to gg$ and $g \to q\bar{q}$ splittings, resulting in the appearance of both P_{gg} and P_{qg} splitting functions in its definition. Note also that the factor of $1/2$ multiplying P_{gg} [500] accounts for the presence of identical gluons in the final state and avoids double-counting. From the splitting functions given in Eq. (2.3), we note that, for the unregularized kernels within the integration domain $z \in [\delta, 1-\delta]$, the following identity holds:

$$P_{qq}(z) = zP_{qq}(z) + (1-z)P_{gq}(1-z)\,. \tag{5.30}$$

Using this relation, one obtains:

$$\begin{aligned}\Gamma_{qq}(\delta) &= \int_\delta^{1-\delta} dz\, P_{qq}(z) = \int_\delta^{1-\delta} dz\;\left(z\,P_{qq}(z) + (1-z)P_{gq}(1-z)\right)\\ &= \int_\delta^{1-\delta} dz\, z\left(P_{qq}(z) + P_{gq}(z)\right),\end{aligned} \tag{5.31}$$

where, in the last step, we performed the variable change $z' = 1-z$ on the second part of the integration. Similarly, for the gluon case:

$$\begin{aligned}\Gamma_{gg}(\delta) &= \int_\delta^{1-\delta} dz\;\left[\frac{1}{2}P_{gg}(z) + N_f(t)P_{qg}(z)\right]\\ &= \int_\delta^{1-\delta} dz\left\{\frac{1}{2}\left[zP_{gg}(z) + (1-z)P_{gg}(1-z)\right]\right.\\ &\qquad\left. + N_f(t)\left[zP_{qg}(z) + (1-z)P_{qg}(1-z)\right]\right\},\end{aligned} \tag{5.32}$$

where we have also employed the symmetry of the LO splitting functions: $P_{gg}(z) = P_{gg}(1-z)$ and $P_{qg}(z) = P_{qg}(1-z)$. The above equation is then further simplified to:

$$\Gamma_{gg}(\delta) = \int_{\delta}^{1-\delta} dz\, z \left(P_{gg}(z) + \sum_{q} P_{qg}(z) \right) , \tag{5.33}$$

where the sum runs over all quark and antiquark active flavors. Putting everything together, we can write down a unified form of the Sudakov form factor for quarks and gluons:

$$\Delta_f(t_0, t_1) = \exp\left\{ - \int_{t_0}^{t_1} dt \frac{\alpha_s(t)}{2\pi t} \sum_{a=q,g} \int_{\delta}^{1-\delta} dz\, z\, P_{af}(z) \right\} , \quad f = q, g\,. \tag{5.34}$$

Adding two-loop corrections to the DGLAP splitting functions [502], the above formula is then extended to:

$$\Delta_f(t_0, t_1) = \exp\left\{ - \int_{t_0}^{t_1} dt \frac{\alpha_s(t)}{2\pi t} \sum_{a=q,g} \int_{\delta}^{1-\delta} dz \left(z\, P_{af}(z) + \delta_{af} \frac{2C_f}{1-z} \Lambda_2(t) \right) \right\} , \tag{5.35}$$

where $C_f = C_A, C_F$ for gluons and quarks, respectively, and $\Lambda_2(t)$ is given by Eq. (5.15). For the infrared regulator, we adopt $\delta = \sqrt{t/t_1}$, a choice naturally motivated by the kinematics of the branching, in line with Refs. [126, 500]. Notice that the Sudakov form factor as defined above is not guaranteed to be smaller than unity. In fact, if $\delta > 1/2$, or equivalently $t > t_1/4$, the integral becomes negative, which could result in a Sudakov form factor exceeding 1. This can be avoided by setting the lower limit of the z integration to 0 while retaining $1 - \sqrt{t/t_1}$ as the upper bound. The resulting difference with respect to the full result is then of order $\mathcal{O}(\delta) = \mathcal{O}(\sqrt{t/t_1})$. By doing this, we recover the final formula used in our implementation as given in Eq. (5.14). This formula is further simplified upon integrating over z, yielding:

$$\Delta_q(t_0, t_1) = \exp\left\{ - \int_{t_0}^{t_1} \frac{dt}{t} \frac{\alpha_s(t)}{2\pi} \tilde{\Gamma}_{qq}\left(\sqrt{\frac{t}{t_1}} \right) \right\} , \tag{5.36}$$

$$\Delta_g(t_0, t_1) = \exp\left\{ - \int_{t_0}^{t_1} \frac{dt}{t} \frac{\alpha_s(t)}{2\pi} \left[\tilde{\Gamma}_{gg}\left(\sqrt{\frac{t}{t_1}} \right) + N_f(t) \tilde{\Gamma}_{qg}\left(\sqrt{\frac{t}{t_1}} \right) \right] \right\} , \tag{5.37}$$

where $N_f(t)$ is the number of active quark flavors at the energy scale t, and the $\tilde{\Gamma}$ functions are given by the formulas below:

$$\tilde{\Gamma}_{gg}(\delta) = C_A \left[-2(\Lambda_2 + 1) \log\delta - \frac{1}{6}(1-\delta)^2 (11 - (2 - 3\delta)\delta) \right] , \tag{5.38}$$

$$\tilde{\Gamma}_{qq}(\delta) = C_F \left[-2(\Lambda_2 + 1) \log\delta - \frac{3}{2}(1-\delta)^2 \right] , \tag{5.39}$$

$$\tilde{\Gamma}_{qg}(\delta) = \frac{1}{3} T_R (1-\delta)^2 (3\delta^2 + 2(1-\delta))\,. \tag{5.40}$$

These expressions correspond to the Sudakov form factors implemented in our code and are evaluated numerically using the method of Gauss-Legendre quadrature. Sudakov form factors for massive quarks have also been implemented into our code. These become relevant when massive quarks participate in $f \to ab$ splittings, for

instance, when certain quarks are treated as massive or when the energy scale t is sufficiently large to allow for $g \to t\bar{t}$ splittings. The explicit formulas used in our implementation can be found in Ref. [501].

We now rewrite Eqs. (5.36) and (5.37) in a form analogous to the Sudakov form factor presented in the original MiNLO paper [138], making its NLL structure explicit:

$$\Delta_f(t_0, t_1) = \exp\left\{ -\int_{t_0}^{t_1} \frac{dt}{t} \left[A_f(\alpha_s(t)) \log \frac{t_1}{t} + B_f(\alpha_s(t)) + \mathcal{O}\left(\sqrt{\frac{t}{t_1}}\right) \right] \right\} , \quad (5.41)$$

where:

$$A_f = \sum_{i=1}^{\infty} A_{i,f} \alpha_s^i \quad \text{and} \quad B_f = \sum_{i=1}^{\infty} B_{i,f} \alpha_s^i , \quad (5.42)$$

and, in our implementation, only the coefficients $A_{1,f}$, $A_{2,f}$, and $B_{1,f}$ are retained. Their explicit expressions are given below:

$$\begin{aligned}
A_{1,g} &= \frac{C_A}{2\pi} , & A_{2,g} &= \frac{C_A}{4\pi^2} \left[\left(\frac{67}{18} - \frac{\pi^2}{6} \right) C_A - \frac{10}{9} T_R N_f(t) \right] , \\
A_{1,q} &= \frac{C_F}{2\pi} , & A_{2,q} &= \frac{C_F}{4\pi^2} \left[\left(\frac{67}{18} - \frac{\pi^2}{6} \right) C_A - \frac{10}{9} T_R N_f(t) \right] , \\
B_{1,g} &= -\frac{11 C_A - 4 T_R N_f(t)}{12\pi} , & B_{1,q} &= -\frac{3}{4\pi} C_F .
\end{aligned} \quad (5.43)$$

Eq. (5.41) is identical to the Sudakov form factor used in the MiNLO method [138,416] up to power corrections of $\mathcal{O}(\sqrt{t/t_1})$. The effect of these power corrections is studied in Section 6.3. Writing the Sudakov form factor in the form of Eq. (5.41) makes its NLL accuracy manifest. The leading logarithmic contributions are generated by the $A_{1,f}$ term, including the effects of the running coupling, giving rise to terms of the form $\alpha_s^n L^{n+1}$, where $L = \log(t_1/t_0)$. The inclusion of $A_{2,f}$ and $B_{1,f}$ ensures next-to-leading logarithmic accuracy, corresponding to contributions of order $\alpha_s^n L^n$.

Finally, we comment on the definitions of the Sudakov form factors for internal and external lines given in Eqs. (5.11) and (5.13). In particular, we emphasize that defining these Sudakov factors naively, i.e. without introducing the ratios appearing in those equations, would spoil their probabilistic interpretation. This is because in Eqs. (5.36) and (5.37), the integrated functions $\tilde{\Gamma}$ in the exponents depend explicitly on the upper integration limit t_1. By defining the Sudakov form factors in the ratio form of Eqs. (5.11) and (5.13), one ensures that for three successive branchings $t_1 < t_2 < t_3$ the identity

$$\Delta_f^{\text{int/ext}}(t_1, t_3) = \Delta_f^{\text{int/ext}}(t_1, t_2)\, \Delta_f^{\text{int/ext}}(t_2, t_3) \quad (5.44)$$

holds. This expresses that the probability of no resolvable emission between scales t_1 and t_3 equals the product of the no-emission probabilities between t_1 and t_2 and between t_2 and t_3. If, instead, internal and external Sudakov form factors were defined without these ratios, it is straightforward to show that the above property would no longer hold.

5.5 Additional notes on the implementation

The implementation of the MiNLO method into our code is described in Sec. 5.1, 5.2. In this section, we focus on the more technical aspects of the implementation,

describing in more detail how we treat clusterings with initial-state partons as well as unordered branchings. Further details on how the MiNLO method can be enabled in the reweighting part of the code, as well as the cross-checks performed to validate our implementation, can be found in Appendices A.1 and A.2.

5.5.1 Clusterings with initial-state partons

By labeling a final-state particle with f and an initial-state one with i, in our implementation, which is aligned to what has been implemented in the SHERPA code [410–413], clusterings with initial-state partons are allowed if and only if:

$$\begin{aligned} y_f > 0 \quad &\text{and} \quad p_{i,z} > 0 \\ &\text{or} \\ y_f < 0 \quad &\text{and} \quad p_{i,z} < 0 \,, \end{aligned} \tag{5.45}$$

where y_f denotes the rapidity of the final-state parton. To check if the above condition is fulfilled, we first boost the system of particles in the CM frame of the incoming beams and then rotate the system such that the initial-state partons only acquire momenta in the z axis. In general, this condition resolves the ambiguity whenever an outgoing parton could be clustered with both initial-state partons. The condition (5.45) is equivalent to what has been described in Ref. [501], where, to resolve the ambiguity, the clustering that minimizes the invariant mass of the system is performed. However, in our implementation, the condition (5.45) must always be fulfilled even in cases where only one clustering with an initial-state parton is available. In practice, this means that a wide-angle emission in the opposite direction of the incoming beam is considered unlikely, and alternative clusterings are considered in this case.

Another thing that should be noted is that the boost to the CM frame of the initial-state partons is only temporarily performed just to check if the condition (5.45) is met. In general, if a final-state parton is clustered with an initial-state one, the new pair of incoming partons will no longer be in their CM frame. In our implementation, the inverse k_T-algorithm continues by considering the p_T of the partons in the original event, that is, without performing any boost to the CM frame of the two initial-state partons.

5.5.2 Unordered clusterings

We adopt the original MiNLO proposal [138] regarding the treatment of unordered branchings. This means that if at any point q_{i+1} is smaller than q_i, the particles that participated in the $(i+1)$-th clustering will be considered part of the core process and the clustering will be undone. After that, the condition $q_i < q_{core}$ also needs to be checked. If this is satisfied, q_{core} is evaluated based on the kinematics of the particles in the core process. If it is not fulfilled, we set the core scale equal to the largest nodal scale, that is $q_{core} = q_i$, and the algorithm terminates. The same logic is adopted if the last nodal scale q_n is larger than q_{core}, by forcing $q_{core} = q_n$. Another important point concerns the treatment of an unordered clustering when applying the MiNLO method to a process that is already a core process, for example, applying MiNLO to a $t\bar{t}$ sample. In such cases, it may occur that the clustering scale from the real emission, q_0, exceeds the core scale, i.e., $q_0 > q_{core}$. Since q_0 is not

included among the nodal scales, we choose not to set $q_{core} = q_0$. Instead, q_{core} is determined based solely on the kinematics of the core-process particles, after absorbing the kinematics of the real emission into the primary system. The above description comprises our default setup.

Chapter 6

MiNLO predictions for $pp \to t\bar{t}W^+ +$ jets in QCD

In this chapter, we apply the MiNLO method to the fully off-shell $pp \to t\bar{t}W^+$ process in association with up to two jets in the multilepton channel. Our objective is to estimate, for the first time, the effect of the MiNLO method on a fully off-shell sample and to study the sensitivity of the results to the choice of renormalization and factorization scales. As the inclusion of additional jets is crucial for accurately describing the dynamics of the fully off-shell $pp \to t\bar{t}W^+$ process, the application of the MiNLO method allows us to improve our understanding of $t\bar{t}W^+$ dynamics by dynamically determining the scales associated with the extra jets through the reconstruction of the most probable sequence of parton branchings. We further aim to demonstrate the level of agreement between standard NLO and MiNLO both at the integrated and differential cross-section levels. Special emphasis is also given in the study of the systematic uncertainties, which involves using the $\text{MiNLO}_{\text{no}\xi_{\text{F}}}$ setup as outlined in Sec. 5.1 rather than the default MiNLO implementation, as well as employing two distinct ways to estimate the magnitude of the scale uncertainties, as discussed in Sec. 5.3. In addition, we investigate the impact of the resolution parameter R in the inverse k_T-clustering algorithm of Eq. (5.2), by providing results for different values of R. Finally, to improve the full off-shell predictions for the $pp \to t\bar{t}W^+ + X$ process, we present merged results where the fully off-shell $pp \to t\bar{t}W^+ + X$, $pp \to t\bar{t}W^+j + X$ and $pp \to t\bar{t}W^+jj$ processes are properly combined after introducing an appropriate merging scale. To avoid confusion, we emphasize that merged predictions using the MiNLO method available in the literature do not require the introduction of any merging scale, see e.g. Refs. [416, 503]. In these studies, the MiNLO method is applied alongside the POWHEG framework [75–77] for matching to parton-shower algorithms, primarily for simple color-singlet processes whose resummation structure is sufficiently well understood. Then, after appropriately setting the scale choice for the additional α_s coupling at NLO and properly modifying the Sudakov form factors, NLO accuracy is maintained in observables both exclusive and inclusive over the extra QCD radiation. In our case, however, we consider fixed-order, full off-shell predictions with fiducial phase-space cuts also applied to the light jets. While, in principle, the underlying idea of the aforementioned approach could be adopted by avoiding cuts on the additional light jets, its consistent implementation in this setup would require a dedicated treatment and comparison with resummation formulas that are not yet fully known for processes of this complexity.

The structure of this chapter is as follows: In Sec. 6.1, we briefly provide an overview of the computational setup used for performing all the calculations. Sec. 6.2 presents a comparison between standard NLO and MiNLO at the integrated fiducial cross-section level for the $pp \to t\bar{t}W^+ + \{0, 1, 2\}$ jets processes. This section also addresses the impact of systematic uncertainties associated with the MiNLO framework, as previously mentioned. In Sec. 6.3 we assess the effect of employing the original MiNLO Sudakov form factors [138] instead of our default ones. Predictions at the differential cross-section level are discussed in Sec. 6.4. Lastly, the merged predictions and the comparison with the fully off-shell NLO $pp \to t\bar{t}W^+ + X$ sample are presented in Sec. 6.5.

6.1 Description of the calculation and computational setup

We compare the standard NLO and MiNLO methods for the $pp \to e^+\nu_e\,\mu^-\bar{\nu}_\mu\,\tau^+\nu_\tau\,b\bar{b} + X$ process in association with up to two jets at the LHC with a center-of-mass energy of $\sqrt{s} = 13\,\text{TeV}$. For simplicity, we refer to these multi-lepton final-state processes as $pp \to t\bar{t}W^+ + X$, $pp \to t\bar{t}W^+j + X$ and $pp \to t\bar{t}W^+jj$, indicating the presence of (at least) zero, one and two extra jets in the final state, respectively. Results are presented at both LO and NLO accuracy in perturbative QCD. The corresponding perturbative orders are $\mathcal{O}(\alpha_s^2\alpha^6)$ at LO and $\mathcal{O}(\alpha_s^3\alpha^6)$ at NLO for the $pp \to t\bar{t}W^+ + X$ process, and $\mathcal{O}(\alpha_s^3\alpha^6)$ at LO and $\mathcal{O}(\alpha_s^4\alpha^6)$ at NLO for $pp \to t\bar{t}W^+j + X$. For the $pp \to t\bar{t}W^+jj$ process, results are provided only at LO accuracy ($\mathcal{O}(\alpha_s^4\alpha^6)$) due to the considerable complexity of computing NLO corrections with full off-shell effects for a final state containing up to eleven particles (including the real radiation). For all these processes, the core system in the MiNLO method comprises the decay products of the $pp \to t\bar{t}W^+$ system, namely $e^+\nu_e\,\mu^-\bar{\nu}_\mu\,\tau^+\nu_\tau\,b\bar{b}$. For performing the computations, we adopt the numerical SM input parameters from Ref. [337]:

$$\begin{aligned}
&G_\mu = 1.166378 \times 10^{-5}\ \text{GeV}^{-2}, && m_t = 172.5\ \text{GeV},\\
&m_W = 80.379\ \text{GeV}, && \Gamma_W^{\text{NLO}} = 2.0972\ \text{GeV},\\
&m_Z = 91.1876\ \text{GeV}, && \Gamma_Z^{\text{NLO}} = 2.5074\ \text{GeV},\\
&\Gamma_{t,\,\text{off-shell}}^{\text{LO}} = 1.45766\ \text{GeV}, && \Gamma_{t,\,\text{off-shell}}^{\text{NLO}} = 1.33254\ \text{GeV},
\end{aligned} \tag{6.1}$$

and employ the (N)LO NNPDF3.1 [474] PDF set for the (N)LO calculations. As the primary focus is on the impact of the MiNLO method on the calculation, we refrain from using alternative PDF sets as well as reporting the size of PDF uncertainties. However, as demonstrated in Refs. [332, 337], the effect of PDF uncertainties is generally found to be small, with the main source of theoretical error arising from scale variation. In addition, we use $N_f = 5$ active flavors in the PDFs and impose the following fiducial cuts on the final-state objects:

$$\begin{aligned}
&p_T(\ell) > 25\ \text{GeV}\,, && p_T(b) > 25\ \text{GeV}\,, && p_T(j) > 25\ \text{GeV}\,,\\
&|y(\ell)| < 2.5\,, && |y(b)| < 2.5\,, && |y(j)| < 2.5\,,\\
&\Delta R_{\ell\ell} > 0.4\,, && \Delta R_{bb} > 0.4\,, && \Delta R_{b\ell} > 0.4\,,\\
&\Delta R_{j\ell} > 0.4\,, && \Delta R_{bj} > 0.4\,, && \Delta R_{jj} > 0.4\,,
\end{aligned} \tag{6.2}$$

where $\ell = e^{\pm}, \mu^{\pm}, \tau^{\pm}$ and b, j refer to b and light jets, respectively. All the above are in accordance with Ref. [337], which means that the existing ROOT NTUPLE FILES [440, 441] for the $pp \to t\bar{t}W^+ + X$ and $pp \to t\bar{t}W^+j + X$ processes are used, without the need to generate them from scratch. This is possible since the MiNLO method, as implemented in the HEPLOT program [442], can be directly used by simply reweighting the standard NLO calculations, as described in Chapter 5. In contrast, due to the lack of ROOT NTUPLE FILES for the LO $pp \to t\bar{t}W^+jj$, the events are generated from scratch. For all the fully off-shell $pp \to t\bar{t}W^+$ + jets processes, jets are constructed from all partons with $|\eta| < 5$ using the anti-k_T clustering algorithm [477] with a resolution parameter $R = 0.4$.

The use of various scale choices for performing the calculations is thoroughly examined in this chapter. Although the MiNLO method extracts the scales associated with the extra jets based on the most likely branching history, the procedure of selecting a core scale remains arbitrary. For processes involving one or two final-state core particles, such as Drell-Yan or $t\bar{t}$ production, the ambiguity in selecting an optimal core scale is relatively low. For instance, in the original MiNLO paper [138], in which a phenomenological study of the H+jets and Z+jets processes was provided, the core scale was set equal to the invariant mass of the core system, corresponding to m_H and m_Z. This is to be expected, as these scales are well-suited to accurately describe the kinematics of the primary system. In our case, however, the situation is much more complicated. The presence of multiple final-state partons makes the search for an optimal core scale a non-trivial task. For this reason, it is important to explore various scale choices to assess how the MiNLO results are affected by these variations. Thus, results are provided for the following scales:

$$\mu_0 = m_t + \frac{m_W}{2},\ \frac{E_T}{2},\ \frac{E_T}{3},\ \frac{H_T}{2},\ \frac{H_T}{3}\,, \tag{6.3}$$

where H_T is the scalar p_T sum defined as follows:

$$H_T = p_T(e^+) + p_T(\mu^-) + p_T(\tau^+) + p_T^{miss} + p_T(b_1) + p_T(b_2) + \sum_j p_T(j)\,, \tag{6.4}$$

and E_T is the transverse energy given by:

$$E_T = \sqrt{m_t^2 + p_T^2(t)} + \sqrt{m_t^2 + p_T^2(\bar{t})} + \sqrt{m_W^2 + p_T^2(W)} + \sum_j p_T(j)\,. \tag{6.5}$$

On the one hand, for the standard NLO calculations, we set $\mu_R = \mu_F = \mu_0$ for the central choice of the renormalization and factorization scales. Also, the $\sum_j p_T(j)$ is relevant only for the extra resolved jets relative to $e^+\nu_e\,\mu^-\bar{\nu}_\mu\,\tau^+\nu_\tau\,b\bar{b}$, without considering the transverse momentum of the extra jet at NLO, even if resolved and passed all cuts. Hence, the aforementioned sum includes zero, one and two jets for the $pp \to t\bar{t}W^+ + X$, $pp \to t\bar{t}W^+j + X$ and $pp \to t\bar{t}W^+jj$ processes, respectively. For the MiNLO results, on the other hand, μ_0 defines the core scale of the computation, and thus $q_{core} = \mu_0$ in line with our notation in Chapter 5. In this case, the $\sum_j p_T(j)$ includes all extra QCD partons with respect to $e^+\nu_e\,\mu^-\bar{\nu}_\mu\,\tau^+\nu_\tau\,b\bar{b}$ that could be regarded as part of the primary system. This could happen only in cases of unordered clusterings, as discussed in Sec. 5.5.2, where the explicit kinematics of the additional QCD partons are included in the definition of the core scale. Nevertheless,

in the case of ordered clusterings, these extra partons are always absorbed in the kinematics of the core system by means of the inverse k_T-clustering algorithm, and as there are no extra partons relative to $e^+\nu_e\,\mu^-\bar{\nu_\mu}\,\tau^+\nu_\tau\,b\bar{b}$, the $\sum_j p_T(j)$ is absent in the above definitions. We also note that, in addition to the differences mentioned earlier regarding the definitions of scales in the two approaches, the kinematics of the QCD core particles can generally differ between standard NLO and MiNLO. In the MiNLO method, the momenta of b and light jets present in the q_{core} scale definitions do not typically correspond to their momenta in the standard NLO calculations. To illustrate this point, we discuss a simple LO example by focusing on the $u\bar{d} \to e^+\nu_e\,\mu^-\bar{\nu}_\mu\,\tau^+\nu_\tau\,b\bar{b}\,gg$ subprocess. In the MiLO framework, the two emitted gluons can be clustered together to form a pseudogluon, which is then subsequently clustered with a b quark. As a result, once the clustering algorithm terminates and the core system is reached, the momentum of the resulting pseudo b jet will include contributions from both gluons, contrary to the standard LO calculation. At the same time, the kinematics of the leptons after the MiNLO method is applied are the same as in the standard NLO calculations since leptons are not involved in the inverse k_T-clustering algorithm. Finally, we comment on the reconstruction of the top quarks and the W^+ boson, which is necessary for determining the E_T scale in Eq. (6.5). Specifically, the kinematics of the top quarks and the W^+ boson are reconstructed by minimizing the following quantity:

$$Q = |M(t) - m_t| + |M(\bar{t}) - m_t| + |M(W) - m_W|\,, \tag{6.6}$$

after considering all possible pairs of partons that could produce t, $\bar{t}$ and W^+. In practice, all possible $\ell^+\nu_\ell$ pairs are used to reconstruct the W^+ boson, while various combinations such as $\ell\,\nu_\ell\,b$, $\ell\,\nu_l\,b\,j$ and $\ell\,\nu_l\,b\,j\,j$ are employed for reconstructing the top quarks, where b represents both a b and a $\bar{b}$, and ℓ can be either positively or negatively charged. The combination of pairs that minimizes Q is then used to reconstruct the kinematics of the top quarks and the W^+ boson.

To estimate the size of the theoretical error inherited in the perturbative treatment of the computations, we employ the standard seven-point scale variation and consider the minimum and maximum cross sections obtained after utilizing the following (ξ_R, ξ_F) pairs:

$$(\xi_R\,,\xi_F) = \Big\{\,(2,1)\,,(0.5,1)\,,(1,2)\,,(1,1),(1,0.5),(2,2),(0.5,0.5)\Big\}\,, \tag{6.7}$$

where ξ_R and ξ_F are the renormalization and factorization scale factors, respectively. For the standard NLO calculations, the renormalization and factorization scales are determined by $\mu_R = \xi_R\mu_0$ and $\mu_F = \xi_F\mu_0$. In the case of the MiNLO method, scale variation is performed according to our default setup described in Sec. 5.3. More specifically, the nodal scales $\{q_i\}$ appearing as arguments of the strong coupling constants are rescaled according to Eq. (5.22), μ_R is given by Eq. (5.23), and the additional power of α_s in the NLO calculation is determined from Eq. (5.24). Lastly, Sudakov form factors are influenced only by factorization scale variation according to Eqs. (5.11) - (5.13). The resolution parameter R in the inverse k_T-clustering algorithm (Eq. (5.2)) is set to $R = 0.4$, unless stated otherwise.

However, as previously mentioned, while this setup represents our default configuration, we also study alternative methods such as $\texttt{MiNLO}_{\text{var}_2}$ and $\texttt{MiNLO}_{\text{no}\xi_\text{F}}$, defined in Secs. 5.3 and 5.1, respectively, as part of our systematic uncertainties analysis.

μ_0	σ^{LO} [ab]	σ^{MiLO} [ab]	σ^{NLO} [ab]	σ^{MiNLO} [ab]	$\frac{\sigma^{\text{NLO}}}{\sigma^{\text{LO}}}$	$\frac{\sigma^{\text{MiNLO}}}{\sigma^{\text{MiLO}}}$	$\frac{\sigma^{\text{MiNLO}}}{\sigma^{\text{NLO}}}$
			$pp \to t\bar{t}W^+$				
$m_t + m_W/2$	$202.4^{+23.7\%}_{-17.9\%}$	$202.4^{+23.7\%}_{-17.9\%}$	$252.5^{+4.5\%}_{-6.8\%}$	$252.5^{+4.5\%}_{-6.8\%}$	1.25	1.25	1.00
$E_T/2$	$177.0^{+22.2\%}_{-17.1\%}$	$177.0^{+22.2\%}_{-17.1\%}$	$240.4^{+6.3\%}_{-7.6\%}$	$236.3^{+5.5\%}_{-7.2\%}$	1.36	1.34	0.98
$E_T/3$	$198.8^{+23.3\%}_{-17.7\%}$	$198.8^{+23.3\%}_{-17.7\%}$	$249.9^{+4.6\%}_{-6.8\%}$	$244.6^{+3.4\%}_{-6.2\%}$	1.26	1.23	0.98
$H_T/2$	$192.1^{+23.0\%}_{-17.5\%}$	$192.1^{+23.0\%}_{-17.5\%}$	$246.6^{+5.0\%}_{-7.0\%}$	$240.4^{+3.7\%}_{-6.3\%}$	1.28	1.25	0.97
$H_T/3$	$216.4^{+24.1\%}_{-18.2\%}$	$216.4^{+24.1\%}_{-18.2\%}$	$254.8^{+2.8\%}_{-5.9\%}$	$246.7^{+2.5\%}_{-4.9\%}$	1.18	1.14	0.97
			$pp \to t\bar{t}W^+j$				
$m_t + m_W/2$	$141.1^{+40.7\%}_{-27.0\%}$	$133.3^{+34.0\%}_{-23.4\%}$	$144.7^{+0.3\%}_{-14.0\%}$	$140.9^{+1.6\%}_{-11.2\%}$	1.03	1.06	0.97
$E_T/2$	$104.0^{+36.6\%}_{-25.2\%}$	$94.7^{+32.1\%}_{-22.4\%}$	$140.1^{+3.8\%}_{-10.0\%}$	$136.5^{+6.1\%}_{-9.6\%}$	1.35	1.44	0.97
$E_T/3$	$124.5^{+38.7\%}_{-26.1\%}$	$121.4^{+33.5\%}_{-23.1\%}$	$144.9^{+1.3\%}_{-7.0\%}$	$141.7^{+1.4\%}_{-5.9\%}$	1.16	1.17	0.98
$H_T/2$	$115.8^{+37.8\%}_{-25.7\%}$	$112.2^{+33.1\%}_{-22.9\%}$	$142.6^{+1.5\%}_{-8.2\%}$	$139.5^{+2.0\%}_{-6.8\%}$	1.23	1.24	0.98
$H_T/3$	$139.3^{+40.0\%}_{-26.7\%}$	$141.3^{+34.7\%}_{-23.7\%}$	$144.3^{+1.0\%}_{-12.5\%}$	$138.4^{+3.5\%}_{-17.5\%}$	1.04	0.98	0.96

Table 6.1: *Integrated fiducial cross sections for the fully off-shell* $pp \to e^+\nu_e\,\mu^-\bar{\nu}_\mu\,\tau^+\nu_\tau\,b\bar{b} + X$ *and* $pp \to e^+\nu_e\,\mu^-\bar{\nu}_\mu\,\tau^+\nu_\tau\,b\bar{b}\,j + X$ *processes at the LHC with* $\sqrt{s} = 13\,\text{TeV}$*, obtained using the standard (N)LO and* `Mi(N)LO` *methods. Results are presented for several scale choices, including the scale uncertainties obtained using the seven-point scale variation (Eq.* (6.7)*). Also shown are* $\mathcal{K} = \sigma^{\texttt{(Mi)NLO}}/\sigma^{\texttt{(Mi)LO}}$ *factors and the ratio of the central* `MiNLO` *to the standard NLO cross sections.*

In the latter case, the only difference from our default setup is that Sudakov form factors remain unchanged after scale variation, effectively defining $q_{res} = q_1$ at all times. In contrast, for the former case, the only distinction lies in how we determine the renormalization scale and handle the extra coupling of α_s at NLO.

6.2 MiNLO vs NLO: Integrated fiducial results

We start by presenting the integrated fiducial results for the fully off-shell $pp \to t\bar{t}W^+ + X$ and $pp \to t\bar{t}W^+j + X$ processes, by reporting predictions from both the standard NLO calculations and those obtained using the MiNLO framework in Table 6.1. The results are displayed for various scale choices both at LO and NLO in QCD, including $\mathcal{K}$ factors and the ratios between MiNLO and standard NLO. First, we comment that the LO and MiLO results for the $pp \to t\bar{t}W^+ + X$ process are exactly the same. This is to be expected since the decay products of the $t\bar{t}W^+$ system define the core process and there are no extra QCD partons for the MiLO method to be applied. The situation changes at NLO in QCD, where standard NLO and MiNLO results differ due to the presence of an extra emission. In particular, although there are no Sudakov form factors in this case, as the only nodal scale q_0 associated with the real emission is discarded from the computation, the renormalization and factorization scales can generally differ between the two approaches. For instance, it may occur

that no clustering is available for the real emission due to the rapidity condition discussed in Sec. 5.5.1. This could happen in cases like the $ug \to t\bar{t}W^+d$ subprocess at NLO, if the d quark is emitted in a direction opposite to that of the incoming gluon. In such instances, the kinematics of the real emission are incorporated into the dynamical core scale definitions E_T and H_T when MiNLO is applied, while they are always ignored in the standard NLO calculations. The above consideration also explains why the NLO and MiNLO results coincide when a fixed scale is used instead. Nevertheless, comparing the two methods shows that these effects have only a mild impact on the MiNLO results, leading to differences of at most 3% relative to standard NLO, depending on the chosen scale. We finally highlight that the magnitude of NLO scale uncertainties is of the same size between the two different approaches, yielding values that are only slightly smaller when MiNLO is employed.

We now shift our focus to the $pp \to t\bar{t}W^+j + X$ process, which already involves one extra jet relative to the core system at LO. We notice that both MiLO and MiNLO uncertainties are smaller relative to the standard LO and NLO ones, for most of the scale choices considered. Indeed, the reduction is about $4 - 7$ and $1 - 3$ percentage points for MiLO and MiNLO, respectively. The only exception occurs with the dynamical scale choice $\mu_0 = H_T/3$, where the scale uncertainties are greater for MiNLO, amounting to roughly 18% compared to 13% for the standard NLO calculation. Furthermore, the use of the MiNLO method leads to a wider spread of $\mathcal{K} = \sigma^{\text{(Mi)NLO}}/\sigma^{\text{(Mi)LO}}$ factors, which range from 0.98 to 1.44 depending on the scale choice. In contrast, the corresponding range when the calculation is performed using the standard NLO approach is between $1.03 - 1.35$. Overall, the two methods agree quite well with each other within the theoretical errors with differences of at most 4%.

Finally, results for the fully off-shell $pp \to t\bar{t}W^+jj$ process are presented in Table 6.2 at LO in QCD. We find differences of at most 13% between MiLO and LO, which are nonetheless covered by the large-scale uncertainty bands. Indeed, for the standard LO calculations, the magnitude of the uncertainties is as high as 59%, while it significantly reduces by $4 - 10$ percentage points upon applying the MiLO method. This indicates that the more jets included in the process, the greater the effect of the MiNLO method on the calculations. It is important to highlight, however, that while employing the MiNLO framework for the $pp \to t\bar{t}W^+ +$ jets processes reduces scale dependence, it does not entirely eliminate it. This behavior is expected given that only one (two) α_s coupling(s) are determined through the MiNLO method in the $pp \to t\bar{t}W^+j + X$ ($pp \to t\bar{t}W^+jj$) process. The remaining strong coupling constants are instead evaluated at the core scale, the choice of which remains arbitrary.

6.2.1 Study of the systematic uncertainties in the MiNLO method

In this subsection, we explore the impact of systematic uncertainties associated with the MiNLO method by investigating alternative ways for performing scale variation and utilizing different values for the resolution parameter R in the inverse k_T-clustering algorithm. In particular, we present results for the $pp \to t\bar{t}W^+j + X$ process using the $\text{MiNLO}_{\text{var}_2}$ and $\text{MiNLO}_{\text{no}\xi_{\text{F}}}$ methods outlined in Secs. 5.3 and 5.1. Additionally, we examine the effects of setting $R = 1.0$ instead of the default value of $R = 0.4$ in the clustering algorithm of Eq. (5.2). By doing so, we aim to assess the

$pp \to t\bar{t}W^+jj$

μ_0	σ^{LO} [ab]	σ^{MiLO} [ab]	$\frac{\sigma^{\text{MiLO}}}{\sigma^{\text{LO}}}$
$m_t + m_W/2$	$80.3^{+58.8\%}_{-34.6\%}$	$72.0^{+48.9\%}_{-30.3\%}$	0.90
$E_T/2$	$47.7^{+51.2\%}_{-31.8\%}$	$41.3^{+46.5\%}_{-29.3\%}$	0.87
$E_T/3$	$60.4^{+54.2\%}_{-33.0\%}$	$57.9^{+48.1\%}_{-30.0\%}$	0.96
$H_T/2$	$53.7^{+52.7\%}_{-32.4\%}$	$50.8^{+47.6\%}_{-29.8\%}$	0.95
$H_T/3$	$68.5^{+55.9\%}_{-33.6\%}$	$69.2^{+49.3\%}_{-30.4\%}$	1.01

Table 6.2: *Integrated fiducial cross sections for the fully off-shell* $pp \to e^+\nu_e\,\mu^-\bar{\nu}_\mu\,\tau^+\nu_\tau\,b\bar{b}\,jj$ *process at the LHC with* $\sqrt{s} = 13\,\text{TeV}$*, obtained using the standard LO and* MiLO *methods for various scale choices. Also shown are scale uncertainties obtained from the seven-point scale variation of Eq.* (6.7) *and the relative* $\sigma^{\text{MiLO}}/\sigma^{\text{LO}}$ *ratio.*

μ_0	σ^{MiNLO} [ab]	$\sigma^{\text{MiNLO}}_{R=1.0}$ [ab]	$\sigma^{\text{MiNLO}}_{\text{var}_2}$ [ab]	$\sigma^{\text{MiNLO}}_{\text{no}\xi_\text{F}}$ [ab]	$\frac{\sigma^{\text{MiNLO}}_{R=1.0}}{\sigma^{\text{MiNLO}}}$	$\frac{\sigma^{\text{MiNLO}}_{\text{var}_2}}{\sigma^{\text{MiNLO}}}$
$E_T/2$	$136.5^{+6.1\%}_{-9.6\%}$	$135.3^{+7.0\%}_{-10.5\%}$	$135.0^{+5.9\%}_{-9.3\%}$	$136.5^{+7.0\%}_{-12.2\%}$	0.99	0.99
$H_T/2$	$139.5^{+2.0\%}_{-6.8\%}$	$137.9^{+3.3\%}_{-7.5\%}$	$138.1^{+1.8\%}_{-6.6\%}$	$139.5^{+2.6\%}_{-9.0\%}$	0.99	0.99

Table 6.3: *Comparison between the default* MiNLO *configuration and the alternative prescriptions for the* $pp \to e^+\nu_e\,\mu^-\bar{\nu}_\mu\,\tau^+\nu_\tau\,b\bar{b}\,j + X$ *process at the LHC with* $\sqrt{s} = 13\,\text{TeV}$*, for the* $\mu_0 = E_T/2$ *and* $\mu_0 = H_T/2$ *scale choices. In addition to our default setup, results are displayed for the following cases: a) the usage of* $R = 1.0$ *in the inverse* k_T*-clustering algorithm of Eq.* (5.2)*, b) the alternative method to perform scale variation according to Eqs.* (5.25)-(5.27)*, labelled as* $\text{MiNLO}_{\text{var}_2}$ *and c) the prescription where no scale variation is applied in the Sudakov form factors by setting* $q_{res} = q_1$ *in Eq. 5.12 at all times, denoted as* $\text{MiNLO}_{\text{no}\xi_\text{F}}$*. Also shown are scale uncertainties obtained from the standard seven-point scale variation and the ratios of* $\text{MiNLO}_{R=1.0}$ *and* $\text{MiNLO}_{\text{var}_2}$ *to the default* MiNLO *cross sections.*

sensitivity of the MiNLO results under these alternative prescriptions. The findings are summarized in Table 6.3, only for the $\mu_0 = E_T/2$ and $\mu_0 = H_T/2$ scales, but similar conclusions were drawn for the other scale choices we considered. First, we observe that the overall impact of these alternative approaches is negligible, with deviations of only 1% relative to our default configuration. Second, the use of $R = 1.0$ and $\text{MiNLO}_{\text{no}\xi_\text{F}}$ results in a slight increase in the size of the theoretical uncertainties compared to the default MiNLO method. However, this trend is not observed in the case of $\text{MiNLO}_{\text{var}_2}$, where the scale uncertainties remain consistent in magnitude.

The above considerations are, however, limited to the case where scale variation is performed using the conventional seven-point scale variation. To gain a more

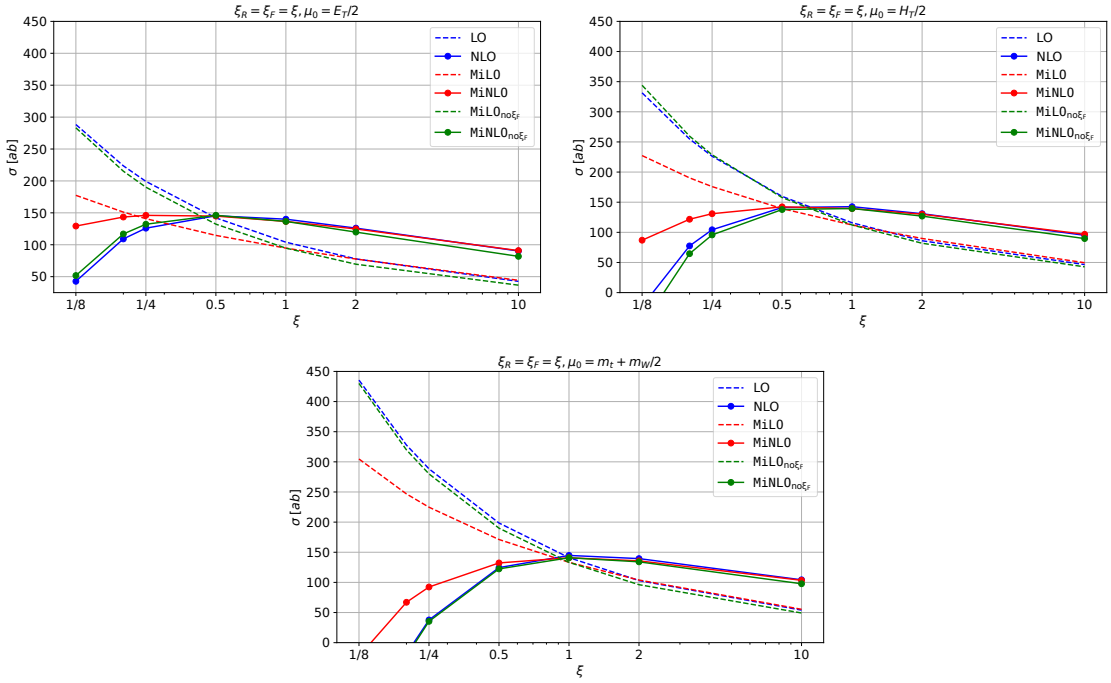

Figure 6.1: *Integrated fiducial cross sections for the fully off-shell* $pp \to e^+\nu_e\,\mu^-\bar{\nu}_\mu\,\tau^+\nu_\tau\,b\bar{b}\,j + X$ *process at the LHC with* $\sqrt{s} = 13\,\text{TeV}$*, as a function of the scale-variation factor* $\xi = \xi_R = \xi_F$ *for the following scale choices:* $\mu_0 = m_t + m_W/2, E_T/2, H_T/2$*. Results are displayed using the standard* $(N)LO$ *and the* `Mi(N)LO` *method with blue and red, respectively. Also shown with green are predictions for the* `Mi(N)LO` *case where no scale variation is applied in the Sudakov form factors, denoting as* `Mi(N)LO`$_{\text{no}\xi_F}$.

comprehensive view of the scale dependence for MiNLO and NLO, in the following, the cross-section is presented as a function of $\xi = \xi_R = \xi_F$, where ξ_R and ξ_F are the renormalization and factorization scale factors, respectively. In particular, the cross-section dependence is illustrated over a wide range of ξ, from 1/8 to 10. By doing so, we aim to understand how the two different methods behave in cases where extreme ξ values are applied. Concerning the MiNLO method, we also display the results for the MiNLO$_{\text{no}\xi_F}$ scenario, which constitutes the original proposal of the MiNLO paper [138]. The results are shown in Fig. 6.1 for the following scale choices $\mu_0 = m_t + m_W/2, E_T/2, H_T/2$. From Fig. 6.1 we find notable differences between the various methods, especially in the low-ξ regimes. In these regions, cross sections can become negative for the dynamical $\mu_0 = H_T/2$ and the fixed scale. We have chosen not to present these negative outcomes as they are unphysical. In general, the Mi(N)LO$_{\text{no}\xi_F}$ and standard (N)LO cases tend to agree more across the entire plotted ranges, while predictions for the default Mi(N)LO setup seem to be more stable as $\xi \to 1/8$. By "stable", we mean that the Mi(N)LO results in this range are closer to our central setup where $\xi = 1$ has been utilized. In addition, for the $\mu_0 = H_T/2$ scale choice, the negative cross sections observed for NLO and MiNLO$_{\text{no}\xi_F}$ are absent when employing the MiNLO method, leading to improved predictions. However, for $\xi > 1/2$, all different approaches agree quite well, yielding similar results. This behavior is expected, since for large ξ values the α_s arguments tend to be high. At these high energies, the strong coupling constant α_s varies only slightly, causing

the α_s values among the different methods to be very similar. Furthermore, in the default Mi(N)LO approach, the q_{res} scale tends to increase as ξ_F grows, leading to a strong suppression of the effect of the Sudakov form factors for the initial lines, as the interval $(\xi_F q_1, q_{core})$ becomes narrower. Consequently, the Mi(N)LO results closely resemble those from the standard (N)LO calculation since Sudakov form factors are very close to unity. In contrast, when no variation is applied in the Sudakovs, QCD emissions are resummed over a broader range (q_1, q_{core}), leading to results that are slightly smaller compared to the aforementioned approaches due to lower no-emission probabilities. In particular, the differences between $\texttt{MiNLO}_{\text{no}\xi_\text{F}}$ and the other cases are between $6\% - 13\%$ when $\xi = 10$. Overall, the treatment of the Sudakov form factors under scale variation is highly sensitive only when values of $\xi < 1/2$ are employed. In this regime, potentially large logarithms in the Mi(N)LO method are resummed along the incoming lines over a wider range compared to $\texttt{Mi(N)LO}_{\text{no}\xi_\text{F}}$, where the corresponding range is more limited due to $q_{res} = q_1$. Finally, we comment that the above remarks are universal among all scale choices depicted.

To obtain a more complete picture of the scale variation, in Fig. 6.2 we present the two-dimensional contour plots of the LO and MiLO cross sections when ξ_R and ξ_F are varied independently. More specifically, we plot the ratio of the cross section obtained under scale variation $\sigma(\xi_R, \xi_F)$ to the central prediction σ_{central}. Results are displayed only for the $\mu_0 = E_T/2$ dynamical scale, but similar conclusions have been drawn for the other scales we examined. The upper left (right) plot shows the MiLO ($\texttt{MiLO}_{\text{no}\xi_\text{F}}$) predictions, while the bottom one illustrates the standard LO results. Although we are mostly interested in the differences between the various methods at NLO, we first present the LO contour plots, as we can easily draw some useful conclusions from them. Indeed, the MiLO weight given by Eq. (5.16) is rather simple compared to the MiNLO one, where multiple pieces of the calculation make the analysis more complicated. First, we notice that the $\texttt{MiLO}_{\text{no}\xi_\text{F}}$ and LO predictions exhibit a similar behavior, featuring large ratios up to 3 in the bottom left corner and small ones up to 0.4 in the upper right corners. On the other hand, the MiLO results show an inverted pattern, with the largest and smallest ratios appearing in the upper left and bottom right corners, respectively. The differences between MiLO and the other approaches as $\xi_R, \xi_F \to 1/8$ have already been discussed before, and they primarily arise because, in the default MiLO method, Sudakov form factors resum large logarithms over a wider range. Indeed, by comparing the MiLO and $\texttt{MiLO}_{\text{no}\xi_\text{F}}$ weights according to Eq. (5.16), we notice that their only distinction lies in the treatment of the Sudakov form factors under scale variation. For small ξ_F values, large logarithms are resummed in a bigger range for MiLO, resulting in smaller matrix-element weights, and thus smaller $\sigma^{\texttt{MiLO}_{\text{no}\xi_\text{F}}}/\sigma^{\texttt{MiLO}_{\text{no}\xi_\text{F}}}_{\text{central}}$ ratios. On the contrary, when $\xi_F \to 8$ and $\xi_R \to 1/8$, the effects of Sudakov form factors in the MiLO method are highly suppressed, as the interval $(\xi_F q_1, q_{core})$ becomes very narrow. This is not the case for the $\texttt{MiLO}_{\text{no}\xi_\text{F}}$ setup, where Sudakov form factors remain unaffected by scale variation. Hence, the former exhibits Sudakov weights close to unity, while the latter yields smaller ones, explaining the significant enhancements seen in the upper left region of the MiLO plot. Finally, the $\texttt{MiLO}_{\text{no}\xi_\text{F}}$ and LO predictions are found to be similar. For instance, in the upper left corner, even though the q_1 scale entering Eq. (5.16) is generally smaller than the reference scale $\mu_0 = E_T/2$ used in the standard LO computation, the enhancement due to the larger strong coupling constant is compensated by the Sudakov suppression, which is absent in the LO

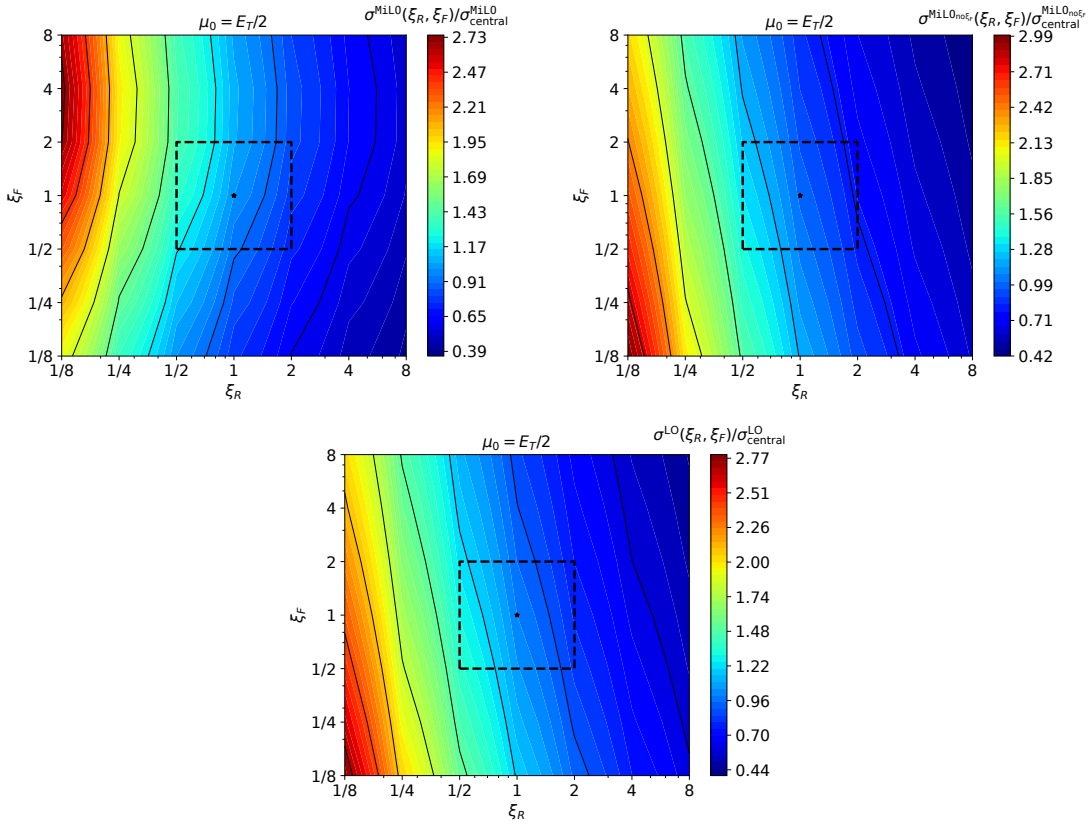

Figure 6.2: *Contour plots for the fully off-shell* $pp \to e^+\nu_e\,\mu^-\bar{\nu}_\mu\,\tau^+\nu_\tau\,b\bar{b}\,j$ *process at the LHC with* $\sqrt{s} = 13\,\text{TeV}$ *for* MiLO *(uuper left),* $\text{MiLO}_{\text{no}\xi_\text{F}}$ *(upper right) and LO (bottom), using the* $\mu_0 = E_T/2$ *scale. Results are displayed for the cross section obtained by varying* ξ_R *and* ξ_F *independently, normalized to the corresponding central prediction where* $\xi_R = \xi_F = 1$*. The black squares cover the region associated to the standard 7-point scale variation, including the additional* $(\xi_R, \xi_F) = \{(1/2, 2), (2, 1/2)\}$ *points.*

case. Finally, we highlight that the mentioned differences occur only if extreme ξ_R and ξ_F values are used. As shown by the black squares, under the traditional 7-point scale variation, all approaches produce similar outcomes.

Having discussed the LO plots, we now proceed to the corresponding NLO ones, as displayed in Fig. 6.3. As in Fig. 6.2, the upper left and right plots display the MiNLO and $\text{MiNLO}_{\text{no}\xi_\text{F}}$ results, while the bottom plot corresponds to the standard NLO predictions. Similarly to what has been observed in the LO contour plots, also here, the MiNLO predictions follow an inverted pattern, with the main differences from the other approaches arising from the ξ_F variations as ξ_R becomes small. For the MiNLO case, the scale-variation uncertainties reach up to 84% in regions where ξ_R and ξ_F take very different values, specifically in the regime around $(\xi_R, \xi_F) = (1/8, 8)$. On the contrary, for the $\text{MiNLO}_{\text{no}\xi_\text{F}}$ and standard NLO cases, the corresponding uncertainties are at most 69%, in regions where ξ_R and ξ_F acquire similar, either very small or very large, values. In summary, the origin of the aforementioned differences between the various methods is mainly due to the treatment of the Sudakov form factors under scale variation, as already discussed in the case of the LO contour plots. Although significant differences are observed between the various methods when ξ_R

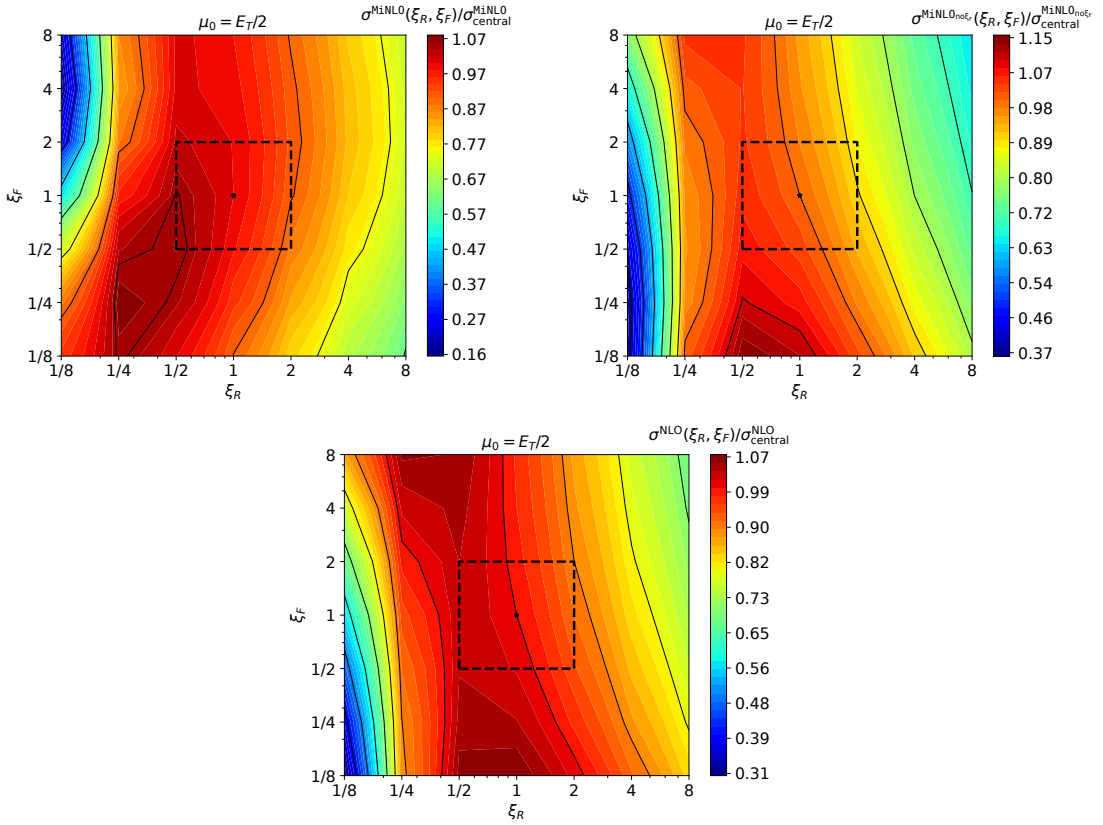

Figure 6.3: *Same as Fig. 6.2 but for the* MiNLO *(upper left),* $\texttt{MiNLO}_{\text{no}\xi_F}$ *(upper right) and NLO (bottom) cases.*

acquires very small values, under the seven-point scale variation, all methods yield consistent outcomes, as displayed from the regions inside the black squares.

6.2.2 The MiNLO behavior with suboptimal scales and various transverse momentum thresholds

Nonetheless, such extreme scale variations, as those discussed in the previous subsection, are very rarely employed in practical applications. In other words, although deviations between MiNLO and $\texttt{MiNLO}_{\text{no}\xi_F}$ are pronounced outside the conventional seven-point scale variation, these effects are not very phenomenologically relevant. In fact, theoretical uncertainties arising from extreme values of ξ_R and ξ_F often provide a conservative overestimate of the theoretical error. Hence, it would be more appealing to investigate the effects of the MiNLO method when a non-optimal scale is chosen for performing the calculation, rather than conducting extreme scale variations around a central scale choice, which is known to perform well. For this purpose, we present results for the fully off-shell $pp \to t\bar{t}W^+j + X$ process using both the standard NLO and MiNLO approaches for the $\mu_0 = E_T/8$ and $\mu_0 = H_T/8$ scale choices. These scales are considered non-optimal for this process as they are associated with substantial NLO scale uncertainties. Therefore, by comparing the results from MiNLO with those from standard NLO, we aim to evaluate the impact of the MiNLO framework when suboptimal scales are employed. The cross sections are demonstrated in the upper panels of Fig. 6.4 for various $p_{T,j}$ thresholds, while the

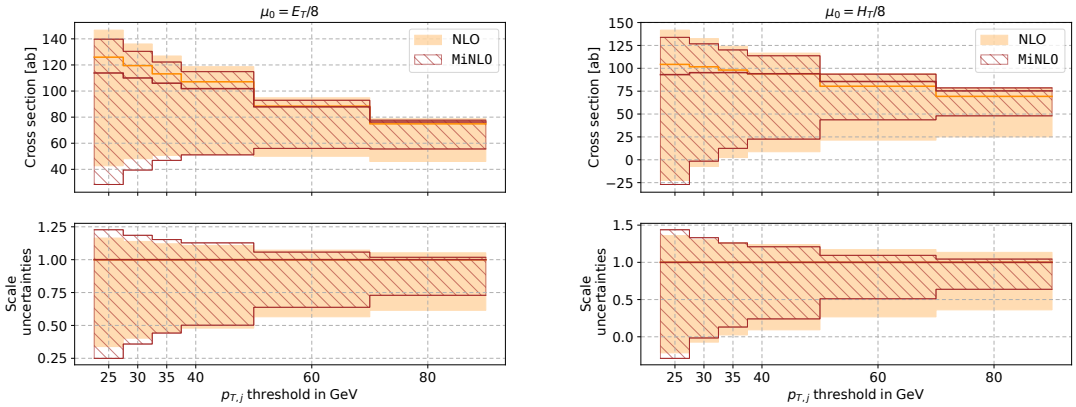

Figure 6.4: *Integrated fiducial cross sections for the fully off-shell* $pp \to e^+\nu_e\,\mu^-\bar{\nu}_\mu\,\tau^+\nu_\tau\,b\bar{b}\,j + X$ *process at the LHC with* $\sqrt{s} = 13\,\text{TeV}$*, for the following* $p_{T,j}$ *thresholds:* $25, 30, 35, 40, 60$ *and* 80 *GeV. The upper panels display the absolute predictions obtained using the standard NLO and* MiNLO *approaches for the* $\mu_0 = E_T/8$ *(left) and* $\mu_0 = H_T/8$ *(right) scales, while the bottom panels demonstrate the size of the scale uncertainties from the seven-point scale variation.*

bottom panels depict the size of the scale uncertainties for the two approaches. We observe that for the $p_{T,j} = 25\,\text{GeV}$ threshold both standard NLO and MiNLO exhibit large uncertainties, reaching values up to 75% for $\mu_0 = E_T/8$ and exceeding 100% for $\mu_0 = H_T/8$. This indicates that, in this case, the usage of the MiNLO framework does not improve the NLO predictions for this process. However, as the $p_{T,j}$ threshold increases, we find a substantial reduction in the magnitude of the scale uncertainties when MiNLO is employed. For instance, for the $\mu_0 = H_T/8$ scale choice and when $p_{T,j} = 80\,\text{GeV}$, the MiNLO uncertainties are nearly half in size compared to those from standard NLO. By imposing a large threshold on the transverse momentum of the light jet, we increase the likelihood that the nodal scale q_1 extracted from the MiNLO method exceeds the core scale. In such cases, an unordered clustering occurs and the core scale is forced to be equal to q_1, based on what is described in Sec. 5.5.2. This effectively eliminates the problematic scale from the computation, explaining why the MiNLO predictions exhibit smaller scale uncertainties compared to the standard NLO calculations.

To further investigate the impact of the $p_{T,j}$ threshold on the computations, in Fig. 6.5 we show similar results, but this time for the well-behaved $\mu_0 = E_T/2$ and $\mu_0 = H_T/2$ scales. In this case, contrary to what has been observed with the sub-optimal scales, the standard NLO uncertainties tend to grow as the $p_{T,j}$ threshold rises for both dynamical scales. While a similar trend is noted for the MiNLO uncertainties, they consistently remain smaller than those from standard NLO, with more pronounced differences at higher $p_{T,j}$ thresholds. Therefore, reinforcing our earlier conclusion, we deduce that the MiNLO predictions yield smaller theoretical errors for larger values of the $p_{T,j}$ thresholds. Nonetheless, for well-behaved scale choices, the discrepancies in the magnitude of the scale uncertainties are less pronounced. Additionally, we note that, although the previous conclusion applies to the other scales we examined, an exception arises for the fixed scale choice $\mu_0 = m_t + m_W/2$. In this case, both standard NLO and MiNLO uncertainties exhibit an inverted pattern, decreasing in size as the $p_{T,j}$ threshold increases. Nevertheless, even in this scenario,

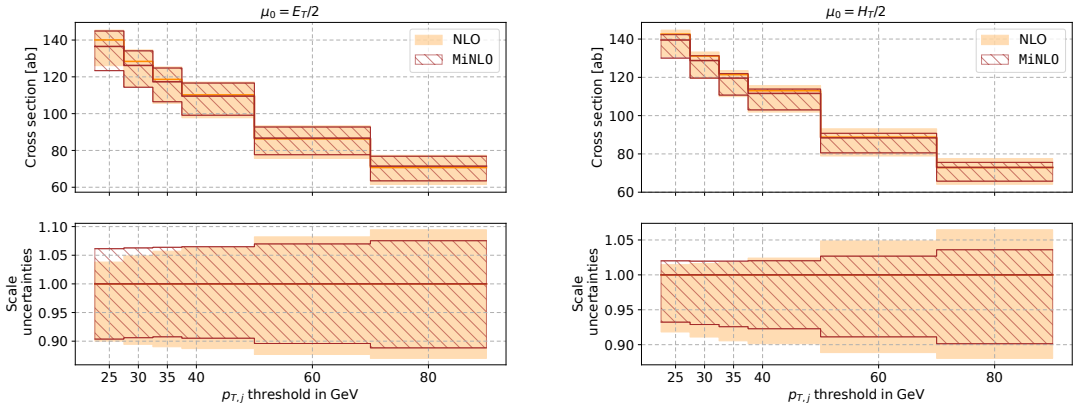

Figure 6.5: *Same as Fig. 6.4 but for the* $\mu_0 = E_T/2$ *(left) and* $\mu_0 = H_T/2$ *(right) scale choices.*

the MiNLO uncertainties remain smaller across all scanned $p_{T,j}$ threshold values.

6.3 On the form of the Sudakov form factors

In this section, we investigate the impact of employing the MiNLO Sudakov form factors in which the power corrections $\mathcal{O}(\sqrt{t/t_1})$ appearing in Eq. (5.41) are not included. In this case, the Sudakov form factors can exceed unity and therefore cannot be interpreted as no-emission probabilities. Results obtained with this prescription are presented in Table 6.4 for the scale choices $\mu_0 = m_t + m_W/2$, $H_T/2$, and $\mu_0 = E_T/2$, and are denoted as $\texttt{MiNLO}_{\text{noprob}}$ to indicate the non-probabilistic nature of the Sudakov factors used. Additionally, we present results for the $\texttt{MiNLO}_{\text{noprob}'}$ setup in which Sudakov form factors are forced to be 1 in case they exceed unity. For completeness, we also include the MiNLO predictions obtained with our default setup, where the Sudakov form factors defined in Eq. (5.14) are employed. We find that scale uncertainties are considerably larger when the original MiNLO Sudakov form factors are utilized for the $\mu_0 = m_t + m_W/2$ and $\mu_0 = H_T/2$ scale choices. The dynamical $\mu_0 = E_T/2$ scale exhibits the opposite behavior, yielding smaller theoretical errors. In particular, for the fixed scale choice the uncertainty can reach up to 34%, compared to 11% in our default setup. A similar, though less pronounced, enhancement is observed for $\mu_0 = H_T/2$. To investigate this, we present below the form of the Sudakov form factors in the $\texttt{MiNLO}_{\text{noprob}}$ setup after solving the integral in the exponent analytically and assuming, for simplicity, that the α_s coupling constant remains constant upon integration and that $N_f = 5$. In this case, the Sudakov form factors for quarks and gluons, between the nodal scale q_1 and the core scale q_{core}, take the following form:

$$\Delta_q(t_1, t_{core}) = \exp\left\{-\frac{\alpha_s C_F}{4\pi}\left((1+\Lambda_2)\log^2\frac{t_{core}}{t_1} - 3\log\frac{t_{core}}{t_1}\right)\right\}, \tag{6.8}$$

$$\Delta_g(t_1, t_{core}) = \exp\left\{-\frac{\alpha_s}{4\pi}\left(C_A(1+\Lambda_2)\log^2\frac{t_{core}}{t_1} - \frac{1}{3}(11C_A - 20T_R)\log\frac{t_{core}}{t_1}\right)\right\}, \tag{6.9}$$

μ_0	$\sigma^{\text{MiNLO}_{\text{noprob}}}$ [ab]	$\sigma^{\text{MiNLO}_{\text{noprob}'}}$ [ab]	σ^{MiNLO} [ab]
$m_t + m_W/2$	$126.2^{+7.5\%}_{-33.7\%}$	$128.8^{+5.7\%}_{-30.1\%}$	$140.9^{+1.6\%}_{-11.2\%}$
$H_T/2$	$131.1^{+4.4\%}_{-18.8\%}$	$132.7^{+3.1\%}_{-16.5\%}$	$139.5^{+2.0\%}_{-6.8\%}$
$E_T/2$	$134.5^{+1.8\%}_{-6.5\%}$	$135.1^{+0.6\%}_{-5.4\%}$	$136.5^{+6.1\%}_{-9.6\%}$

Table 6.4: *Integrated fiducial cross sections for the fully off-shell* $pp \to e^+\nu_e\,\mu^-\bar{\nu}_\mu\,\tau^+\nu_\tau\,b\bar{b}\,j + X$ *process at the LHC with* $\sqrt{s} = 13\,\text{TeV}$*, using the* MiNLO *Sudakov form factors where the* $\mathcal{O}(\sqrt{t/t_1})$ *terms in Eq. (5.41) are not included, labeled as* $\text{MiNLO}_{\text{noprob}}$*, together with results obtained using our default setup, denoted as* MiNLO*. Results are also shown for the "noprob" Sudakov setup with the Sudakov factors set to unity whenever they exceed one, labeled as* $\text{MiNLO}_{\text{noprob}'}$*. Results are provided for the following core-scale choices:* $\mu_0 = m_t + m_W/2$*,* $\mu_0 = H_T/2$ *and* $\mu_0 = E_T/2$*, including the uncertainties obtained from the standard seven-point scale variation.*

where $t_1 = q_1^2$ and $t_{core} = q_{core}^2$. For moderate α_s values, the two-loop correction factor Λ_2 is well below 0.1, allowing us to approximate $1 + \Lambda_2 \approx 1$ in the following, without affecting the validity of the argument. Under this approximation, one finds that for

$$\log\left(\frac{q_{core}}{q_1}\right) < \frac{3}{2} \Rightarrow \frac{q_{core}}{q_1} < e^{3/2} \approx 4.5\,, \tag{6.10}$$

in the quark case, and

$$\log\left(\frac{q_{core}}{q_1}\right) < \frac{23}{18} \Rightarrow \frac{q_{core}}{q_1} < e^{23/18} \approx 3.6\,, \tag{6.11}$$

in the gluon case, the expressions appearing in the exponents become negative, yielding Sudakov form factors that exceed unity. This behavior reflects the fact that the original MiNLO Sudakov form factors are mainly designed to resum logarithmically enhanced contributions in the soft and collinear regions, where the nodal scale q_1 is parametrically smaller than the hard scale q_{core}. In such configurations, the double-logarithmic contributions $\log^2(t_{core}/t_1)$ dominate over the single logarithmic terms $\log(t_{core}/t_1)$, ensuring a suppressive Sudakov exponent. However, in our case, the fiducial cuts imposed on the additional jet do not generate such a strong hierarchy between the nodal and core scales. As a consequence, the next-to-leading logarithmic terms become numerically comparable to the leading-logarithmic contribution. In particular, for the fixed scale choice $\mu_0 = m_t + m_W/2 = 212.69\,\text{GeV}$, quark and gluon emissions with transverse momenta above roughly 50 GeV and 60 GeV, respectively, already correspond to configurations for which the ratio q_{core}/q_1 becomes sufficiently small that the single-logarithmic contributions are numerically comparable to, or larger than, the leading double-logarithmic terms entering the

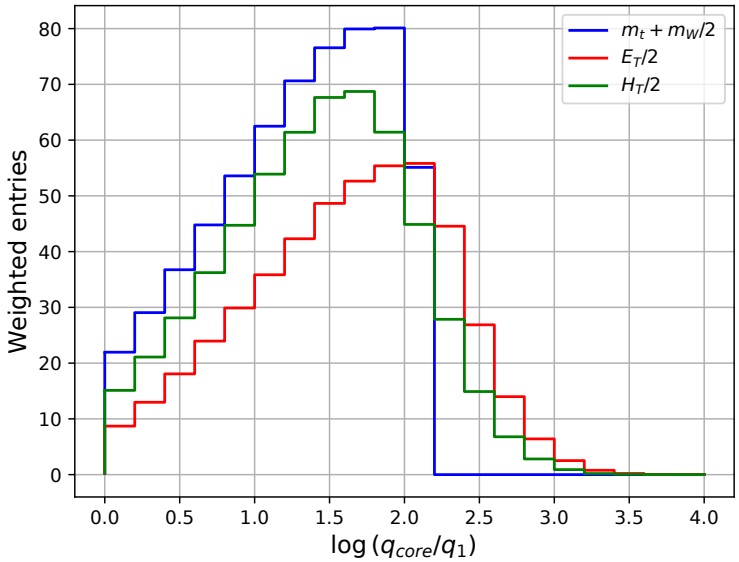

Figure 6.6: *Leading order weighted entries for the* $\log(q_{core}/q_1)$ *ratio in the full off-shell* $pp \to t\bar{t}W^+j$ *process, upon applying the* `MiLO` *method. Results are shown for three different core-scale values:* $q_{core} = m_t + m_W/2, E_T/2$ *and* $q_{core} = H_T/2$. *Unordered clusterings which would result in* $q_{core} = q_1$ *and thus* $\log(q_{core}/q_1) = 0$ *are not included in the plot.*

Sudakov exponent. As a consequence, the logarithmic hierarchy assumed in the original `MiNLO` construction is no longer numerically well satisfied in this region of phase space. Hence, the Sudakov exponent may become positive, leading to Sudakov form factors larger than unity and enhanced sensitivity to scale variations. Although the $\mu_0 = H_T/2$ scale choice leads to smaller uncertainties than the fixed scale $\mu_0 = m_t + m_W/2$, it still yields a substantial fraction of events for which the separation between the nodal scale q_1 and the core scale q_{core} remains moderate. Consequently, the single-logarithmic contributions can still compete numerically with the leading double-logarithmic terms in the Sudakov exponent, leading to the same qualitative behavior discussed above. Finally, the $\mu_0 = E_T/2$ scale choice exhibits a stronger event-by-event correlation with the hardness of the emitted radiation. As a consequence, configurations with only moderate separation between the nodal scale q_1 and the core scale q_{core} occur less frequently, ensuring that the logarithmic hierarchy underlying the original `MiNLO` Sudakov construction remains numerically more stable across the relevant phase space. This could possibly explain the relatively small scale uncertainties even when the $\texttt{MiNLO}_{\text{noprob}}$ setup is employed. To illustrate the typical hierarchy between the nodal and core scales entering the Sudakov form factors, in Fig. 6.6 we present the LO-weighted distribution in the variable $L = \log(q_{\text{core}}/q_1)$. Although this quantity is not a physical observable, it provides a useful diagnostic of the phase-space regions probed by the `MiNLO` construction and indicates how often the nodal and core scales are only moderately separated. We present this at LO to avoid potential negative weights that could obscure the underlying message. Indeed, we find that the peak of the distribution when the $\mu_0 = E_T/2$ scale is used is shifted towards large logarithmic values compared to the fixed and the $\mu_0 = H_T/2$ scales, peaking around $L \approx 2$. On top of that, a substantial

number of entries are found at large L values above that peak. In contrast, for the $\mu_0 = m_t + m_W/2$ scale choice, a considerably larger number of weighted entries is found in the regime where the Sudakov form factor becomes larger than 1. Finally, we notice that in the $\texttt{MiNLO}_{\text{noprob}'}$ setup, where Sudakov form factors are forced to be smaller than or equal to 1, scale uncertainties are only slightly reduced compared to the $\texttt{MiNLO}_{\text{noprob}}$ case. From the above discussion, we conclude that for fixed-order calculations in the presence of fiducial phase-space cuts, the probabilistic Sudakov form factors defined in Eq. (5.14) provide a more robust description of the relevant kinematic configurations. In particular, by enforcing a probabilistic smooth interpretation of the no-emission probability through the $\mathcal{O}(\sqrt{t_{core}/t_1})$ corrections and preventing Sudakov form factors larger than unity, they yield substantially improved stability under renormalization and factorization scale variations in regions where the logarithmic hierarchy between the nodal and core scales is only moderate.

6.4 MiNLO vs NLO: Differential cross-section distributions

Up to this point, results have been presented only at the level of integrated fiducial cross sections. To fully investigate the effects of the MiNLO framework in our computations, it is essential to also present results at the differential cross-section level. This allows us to assess the impact of the MiNLO method across various regions of the phase space. To this end, we perform a comparison between standard NLO and MiNLO for the fully off-shell $pp \to e^+\nu_e\,\mu^-\bar{\nu}_\mu\,\tau^+\nu_\tau\,b\bar{b}\,j + X$ process for the following classes of observables: a) dimensionful observables involving light jets in their definition, b) dimensionful observables related to the kinematics of b jets and charged leptons, and c) dimensionless observables. The results are illustrated in Figs. 6.7 - 6.9, focusing on the transverse momentum of the hardest light jet $p_{T,\,j_1}$, the sum of the transverse momenta of the b and light jets (denoted as $H_{T,\,j}$), as well as the transverse momenta of the hardest b jet and positively charged lepton (labeled as $p_{T,\,b_1}$ and $p_{T,\,\ell_1^+}$, respectively). In addition, we show the angular separations between the hardest b and light jet ($\Delta R_{j_1 b_1}$) and between the two hardest positively charged leptons ($\Delta R_{\ell_1^+\ell_2^+}$). We refrain from presenting results for all the dynamical scales from Eq. (6.3), as they exhibit a similar behavior. For this reason, in all figures, results are displayed only for the dynamical $\mu_0 = E_T/2$ (left) and the fixed $\mu_0 = m_t + m_W/2$ (right) scale choices. As already discussed in Sec. 4.2.3, utilizing a fixed scale often leads to poor performance in the high-p_T regions of certain dimensionful observables, resulting in substantial NLO uncertainties or NLO QCD corrections falling outside the LO uncertainty bands. Particularly for the $pp \to t\bar{t}W^+ + X$ process in the multilepton channel [332], NLO uncertainties obtained with a fixed scale were found to be generally larger compared to those associated with a dynamical scale. We therefore present results also for the fixed scale choice $\mu_0 = m_t + m_W/2$ to determine whether this behavior persists once the MiNLO method is applied. The absolute NLO and MiNLO predictions are displayed in the upper panels of Figs. 6.7 - 6.9, while the MiNLO/NLO ratio is demonstrated in the middle panels. Finally, the bottom panels illustrate the magnitude of the scale uncertainties for the two approaches, normalized to their corresponding results.

We start by discussing the results presented in Fig. 6.7. First, we notice that

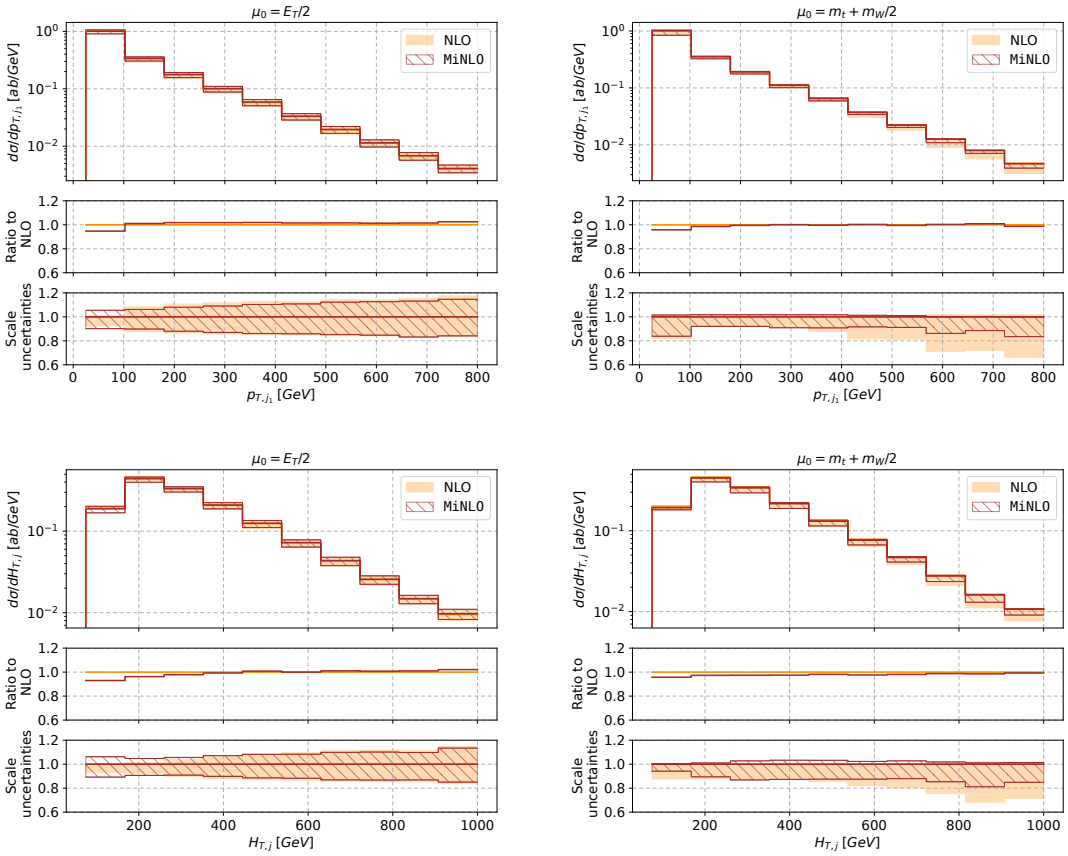

Figure 6.7: *Comparison between standard NLO and* `MiNLO` *for the* $pp \to e^+\nu_e\,\mu^-\bar{\nu}_\mu\,\tau^+\nu_\tau\,b\bar{b}\,j + X$ *process at the LHC with* $\sqrt{s} = 13\,\text{TeV}$*, using the dynamical* $\mu_0 = E_T/2$ *(left) and the fixed* $\mu_0 = m_t + m_W/2$ *(right) scale choices for the* p_{T,j_1} *and* $H_{T,j}$ *observables. The upper panels display the absolute predictions, while the middle panels depict the ratio to the standard NLO calculation. The size of the normalized scale uncertainties obtained from the seven-point scale variation is demonstrated in the bottom panels, both for standard NLO and* `MiNLO`*.*

standard NLO and `MiNLO` yield consistent outcomes across the entire plotted ranges, with mild differences up to 7% near the threshold regions. Second, for the dynamical scale, the magnitude of the theoretical uncertainties is similar between the two approaches for both the $p_{T,j}$ and the $H_{T,j}$ observables, reaching values between $15\% - 20\%$ in the high-p_T areas. The fixed scale choice $\mu_0 = m_t + m_W/2$, on the other hand, exhibits a distinct behavior, with substantial differences in the size of the theoretical uncertainties between standard NLO and `MiNLO`. Specifically, in the tails of the distributions, scale uncertainties are nearly half in size when the `MiNLO` method is employed, amounting to roughly 17% for p_{T,j_1} and 20% for $H_{T,j}$. In contrast, the corresponding uncertainties from the standard NLO calculations reach values as high as 34% for $p_{T,j}$ and 32% for $H_{T,j}$. To explain this behavior we note that the emission of a highly energetic jet increases the likelihood that the nodal scale q_1 extracted from the `MiNLO` method exceeds the fixed core scale. In such an unordered clustering scenario, as has been thoroughly discussed before, the core scale is set equal to the nodal scale q_1. Hence, in the high-p_T regions, the non-optimal behavior associated with the fixed scale is mitigated by enhancing its potential replacement with the q_1

scale, which more accurately captures the dynamics in this regime. This behavior is illustrated more clearly in the $H_{T,j}$ observable. Specifically, from the inverse k_T-clustering algorithm of Eq. (5.2), it is evident that the value of the q_1 scale depends on the transverse momentum of the light and b jets. Therefore, if q_1 becomes greater than $\mu_0 = m_t + m_W/2 \approx 212.7\,\text{GeV}$, then the core scale is effectively set equal to q_1. This situation can occur, for instance, when both b jets and the additional jet acquire transverse momenta greater than 212.7 GeV. Then, $H_{T,j} = p_{T,b_1} + p_{T,b_2} + p_{T,j_1}$ is larger than roughly 638 GeV and the $\mu_0 = m_t + m_W/2$ scale is completely discarded from the computation. Indeed, as shown in the bottom panel of Fig. 6.7, for values above approximately 600 GeV, the MiNLO scale uncertainties are consistently smaller than the standard NLO ones, thereby verifying our previous statement.

However, as illustrated in Fig. 6.8, the kinematics of the b jets and charged leptons are less influenced by the MiNLO method. The middle panels reveal that the MiNLO/NLO ratio remains very close to one across the entire ranges of the p_{T,b_1} and p_{T,ℓ_1^+} observables. On top of that, the size of the theoretical uncertainties is consistent between standard NLO and MiNLO for both scale choices depicted. In this case, the application of the MiNLO framework fails to mitigate the significant NLO uncertainties present in the high-p_T tails of p_{T,b_1} and p_{T,ℓ_1^+}, when the $\mu_0 = m_t + m_W/2$ scale is used. These uncertainties are as high as 40% and 90% regardless of whether the standard NLO or the MiNLO method is employed. On the one hand, for observables related to charged leptons this outcome is expected, as leptons do not participate in the clustering algorithm of the MiNLO method, leaving their kinematics unchanged. On the other hand, although the same is not true for the b jets, the presence of a highly energetic b jet is not sufficient for the fixed scale to be discarded from the computation in the high-p_T regime. Specifically, if the transverse momentum of the extra emitted light jet is less than 212.7 GeV, it directly follows from Eq. (5.2) that q_1 will be smaller than $\mu_0 = m_t + m_W/2$. Indeed, the light jet is predominantly produced with relatively small transverse momentum, as evident from the peak of the p_{T,j_1} distribution in Fig. (6.7), which is located below the value of 100 GeV. Thus, the use of $\mu_0 = m_t + m_W/2$ as the core scale will persist even in the high-p_T region of p_{T,b_1}.

We now shift our focus to the dimensionless observables demonstrated in Fig. 6.9. We find only minor deviations of at most 7% between standard NLO and MiNLO for the $\Delta R_{j_1 b_1}$ observable, which are nonetheless covered by the scale-uncertainty bands. For the angular separation between the two hardest positively charged leptons, the differences between the two approaches are negligible. Regarding the scale uncertainties, we observe a similar magnitude between standard NLO and MiNLO with small differences near the bulk of the events, especially when the fixed scale is employed. In particular, in these areas, MiNLO uncertainties are slightly smaller compared to those from the standard NLO computations, amounting to roughly 11% and 14%, respectively. Nevertheless, these discrepancies can be attributed to those already observed at the integrated level.

We conclude this part by highlighting that standard NLO and MiNLO are fully compatible at the differential cross-section level for all observables and scale choices we examined. While theoretical uncertainties are quite similar for the dynamical scales in both methods, when employing a fixed scale, MiNLO significantly reduces the magnitude of the theoretical error in the tails of dimensionful observables related to light jets.

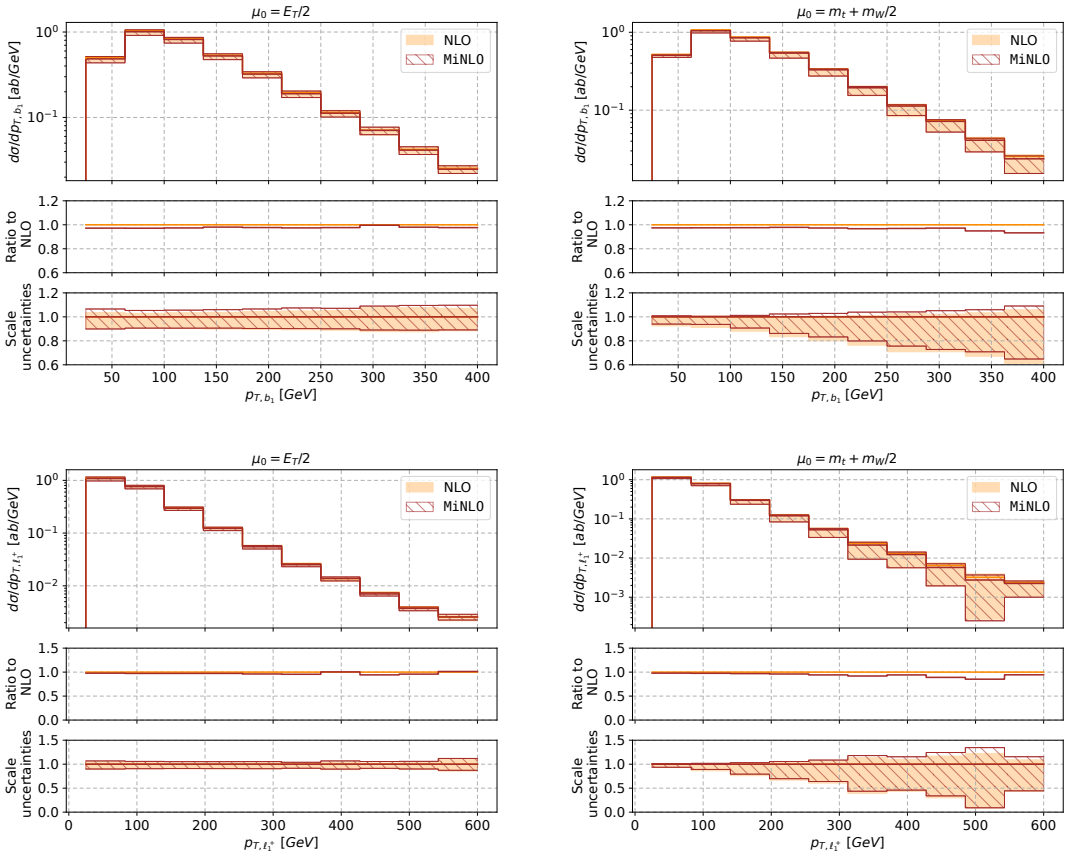

Figure 6.8: *Same as Fig. 6.7 but for the p_{T,b_1} (top) and the p_{T,ℓ_1^+} (bottom) distributions.*

We now move on and present differential distributions for the fully off-shell $pp \to e^+\nu_e\,\mu^-\bar{\nu}_\mu\,\tau^+\nu_\tau\,b\bar{b}\,jj$ process by comparing standard LO and MiLO. The objective is to study the behavior of the MiLO framework when more than one jet is present relative to the primary system in the final state. For this reason, we focus only on observables related to the kinematics of the light jets j_1 and j_2 as these are directly affected by the MiLO method. Results are presented in Figs. 6.10 and 6.12 for the p_{T,j_1}, p_{T,j_2}, $M_{j_1j_2}$ and $\Delta R_{j_1j_2}$ observables, following the same structure as in Figs. 6.7 - 6.9. In Fig. 6.10 significant shape distortions are found between standard LO and MiLO, especially in the tails of p_{T,j_1} and p_{T,j_2}. Specifically, the differences between the two methods are at the level of $25\% - 30\%$ for the transverse momentum of the hardest light jet for both the $\mu_0 = E_T/2$ and $\mu_0 = m_t + m_W/2$ scale choices. In contrast, the transverse momentum of the second hardest light jet exhibits a distinct behavior. In particular, when employing a dynamical scale, MiLO predictions are approximately 20% larger than those from standard LO in the high-p_T tail, while they are significantly smaller by roughly 45% when utilizing a fixed scale instead. To further investigate this behavior, in Fig. 6.11 we display the same observable for both scale choices normalized to their corresponding cross sections. Additionally, the middle and bottom panels illustrate the normalized ratios of the results obtained using the fixed scale $\mu_0 = m_t + m_W/2$ (denoted as (Mi)LO$_{\text{fix}}$) relative to those derived from the dynamical scale $\mu_0 = E_T/2$ (labeled as (Mi)LO$_{\text{dyn}}$) for the standard LO and MiLO calculations. Plotting the normalized distributions allows us

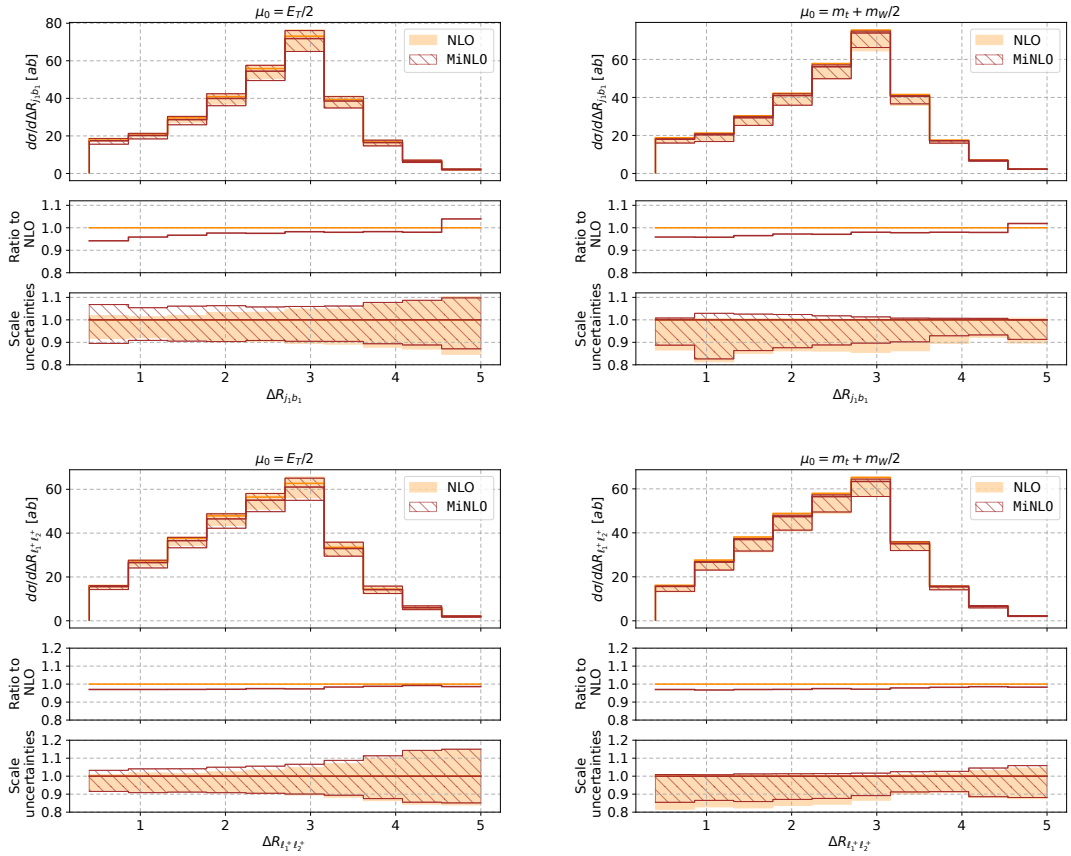

Figure 6.9: *Same as Fig. 6.7 but for the* $\Delta R_{j_1 b_1}$ *(top) and the* $\Delta R_{\ell_1^+ \ell_2^+}$ *(bottom) distributions.*

to identify potential shape distortions, as the integrated fiducial cross sections differ significantly between the fixed and dynamical scales (see Table 6.2). From the middle panel of Fig. 6.11, large shape distortions are observed between $\mathrm{LO}_{\mathrm{dyn}}$ and $\mathrm{LO}_{\mathrm{fix}}$ reaching up to 75%. In contrast, when the MiLO method is applied, these distortions are considerably reduced to only 20% in the tails. This indicates that employing the MiLO framework helps to bring the normalized predictions obtained with the fixed and dynamical scales closer together, whereas the standard LO calculations fail to do so, resulting in substantial shape differences between the two scales in the high-p_T tails. Thus, the MiLO results exhibit a reduced overall scale sensitivity also at the differential level. Returning to Fig. 6.10, we also highlight that for both scale choices considered, the MiLO theoretical uncertainties are smaller compared to those from standard LO. These differences are especially pronounced in the tails of the distributions, where the MiLO scale uncertainties are noticeably reduced.

Shifting our focus to Fig. 6.12, we notice that MiLO and standard LO are in a better agreement with each other for the $M_{j_1 j_2}$ and $\Delta R_{j_1 j_2}$ observables, with deviations of at most 20% in certain phase-space regions. Furthermore, both standard LO and MiLO predictions produce similar shapes for the $\Delta R_{j_1 j_2}$ distribution, as indicated by the relatively flat MiLO/LO ratio. However, while the same is true for the $M_{j_1 j_2}$ observable when the fixed scale is employed, small shape distortions are observed for the dynamical scale. These differences are, nonetheless, covered by the large scale-uncertainty bands. Finally, similar to what was observed before, the

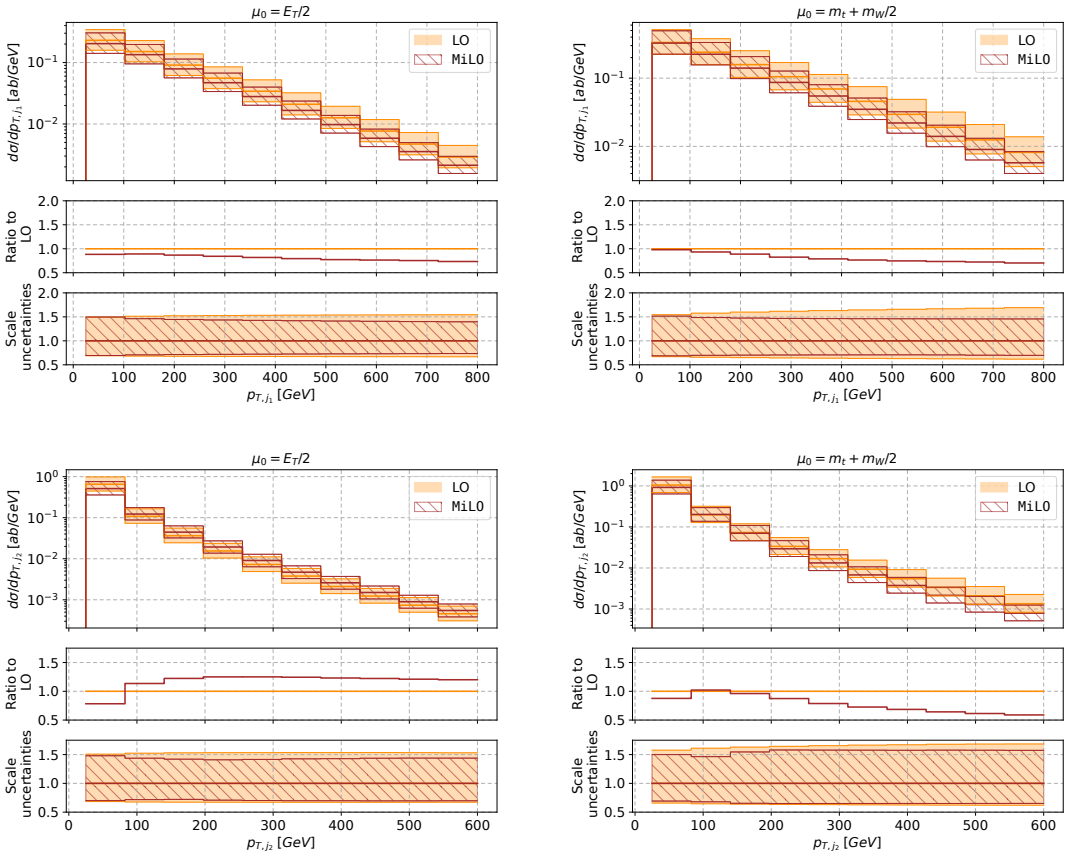

Figure 6.10: *Comparison between standard LO and* `MiLO` *for the fully off-shell* $pp \to e^+\nu_e\,\mu^-\bar{\nu}_\mu\,\tau^+\nu_\tau\,b\bar{b}\,jj$ *process at the LHC with* $\sqrt{s} = 13\,\text{TeV}$*, using the dynamical* $\mu_0 = E_T/2$ *(left) and the fixed* $\mu_0 = m_t + m_W/2$ *(right) scale choices for the* p_{T,j_1} *and* p_{T,j_2} *observables. The upper panels display the absolute predictions, while the middle panels depict the ratio to the standard LO calculation. The size of the normalized scale uncertainties obtained from the seven-point scale variation is demonstrated in the bottom panels, both for standard LO and* `MiLO`*.*

theoretical uncertainties from `MiLO` are either smaller than or comparable to those from standard LO across the entire plotted ranges.

6.5 Merged predictions

In the final section of this chapter, we present merged predictions of the fully off-shell

$$\begin{aligned} pp &\to e^+\nu_e\,\mu^-\bar{\nu}_\mu\,\tau^+\nu_\tau\,b\bar{b} + X\,, \\ pp &\to e^+\nu_e\,\mu^-\bar{\nu}_\mu\,\tau^+\nu_\tau\,b\bar{b}\,j + X\,, \\ pp &\to e^+\nu_e\,\mu^-\bar{\nu}_\mu\,\tau^+\nu_\tau\,b\bar{b}\,jj \end{aligned} \tag{6.12}$$

processes at NLO in QCD, by introducing an appropriate merging-scale parameter $p_{T,merging}$. The merging of the above samples with different jet multiplicities is done

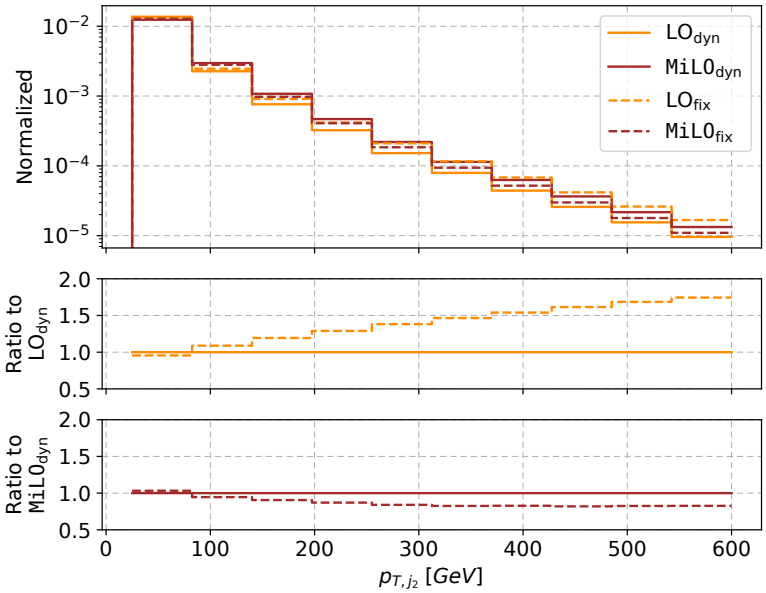

Figure 6.11: *Normalized differential distributions for the fully off-shell* $pp \to e^+\nu_e\,\mu^-\bar{\nu}_\mu\,\tau^+\nu_\tau\,b\bar{b}\,jj$ *process at the LHC with* $\sqrt{s} = 13\,\text{TeV}$*, using the fixed* $\mu_0 = m_t + m_W/2$ *(labeled with the subscript "fix") and the dynamical* $\mu_0 = E_T/2$ *(labeled with the subscript "dyn") scale choices for the* p_{T,j_2} *observable. Results are displayed both for standard LO and* MiLO*, including the ratio to* LO_{dyn} *and* $\texttt{MiLO}_{\text{dyn}}$ *in the middle and bottom panels, respectively.*

either up to one or two jets according to the following formulas:

$$\left(\sigma^{\texttt{MiNLO}}_{pp\to t\bar{t}W^+ + jets}\right)^{\text{up to 1 jet}}_{\text{merged}} = \left(\sigma^{\texttt{MiNLO}}_{pp\to t\bar{t}W^+}\right)_{\text{excl}} + \left(\sigma^{\texttt{MiNLO}}_{pp\to t\bar{t}W^+ j}\right)_{\text{incl}}, \tag{6.13}$$

$$\left(\sigma^{\texttt{MiNLO}}_{pp\to t\bar{t}W^+ + jets}\right)^{\text{up to 2 jets}}_{\text{merged}} = \left(\sigma^{\texttt{MiNLO}}_{pp\to t\bar{t}W^+}\right)_{\text{excl}} + \left(\sigma^{\texttt{MiNLO}}_{pp\to t\bar{t}W^+ j}\right)_{\text{excl}} + \left(\sigma^{\texttt{MiLO}}_{pp\to t\bar{t}W^+ jj}\right), \tag{6.14}$$

where the MiNLO method is applied independently to each sample. As discussed at the beginning of this chapter, the above method for merging samples with different jet multiplicities is not the one originally proposed in Ref. [416]. As a consequence, the Sudakov form factors do not ensure a smooth transition between samples. In fact, we have explicitly verified that the merged results obtained using the standard NLO approach are very similar to those obtained in our MiNLO setup, with only minor differences that fall well within the theoretical uncertainties. For this reason, we present results only for the latter case, highlighting, however, that both methods yield consistent outcomes that agree with each other within the theoretical errors. In the above formulas, the $pp \to t\bar{t}W^+$ sample is exclusive to any radiation above the merging scale, which in practice means that any real emission radiation with transverse momentum above $p_{T,merging}$ is vetoed. A similar logic applies to the exclusive $pp \to t\bar{t}W^+ j$ sample when the merging includes up to two jets. In this scenario, the hardest light jet must satisfy $p_{T,j_1} > p_{T,merging}$, while any potential second light jet should have a transverse momentum below the merging scale. If the merging is performed up to one jet, there are no restrictions on the transverse momentum of the second hardest light jet j_2, and the sample is therefore inclusive to any extra radiation. Finally, in the $pp \to t\bar{t}W^+ jj$ sample, the transverse mo-

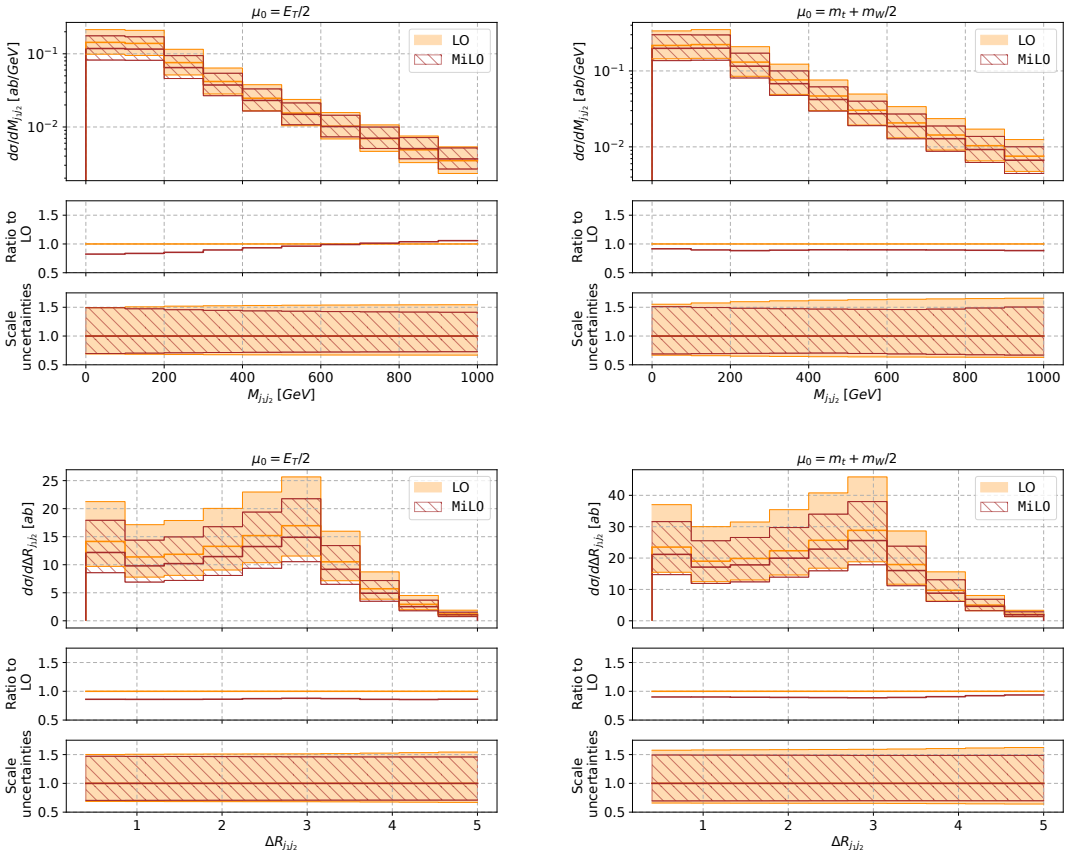

Figure 6.12: *Same as Fig. 6.10 but for the $M_{j_1j_2}$ (top) and $\Delta R_{j_1j_2}$ (bottom) distributions.*

menta of both light jets remain unrestricted as long as they pass the generation cuts (Eq. (6.2)). This approach, referred to as MiNLO $\oplus$ Direct sum, ensures that there is no double counting of contributions, thereby providing consistent results. Nonetheless, the choice of the merging-scale parameter $p_{T,\,merging}$ remains arbitrary. On the one hand, large values for the merging scale suggest that hard real emissions are mainly described by lower-multiplicity samples, thereby reducing the effective contribution of higher-multiplicity matrix elements and diminishing the purpose of the merging procedure. On the other hand, choosing the merging scale too close to the generation cut implies that the description of most of the phase space relies on higher-multiplicity samples, which may lead to large uncertainties. To more thoroughly examine the dependence of the merged-predictions on this parameter, in Fig. 6.13 we present the integrated merged results for several values of $p_{T,\,merging}$. The results are shown for the following scale choices: $\mu_0 = E_T/2, E_T/3, H_T/2, H_T/3$ and for merging up to one and two jets according to Eqs. (6.13) and (6.14). The upper panels display the merged predictions, labeled as MiNLO $\oplus$ Direct sum along with the inclusive full off-shell NLO $pp \to e^+\nu_e\,\mu^-\bar{\nu}_\mu\,\tau^+\nu_\tau\,b\bar{b} + X$ cross section, denoted as $t\bar{t}W^+ + X$. The middle panels illustrate the size of the scale uncertainties for both cases normalized to their corresponding predictions, while in the bottom panels, the ratio to the inclusive $t\bar{t}W^+ + X$ sample is also demonstrated. The first universal comment from Fig. 6.13 is that for all scale choices depicted, the merged cross sections exhibit substantial scale uncertainties at low values of the $p_{T,\,merging}$ param-

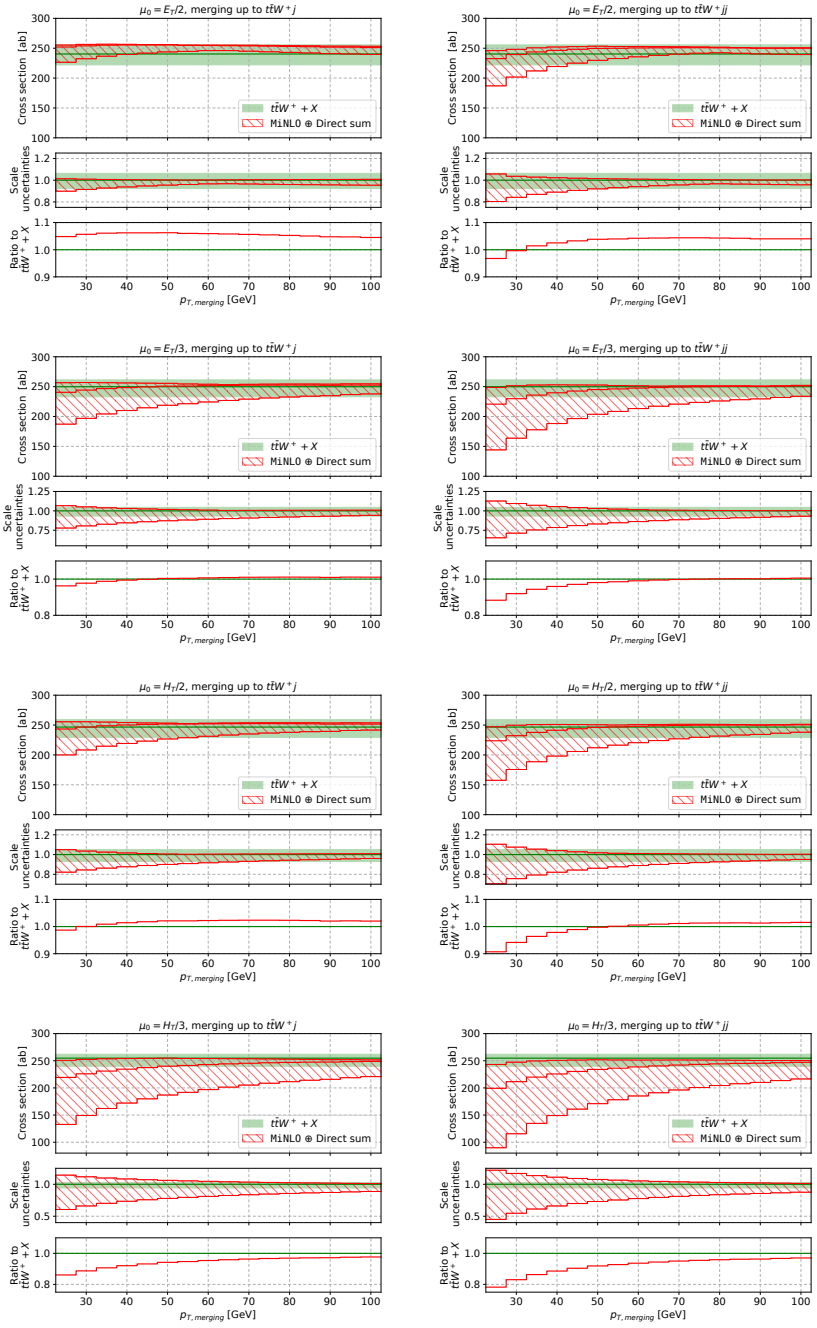

Figure 6.13: *Integrated cross sections after merging the fully off-shell* $pp \to e^+\nu_e\,\mu^-\bar{\nu}_\mu\,\tau^+\nu_\tau\,b\bar{b}$ + jets *processes including up to one (left) or two (right) jets, according to Eqs.* (6.13) *and* (6.14) *after employing the* MiNLO *method to the individual samples. The results are displayed using a center-of-mass energy of* $\sqrt{s} = 13\,\text{TeV}$ *at the LHC and for multiple values of the merging parameter* $p_{T,merging} \in [25, 100]\,\text{GeV}$. *Also shown with green are the cross sections for the NLO inclusive* $pp \to e^+\nu_e\,\mu^-\bar{\nu}_\mu\,\tau^+\nu_\tau\,b\bar{b} + X$ *sample, the size of the scale uncertainties for the two approaches in the middle panels and the ratio to the inclusive* $pp \to e^+\nu_e\,\mu^-\bar{\nu}_\mu\,\tau^+\nu_\tau\,b\bar{b} + X$ *NLO sample in the bottom panels. The predictions are illustrated after utilizing the following scale choices:* $\mu_0 = E_T/2, E_T/3, H_T/2, H_T/3$ *based on the definitions in Eqs.* (6.4) *and* (6.5).

eter, while the magnitude of the theoretical errors reduces as $p_{T,\,merging}$ increases. However, the actual size of the scale uncertainties strongly depends on the scale choice, varying between $10\% - 50\%$ when $p_{T,\,merging}$ is close to the generation cut. Although differences in uncertainty sizes among the various scales persist at larger merging-scale values, they are less pronounced, ranging from $5\% - 10\%$. Additionally, we notice that the inclusion of a second leading-order light jet in the merging procedure results in larger theoretical uncertainties compared to merging up to one jet, with most pronounced differences occurring again in the region near the generation cut. This is to be expected, since by employing small $p_{T,\,merging}$ values one relies more on the higher-jet multiplicities, and in particular the $pp \to t\bar{t}W^+jj$ sample, the accuracy of which is only LO. It is worth mentioning that in this regime, the merged uncertainties are significantly larger compared to those from the inclusive full off-shell NLO $pp \to e^+\nu_e\,\mu^-\bar{\nu}_\mu\,\tau^+\nu_\tau\,b\bar{b} + X$ sample. This indicates that selecting small values for the merging parameter does not lead to improved predictions for this process. Furthermore, the large deviations among the various scales suggest that the use of the `MiNLO` method does not help to reduce the scale sensitivity of the merged results. This is because of the sharp vetoing of additional radiation in exclusive regions of the phase space. Consequently, the impact of the Sudakov form factors and the scale setting for extra emissions based on the most probable branching history is modest, while the dominant influence arises from the remaining strong coupling constants evaluated at the arbitrarily-chosen core scale. Returning to Fig. 6.13, we note that the ratio to the full off-shell NLO $pp \to e^+\nu_e\,\mu^-\bar{\nu}_\mu\,\tau^+\nu_\tau\,b\bar{b} + X$ sample is also quite sensitive to both scale choice and value of $p_{T,\,merging}$, with the largest deviations observed in the low $p_{T,\,merging}$ regime. For instance, for the $\mu_0 = E_T/2$ scale choice, the aforementioned ratio ranges between $1.04 - 1.06$, while for $\mu_0 = H_T/3$ it constantly remains below 1, reaching values up to 0.85 near the threshold. Incorporating the second leading jet in the merging procedure reduces the ratio to the full off-shell $pp \to e^+\nu_e\,\mu^-\bar{\nu}_\mu\,\tau^+\nu_\tau\,b\bar{b} + X$ sample for small $p_{T,\,merging}$ values, while its effect diminishes as the value of the merging-scale parameter grows. In general, the substantial theoretical errors of the merged results when small $p_{T,\,merging}$ values are used are primarily driven by the large uncertainties associated with the exclusive samples. This has also been partially studied in Ref. [337], where similar large uncertainties were observed in the exclusive full off-shell $pp \to t\bar{t}W^+$ and $pp \to t\bar{t}W^+j$ NLO samples. To further clarify this, in Table 6.5 we present the merged cross sections obtained using $\mu_0 = E_T/2$ and $p_{T,\,merging} = 25\,\text{GeV}$ for all (ξ_R, ξ_F) setups of the seven-point scale variation, along with the corresponding individual uncertainties from the inclusive and exclusive samples. We observe that the large 20% uncertainty originates from the $(\xi_R, \xi_F) = (1/2, 1/2)$ setup, in which both the $pp \to t\bar{t}W^+$ and $pp \to t\bar{t}W^+j$ exclusive samples exhibit large theoretical errors, amounting to 29% and 26%, respectively. It is also worth noting that both samples contribute with the same sign in the overall error. Hence, when both uncertainty values are large, a considerable counterbalancing contribution in the opposite direction is required from the $pp \to t\bar{t}W^+jj$ sample to mitigate the overall uncertainty. This implies that the merged cross section along with its uncertainty is highly sensitive to the LO predictions of the $pp \to t\bar{t}W^+jj$ process. To gain more reliable predictions, one should therefore include the NLO $pp \to t\bar{t}W^+jj$ sample in the merging procedure, which is beyond the scope of this thesis. To further illustrate this point, we just mention that if the `MiNLO` cross section is higher than

(ξ_R, ξ_F)	$\sigma^{\text{MiNLO}}_{t\bar{t}W^+}(N_j = 0)$ [ab]	$\sigma^{\text{MiNLO}}_{t\bar{t}W^+j}(N_j = 1)$ [ab]	$\sigma^{\text{MiLO}}_{t\bar{t}W^+jj}(N_j = 2)$ [ab]	$\sigma^{\text{MiNLO}}_{merged}$ [ab]
$(1, 1)$	$115.5^{+13\%}_{-29\%}$	$75.8^{+9\%}_{-27\%}$	$41.3^{+46\%}_{-29\%}$	$232.6^{+6\%}_{-20\%}$

(ξ_R, ξ_F)	$\delta\sigma^{\text{MiNLO}}_{t\bar{t}W^+}(N_j = 0)$ [ab]	$\delta\sigma^{\text{MiNLO}}_{t\bar{t}W^+j}(N_j = 1)$ [ab]	$\delta\sigma^{\text{MiLO}}_{t\bar{t}W^+jj}(N_j = 2)$	$\delta\sigma^{\text{MiNLO}}_{merged}$ [ab]
$(2, 2)$	$+14.7$ $(+13\%)$	$+6.7$ $(+9\%)$	-7.9 (-19%)	13.4 $(+6\%)$
$(1/2, 1/2)$	-33.9 (-29%)	-19.6 (-26%)	$+8.0$ $(+19\%)$	-45.6 (-20%)
$(2, 1)$	$+12.9$ $(+11\%)$	$+4.2$ $(+6\%)$	-12.1 (-29%)	$+5.0$ $(+2\%)$
$(1/2, 1)$	-28.8 (-25%)	-20.1 (-27%)	$+19.2$ $(+46\%)$	-29.7 (-13%)
$(1, 2)$	$+3.5$ $(+3\%)$	$+1.2$ $(+2\%)$	$+6.0$ $(+15\%)$	$+11.0$ $(+5\%)$
$(1, 1/2)$	-2.8 (-2%)	-3.1 (-4%)	-7.6 (-18%)	-13.4 (-6%)

Table 6.5: *Merged results of the fully off-shell* $pp \to t\bar{t}W^+ +$ jets *processes in the multilepton channel at the LHC with* $\sqrt{s} = 13\,\text{TeV}$*, obtained using the* MiNLO $\oplus$ *Direct sum procedure with up to 2 jets (Eq.* (6.14)*) and a merging parameter equal to* $p_{T,merging} = 25\ GeV$*, for the* $\mu_0 = E_T/2$ *scale choice. Results are also shown separately for the seven* (ξ_R, ξ_F) *setups used in the standard seven-point scale variation.*

the MiLO one for the $pp \to t\bar{t}W^+jj + X$ process, the sizable overall uncertainty of the merged result stemming from the exclusive samples can be compensated by the larger overall weight of the NLO $pp \to t\bar{t}W^+jj + X$ contribution into the merged cross section.

From all the above, it is evident that the scale choice which enhances the predictions for the fully off-shell NLO $pp \to t\bar{t}W^+ + X$ process is $\mu_0 = E_T/2$. In this scenario, the theoretical uncertainties of the merged predictions are smaller than those of the inclusive NLO $pp \to t\bar{t}W^+ + X$ process for merging-scale values above approximately 55 GeV, particularly when the merging also incorporates the LO fully off-shell $pp \to t\bar{t}W^+jj$ sample. If this sample is excluded from the merging procedure, all scanned $p_{T,\,merging}$ values above 40 GeV yield smaller scale uncertainties, with values around 60 GeV resulting in the smallest theoretical errors. In addition, around this value, the merged cross section is about $4\% - 6\%$ larger than that of the inclusive $pp \to t\bar{t}W^+ + X$ process. These differences are, however, encompassed by the scale uncertainties of the latter, which are roughly 8%.

In the following, we proceed by presenting merged results at the differential cross-section level, focusing solely on the $\mu_0 = E_T/2$ scale and adopting $p_{T,\,merging} = 60\,\text{GeV}$, while also incorporating the LO fully off-shell $pp \to t\bar{t}W^+jj$ sample into the merging procedure. We have explicitly verified that excluding this sample produces results that are compatible within the uncertainties, as the influence of the second leading-order light jet in the merging is mild for $p_{T,\,merging}$ values away from the generation cut. In fact, only small normalization differences are found but no shape distortions between merging up to one or up to two jets. However, alternative choices of $p_{T,\,merging}$ could be employed, potentially leading to significantly different predictions. On top of that, one may in principle introduce distinct merging parameters for vetoing radiation in Eq. (6.14). In such a setup, any radiation with $p_T > p'_{T,\,merging}$ is vetoed in the $pp \to t\bar{t}W^+$ process, while in

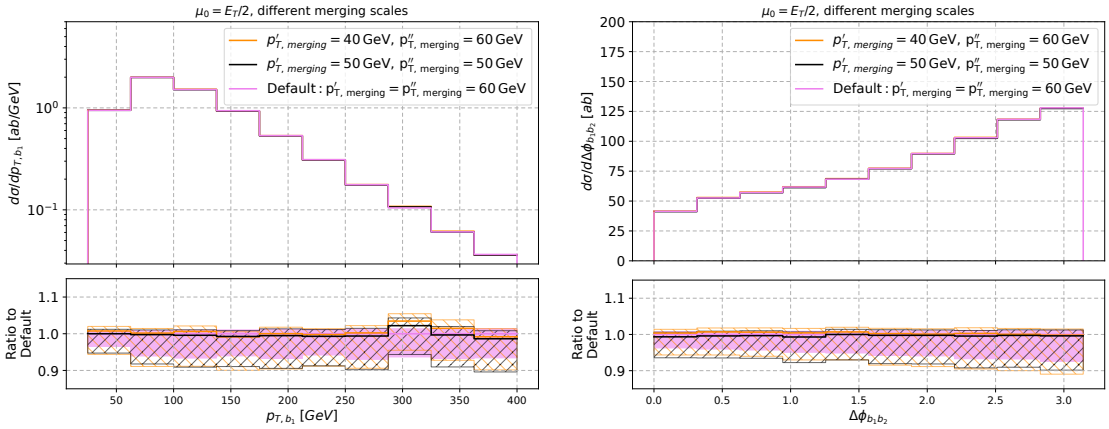

Figure 6.14: *Differential merged predictions for the fully off-shell* $pp \to e^+\nu_e\,\mu^-\bar{\nu}_\mu\,\tau^+\nu_\tau\,b\bar{b}$ + jets *process at the LHC with* $\sqrt{s} = 13\,\text{TeV}$*, obtained using Eq. (6.14) and the* $\mu_0 = E_T/2$ *scale. The scale* $p'_{T,\,merging}$ *sets the maximum transverse momentum for emissions in the* $pp \to t\bar{t}W^+ + X$ *sample and the minimum* p_T *for the leading jet in* $pp \to t\bar{t}W^+j + X$*, while* $p''_{T,\,merging}$ *sets the veto for the second jet in* $pp \to t\bar{t}W^+j + X$ *and the minimum transverse momentum for both jets in the* $pp \to t\bar{t}W^+jj$ *sample. The upper panels display the absolute results, while the lower panels demonstrate the magnitude of scale uncertainties for all setups, derived from seven-point scale variation and normalized to the default configuration.*

$pp \to t\bar{t}W^+j$ the leading jet is required to satisfy $p_T > p'_{T,\,merging}$ and the second (if present) to fulfill $p_T < p''_{T,\,merging}$, where $p'_{T,\,merging}$ and $p''_{T,\,merging}$ may differ. In this case, to avoid double counting, both leading jets in the $pp \to t\bar{t}W^+jj$ sample must satisfy $p_T > p''_{T,\,merging}$. To investigate the effects of using different merging-scale parameters, in Fig. 6.14 we present differential results for three distinct scenarios: $p'_{T,\,merging} = p''_{T,\,merging} = 60\,\text{GeV}$ (Default), $p'_{T,\,merging} = p''_{T,\,merging} = 50\,\text{GeV}$ and $p'_{T,\,merging} = 40\,\text{GeV}$, $p''_{T,\,merging} = 60\,\text{GeV}$. We focus only on the transverse momentum of the hardest b jet and the azimuthal angle between the two hardest b jets, but the same conclusions were drawn for all observables examined. In addition to the absolute predictions in the upper panels, the bottom panels display the size of the scale uncertainties for each setup normalized to our default configuration. First, we find only minor deviations between the different setups, which are nonetheless covered by the scale-uncertainty bands. Second, we notice that the alternative setups yield larger overall theoretical uncertainties compared to the case where $p'_{T,\,merging} = p''_{T,\,merging} = 60\,\text{GeV}$. This behavior reflects the differences previously noted at the integrated fiducial cross-section level. Given that no significant discrepancies are observed among the various setups, in what follows, we stick to our default configuration in which $p_{T,\,merging} = 60\,\text{GeV}$ is utilized. The differential merged results are demonstrated in Figs. 6.15 - 6.17, along with the corresponding predictions from the fully off-shell inclusive $pp \to t\bar{t}W^+ + X$ NLO sample. All figures follow the same layout as the individual plots in Fig. 6.13: the upper panels show the absolute predictions, the middle panels display the scale uncertainties, and the bottom panels present the ratio to the inclusive $pp \to t\bar{t}W^+ + X$ process. In Fig. 6.15, the following observables are shown: p_{T,b_1}, p_{T,b_1b_2}, $H_{T,b}$ and $p_{T,miss}$. In all cases, the ratio of the merged predictions to the inclusive $pp \to t\bar{t}W^+ + X$ results increases in the high-p_T region, while remaining below 1.05 near the bulk of the

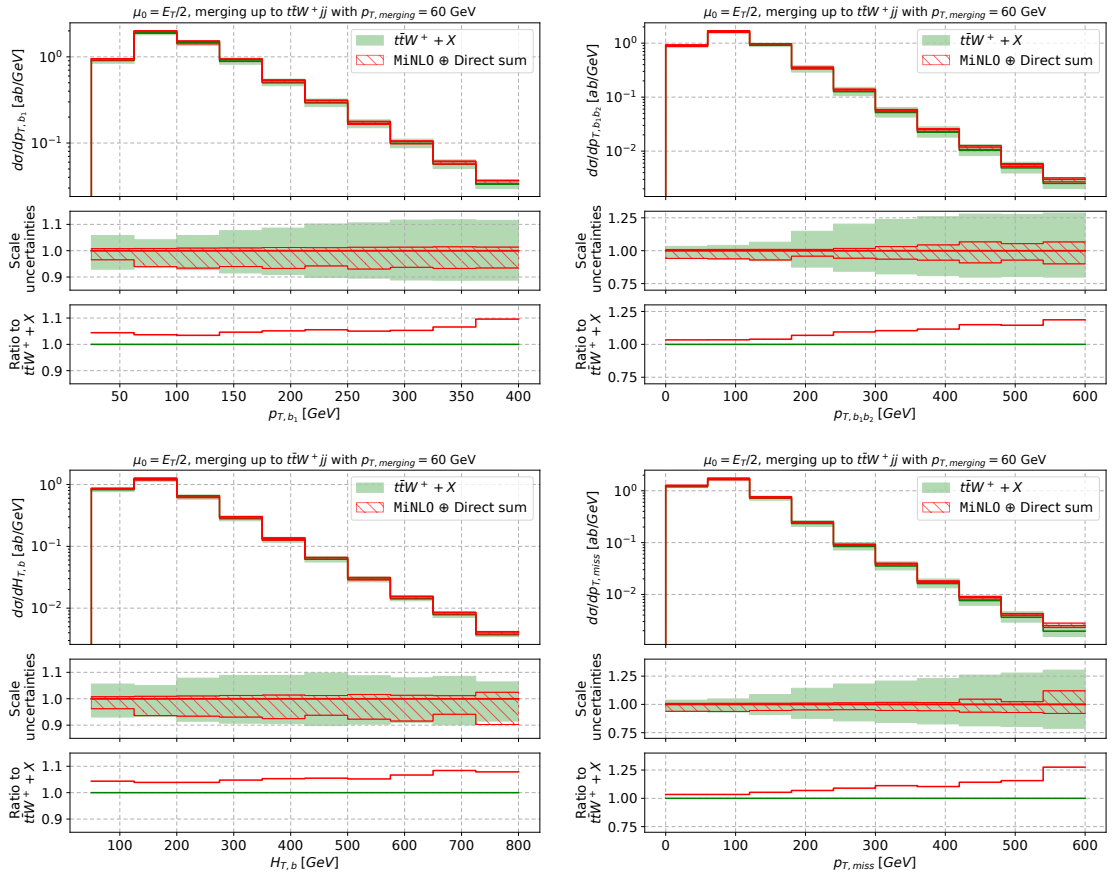

Figure 6.15: *Differential cross-section distributions for the fully off-shell* $pp \to e^+\nu_e\,\mu^-\bar{\nu}_\mu\,\tau^+\nu_\tau\,b\bar{b} +$ jets *processes, including up to two jets according to Eq.* (6.14)*, by utilizing* $p_{T,merging} = 60\,\text{GeV}$ *as the merging-scale parameter. Also shown are the corresponding predictions for the fully off-shell* $pp \to e^+\nu_e\,\mu^-\,\bar{\nu}_\mu\,\tau^+\nu_\tau\,b\bar{b} + X$ *NLO process, along with scale-uncertainty bands derived from standard seven-point scale variation. The observables displayed are the following:* $p_{T,b_1}, p_{T,b_1b_2}, H_{T,b}$*, and* $p_{T,miss}$*. All results are generated using a center-of-mass energy of* $\sqrt{s} = 13\,\text{TeV}$ *at the LHC and employing the dynamical scale choice of* $\mu_0 = E_T/2$*. The middle panels depict the magnitude of scale uncertainties for each approach normalized to their corresponding results, while the bottom panels illustrate the ratio to the inclusive* $pp \to e^+\nu_e\,\mu^-\,\bar{\nu}_\mu\,\tau^+\nu_\tau\,b\bar{b} + X$ *sample.*

events. Notably, the most pronounced differences are observed in the tails of the p_{T,b_1b_2} and $p_{T,miss}$ distributions, reaching approximately 20% and 25%, respectively. In these regions, the theoretical uncertainties from the $pp \to t\bar{t}W^+ + X$ process are substantial, exceeding 25%. As a consequence, the discrepancies described above are only slightly covered by the green scale-uncertainty bands. Meanwhile, the MiNLO ⊕ Direct sum predictions yield considerably smaller uncertainties, amounting to at most 12%. Regarding the p_{T,b_1} and $H_{T,b}$ distributions, the ratio of the merged prediction relative to the $t\bar{t}W^+$ NLO sample remains consistently below 1.10. Nevertheless, even in these cases, merging the $pp \to t\bar{t}W^+ +$ jets samples reduces the theoretical uncertainties across all plotted ranges, resulting in an improved modeling of the $pp \to t\bar{t}W^+ + X$ process.

We now shift our focus to observables related to the charged leptons in the final

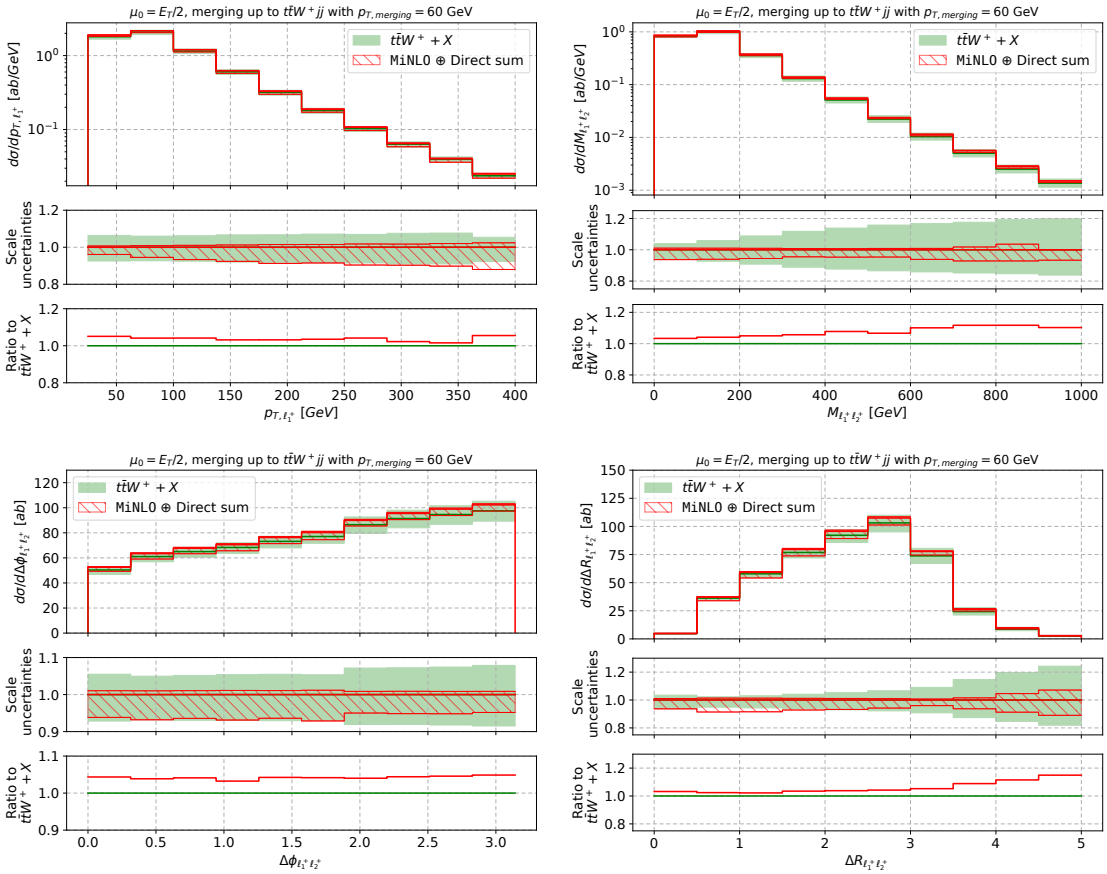

Figure 6.16: *Same as Fig. 6.15 but for the* p_{T,ℓ_1^+}, $M_{\ell_1^+\ell_2^+}$, $\Delta\phi_{\ell_1^+\ell_2^+}$ *and* $\Delta R_{\ell_1^+\ell_2^+}$ *distributions.*

state. Specifically, in Fig. 6.16 we show the transverse momentum of the hardest positively charged lepton p_{T,ℓ_1^+}, the invariant mass of the two positively charged leptons $M_{\ell_1^+\ell_2^+}$, as well as the azimuthal angle and angular separation between these two leptons, denoted as $\Delta\phi_{\ell_1^+\ell_2^+}$ and $\Delta R_{\ell_1^+\ell_2^+}$, respectively. Overall, also for the leptonic observables, merging the $pp \to t\bar{t}W^+ +$ jets processes results in smaller theoretical errors and enhances the modeling of the $pp \to t\bar{t}W^+ + X$ process. For instance, in the case of the invariant mass $M_{\ell_1^+\ell_2^+}$, the merged uncertainties remain remarkably the same across the entire plotted range, never exceeding 7%, while those from the inclusive $pp \to t\bar{t}W^+ + X$ sample reach as high as 20% in the tail of the distribution. On the other hand, for the other observables shown, the scale uncertainties from the MiNLO ⊕ Direct sum approach may be slightly larger or comparable to those from $pp \to t\bar{t}W^+ + X$, but they always remain smaller in regions where most events are populated. Finally, the discrepancies between the two approaches are rather modest, constantly remaining below 15%.

Nevertheless, there are certain types of observables where the theoretical uncertainties from the merged predictions are not guaranteed to be smaller than those from the inclusive $pp \to t\bar{t}W^+ + X$ process, even in regions where most events are concentrated. To illustrate this, in Fig. 6.17, we display the rapidity of the hardest positively charged lepton, $y_{\ell_1^+}$, and its azimuthal angle relative to the muon, labelled as $\Delta\phi_{\ell_1^+\mu^-}$. In both cases, near the bulk of the events, the MiNLO ⊕ Direct sum uncertainties are larger compared to those from the $pp \to t\bar{t}W^+ + X$ process, although

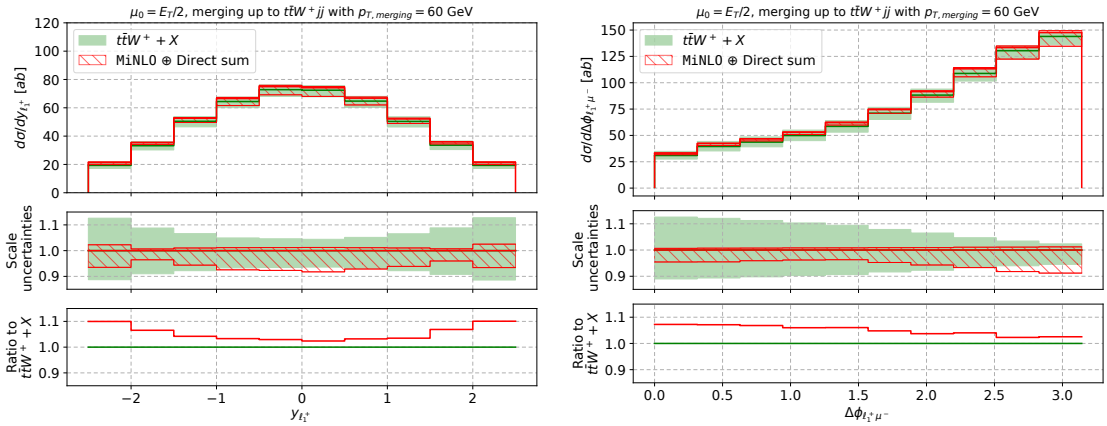

Figure 6.17: *Same as Fig. 6.15 but for the* $y_{\ell_1^+}$ *and* $\Delta\phi_{\ell_1^+\mu^-}$ *distributions.*

they are noticeably smaller in other phase-space regions. In addition, the differences between the two approaches remain below 2%−3% in areas where most events are expected, while they become more pronounced in regions with fewer populated events. However, the latter discrepancies are relatively modest since the ratio of the merged predictions to the inclusive $pp \to t\bar{t}W^+ + X$ results reaches a maximum of around 1.10, which lies well within the scale-uncertainty bands.

Chapter 7

Conclusions

In this thesis, the primary focus is on top-quark associated processes in which additional heavy particles are produced together with a $t\bar{t}$ pair. In particular, two of the rarest processes at the LHC are studied: the production of four top quarks and the production of a W^+ boson in association with a $t\bar{t}$ pair and additional jets.

For the $pp \to t\bar{t}t\bar{t}$ process, the main objective is to improve the theoretical predictions available in the literature by providing precise calculations at NLO in QCD. In these calculations, NLO QCD corrections are included both in the production and in the decay stages of the top quarks, thereby preserving spin correlations at NLO accuracy. This is particularly important because, in many existing studies, the decays of the top quarks are treated only at LO accuracy, which effectively limits the accuracy of spin correlations to LO. While matching the results to parton-shower algorithms leads to phenomenologically more realistic predictions that can be directly compared with experimental data, improving the accuracy of the matrix-element calculation itself is equally important. Since NNLO predictions for this process are currently beyond reach, the present work focuses on improving the description of $t\bar{t}t\bar{t}$ decays by incorporating higher-order QCD effects in the decays already at the matrix-element level. The results are presented for the 4ℓ and 3ℓ channels using a center-of-mass energy of $\sqrt{s} = 13.6\,\text{TeV}$ at the LHC. Both of these channels provide clean signatures in $t\bar{t}t\bar{t}$ experimental searches at the LHC and have already been targeted by the ATLAS and CMS collaborations. The calculations are performed within the narrow-width approximation (NWA), where the top quarks and the $W^\pm$ bosons are treated exactly on shell. Since different NWA treatments are possible, we investigate several setups. In particular, we consider the case where QCD corrections are applied only to the production stage of the top quarks, denoted as $\text{NLO}_{\text{LO}_{\text{dec}}}$, as well as the scenario in which QCD corrections are included in both production and decay stages and the top-quark width is expanded in α_s. The latter constitutes our default setup and is labeled as NLO_{exp}, or simply NLO. Finally, we also examine the effect of not expanding the top-quark width, referred to as NLO_{full}.

For the 4ℓ channel, we find that incorporating QCD effects in the top-quark decays is essential as it reduces the size of scale uncertainties from 23% to 20%. If the NLO_{full} setup is employed, the reduction is even more pronounced, resulting in scale uncertainties of the order of 15%. The differences between the various NWA setups are found to be between $8\% - 12\%$, which is well within the theoretical uncertainties for this process. Interestingly, the projected uncertainties at the High-Luminosity LHC (HL-LHC) are estimated at $15\%-18\%$, highlighting the importance

of including QCD corrections in the top-quark decays for a more accurate comparison with the future experimental data.

For the 3ℓ channel, preserving the validity of the perturbative expansion requires imposing a restriction on the invariant mass of the two light jets. In the absence of such a constraint, very large corrections are observed, with $\mathcal{K} = \sigma^{\mathrm{NLO}}/\sigma^{\mathrm{LO}}$ reaching values of 1.8–2.3, indicating a breakdown of the perturbative description. To ensure a stable perturbative behavior, the invariant mass of the light-jet pair M_{jj} is required to lie close to the $W^{\pm}$ boson mass m_W, implemented through the condition $|M_{jj} - m_W| < Q_{cut}$. We present results for several values of Q_{cut} and analyze the sensitivity of the fiducial cross sections to this parameter. The different NWA treatments are found to be particularly sensitive to the choice of Q_{cut}, with more pronounced differences for smaller values of this parameter. For the choice $Q_{cut} = 25\,\mathrm{GeV}$, the QCD corrections remain moderate, and the scale uncertainties lie in the range 19%–25%, depending on the NWA setup considered. Contrary to the study of the 4ℓ channel, where QCD corrections remain modest for most of the observables examined at the differential cross-section level, the 3ℓ channel exhibits substantial shape distortions between the NLO and LO predictions. These large NLO effects arise primarily from new topologies that open up at NLO and are absent at LO. We find that observables related to light jet kinematics are especially sensitive to these effects, leading to gigantic $\mathcal{K}$ factors in certain phase-space regions. In addition, including QCD corrections in the decays of the top quarks proves to be essential, especially for dimensionless observables sensitive to spin correlations. In these cases, differences between the $\mathrm{NLO}_{\mathrm{exp}}$ and $\mathrm{NLO}_{\mathrm{LO_{dec}}}$ setups can reach up to 22%, exceeding the NLO uncertainty bands. Overall, the results for both channels demonstrate that including NLO QCD corrections in top-quark decays constitutes an important step toward improving the theoretical precision of four-top production at the LHC and will be essential for meaningful comparisons with future HL-LHC measurements.

Beyond the standard NLO fixed-order calculations, we also investigate the `MiNLO` method, in which the renormalization and factorization scales are dynamically determined by identifying the most probable sequence of parton branchings. The additional inclusion of Sudakov form factors further enhances the accuracy of the computation by accounting for the probability of no resolvable emissions between two given scales. We present the implementation of the `MiNLO` method within the Helac-Nlo framework in a fully generic way that can be applied to arbitrary processes. Special emphasis is devoted to assessing the impact of systematic uncertainties associated with the various options available within the `MiNLO` framework.

We apply the `MiNLO` method to the fully off-shell $pp \to t\bar{t}W^+ + \{0, 1, 2\}$ jets processes in the multilepton channel at the LHC with $\sqrt{s} = 13\,\mathrm{TeV}$. As some tension between theoretical predictions and experimental data persists for the $pp \to t\bar{t}W^+$ process, it is important to push towards more accurate theoretical predictions that may provide further insight into the comparison with the experimental measurements. In this thesis, we improve the full off-shell predictions by dynamically extracting the scales associated with the additional jets relative to the $t\bar{t}W^+$ system through the application of the `MiNLO` method. To assess the scale sensitivity of the method, several scale choices are examined. We find that the `MiNLO` and NLO predictions are compatible within theoretical uncertainties, while `MiNLO` generally exhibits a reduced scale dependence for most of the scale choices considered. Interestingly, this reduction becomes more pronounced with increasing jet multiplicity.

In particular, for the LO fully off-shell $pp \to t\bar{t}W^+jj$ process, we observe a decrease in the size of the uncertainties of about $9\% - 17\%$. This behavior indicates that the motivation for applying the MiNLO method becomes stronger as additional jets are included with respect to the underlying hard process. The effects of the MiNLO method become more pronounced when suboptimal scales are employed or when large transverse momentum thresholds are imposed in the event generation. In such cases, the MiNLO scale uncertainties can be reduced by up to a factor of two compared to those obtained with standard NLO predictions. At the differential cross-section level, NLO and MiNLO predictions generally exhibit similar behavior. However, MiNLO provides improved predictions for certain dimensionful observables related to light jets when fixed scale choices are used, resulting in smaller scale uncertainties. Furthermore, we investigate the impact of various prescriptions entering the MiNLO method, including the procedure used for scale variations, the choice of the resolution parameter in the inverse k_T-clustering algorithm, and the form of the Sudakov form factors employed. We find that the differences among the alternative prescriptions are generally negligible, with the only significant effects arising from the choice of Sudakov form factors. In particular, the Sudakov form factors used in the original MiNLO paper [138] lead, in general, to substantially larger uncertainties, reaching values up to three times larger than those obtained in our default setup.

Finally, we present results for the merging of the fully off-shell $pp \to t\bar{t}W^+ +$ jets samples, after introducing an appropriate merging-scale parameter to avoid double counting of contributions. As highlighted in the text, this merging corresponds to a direct sum of exclusive samples in which the MiNLO method is applied separately and should not be confused with the widely employed merging procedure originally proposed in Ref. [416] where no merging scale is introduced. In general, merging is important for improving the overall modeling of the fully off-shell $pp \to t\bar{t}W^+$ process. We find that the results are highly sensitive both to the scale choice used in the calculation and to the value of the merging-scale parameter $p_{T,\,merging}$. Among the scales considered, the best performance is obtained with the dynamical scale $\mu_0 = E_T/2$, defined as the transverse energy of the $t\bar{t}W^+$ system. Even with this choice, merged predictions for $p_{T,\,merging}$ values below 40 GeV exhibit larger uncertainties than those of the inclusive $t\bar{t}W^+ + X$ NLO sample. For larger $p_{T,\,merging}$ values, however, the merged predictions lead to reduced theoretical uncertainties. This reduction improves the description of the full off-shell $t\bar{t}W^+$ dynamics and may become relevant for future experimental analyses targeting this process. A similar behavior is observed at the differential cross-section level, where scale uncertainties decrease once appropriate values of the merging-scale parameter are chosen.

Appendix A

Appendix

A.1 The MiNLO input card

The MiNLO method has been implemented into the HELAC-NLO framework [388], particularly in the HEPLOT program [442], which is used internally for reweighting purposes. For enabling the method, one needs to modify the minlo_input_card, containing the following settings:

- MINLO: true/false. If true, the MiNLO method is used. Otherwise, the calculation is performed using the standard NLO approach, and all settings below are ignored.
- CORE_SCALE: A string used as a label to identify the definition of the core scale. The exact definition of this scale should be given within the corescale() function in the src/Event.C file in HEPLOT.
- QCD_CORE_PARTICLES: the ID of the QCD particles comprising the core system in the final state, according to the standard Particle Data Group (PDG) format [50], e.g. $6\ -6$ for the $pp \to t\bar{t}$ + jets processes.
- SCALE_VARIATION: 1 (default) or 2.
  - 1: Scale variation according to the original MiNLO prescription, as described in Sec. 5.3.
  - 2: Scale variation according to Refs. [126, 501], as described in Sec. 5.3.
- XIF_SUDAKOVS: 0 or 1 (default).
  - 0: No ξ_F variation in the Sudakovs, referring to $\texttt{MiNLO}_{\text{no}\xi_{\text{F}}}$.
  - 1: Factorization scale variation is performed in the Sudakovs according to Eqs. (5.11), (5.12) and (5.13).
- MINLO_R: The resolution parameter R used in the k_T-clustering algorithm of Eq. (5.2).
- TOP_MASS: The top-quark mass in GeV needed for the evaluation of $N_f(t)$ and for the calculation of the Sudakov integrand in general.

An example of how the minlo_input_card looks like for the $pp \to t\bar{t}+$jets processes is displayed in Fig. A.1.

```
MINLO: true
CORE_SCALE: ET/2
QCD_CORE_PARTICLES: 6 -6
SCALE_VARIATION: 1
XIF_SUDAKOVS: 1
MINLO_R: 1.0
TOP_MASS: 173.2
```

Figure A.1: *Example of the MiNLO input card for the* $pp \to t\bar{t}+$jets *processes.*

A.2 Cross checks for the MiNLO implementation

We have performed several cross-checks to verify the validity of our implementation. More specifically, we tested the MiNLO method both at LO and NLO accuracy directly with the Sherpa code [410–413], where MiNLO is available and can also be used for fixed-order calculations. The comparison was performed for the stable $pp \to t\bar{t}$ process with up to 3 jets at LO and 2 jets at NLO accuracy. The results were obtained using a center of mass energy equal to $\sqrt{s} = 13$ TeV, a fiducial phase space cut of $p_{T,j} > 25$ GeV for the light jets, the $m_t = 173.2$ GeV top mass and the CT14nlo PDF set [471]. We also used the following dynamical scale-choice:

$$\mu_0 = \frac{E_T}{2} = \frac{\sum_{i=t,\bar{t}} \sqrt{m_i^2 + p_{T,i}^2}}{2}, \tag{A.1}$$

where light jets can also be included in the sum only in cases where they are treated as part of the primary system. Regarding the MiNLO settings, we employed a resolution parameter equal to $R = 1.0$ for the inverse k_T-clustering algorithm and used the prescription from Refs. [126,501] for the evaluation of the renormalization scale and the extra strong coupling, as explained in Sec. 5.3. As a first step, we compared the Sudakov weight w_{Sudakov}, the nodal scales, the μ_R and q_{core} scales, as well as the $\alpha_s^{(n+m+1)}$ coupling for several phase-space points. Examples of such phase-space points are displayed below for the Born piece of the $gg \to t\bar{t}g$ subprocess, where the Sudakov subtraction is also included, and for the $\mathcal{R}-\mathcal{S}$ term of the $gg \to t\bar{t}ggg$ and $gu \to t\bar{t}c\bar{c}u$ subprocesses.

1. $gg \to t\bar{t}g$ subprocess (subtracted Born term $\mathcal{B}$ as given in Eq. (5.21)):

Type	p_x [GeV]	p_y [GeV]	p_z [GeV]	E [GeV]
g	0	0	103.328356112770	103.328356112770
g	-0	-0	-1182.12309037673	1182.12309037673
g	-9.435761096532	-151.341598784394	-31.044602584095	154.780749641846
t	-35.434144400221	-13.816581579615	-364.869723232313	405.677989848533
$\bar{t}$	44.869905496752	165.158180364009	-682.880408447796	724.992706999364

	SHERPA	HEPLOT
w_{Sudakov}	0.997713295553	0.997713295553
q_1 [GeV]	151.635461255233	151.635461255233
q_{core} [GeV]	210.409720855166	210.409720855166
$\alpha_s^{(n+m+1)}$	0.106391362603	0.106391362603

2. $gg \to t\bar{t}ggg$ subprocess ($\mathcal{R} - \mathcal{S}$ part):

Type	p_x [GeV]	p_y [GeV]	p_z [GeV]	E [GeV]
g	0,	0	-1006.65582747817	1006.65582747817
g	-0	-0	559.236440130181	559.236440130181
g	-78.107539952349	-77.248410284959	-181.790238797365	212.404791873828
g	37.144548347715	36.350845323541	-50.229437205834	72.277920485488
g	97.819509084225	52.247551913132	115.646168468072	160.22640019591
t	262.929245800577	86.541549716352	261.870130061459	418.56353537184
$\bar{t}$	-319.785763280168	-97.891536668066	-592.916009874319	702.419619681283

	SHERPA	HEPLOT
w_{Sudakov}	0.734755400480	0.734755400475
q_1 [GeV]	109.854925647242	109.854925647242
q_2 [GeV]	110.898435689573	110.898435689572
μ_R [GeV]	192.424912285012	192.424912288438
q_{core} [GeV]	351.574048223905	351.574048223905
$\alpha_s^{(n+m+1)}$	0.106082536865	0.106082536865

3. $gu \to t\bar{t}c\bar{c}u$ subprocess ($\mathcal{R} - \mathcal{S}$ part):

Type	p_x [GeV]	p_y [GeV]	p_z [GeV]	E [GeV]
g	-0	-0	948.348450370996	948.348450370996
u	0	0	-185.120556691368	185.120556691368
u	112.306762385601	-68.048693152855	236.709348188877	270.69309011748
c	-0.074561025648	0.006298652314	-11.055865984183	11.056119196163
$\bar{c}$	-82.0572343657	125.867106115529	305.078291883043	340.071584070061
t	38.751420602778	-131.519066572819	23.636210578763	222.161760709269
$\bar{t}$	-68.926387597031	73.69435495783	208.859909013128	289.48645296939

	SHERPA	HEPLOT
w_{Sudakov}	0.964154916442	0.964154916442
q_1 [GeV]	131.314254813966	131.314254813966
q_2 [GeV]	150.298855092298	150.298855092298
μ_R [GeV]	171.495352738380	171.495352738453
q_{core} [GeV]	210.675094550737	210.675094550737
$\alpha_s^{(n+m+1)}$	0.107756437025	0.107756437025

From the above tables, we notice that our implementation, denoted as HEPLOT,

agrees perfectly with the Shepra code at the matrix element level. Indeed, the Sudakov weights agree to $10-12$ digits, while the nodal scales, the core scale, and the $\alpha_s^{(n+m+1)}$ coupling are identical between SHERPA and HEPLOT. The renormalization scale μ_R also shows very good agreement, at the level of 8–9 digits. The slightly reduced precision in this case originates from its evaluation through Eqs. (5.26) and (5.25), where the effective scale q_{eff} is obtained using numerical methods. Since the numerical procedures used in our implementation differ from those internal to SHERPA, a small discrepancy at the 8–9th digit level is expected.

After the comparison at the matrix element level, we also tested our implementation at the integrated fiducial cross-section level. The central predictions are displayed in Table A.1 obtained using our implementation (HEPLOT) and the SHERPA code. [1] Also shown is the statistical significance of the difference between SHERPA and HEPLOT, denoted as σ_{dev}.

Process	$\sigma^{\texttt{MiLO}}_{\text{SHERPA}}$ [pb]	$\sigma^{\texttt{MiLO}}_{\text{HEPLOT}}$ [pb]	σ_{dev}	$\sigma^{\texttt{MiNLO}}_{\text{SHERPA}}$ [pb]	$\sigma^{\texttt{MiNLO}}_{\text{HEPLOT}}$ [pb]	σ_{dev}
$pp \to t\bar{t}j$	262.14(6)	262.12(5)	0.13	381.26(67)	381.08(52)	0.21
$pp \to t\bar{t}jj$	113.41(4)	113.40(2)	0.22	161.5(1.9)	160.1(1.3)	0.61
$pp \to t\bar{t}jjj$	41.153(23)	41.126(14)	1.00	–	–	–

Table A.1: *Integrated fiducial cross sections using the* `MiLO` *and* `MiNLO` *frameworks for the* $pp \to t\bar{t}+$ jets *processes. Results are obtained using the* SHERPA *code and our implementation (*HEPLOT*), with the statistical significance of their difference, denoted by* σ_{dev}*, also depicted.*

We observe an excellent level of agreement of $0.13-1.00\,\sigma$ between SHERPA and HEPLOT. For the $pp \to t\bar{t}jjj$ process, results were obtained only at LO accuracy due to the complexity of the process at NLO, which involves up to 4 light QCD partons. Therefore, our implementation has been validated for processes containing up to three light jets in the final state, in addition to those potentially present in the core process.

[1] In contrast to our default setup, for the $t\bar{t}j$ `MiNLO` cross section, and for the purpose of testing alternative prescriptions, if q_{core} is larger than the last extracted nodal scale, the last branching is undone and the core scale is re-evaluated, treating the partons involved in the last clustering as part of the primary system.

Bibliography

[1] Murray Gell-Mann. A Schematic Model of Baryons and Mesons. *Phys. Lett.*, 8:214–215, 1964.

[2] G. Zweig. *An SU(3) model for strong interaction symmetry and its breaking. Version 2, Part of Developments in the Quark Theory of Hadrons. Vol. 1, DOI:10.17181/CERN-TH-401*, pages 22–101. 1964.

[3] Murray Gell-Mann. The Eightfold Way: A Theory of strong interaction symmetry, California Institute of Technology Report CTSL-20, TID-12608. 1961.

[4] Yuval Ne'eman. Derivation of strong interactions from a gauge invariance. *Nucl. Phys.*, 26:222–229, 1961.

[5] S. L. Glashow, J. Iliopoulos, and L. Maiani. Weak Interactions with Lepton-Hadron Symmetry. *Phys. Rev. D*, 2:1285–1292, 1970.

[6] J. J. Aubert et al. Experimental Observation of a Heavy Particle J. *Phys. Rev. Lett.*, 33:1404–1406, 1974.

[7] J. E. Augustin et al. Discovery of a Narrow Resonance in e^+e^- Annihilation. *Phys. Rev. Lett.*, 33:1406–1408, 1974.

[8] J. H. Christenson, J. W. Cronin, V. L. Fitch, and R. Turlay. Evidence for the 2π Decay of the K_2^0 Meson. *Phys. Rev. Lett.*, 13:138–140, 1964.

[9] Nicola Cabibbo. Unitary Symmetry and Leptonic Decays. *Phys. Rev. Lett.*, 10:531–533, 1963.

[10] Makoto Kobayashi and Toshihide Maskawa. CP Violation in the Renormalizable Theory of Weak Interaction. *Prog. Theor. Phys.*, 49:652–657, 1973.

[11] S. W. Herb et al. Observation of a Dimuon Resonance at 9.5 GeV in 400 GeV Proton-Nucleus Collisions. *Phys. Rev. Lett.*, 39:252–255, 1977.

[12] Martin L. Perl et al. Evidence for Anomalous Lepton Production in e+ - e- Annihilation. *Phys. Rev. Lett.*, 35:1489–1492, 1975.

[13] Stephen L. Adler. Axial vector vertex in spinor electrodynamics. *Phys. Rev.*, 177:2426–2438, 1969.

[14] J. S. Bell and R. Jackiw. A PCAC puzzle: $\pi^0 \to \gamma\gamma$ in the σ model. *Nuovo Cim. A*, 60:47–61, 1969.

[15] Eduard Boos, Oleg Brandt, Dmitri Denisov, Sergey Denisov, and Paul Grannis. The top quark (20 years after its discovery). *Phys. Usp.*, 58(12):1133–1158, 2015.

[16] G. S. Abrams et al. Searches for New Quarks and Leptons Produced in Z Boson Decay. *Phys. Rev. Lett.*, 63:2447, 1989.

[17] D. Decamp et al. A Search for New Quarks and Leptons From Z^0 Decay. *Phys. Lett. B*, 236:511–522, 1990.

[18] P. Abreu et al. Search for the T and b′ Quarks in Hadronic Decays of the Z^0 Boson. *Phys. Lett. B*, 242:536–546, 1990.

[19] M. Z. Akrawy et al. A Search for the Top and b' Quarks in Hadronic Z^0 Decays. *Phys. Lett. B*, 236:364–374, 1990.

[20] S. Abachi et al. Search for high mass top quark production in $p\bar{p}$ collisions at $\sqrt{s} = 1.8$ TeV. *Phys. Rev. Lett.*, 74:2422–2426, 1995.

[21] F. Abe et al. Evidence for top quark production in $\bar{p}p$ collisions at $\sqrt{s} = 1.8$ TeV. *Phys. Rev. D*, 50:2966–3026, 1994.

[22] F. Abe et al. Observation of top quark production in $\bar{p}p$ collisions. *Phys. Rev. Lett.*, 74:2626–2631, 1995.

[23] S. Abachi et al. Observation of the top quark. *Phys. Rev. Lett.*, 74:2632–2637, 1995.

[24] Georges Aad et al. The ATLAS experiment at the CERN Large Hadron Collider: a description of the detector configuration for Run 3. *JINST*, 19(05):P05063, 2024.

[25] Giuseppe Degrassi, Stefano Di Vita, Joan Elias-Miro, Jose R. Espinosa, Gian F. Giudice, Gino Isidori, and Alessandro Strumia. Higgs mass and vacuum stability in the Standard Model at NNLO. *JHEP*, 08:098, 2012.

[26] K. Agashe et al. Report of the Topical Group on Top quark physics and heavy flavor production for Snowmass 2021, arXiv:2209.11267 [hep-ph]. 2022.

[27] André H. Hoang. What is the Top Quark Mass? *Ann. Rev. Nucl. Part. Sci.*, 70:225–255, 2020.

[28] S. Alekhin, A. Djouadi, and S. Moch. The top quark and Higgs boson masses and the stability of the electroweak vacuum. *Phys. Lett. B*, 716:214–219, 2012.

[29] Anders Andreassen, William Frost, and Matthew D. Schwartz. Scale Invariant Instantons and the Complete Lifetime of the Standard Model. *Phys. Rev. D*, 97(5):056006, 2018.

[30] Andre H. Hoang, Christopher Lepenik, and Moritz Preisser. On the Light Massive Flavor Dependence of the Large Order Asymptotic Behavior and the Ambiguity of the Pole Mass. *JHEP*, 09:099, 2017.

[31] M. Beneke, P. Marquard, P. Nason, and M. Steinhauser. On the ultimate uncertainty of the top quark pole mass. *Phys. Lett. B*, 775:63–70, 2017.

[32] Peter Bärnreuther, Michal Czakon, and Alexander Mitov. Percent Level Precision Physics at the Tevatron: First Genuine NNLO QCD Corrections to $q\bar{q} \to t\bar{t} + X$. *Phys. Rev. Lett.*, 109:132001, 2012.

[33] Michal Czakon and Alexander Mitov. NNLO corrections to top pair production at hadron colliders: the quark-gluon reaction. *JHEP*, 01:080, 2013.

[34] Michal Czakon and Alexander Mitov. NNLO corrections to top-pair production at hadron colliders: the all-fermionic scattering channels. *JHEP*, 12:054, 2012.

[35] Michał Czakon, Paul Fiedler, and Alexander Mitov. Total Top-Quark Pair-Production Cross Section at Hadron Colliders Through $O(\alpha_S^4)$. *Phys. Rev. Lett.*, 110:252004, 2013.

[36] G. Aad et al. Combination of inclusive top-quark pair production cross-section measurements using ATLAS and CMS data at $\sqrt{s} = 7$ and 8 TeV. *JHEP*, 07:213, 2023.

[37] Georges Aad et al. Determination of the top-quark pole mass using $t\bar{t}$ + 1-jet events collected with the ATLAS experiment in 7 TeV pp collisions. *JHEP*, 10:121, 2015.

[38] Georges Aad et al. Measurement of the top-quark mass in $t\bar{t}$ + 1-jet events collected with the ATLAS detector in pp collisions at $\sqrt{s} = 8$ TeV. *JHEP*, 11:150, 2019.

[39] Armen Tumasyan et al. Measurement of the top quark pole mass using t$\bar{\text{t}}$+jet events in the dilepton final state in proton-proton collisions at $\sqrt{s} = 13$ TeV. *JHEP*, 07:077, 2023.

[40] Georges Aad et al. Precise measurement of the $t\bar{t}$ production cross-section and lepton differential distributions in $e\mu$ dilepton events from $\sqrt{s} = 13$ TeV pp collisions with the ATLAS detector. *Eur. Phys. J. C*, 86(5):470, 2026.

[41] Georges Aad et al. Measurement of the top-quark pole mass in dileptonic $t\bar{t}$ + 1-jet events at $\sqrt{s} = 13$ TeV with the ATLAS experiment. *JHEP*, 12:023, 2025.

[42] Albert M Sirunyan et al. Measurement of t$\bar{\text{t}}$ normalised multi-differential cross sections in pp collisions at $\sqrt{s} = 13$ TeV, and simultaneous determination of the strong coupling strength, top quark pole mass, and parton distribution functions. *Eur. Phys. J. C*, 80(7):658, 2020.

[43] M. Aaboud et al. Measurement of lepton differential distributions and the top quark mass in $t\bar{t}$ production in pp collisions at $\sqrt{s} = 8$ TeV with the ATLAS detector. *Eur. Phys. J. C*, 77(11):804, 2017.

[44] Kaoru Hagiwara, Yukinari Sumino, and Hiroshi Yokoya. Bound-state Effects on Top Quark Production at Hadron Colliders. *Phys. Lett. B*, 666:71–76, 2008.

[45] Y. Kiyo, Johann H. Kuhn, S. Moch, M. Steinhauser, and P. Uwer. Top-quark pair production near threshold at LHC. *Eur. Phys. J. C*, 60:375–386, 2009.

[46] Wan-Li Ju, Guoxing Wang, Xing Wang, Xiaofeng Xu, Yongqi Xu, and Li Lin Yang. Top quark pair production near threshold: single/double distributions and mass determination. *JHEP*, 06:158, 2020.

[47] LHCTopWG Summary Plots - Top Quark Mass. `https://twiki.cern.ch/twiki/bin/view/LHCPhysics/LHCTopWGSummaryPlots#Top_Quark_Mass`, copyright terms of the CC-BY-4.0 license apply, 2026.

[48] Aram Hayrapetyan et al. Combination of Measurements of the Top Quark Mass from Data Collected by the ATLAS and CMS Experiments at $\sqrt{s} = 7$ and 8 TeV. *Phys. Rev. Lett.*, 132(26):261902, 2024.

[49] Armen Tumasyan et al. Measurement of the top quark mass using a profile likelihood approach with the lepton + jets final states in proton–proton collisions at $\sqrt{s} = 13\,\text{TeV}$. *Eur. Phys. J. C*, 83(10):963, 2023.

[50] S. Navas et al. Review of particle physics. *Phys. Rev. D*, 110(3):030001, 2024.

[51] Long Chen, Xiang Chen, Xin Guan, and Yan-Qing Ma. Top-quark decay at next-to-next-to-next-to-leading order in QCD. *Phys. Rev. D*, 114(3):034005, 2026.

[52] Andrzej Czarnecki and Kirill Melnikov. Two loop QCD corrections to top quark width. *Nucl. Phys. B*, 544:520–531, 1999.

[53] Long-Bin Chen, Hai Tao Li, Jian Wang, and Yefan Wang. Analytic result for the top-quark width at next-to-next-to-leading order in QCD. *Phys. Rev. D*, 108(5):054003, 2023.

[54] Ansgar Denner and Thomas Sack. The Top width. *Nucl. Phys. B*, 358:46–58, 1991.

[55] G. Eilam, R. R. Mendel, R. Migneron, and A. Soni. Radiative corrections to top quark decay. *Phys. Rev. Lett.*, 66:3105–3108, 1991.

[56] ATLAS Collaboration. Measurement of the top-quark decay width in top-quark pair events in the dilepton channel at $\sqrt{s} = 13$ TeV with the ATLAS detector, ATLAS-CONF-2019-038. 2019.

[57] Christian Herwig, Tomáš Ježo, and Benjamin Nachman. Extracting the Top-Quark Width from Nonresonant Production. *Phys. Rev. Lett.*, 122(23):231803, 2019.

[58] Vardan Khachatryan et al. Measurement of the Ratio $\mathcal{B}(t \to Wb)/\mathcal{B}(t \to Wq)$ in pp Collisions at $\sqrt{s} = 8$ TeV. *Phys. Lett. B*, 736:33–57, 2014.

[59] Morad Aaboud et al. Measurements of top-quark pair spin correlations in the $e\mu$ channel at $\sqrt{s} = 13$ TeV using pp collisions in the ATLAS detector. *Eur. Phys. J. C*, 80(8):754, 2020.

[60] Albert M Sirunyan et al. Measurement of the top quark polarization and $t\bar{t}$ spin correlations using dilepton final states in proton-proton collisions at $\sqrt{s} =$ 13 TeV. *Phys. Rev. D*, 100(7):072002, 2019.

[61] Georges Aad et al. Observation of quantum entanglement with top quarks at the ATLAS detector. *Nature*, 633(8030):542–547, 2024.

[62] Aram Hayrapetyan et al. Observation of quantum entanglement in top quark pair production in proton–proton collisions at $\sqrt{s} = 13$ TeV. *Rept. Prog. Phys.*, 87(11):117801, 2024.

[63] Alexander Huss, Joey Huston, Stephen Jones, Mathieu Pellen, and Raoul Röntsch. Les Houches 2023 – Physics at TeV Colliders: Report on the Standard Model Precision Wishlist, SciPost Phys. Comm. Rep. 21. 2026.

[64] P. Nason, S. Dawson, and R. Keith Ellis. The Total Cross-Section for the Production of Heavy Quarks in Hadronic Collisions. *Nucl. Phys. B*, 303:607–633, 1988.

[65] P. Nason, S. Dawson, and R. Keith Ellis. The One Particle Inclusive Differential Cross-Section for Heavy Quark Production in Hadronic Collisions. *Nucl. Phys. B*, 327:49–92, 1989. [Erratum: Nucl.Phys.B 335, 260–260 (1990)].

[66] W. Beenakker, H. Kuijf, W. L. van Neerven, and J. Smith. QCD Corrections to Heavy Quark Production in $p\bar{p}$ Collisions. *Phys. Rev. D*, 40:54–82, 1989.

[67] W. Beenakker, W. L. van Neerven, R. Meng, G. A. Schuler, and J. Smith. QCD corrections to heavy quark production in hadron hadron collisions. *Nucl. Phys. B*, 351:507–560, 1991.

[68] W. Beenakker, Ansgar Denner, W. Hollik, R. Mertig, T. Sack, and D. Wackeroth. Electroweak one loop contributions to top pair production in hadron colliders. *Nucl. Phys. B*, 411:343–380, 1994.

[69] Johann H. Kuhn, A. Scharf, and P. Uwer. Electroweak corrections to top-quark pair production in quark-antiquark annihilation. *Eur. Phys. J. C*, 45:139–150, 2006.

[70] Werner Bernreuther, Michael Fuecker, and Zong-Guo Si. Weak interaction corrections to hadronic top quark pair production. *Phys. Rev. D*, 74:113005, 2006.

[71] Johann H. Kuhn, A. Scharf, and P. Uwer. Electroweak effects in top-quark pair production at hadron colliders. *Eur. Phys. J. C*, 51:37–53, 2007.

[72] Wolfgang Hollik and Monika Kollar. NLO QED contributions to top-pair production at hadron collider. *Phys. Rev. D*, 77:014008, 2008.

[73] Stefano Frixione and Bryan R. Webber. Matching NLO QCD computations and parton shower simulations. *JHEP*, 06:029, 2002.

[74] Stefano Frixione, Paolo Nason, and Bryan R. Webber. Matching NLO QCD and parton showers in heavy flavor production. *JHEP*, 08:007, 2003.

[75] Paolo Nason. A New method for combining NLO QCD with shower Monte Carlo algorithms. *JHEP*, 11:040, 2004.

[76] Stefano Frixione, Paolo Nason, and Carlo Oleari. Matching NLO QCD computations with Parton Shower simulations: the POWHEG method. *JHEP*, 11:070, 2007.

[77] Simone Alioli, Paolo Nason, Carlo Oleari, and Emanuele Re. A general framework for implementing NLO calculations in shower Monte Carlo programs: the POWHEG BOX. *JHEP*, 06:043, 2010.

[78] John M. Campbell, R. Keith Ellis, Paolo Nason, and Emanuele Re. Top-Pair Production and Decay at NLO Matched with Parton Showers. *JHEP*, 04:114, 2015.

[79] A. Denner, S. Dittmaier, S. Kallweit, and S. Pozzorini. NLO QCD corrections to WWbb production at hadron colliders. *Phys. Rev. Lett.*, 106:052001, 2011.

[80] Giuseppe Bevilacqua, Michal Czakon, Andreas van Hameren, Costas G. Papadopoulos, and Malgorzata Worek. Complete off-shell effects in top quark pair hadroproduction with leptonic decay at next-to-leading order. *JHEP*, 02:083, 2011.

[81] Ansgar Denner, Stefan Dittmaier, Stefan Kallweit, and Stefano Pozzorini. NLO QCD corrections to off-shell top-antitop production with leptonic decays at hadron colliders. *JHEP*, 10:110, 2012.

[82] Rikkert Frederix. Top Quark Induced Backgrounds to Higgs Production in the $WW^{(*)} \to ll\nu\nu$ Decay Channel at Next-to-Leading-Order in QCD. *Phys. Rev. Lett.*, 112(8):082002, 2014.

[83] F. Cascioli, S. Kallweit, P. Maierhöfer, and S. Pozzorini. A unified NLO description of top-pair and associated Wt production. *Eur. Phys. J. C*, 74(3):2783, 2014.

[84] Gudrun Heinrich, Andreas Maier, Richard Nisius, Johannes Schlenk, and Jan Winter. NLO QCD corrections to $W^+W^-b\bar{b}$ production with leptonic decays in the light of top quark mass and asymmetry measurements. *JHEP*, 06:158, 2014.

[85] Ansgar Denner and Mathieu Pellen. NLO electroweak corrections to off-shell top-antitop production with leptonic decays at the LHC. *JHEP*, 08:155, 2016.

[86] Ansgar Denner and Mathieu Pellen. Off-shell production of top-antitop pairs in the lepton+jets channel at NLO QCD. *JHEP*, 02:013, 2018.

[87] Leon Mans, Daniel Stremmer, and Malgorzata Worek. Complete NLO corrections to off-shell $t\bar{t}$ production in the ℓ + j decay channel. *JHEP*, 07:10, 2026.

[88] Tomáš Ježo, Jonas M. Lindert, Paolo Nason, Carlo Oleari, and Stefano Pozzorini. An NLO+PS generator for $t\bar{t}$ and Wt production and decay including non-resonant and interference effects. *Eur. Phys. J. C*, 76(12):691, 2016.

[89] Tomáš Ježo, Jonas M. Lindert, and Stefano Pozzorini. Resonance-aware NLOPS matching for off-shell $t\bar{t}$ + tW production with semileptonic decays. *JHEP*, 10:008, 2023.

[90] Michal Czakon, Paul Fiedler, David Heymes, and Alexander Mitov. NNLO QCD predictions for fully-differential top-quark pair production at the Tevatron. *JHEP*, 05:034, 2016.

[91] Michal Czakon, David Heymes, and Alexander Mitov. Dynamical scales for multi-TeV top-pair production at the LHC. *JHEP*, 04:071, 2017.

[92] Stefano Catani, Simone Devoto, Massimiliano Grazzini, Stefan Kallweit, and Javier Mazzitelli. Top-quark pair production at the LHC: Fully differential QCD predictions at NNLO. *JHEP*, 07:100, 2019.

[93] Michal Czakon, David Heymes, Alexander Mitov, Davide Pagani, Ioannis Tsinikos, and Marco Zaro. Top-pair production at the LHC through NNLO QCD and NLO EW. *JHEP*, 10:186, 2017.

[94] Arnd Behring, Michal Czakon, Alexander Mitov, Andrew S. Papanastasiou, and Rene Poncelet. Higher order corrections to spin correlations in top quark pair production at the LHC. *Phys. Rev. Lett.*, 123(8):082001, 2019.

[95] Michal Czakon, Alexander Mitov, and Rene Poncelet. NNLO QCD corrections to leptonic observables in top-quark pair production and decay. *JHEP*, 05:212, 2021.

[96] Jun Gao and Andrew S. Papanastasiou. Top-quark pair-production and decay at high precision. *Phys. Rev. D*, 96(5):051501, 2017.

[97] Javier Mazzitelli, Pier Francesco Monni, Paolo Nason, Emanuele Re, Marius Wiesemann, and Giulia Zanderighi. Next-to-Next-to-Leading Order Event Generation for Top-Quark Pair Production. *Phys. Rev. Lett.*, 127(6):062001, 2021.

[98] Javier Mazzitelli, Pier Francesco Monni, Paolo Nason, Emanuele Re, Marius Wiesemann, and Giulia Zanderighi. Top-pair production at the LHC with MINNLO$_{PS}$. *JHEP*, 04:079, 2022.

[99] Pier Francesco Monni, Paolo Nason, Emanuele Re, Marius Wiesemann, and Giulia Zanderighi. MiNNLO$_{PS}$: a new method to match NNLO QCD to parton showers. *JHEP*, 05:143, 2020. [Erratum: JHEP 02, 031 (2022)].

[100] Pier Francesco Monni, Emanuele Re, and Marius Wiesemann. MiNNLO$_{\rm PS}$: optimizing $2 \to 1$ hadronic processes. *Eur. Phys. J. C*, 80(11):1075, 2020.

[101] Nikolaos Kidonakis and George F. Sterman. Subleading logarithms in QCD hard scattering. *Phys. Lett. B*, 387:867–874, 1996.

[102] Nikolaos Kidonakis and George F. Sterman. Resummation for QCD hard scattering. *Nucl. Phys. B*, 505:321–348, 1997.

[103] Nikolaos Kidonakis. Two-loop soft anomalous dimensions and NNLL resummation for heavy quark production. *Phys. Rev. Lett.*, 102:232003, 2009.

[104] Andrea Ferroglia, Matthias Neubert, Ben D. Pecjak, and Li Lin Yang. Two-loop divergences of scattering amplitudes with massive partons. *Phys. Rev. Lett.*, 103:201601, 2009.

[105] Andrea Ferroglia, Matthias Neubert, Ben D. Pecjak, and Li Lin Yang. Two-loop divergences of massive scattering amplitudes in non-abelian gauge theories. *JHEP*, 11:062, 2009.

[106] Nikolaos Kidonakis. Next-to-next-to-leading soft-gluon corrections for the top quark cross section and transverse momentum distribution. *Phys. Rev. D*, 82:114030, 2010.

[107] Nikolaos Kidonakis. NNNLO soft-gluon corrections for the top-antitop pair production cross section. *Phys. Rev. D*, 90(1):014006, 2014.

[108] Nikolaos Kidonakis. NNNLO soft-gluon corrections for the top-quark p_T and rapidity distributions. *Phys. Rev. D*, 91(3):031501, 2015.

[109] Nikolaos Kidonakis. The top quark forward-backward asymmetry at approximate N^{3}LO. *Phys. Rev. D*, 91(7):071502, 2015.

[110] Nikolaos Kidonakis. Top-quark double-differential distributions at approximate N^{3}LO. *Phys. Rev. D*, 101(7):074006, 2020.

[111] P. Azzi et al. Report from Working Group 1: Standard Model Physics at the HL-LHC and HE-LHC. *CERN Yellow Rep. Monogr.*, 7:1–220, 2019.

[112] LHCTopWG Summary Plots - Pair production cross section. `https://twiki.cern.ch/twiki/bin/view/LHCPhysics/LHCTopWGSummaryPlots#Pair_production_cross_section`, copyright terms of the CC-BY-4.0 license apply, 2026.

[113] Armen Tumasyan et al. Measurement of differential $t\bar{t}$ production cross sections in the full kinematic range using lepton+jets events from proton-proton collisions at $\sqrt{s} = 13$ TeV. *Phys. Rev. D*, 104(9):092013, 2021.

[114] Georges Aad et al. Measurements of differential cross-sections in top-quark pair events with a high transverse momentum top quark and limits on beyond the Standard Model contributions to top-quark pair production with the ATLAS detector at $\sqrt{s} = 13$ TeV. *JHEP*, 06:063, 2022.

[115] Massimiliano Grazzini, Stefan Kallweit, and Marius Wiesemann. Fully differential NNLO computations with MATRIX. *Eur. Phys. J. C*, 78(7):537, 2018.

[116] Michal Czakon, David Heymes, and Alexander Mitov. High-precision differential predictions for top-quark pairs at the LHC. *Phys. Rev. Lett.*, 116(8):082003, 2016.

[117] LHCTopWG Summary Plots - Spin Correlation. `https://twiki.cern.ch/twiki/bin/view/LHCPhysics/LHCTopWGSummaryPlots#Spin_Correlation`, copyright terms of the CC-BY-4.0 license apply, 2026.

[118] David L. Rainwater and D. Zeppenfeld. Observing $H \to W^*W^* \to e^{\pm}\mu\mp \not{p}_T$ in weak boson fusion with dual forward jet tagging at the CERN LHC. *Phys. Rev. D*, 60:113004, 1999. [Erratum: Phys.Rev.D 61, 099901 (2000)].

[119] N. Kauer, T. Plehn, David L. Rainwater, and D. Zeppenfeld. $H \to W^+W^-$ as the discovery mode for a light Higgs boson. *Phys. Lett. B*, 503:113–120, 2001.

[120] S. Dittmaier, P. Uwer, and S. Weinzierl. NLO QCD corrections to $t\bar{t}$ + jet production at hadron colliders. *Phys. Rev. Lett.*, 98:262002, 2007.

[121] S. Dittmaier, P. Uwer, and S. Weinzierl. Hadronic top-quark pair production in association with a hard jet at next-to-leading order QCD: Phenomenological studies for the Tevatron and the LHC. *Eur. Phys. J. C*, 59:625–646, 2009.

[122] Christian Gütschow, Jonas M. Lindert, and Marek Schönherr. Multi-jet merged top-pair production including electroweak corrections. *Eur. Phys. J. C*, 78(4):317, 2018.

[123] Adam Kardos, Costas Papadopoulos, and Zoltan Trocsanyi. Top quark pair production in association with a jet with NLO parton showering. *Phys. Lett. B*, 705:76–81, 2011.

[124] M. Czakon, H. B. Hartanto, M. Kraus, and M. Worek. Matching the Nagy-Soper parton shower at next-to-leading order. *JHEP*, 06:033, 2015.

[125] Simone Alioli, Sven-Olaf Moch, and Peter Uwer. Hadronic top-quark pair-production with one jet and parton showering. *JHEP*, 01:137, 2012.

[126] Stefan Höche, Philipp Maierhöfer, Niccolo Moretti, Stefano Pozzorini, and Frank Siegert. Next-to-leading order QCD predictions for top-quark pair production with up to three jets. *Eur. Phys. J. C*, 77(3):145, 2017.

[127] Kirill Melnikov and Markus Schulze. NLO QCD corrections to top quark pair production in association with one hard jet at hadron colliders. *Nucl. Phys. B*, 840:129–159, 2010.

[128] Kirill Melnikov, Andreas Scharf, and Markus Schulze. Top quark pair production in association with a jet: QCD corrections and jet radiation in top quark decays. *Phys. Rev. D*, 85:054002, 2012.

[129] G. Bevilacqua, H. B. Hartanto, M. Kraus, and M. Worek. Top Quark Pair Production in Association with a Jet with Next-to-Leading-Order QCD Off-Shell Effects at the Large Hadron Collider. *Phys. Rev. Lett.*, 116(5):052003, 2016.

[130] G. Bevilacqua, H. B. Hartanto, M. Kraus, and M. Worek. Off-shell Top Quarks with One Jet at the LHC: A comprehensive analysis at NLO QCD. *JHEP*, 11:098, 2016.

[131] Simon Badger, Matteo Becchetti, Ekta Chaubey, and Robin Marzucca. Two-loop master integrals for a planar topology contributing to pp $\to t\bar{t}j$. *JHEP*, 01:156, 2023.

[132] Simon Badger, Matteo Becchetti, Nicolò Giraudo, and Simone Zoia. Two-loop integrals for $t\bar{t}$+jet production at hadron colliders in the leading colour approximation. *JHEP*, 07:073, 2024.

[133] Simon Badger, Matteo Becchetti, Colomba Brancaccio, Heribertus Bayu Hartanto, and Simone Zoia. Numerical evaluation of two-loop QCD helicity amplitudes for $gg \to t\bar{t}g$ at leading colour. *JHEP*, 03:070, 2025.

[134] Simon Badger, Matteo Becchetti, Colomba Brancaccio, Michał Czakon, Heribertus Bayu Hartanto, Rene Poncelet, and Simone Zoia. Double virtual QCD corrections to $t\bar{t}$+jet production at the LHC. *JHEP*, 05:044, 2026.

[135] Simon Badger, Colomba Brancaccio, Matteo Becchetti, Michał Czakon, Heribertus Bayu Hartanto, Rene Poncelet, and Simone Zoia. Higher-Order QCD Corrections to Top-Quark Pair Production in Association with a Jet. *Phys. Rev. Lett.*, 137(2):021901, 2026.

[136] G. Bevilacqua, M. Czakon, C. G. Papadopoulos, and M. Worek. Dominant QCD Backgrounds in Higgs Boson Analyses at the LHC: A Study of $pp \to t\bar{t}$ + 2 jets at Next-To-Leading Order. *Phys. Rev. Lett.*, 104:162002, 2010.

[137] G. Bevilacqua, M. Czakon, C. G. Papadopoulos, and M. Worek. Hadronic top-quark pair production in association with two jets at Next-to-Leading Order QCD. *Phys. Rev. D*, 84:114017, 2011.

[138] Keith Hamilton, Paolo Nason, and Giulia Zanderighi. MINLO: Multi-Scale Improved NLO. *JHEP*, 10:155, 2012.

[139] Stefan Hoeche, Frank Krauss, Philipp Maierhoefer, Stefano Pozzorini, Marek Schonherr, and Frank Siegert. Next-to-leading order QCD predictions for top-quark pair production with up to two jets merged with a parton shower. *Phys. Lett. B*, 748:74–78, 2015.

[140] Giuseppe Bevilacqua, Michele Lupattelli, Daniel Stremmer, and Malgorzata Worek. Study of additional jet activity in top quark pair production and decay at the LHC. *Phys. Rev. D*, 107(11):114027, 2023.

[141] Axel Bredenstein, Ansgar Denner, Stefan Dittmaier, and Stefano Pozzorini. NLO QCD corrections to $t\bar{t}b\bar{b}$ production at the LHC: 1. Quark-antiquark annihilation. *JHEP*, 08:108, 2008.

[142] A. Bredenstein, A. Denner, S. Dittmaier, and S. Pozzorini. NLO QCD corrections to $pp \to t\bar{t}b\bar{b} + X$ at the LHC. *Phys. Rev. Lett.*, 103:012002, 2009.

[143] G. Bevilacqua, M. Czakon, C. G. Papadopoulos, R. Pittau, and M. Worek. Assault on the NLO Wishlist: $pp \to t\bar{t}b\bar{b}$. *JHEP*, 09:109, 2009.

[144] Axel Bredenstein, Ansgar Denner, Stefan Dittmaier, and Stefano Pozzorini. NLO QCD Corrections to Top Anti-Top Bottom Anti-Bottom Production at the LHC: 2. full hadronic results. *JHEP*, 03:021, 2010.

[145] Malgorzata Worek. On the next-to-leading order QCD K-factor for top $t\bar{t}b\bar{b}$ production at the TeVatron. *JHEP*, 02:043, 2012.

[146] G. Bevilacqua and M. Worek. On the ratio of $t\bar{t}b\bar{b}$ and $t\bar{t}jj$ cross sections at the CERN Large Hadron Collider. *JHEP*, 07:135, 2014.

[147] Adam Kardos and Zoltán Trócsányi. Hadroproduction of t anti-t pair with a b anti-b pair using PowHel. *J. Phys. G*, 41:075005, 2014.

[148] Fabio Cascioli, Philipp Maierhöfer, Niccolo Moretti, Stefano Pozzorini, and Frank Siegert. NLO matching for $t\bar{t}b\bar{b}$ production with massive b-quarks. *Phys. Lett. B*, 734:210–214, 2014.

[149] Tomáš Ježo, Jonas M. Lindert, Niccolo Moretti, and Stefano Pozzorini. New NLOPS predictions for $t\bar{t} + b$ -jet production at the LHC. *Eur. Phys. J. C*, 78(6):502, 2018.

[150] M. V. Garzelli, A. Kardos, and Z. Trócsányi. Hadroproduction of $t\bar{t}b\bar{b}$ final states at LHC: predictions at NLO accuracy matched with Parton Shower. *JHEP*, 03:083, 2015.

[151] G. Bevilacqua, M. V. Garzelli, and A. Kardos. $t\bar{t}b\bar{b}$ hadroproduction with massive bottom quarks with PowHel, arXiv:1709.06915 [hep-ph]. 2017.

[152] Lars Ferencz, Stefan Höche, Judith Katzy, and Frank Siegert. $t\bar{t}b\bar{b}$ at NLO precision in a variable flavor number scheme. *JHEP*, 07:026, 2024.

[153] Rikkert Frederix and Tetiana Moskalets. Five-flavour scheme predictions for $t\bar{t}b\bar{b}$ at next-to-leading order accuracy. *Eur. Phys. J. C*, 84(7):763, 2024.

[154] Ansgar Denner, Jean-Nicolas Lang, and Mathieu Pellen. Full NLO QCD corrections to off-shell $t\bar{t}b\bar{b}$ production. *Phys. Rev. D*, 104(5):056018, 2021.

[155] Giuseppe Bevilacqua, Huan-Yu Bi, Heribertus Bayu Hartanto, Manfred Kraus, Michele Lupattelli, and Malgorzata Worek. $t\bar{t}b\bar{b}$ at the LHC: on the size of corrections and b-jet definitions. *JHEP*, 08:008, 2021.

[156] Giuseppe Bevilacqua, Huan-Yu Bi, Heribertus Bayu Hartanto, Manfred Kraus, Michele Lupattelli, and Malgorzata Worek. $t\bar{t}b\bar{b}$ at the LHC: On the size of off-shell effects and prompt b-jet identification. *Phys. Rev. D*, 107(1):014028, 2023.

[157] Federico Buccioni, Stefan Kallweit, Stefano Pozzorini, and Max F. Zoller. NLO QCD predictions for $t\bar{t}b\bar{b}$ production in association with a light jet at the LHC. *JHEP*, 12:015, 2019.

[158] Georges Aad et al. Measurement of $t\bar{t}$ production with a veto on additional central jet activity in pp collisions at $\sqrt{s} = 7$ TeV using the ATLAS detector. *Eur. Phys. J. C*, 72:2043, 2012.

[159] Georges Aad et al. Measurement of the $t\bar{t}$ production cross-section as a function of jet multiplicity and jet transverse momentum in 7 TeV proton-proton collisions with the ATLAS detector. *JHEP*, 01:020, 2015.

[160] Georges Aad et al. Measurements of fiducial cross-sections for $t\bar{t}$ production with one or two additional b-jets in pp collisions at $\sqrt{s}$ =8 TeV using the ATLAS detector. *Eur. Phys. J. C*, 76(1):11, 2016.

[161] Morad Aaboud et al. Measurement of jet activity in top quark events using the $e\mu$ final state with two b-tagged jets in pp collisions at $\sqrt{s} = 8$ TeV with the ATLAS detector. *JHEP*, 09:074, 2016.

[162] ATLAS Collaboration. Measurement of jets produced in top quark events using the di-lepton final state with 2 b-tagged jets in pp collisions at $\sqrt{s} = 13$ TeV with the ATLAS detector, ATLAS-CONF-2015-065. 2015.

[163] Morad Aaboud et al. Measurement of jet activity produced in top-quark events with an electron, a muon and two b-tagged jets in the final state in pp collisions at $\sqrt{s} = 13$ TeV with the ATLAS detector. *Eur. Phys. J. C*, 77(4):220, 2017.

[164] Morad Aaboud et al. Measurements of differential cross sections of top quark pair production in association with jets in pp collisions at $\sqrt{s} = 13$ TeV using the ATLAS detector. *JHEP*, 10:159, 2018.

[165] Morad Aaboud et al. Measurements of inclusive and differential fiducial cross-sections of $t\bar{t}$ production with additional heavy-flavour jets in proton-proton collisions at $\sqrt{s} = 13$ TeV with the ATLAS detector. *JHEP*, 04:046, 2019.

[166] Georges Aad et al. Measurement of $t\bar{t}$ production in association with additional b-jets in the eμ final state in proton–proton collisions at $\sqrt{s} = 13$ TeV with the ATLAS detector. *JHEP*, 01:068, 2025.

[167] Georges Aad et al. Measurement of top-quark pair production in association with charm quarks in proton–proton collisions at s=13 TeV with the ATLAS detector. *Phys. Lett. B*, 860:139177, 2025.

[168] Serguei Chatrchyan et al. Measurement of Jet Multiplicity Distributions in $t\bar{t}$ Production in pp Collisions at $\sqrt{s} = 7$ TeV. *Eur. Phys. J. C*, 74:3014, 2015. [Erratum: Eur.Phys.J.C 75, 216 (2015)].

[169] Vardan Khachatryan et al. Measurement of $t\bar{t}$ production with additional jet activity, including b quark jets, in the dilepton decay channel using pp collisions at $\sqrt{s} = 8$ TeV. *Eur. Phys. J. C*, 76(7):379, 2016.

[170] CMS Collaboration. Measurement of the differential production cross section for top-quark pairs as a function of jet multiplicity in the lepton+jets final state at $\sqrt{s} = 8$ TeV with the CMS detector, CMS-PAS-TOP-15-006. 2016.

[171] Albert M Sirunyan et al. First measurement of the cross section for top quark pair production with additional charm jets using dileptonic final states in pp collisions at s=13TeV. *Phys. Lett. B*, 820:136565, 2021.

[172] Armen Tumasyan et al. Differential cross section measurements for the production of top quark pairs and of additional jets using dilepton events from pp collisions at $\sqrt{s} = 13$ TeV. *JHEP*, 02:064, 2025.

[173] Albert M Sirunyan et al. Measurements of $t\bar{t}$ cross sections in association with b jets and inclusive jets and their ratio using dilepton final states in pp collisions at $\sqrt{s} = 13$ TeV. *Phys. Lett. B*, 776:355–378, 2018.

[174] Albert M Sirunyan et al. Measurement of the cross section for $\mathrm{t\bar{t}}$ production with additional jets and b jets in pp collisions at $\sqrt{s} = 13$ TeV. *JHEP*, 07:125, 2020.

[175] U. Baur, M. Buice, and Lynne H. Orr. Direct measurement of the top quark charge at hadron colliders. *Phys. Rev. D*, 64:094019, 2001.

[176] Olga Bessidskaia Bylund, Fabio Maltoni, Ioannis Tsinikos, Eleni Vryonidou, and Cen Zhang. Probing top quark neutral couplings in the Standard Model Effective Field Theory at NLO in QCD. *JHEP*, 05:052, 2016.

[177] U. Baur, A. Juste, L. H. Orr, and D. Rainwater. Probing electroweak top quark couplings at hadron colliders. *Phys. Rev. D*, 71:054013, 2005.

[178] Tarek Ibrahim and Pran Nath. The Top quark electric dipole moment in an MSSM extension with vector like multiplets. *Phys. Rev. D*, 82:055001, 2010.

[179] Tarek Ibrahim and Pran Nath. The Chromoelectric Dipole Moment of the Top Quark in Models with Vector Like Multiplets. *Phys. Rev. D*, 84:015003, 2011.

[180] Antonio O. Bouzas and F. Larios. Electromagnetic dipole moments of the Top quark. *Phys. Rev. D*, 87(7):074015, 2013.

[181] Matteo Fael and Thomas Gehrmann. Probing top quark electromagnetic dipole moments in single-top-plus-photon production. *Phys. Rev. D*, 88:033003, 2013.

[182] J. A. Aguilar-Saavedra, E. Álvarez, A. Juste, and F. Rubbo. Shedding light on the $t\bar{t}$ asymmetry: the photon handle. *JHEP*, 04:188, 2014.

[183] Seyed Mohsen Etesami, Sara Khatibi, and Mojtaba Mohammadi Najafabadi. Measuring anomalous $WW\gamma$ and $t\bar{t}\gamma$ couplings using top+γ production at the LHC. *Eur. Phys. J. C*, 76(10):533, 2016.

[184] Markus Schulze and Yotam Soreq. Pinning down electroweak dipole operators of the top quark. *Eur. Phys. J. C*, 76(8):466, 2016.

[185] Kirill Melnikov, Markus Schulze, and Andreas Scharf. QCD corrections to top quark pair production in association with a photon at hadron colliders. *Phys. Rev. D*, 83:074013, 2011.

[186] G. Bevilacqua, H. B. Hartanto, M. Kraus, T. Weber, and M. Worek. Off-shell vs on-shell modelling of top quarks in photon associated production. *JHEP*, 03:154, 2020.

[187] Didar Dobur, Joscha Knolle, Gianny Mestdach, and Kirill Skovpen. Photon radiation effects in kinematic reconstruction of top quarks. *JINST*, 16(12):P12001, 2021.

[188] Peng-Fei Duan, Wen-Gan Ma, Ren-You Zhang, Liang Han, Lei Guo, and Shao-Ming Wang. QCD corrections to associated production of $t\bar{t}\gamma$ at hadron colliders. *Phys. Rev. D*, 80:014022, 2009.

[189] Peng-Fei Duan, Ren-You Zhang, Wen-Gan Ma, Liang Han, Lei Guo, and Shao-Ming Wang. Next-to-leading order QCD corrections to $t\bar{t}\gamma$ production at the 7 TeV LHC. *Chin. Phys. Lett.*, 28:111401, 2011.

[190] Fabio Maltoni, Davide Pagani, and Ioannis Tsinikos. Associated production of a top-quark pair with vector bosons at NLO in QCD: impact on t$\bar{\text{t}}$H searches at the LHC. *JHEP*, 02:113, 2016.

[191] Peng-Fei Duan, Yu Zhang, Yong Wang, Mao Song, and Gang Li. Electroweak corrections to top quark pair production in association with a hard photon at hadron colliders. *Phys. Lett. B*, 766:102–106, 2017.

[192] Davide Pagani, Hua-Sheng Shao, Ioannis Tsinikos, and Marco Zaro. Automated EW corrections with isolated photons: $t\bar{t}\gamma$, $t\bar{t}\gamma\gamma$ and $t\gamma j$ as case studies. *JHEP*, 09:155, 2021.

[193] Adam Kardos and Zoltán Trócsányi. Hadroproduction of t anti-t pair in association with an isolated photon at NLO accuracy matched with parton shower. *JHEP*, 05:090, 2015.

[194] G. Bevilacqua, H. B. Hartanto, M. Kraus, T. Weber, and M. Worek. Hard Photons in Hadroproduction of Top Quarks with Realistic Final States. *JHEP*, 10:158, 2018.

[195] G. Bevilacqua, H. B. Hartanto, M. Kraus, T. Weber, and M. Worek. Precise predictions for $t\bar{t}\gamma/t\bar{t}$ cross section ratios at the LHC. *JHEP*, 01:188, 2019.

[196] Daniel Stremmer and Malgorzata Worek. Complete NLO corrections to top-quark pair production with isolated photons. *JHEP*, 07:091, 2024.

[197] Daniel Stremmer and Malgorzata Worek. NLO QCD predictions for $t\bar{t}\gamma$ with realistic photon isolation. *JHEP*, 01:156, 2025.

[198] Nikolaos Kidonakis and Alberto Tonero. Higher-order corrections in $t\bar{t}\gamma$ cross sections. *Phys. Rev. D*, 107(3):034013, 2023.

[199] Souvik Bera, Colomba Brancaccio, Dhimiter Canko, and Heribertus Bayu Hartanto. One-loop amplitudes for $t\bar{t}j$ and $t\bar{t}\gamma$ productions at the LHC through $\mathcal{O}(\epsilon^2)$. *SciPost Phys.*, 19(6):165, 2025.

[200] Simon Badger, Michał Czakon, Heribertus Bayu Hartanto, Ryan Moodie, Tiziano Peraro, Rene Poncelet, and Simone Zoia. Isolated photon production in association with a jet pair through next-to-next-to-leading order in QCD. *JHEP*, 10:071, 2023.

[201] Matteo Becchetti, Christoph Dlapa, and Simone Zoia. Canonical differential equations for the elliptic two-loop five-point integral family relevant to $t\bar{t}$+jet production at leading color. *Phys. Rev. D*, 112(3):L031501, 2025.

[202] Guoxing Wang and Li Lin Yang. Two-loop QCD amplitudes for $t\bar{t}\gamma$ production at hadron colliders. *JHEP*, 04:005, 2026.

[203] J. Alwall, R. Frederix, S. Frixione, V. Hirschi, F. Maltoni, O. Mattelaer, H. S. Shao, T. Stelzer, P. Torrielli, and M. Zaro. The automated computation of tree-level and next-to-leading order differential cross sections, and their matching to parton shower simulations. *JHEP*, 07:079, 2014.

[204] Adam Kardos and Zoltán Trócsányi. Hadroproduction of t–anti-t pair with two isolated photons with PowHel. *Nucl. Phys. B*, 897:717–731, 2015.

[205] Hans van Deurzen, Rikkert Frederix, Valentin Hirschi, Gionata Luisoni, Pierpaolo Mastrolia, and Giovanni Ossola. Spin Polarisation of $t\bar{t}\gamma\gamma$ production at NLO+PS with GoSam interfaced to MadGraph5_aMC@NLO. *Eur. Phys. J. C*, 76(4):221, 2016.

[206] Daniel Stremmer and Malgorzata Worek. Associated production of a top-quark pair with two isolated photons at the LHC through NLO in QCD. *JHEP*, 08:179, 2023.

[207] Georges Aad et al. Observation of top-quark pair production in association with a photon and measurement of the $t\bar{t}\gamma$ production cross section in pp collisions at $\sqrt{s} = 7$ TeV using the ATLAS detector. *Phys. Rev. D*, 91(7):072007, 2015.

[208] Georges Aad et al. Observation of $t\bar{t}\gamma\gamma$ production at $\sqrt{s}$ =13 TeV with the ATLAS detector. *Phys. Lett. B*, 874:140195, 2026.

[209] Morad Aaboud et al. Measurement of the $t\bar{t}\gamma$ production cross section in proton-proton collisions at $\sqrt{s} = 8$ TeV with the ATLAS detector. *JHEP*, 11:086, 2017.

[210] Albert M Sirunyan et al. Measurement of the semileptonic $\mathrm{t\bar{t}} + \gamma$ production cross section in pp collisions at $\sqrt{s} = 8$ TeV. *JHEP*, 10:006, 2017.

[211] Morad Aaboud et al. Measurements of inclusive and differential fiducial cross-sections of $t\bar{t}\gamma$ production in leptonic final states at $\sqrt{s} = 13$ TeV in ATLAS. *Eur. Phys. J. C*, 79(5):382, 2019.

[212] Georges Aad et al. Measurements of inclusive and differential cross-sections of combined $t\bar{t}\gamma$ and $tW\gamma$ production in the eμ channel at 13 TeV with the ATLAS detector. *JHEP*, 09:049, 2020.

[213] Armen Tumasyan et al. Measurement of the inclusive and differential $t\bar{t}\gamma$ cross sections in the single-lepton channel and EFT interpretation at $\sqrt{s} = 13$ TeV. *JHEP*, 12:180, 2021.

[214] Armen Tumasyan et al. Measurement of the inclusive and differential $\mathrm{t\bar{t}}\gamma$ cross sections in the dilepton channel and effective field theory interpretation in proton-proton collisions at $\sqrt{s}$ =13 TeV. *JHEP*, 05:091, 2022.

[215] Georges Aad et al. Measurements of inclusive and differential cross-sections of $t\bar{t}\gamma$ production in pp collisions at $\sqrt{s} = 13$ TeV with the ATLAS detector. *JHEP*, 10:191, 2024.

[216] Aram Hayrapetyan et al. Inclusive and differential measurements of the $t\bar{t}\gamma$ cross section and the $t\bar{t}\gamma$ / $t\bar{t}$ cross section ratio in proton-proton collisions at $\sqrt{s} = 13$ TeV. *JHEP*, 04:086, 2026.

[217] Nicolas Greiner, Kyoungchul Kong, Jong-Chul Park, Seong Chan Park, and Jan-Christopher Winter. Model-Independent Production of a Top-Philic Resonance at the LHC. *JHEP*, 04:029, 2015.

[218] Peter Cox, Anibal D. Medina, Tirtha Sankar Ray, and Andrew Spray. Novel collider and dark matter phenomenology of a top-philic Z′. *JHEP*, 06:110, 2016.

[219] Nilanjana Kumar and Stephen P. Martin. Vectorlike Leptons at the Large Hadron Collider. *Phys. Rev. D*, 92(11):115018, 2015.

[220] Jeong Han Kim, Kyoungchul Kong, Seung J. Lee, and Gopolang Mohlabeng. Probing TeV scale Top-Philic Resonances with Boosted Top-Tagging at the High Luminosity LHC. *Phys. Rev. D*, 94(3):035023, 2016.

[221] Patrick J. Fox, Ian Low, and Yue Zhang. Top-philic Z' forces at the LHC. *JHEP*, 03:074, 2018.

[222] Ezequiel Alvarez, Aurelio Juste, Manuel Szewc, and Tamara Vazquez Schroeder. Topping-up multilepton plus b-jets anomalies at the LHC with a Z' boson. *JHEP*, 05:125, 2021.

[223] Stefan Bißmann, Gudrun Hiller, Clara Hormigos-Feliu, and Daniel F. Litim. Multi-lepton signatures of vector-like leptons with flavor. *Eur. Phys. J. C*, 81(2):101, 2021.

[224] U. Baur, A. Juste, D. Rainwater, and L. H. Orr. Improved measurement of ttZ couplings at the CERN LHC. *Phys. Rev. D*, 73:034016, 2006.

[225] Edmond L. Berger, Qing-Hong Cao, and Ian Low. Model Independent Constraints Among the $Wtb, Zb\bar{b}$, and $Zt\bar{t}$ Couplings. *Phys. Rev. D*, 80:074020, 2009.

[226] Raoul Röntsch and Markus Schulze. Constraining Couplings of Top Quarks to the Z Boson in $t\bar{t}$ + Z Production at the LHC. *JHEP*, 07:091, 2014. [Erratum: JHEP 09, 132 (2015)].

[227] Ulrich Haisch, Priscilla Pani, and Giacomo Polesello. Determining the CP nature of spin-0 mediators in associated production of dark matter and $t\bar{t}$ pairs. *JHEP*, 02:131, 2017.

[228] G. Bevilacqua, H. B. Hartanto, M. Kraus, T. Weber, and M. Worek. Towards constraining Dark Matter at the LHC: Higher order QCD predictions for $t\bar{t}+Z(Z\to\nu_\ell\bar{\nu}_\ell)$. *JHEP*, 11:001, 2019.

[229] Jonathan Hermann and Malgorzata Worek. The impact of top-quark modelling on the exclusion limits in $t\bar{t}+DM$ searches at the LHC. *Eur. Phys. J. C*, 81(11):1029, 2021.

[230] Achilleas Lazopoulos, Thomas McElmurry, Kirill Melnikov, and Frank Petriello. Next-to-leading order QCD corrections to $t\bar{t}Z$ production at the LHC. *Phys. Lett. B*, 666:62–65, 2008.

[231] Adam Kardos, Zoltan Trocsanyi, and Costas Papadopoulos. Top quark pair production in association with a Z-boson at NLO accuracy. *Phys. Rev. D*, 85:054015, 2012.

[232] S. Frixione, V. Hirschi, D. Pagani, H. S. Shao, and M. Zaro. Electroweak and QCD corrections to top-pair hadroproduction in association with heavy bosons. *JHEP*, 06:184, 2015.

[233] Alessandro Broggio, Andrea Ferroglia, Giovanni Ossola, Ben D. Pecjak, and Ray D. Sameshima. Associated production of a top pair and a Z boson at the LHC to NNLL accuracy. *JHEP*, 04:105, 2017.

[234] Anna Kulesza, Leszek Motyka, Daniel Schwartländer, Tomasz Stebel, and Vincent Theeuwes. Associated production of a top quark pair with a heavy electroweak gauge boson at NLO+NNLL accuracy. *Eur. Phys. J. C*, 79(3):249, 2019.

[235] Anna Kulesza, Leszek Motyka, Daniel Schwartländer, Tomasz Stebel, and Vincent Theeuwes. Associated top quark pair production with a heavy boson: differential cross sections at NLO+NNLL accuracy. *Eur. Phys. J. C*, 80(5):428, 2020.

[236] Nikolaos Kidonakis and Chris Foster. Higher-order soft-gluon corrections for $t\bar{t}Z$ cross sections. *Phys. Lett. B*, 860:139146, 2025.

[237] M. V. Garzelli, A. Kardos, C. G. Papadopoulos, and Z. Trocsanyi. $t\bar{t}W^{\pm}$ and $t\bar{t}Z$ Hadroproduction at NLO accuracy in QCD with Parton Shower and Hadronization effects. *JHEP*, 11:056, 2012.

[238] M. V. Garzelli, A. Kardos, C. G. Papadopoulos, and Z. Trocsanyi. Z^0 - boson production in association with a $t\bar{t}$ pair at NLO accuracy with parton shower effects. *Phys. Rev. D*, 85:074022, 2012.

[239] Margherita Ghezzi, Barbara Jäger, Santiago Lopez Portillo Chavez, Laura Reina, and Doreen Wackeroth. Hadronic production of top-quark pairs in association with a pair of leptons in the POWHEG BOX framework. *Phys. Rev. D*, 106(1):014001, 2022.

[240] Giuseppe Bevilacqua, Heribertus Bayu Hartanto, Manfred Kraus, Jasmina Nasufi, and Malgorzata Worek. NLO QCD corrections to full off-shell production of $t\bar{t}Z$ including leptonic decays. *JHEP*, 08:060, 2022.

[241] Ansgar Denner, Daniele Lombardi, and Giovanni Pelliccioli. Complete NLO corrections to off-shell $t\bar{t}Z$ production at the LHC. *JHEP*, 09:072, 2023.

[242] LHCTopWG Summary Plots - Associated $t\bar{t} + X$ Production. `https://twiki.cern.ch/twiki/bin/view/LHCPhysics/LHCTopWGSummaryPlots#Associated_tt_X_Production`,copyright terms of the CC-BY-4.0 license apply, 2026.

[243] Georges Aad et al. Measurement of the $t\bar{t}W$ and $t\bar{t}Z$ production cross sections in pp collisions at $\sqrt{s} = 8$ TeV with the ATLAS detector. *JHEP*, 11:172, 2015.

[244] Vardan Khachatryan et al. Observation of top quark pairs produced in association with a vector boson in pp collisions at $\sqrt{s} = 8$ TeV. *JHEP*, 01:096, 2016.

[245] Morad Aaboud et al. Measurement of the $t\bar{t}Z$ and $t\bar{t}W$ production cross sections in multilepton final states using 3.2 fb^{-1} of pp collisions at $\sqrt{s} = 13$ TeV with the ATLAS detector. *Eur. Phys. J. C*, 77(1):40, 2017.

[246] Albert M Sirunyan et al. Measurement of the cross section for top quark pair production in association with a W or Z boson in proton-proton collisions at $\sqrt{s} = 13$ TeV. *JHEP*, 08:011, 2018.

[247] Morad Aaboud et al. Measurement of the $t\bar{t}Z$ and $t\bar{t}W$ cross sections in proton-proton collisions at $\sqrt{s} = 13$ TeV with the ATLAS detector. *Phys. Rev. D*, 99(7):072009, 2019.

[248] Albert M Sirunyan et al. Measurement of top quark pair production in association with a Z boson in proton-proton collisions at $\sqrt{s} = 13$ TeV. *JHEP*, 03:056, 2020.

[249] Georges Aad et al. Measurements of the inclusive and differential production cross sections of a top-quark–antiquark pair in association with a Z boson at $\sqrt{s} = 13$ TeV with the ATLAS detector. *Eur. Phys. J. C*, 81(8):737, 2021.

[250] Georges Aad et al. Inclusive and differential cross-section measurements of $t\bar{t}Z$ production in pp collisions at $\sqrt{s} = 13$ TeV with the ATLAS detector, including EFT and spin-correlation interpretations. *JHEP*, 07:163, 2024.

[251] Aram Hayrapetyan et al. Search for physics beyond the standard model in top quark production with additional leptons in the context of effective field theory. *JHEP*, 12:068, 2023.

[252] CMS collaboration. Anomalous couplings in the ttZ final state at the HL-LHC, CMS-PAS-FTR-18-036. 2018.

[253] Georges Aad et al. Observation of a new particle in the search for the Standard Model Higgs boson with the ATLAS detector at the LHC. *Phys. Lett. B*, 716:1–29, 2012.

[254] Serguei Chatrchyan et al. Observation of a New Boson at a Mass of 125 GeV with the CMS Experiment at the LHC. *Phys. Lett. B*, 716:30–61, 2012.

[255] D. de Florian et al. Handbook of LHC Higgs Cross Sections: 4. Deciphering the Nature of the Higgs Sector. *CERN Yellow Rep. Monogr.*, 2:1–869, 2017.

[256] M. Aaboud et al. Observation of Higgs boson production in association with a top quark pair at the LHC with the ATLAS detector. *Phys. Lett. B*, 784:173–191, 2018.

[257] Albert M Sirunyan et al. Observation of $t\bar{t}H$ production. *Phys. Rev. Lett.*, 120(23):231801, 2018.

[258] Georges Aad et al. Search for $H \to \gamma\gamma$ produced in association with top quarks and constraints on the Yukawa coupling between the top quark and the Higgs boson using data taken at 7 TeV and 8 TeV with the ATLAS detector. *Phys. Lett. B*, 740:222–242, 2015.

[259] Georges Aad et al. Search for the Standard Model Higgs boson produced in association with top quarks and decaying into $b\bar{b}$ in pp collisions at $\sqrt{s} = 8$ TeV with the ATLAS detector. *Eur. Phys. J. C*, 75(7):349, 2015.

[260] Georges Aad et al. Search for the Standard Model Higgs boson decaying into $b\bar{b}$ produced in association with top quarks decaying hadronically in pp collisions at $\sqrt{s} = 8$ TeV with the ATLAS detector. *JHEP*, 05:160, 2016.

[261] Serguei Chatrchyan et al. Search for the Standard Model Higgs Boson Produced in Association with a Top-Quark Pair in *pp* Collisions at the LHC. *JHEP*, 05:145, 2013.

[262] Vardan Khachatryan et al. Search for a Standard Model Higgs Boson Produced in Association with a Top-Quark Pair and Decaying to Bottom Quarks Using a Matrix Element Method. *Eur. Phys. J. C*, 75(6):251, 2015.

[263] Georges Aad et al. Search for the associated production of the Higgs boson with a top quark pair in multilepton final states with the ATLAS detector. *Phys. Lett. B*, 749:519–541, 2015.

[264] Vardan Khachatryan et al. Search for the associated production of the Higgs boson with a top-quark pair. *JHEP*, 09:087, 2014. [Erratum: JHEP 10, 106 (2014)].

[265] Morad Aaboud et al. Evidence for the associated production of the Higgs boson and a top quark pair with the ATLAS detector. *Phys. Rev. D*, 97(7):072003, 2018.

[266] Albert M Sirunyan et al. Evidence for associated production of a Higgs boson with a top quark pair in final states with electrons, muons, and hadronically decaying τ leptons at $\sqrt{s} = 13$ TeV. *JHEP*, 08:066, 2018.

[267] Morad Aaboud et al. Search for the standard model Higgs boson produced in association with top quarks and decaying into a $b\bar{b}$ pair in *pp* collisions at $\sqrt{s}$ = 13 TeV with the ATLAS detector. *Phys. Rev. D*, 97(7):072016, 2018.

[268] Georges Aad et al. CP Properties of Higgs Boson Interactions with Top Quarks in the $t\bar{t}H$ and tH Processes Using $H \to \gamma\gamma$ with the ATLAS Detector. *Phys. Rev. Lett.*, 125(6):061802, 2020.

[269] Albert M Sirunyan et al. Measurements of $t\bar{t}H$ Production and the CP Structure of the Yukawa Interaction between the Higgs Boson and Top Quark in the Diphoton Decay Channel. *Phys. Rev. Lett.*, 125(6):061801, 2020.

[270] Armen Tumasyan et al. Search for CP violation in ttH and tH production in multilepton channels in proton-proton collisions at $\sqrt{s} = 13$ TeV. *JHEP*, 07:092, 2023.

[271] Higgs PAG Summary Plots - Summary of run 2 ttH signal strengths. `https://twiki.cern.ch/twiki/bin/view/CMSPublic/SummaryResultsHIG#Summary_of_run_2_ttH_signal_stre`, 2026.

[272] Georges Aad et al. Measurement of Higgs boson decay into b-quarks in associated production with a top-quark pair in pp collisions at $\sqrt{s} = 13$ TeV with the ATLAS detector. *JHEP*, 06:097, 2022.

[273] Georges Aad et al. Measurement of the associated production of a top-antitop-quark pair and a Higgs boson decaying into a $b\bar{b}$ pair in pp collisions at $\sqrt{s} =$ 13 TeV using the ATLAS detector at the LHC. *Eur. Phys. J. C*, 85(2):210, 2025.

[274] Aram Hayrapetyan et al. Measurement of the $t\bar{t}$H and tH production rates in the H $\to b\bar{b}$ decay channel using proton-proton collision data at $\sqrt{s} = 13$ TeV. *JHEP*, 02:097, 2025.

[275] Aram Hayrapetyan et al. Simultaneous Probe of the Charm and Bottom Quark Yukawa Couplings Using $t\bar{t}H$ Events. *Phys. Rev. Lett.*, 136(1):011801, 2026.

[276] Armen Tumasyan et al. Search for Higgs Boson Decay to a Charm Quark-Antiquark Pair in Proton-Proton Collisions at $\sqrt{s}$=13 TeV. *Phys. Rev. Lett.*, 131(6):061801, 2023.

[277] W. Beenakker, S. Dittmaier, M. Kramer, B. Plumper, M. Spira, and P. M. Zerwas. Higgs radiation off top quarks at the Tevatron and the LHC. *Phys. Rev. Lett.*, 87:201805, 2001.

[278] L. Reina and S. Dawson. Next-to-leading order results for $t\bar{t}h$ production at the Tevatron. *Phys. Rev. Lett.*, 87:201804, 2001.

[279] W. Beenakker, S. Dittmaier, M. Kramer, B. Plumper, M. Spira, and P. M. Zerwas. NLO QCD corrections to $t\bar{t}H$ production in hadron collisions. *Nucl. Phys. B*, 653:151–203, 2003.

[280] S. Dawson, L. H. Orr, L. Reina, and D. Wackeroth. Associated top quark Higgs boson production at the LHC. *Phys. Rev. D*, 67:071503, 2003.

[281] S. Dawson, C. Jackson, L. H. Orr, L. Reina, and D. Wackeroth. Associated Higgs boson production with top quarks at the CERN Large Hadron Collider: NLO QCD corrections. *Phys. Rev. D*, 68:034022, 2003.

[282] S. Frixione, V. Hirschi, D. Pagani, H. S. Shao, and M. Zaro. Weak corrections to Higgs hadroproduction in association with a top-quark pair. *JHEP*, 09:065, 2014.

[283] Yu Zhang, Wen-Gan Ma, Ren-You Zhang, Chong Chen, and Lei Guo. QCD NLO and EW NLO corrections to $t\bar{t}H$ production with top quark decays at hadron collider. *Phys. Lett. B*, 738:1–5, 2014.

[284] Anna Kulesza, Leszek Motyka, Tomasz Stebel, and Vincent Theeuwes. Soft gluon resummation for associated $t\bar{t}H$ production at the LHC. *JHEP*, 03:065, 2016.

[285] Alessandro Broggio, Andrea Ferroglia, Ben D. Pecjak, Adrian Signer, and Li Lin Yang. Associated production of a top pair and a Higgs boson beyond NLO. *JHEP*, 03:124, 2016.

[286] Alessandro Broggio, Andrea Ferroglia, Ben D. Pecjak, and Li Lin Yang. NNLL resummation for the associated production of a top pair and a Higgs boson at the LHC. *JHEP*, 02:126, 2017.

[287] Anna Kulesza, Leszek Motyka, Tomasz Stebel, and Vincent Theeuwes. Associated $t\bar{t}H$ production at the LHC: Theoretical predictions at NLO+NNLL accuracy. *Phys. Rev. D*, 97(11):114007, 2018.

[288] Melissa van Beekveld and Wim Beenakker. The role of the threshold variable in soft-gluon resummation of the $t\bar{t}h$ production process. *JHEP*, 05:196, 2021.

[289] Wan-Li Ju and Li Lin Yang. Resummation of soft and Coulomb corrections for $t\bar{t}h$ production at the LHC. *JHEP*, 06:050, 2019.

[290] Rikkert Frederix, Stefano Frixione, Valentin Hirschi, Fabio Maltoni, Roberto Pittau, and Paolo Torrielli. Scalar and pseudoscalar Higgs production in association with a top–antitop pair. *Phys. Lett. B*, 701:427–433, 2011.

[291] M. V. Garzelli, A. Kardos, C. G. Papadopoulos, and Z. Trocsanyi. Standard Model Higgs boson production in association with a top anti-top pair at NLO with parton showering. *EPL*, 96(1):11001, 2011.

[292] Heribertus B. Hartanto, Barbara Jager, Laura Reina, and Doreen Wackeroth. Higgs boson production in association with top quarks in the POWHEG BOX. *Phys. Rev. D*, 91(9):094003, 2015.

[293] Davide Pagani, Timea Vitos, and Marco Zaro. Improving NLO QCD event generators with high-energy EW corrections. *Eur. Phys. J. C*, 84(5):514, 2024.

[294] Ansgar Denner and Robert Feger. NLO QCD corrections to off-shell top-antitop production with leptonic decays in association with a Higgs boson at the LHC. *JHEP*, 11:209, 2015.

[295] Ansgar Denner, Jean-Nicolas Lang, Mathieu Pellen, and Sandro Uccirati. Higgs production in association with off-shell top-antitop pairs at NLO EW and QCD at the LHC. *JHEP*, 02:053, 2017.

[296] Jonathan Hermann, Daniel Stremmer, and Malgorzata Worek. $\mathcal{CP}$ structure of the top-quark Yukawa interaction: NLO QCD corrections and off-shell effects. *JHEP*, 09:138, 2022.

[297] Daniel Stremmer and Malgorzata Worek. Production and decay of the Higgs boson in association with top quarks. *JHEP*, 02:196, 2022.

[298] Stefano Catani, Ignacio Fabre, Massimiliano Grazzini, and Stefan Kallweit. $t\bar{t}H$ production at NNLO: the flavour off-diagonal channels. *Eur. Phys. J. C*, 81(6):491, 2021.

[299] Stefano Catani, Simone Devoto, Massimiliano Grazzini, Stefan Kallweit, Javier Mazzitelli, and Chiara Savoini. Higgs Boson Production in Association with a Top-Antitop Quark Pair in Next-to-Next-to-Leading Order QCD. *Phys. Rev. Lett.*, 130(11):111902, 2023.

[300] Simone Devoto, Massimiliano Grazzini, Stefan Kallweit, Javier Mazzitelli, and Chiara Savoini. Precise predictions for $t\bar{t}H$ production at the LHC: inclusive cross section and differential distributions. *JHEP*, 03:189, 2025.

[301] Roger Balsach et al. State-of-the-art cross sections for $t\bar{t}H$: NNLO predictions matched with NNLL resummation and EW corrections, SciPost Phys. Comm. Rep. 10. 2025.

[302] Jiaqi Chen, Chichuan Ma, Guoxing Wang, Li Lin Yang, and Xiaoping Ye. Two-loop infrared singularities in the production of a Higgs boson associated with a top-quark pair. *JHEP*, 04:025, 2022.

[303] Federico Buccioni, Philipp Alexander Kreer, Xiao Liu, and Lorenzo Tancredi. One loop QCD corrections to gg $\to t\bar{t}H$ at $\mathcal{O}(\epsilon^2)$. *JHEP*, 03:093, 2024.

[304] F. Febres Cordero, G. Figueiredo, M. Kraus, B. Page, and L. Reina. Two-loop master integrals for leading-color $pp \to t\bar{t}H$ amplitudes with a light-quark loop. *JHEP*, 07:084, 2024.

[305] Guoxing Wang, Tianya Xia, Li Lin Yang, and Xiaoping Ye. Two-loop QCD amplitudes for $t\bar{t}H$ production from boosted limit. *JHEP*, 07:121, 2024.

[306] Bakul Agarwal, Gudrun Heinrich, Stephen P. Jones, Matthias Kerner, Sven Yannick Klein, Jannis Lang, Vitaly Magerya, and Anton Olsson. Two-loop amplitudes for $t\bar{t}H$ production: the quark-initiated N_f-part. *JHEP*, 05:013, 2024. [Erratum: JHEP 06, 142 (2024)].

[307] Christian Biello, Chiara Savoini, Chiara Signorile-Signorile, and Marius Wiesemann. Next-to-next-to-leading order event generation for $t\bar{t}H$ production with approximate two-loop amplitude. *JHEP*, 06:070, 2026.

[308] Ilaria Brivio, Sebastian Bruggisser, Fabio Maltoni, Rhea Moutafis, Tilman Plehn, Eleni Vryonidou, Susanne Westhoff, and C. Zhang. O new physics, where art thou? A global search in the top sector. *JHEP*, 02:131, 2020.

[309] F. Maltoni, M. L. Mangano, I. Tsinikos, and M. Zaro. Top-quark charge asymmetry and polarization in $t\bar{t}W^{\pm}$ production at the LHC. *Phys. Lett. B*, 736:252–260, 2014.

[310] Giuseppe Bevilacqua, Huan-Yu Bi, Heribertus Bayu Hartanto, Manfred Kraus, Jasmina Nasufi, and Malgorzata Worek. NLO QCD corrections to off-shell $t\bar{t}W^{\pm}$ production at the LHC: correlations and asymmetries. *Eur. Phys. J. C*, 81(7):675, 2021.

[311] Roberto Contino and Geraldine Servant. Discovering the top partners at the LHC using same-sign dilepton final states. *JHEP*, 06:026, 2008.

[312] Andrea De Simone, Oleksii Matsedonskyi, Riccardo Rattazzi, and Andrea Wulzer. A First Top Partner Hunter's Guide. *JHEP*, 04:004, 2013.

[313] F. M. L. Almeida, Jr., Yara do Amaral Coutinho, Jose Antonio Martins Simoes, P. P. Queiroz Filho, and C. M. Porto. Same sign dileptons as a signature for heavy Majorana neutrinos in hadron hadron collisions. *Phys. Lett. B*, 400:331–334, 1997.

[314] Stefan von Buddenbrock, Nabarun Chakrabarty, Alan S. Cornell, Deepak Kar, Mukesh Kumar, Tanumoy Mandal, Bruce Mellado, Biswarup Mukhopadhyaya, Robert G. Reed, and Xifeng Ruan. Phenomenological signatures of additional scalar bosons at the LHC. *Eur. Phys. J. C*, 76(10):580, 2016.

[315] Stefan von Buddenbrock, Alan S. Cornell, Abdualazem Fadol, Mukesh Kumar, Bruce Mellado, and Xifeng Ruan. Multi-lepton signatures of additional scalar bosons beyond the Standard Model at the LHC. *J. Phys. G*, 45(11):115003, 2018.

[316] Stefan von Buddenbrock, Alan S. Cornell, Elie D. R. Iarilala, Mukesh Kumar, Bruce Mellado, Xifeng Ruan, and Esra Mohammed Shrif. Constraints on a 2HDM with a singlet scalar and implications in the search for heavy bosons at the LHC. *J. Phys. G*, 46(11):115001, 2019.

[317] Stefan Buddenbrock, Alan S. Cornell, Yaquan Fang, Abdualazem Fadol Mohammed, Mukesh Kumar, Bruce Mellado, and Kehinde G. Tomiwa. The emergence of multi-lepton anomalies at the LHC and their compatibility with new physics at the EW scale. *JHEP*, 10:157, 2019.

[318] Valentin Hirschi, Rikkert Frederix, Stefano Frixione, Maria Vittoria Garzelli, Fabio Maltoni, and Roberto Pittau. Automation of one-loop QCD corrections. *JHEP*, 05:044, 2011.

[319] R. Frederix, S. Frixione, V. Hirschi, D. Pagani, H. S. Shao, and M. Zaro. The automation of next-to-leading order electroweak calculations. *JHEP*, 07:185, 2018. [Erratum: JHEP 11, 085 (2021)].

[320] Rikkert Frederix, Davide Pagani, and Marco Zaro. Large NLO corrections in $t\bar{t}W^{\pm}$ and $t\bar{t}t\bar{t}$ hadroproduction from supposedly subleading EW contributions. *JHEP*, 02:031, 2018.

[321] Jeff Asaf Dror, Marco Farina, Ennio Salvioni, and Javi Serra. Strong tW Scattering at the LHC. *JHEP*, 01:071, 2016.

[322] F. Febres Cordero, M. Kraus, and L. Reina. Top-quark pair production in association with a $W^{\pm}$ gauge boson in the POWHEG-BOX. *Phys. Rev. D*, 103(9):094014, 2021.

[323] Rikkert Frederix and Ioannis Tsinikos. Subleading EW corrections and spin-correlation effects in $t\bar{t}W$ multi-lepton signatures. *Eur. Phys. J. C*, 80(9):803, 2020.

[324] Hai Tao Li, Chong Sheng Li, and Shi Ang Li. Renormalization group improved predictions for $t\bar{t}W^{\pm}$ production at hadron colliders. *Phys. Rev. D*, 90(9):094009, 2014.

[325] Alessandro Broggio, Andrea Ferroglia, Giovanni Ossola, and Ben D. Pecjak. Associated production of a top pair and a W boson at next-to-next-to-leading logarithmic accuracy. *JHEP*, 09:089, 2016.

[326] Alessandro Broggio, Andrea Ferroglia, Rikkert Frederix, Davide Pagani, Benjamin D. Pecjak, and Ioannis Tsinikos. Top-quark pair hadroproduction in association with a heavy boson at NLO+NNLL including EW corrections. *JHEP*, 08:039, 2019.

[327] Stefan von Buddenbrock, Richard Ruiz, and Bruce Mellado. Anatomy of inclusive $t\bar{t}W$ production at hadron colliders. *Phys. Lett. B*, 811:135964, 2020.

[328] Rikkert Frederix and Ioannis Tsinikos. On improving NLO merging for $\mathrm{t\bar{t}W}$ production. *JHEP*, 11:029, 2021.

[329] Rikkert Frederix and Stefano Frixione. Merging meets matching in MC@NLO. *JHEP*, 12:061, 2012.

[330] Pierre Artoisenet, Rikkert Frederix, Olivier Mattelaer, and Robbert Rietkerk. Automatic spin-entangled decays of heavy resonances in Monte Carlo simulations. *JHEP*, 03:015, 2013.

[331] John M. Campbell and R. Keith Ellis. $t\bar{t}W^{+-}$ production and decay at NLO. *JHEP*, 07:052, 2012.

[332] Giuseppe Bevilacqua, Huan-Yu Bi, Heribertus Bayu Hartanto, Manfred Kraus, and Malgorzata Worek. The simplest of them all: $t\bar{t}W^{\pm}$ at NLO accuracy in QCD. *JHEP*, 08:043, 2020.

[333] Ansgar Denner and Giovanni Pelliccioli. NLO QCD corrections to off-shell $\mathrm{t\bar{t}W^{+}}$ production at the LHC. *JHEP*, 11:069, 2020.

[334] Ansgar Denner and Giovanni Pelliccioli. Combined NLO EW and QCD corrections to off-shell $\mathrm{t\bar{t}W}$ production at the LHC. *Eur. Phys. J. C*, 81(4):354, 2021.

[335] G. Bevilacqua, H. Y. Bi, F. Febres Cordero, H. B. Hartanto, M. Kraus, J. Nasufi, L. Reina, and M. Worek. Modeling uncertainties of $t\bar{t}W^{\pm}$ multilepton signatures. *Phys. Rev. D*, 105(1):014018, 2022.

[336] Rikkert Frederix, Leif Gellersen, and Jasmina Nasufi. Matrix element corrections in top quark decays for the $t\bar{t}W^{\pm}$ process. *Eur. Phys. J. C*, 84(4):410, 2024.

[337] Huan-Yu Bi, Manfred Kraus, Minos Reinartz, and Malgorzata Worek. NLO QCD predictions for off-shell $t\bar{t}W$ production in association with a light jet at the LHC. *JHEP*, 09:026, 2023.

[338] Nikolaos Dimitrakopoulos and Malgorzata Worek. Multi-scale improved predictions for $pp \to t\bar{t}W^{+} + X$, arXiv:2607.11652 [hep-ph]. 2026.

[339] Luca Buonocore, Simone Devoto, Massimiliano Grazzini, Stefan Kallweit, Javier Mazzitelli, Luca Rottoli, and Chiara Savoini. Precise Predictions for the Associated Production of a W Boson with a Top-Antitop Quark Pair at the LHC. *Phys. Rev. Lett.*, 131(23):231901, 2023.

[340] P. Bärnreuther, M. Czakon, and P. Fiedler. Virtual amplitudes and threshold behaviour of hadronic top-quark pair-production cross sections. *JHEP*, 02:078, 2014.

[341] A. A. Penin. Two-loop photonic corrections to massive Bhabha scattering. *Nucl. Phys. B*, 734:185–202, 2006.

[342] A. Mitov and S. Moch. The Singular behavior of massive QCD amplitudes. *JHEP*, 05:001, 2007.

[343] Thomas Becher and Kirill Melnikov. Two-loop QED corrections to Bhabha scattering. *JHEP*, 06:084, 2007.

[344] Matteo Becchetti, Maximilian Delto, Sara Ditsch, Philipp Alexander Kreer, Mattia Pozzoli, and Lorenzo Tancredi. One-loop QCD corrections to $\bar{u}d \to t\bar{t}W$ at $\mathcal{O}(\varepsilon^2)$. *JHEP*, 09:126, 2025.

[345] Matteo Becchetti, Dhimiter Canko, Vsevolod Chestnov, Tiziano Peraro, Mattia Pozzoli, and Simone Zoia. Two-loop Feynman integrals for leading colour $t\bar{t}W$ production at hadron colliders. *JHEP*, 07:001, 2025.

[346] Nikolaos Kidonakis and Chris Foster. Soft-gluon corrections in tt¯W production. *Phys. Lett. B*, 854:138708, 2024.

[347] Armen Tumasyan et al. Measurement of the cross section of top quark-antiquark pair production in association with a W boson in proton-proton collisions at $\sqrt{s} = 13$ TeV. *JHEP*, 07:219, 2023.

[348] Georges Aad et al. Search for leptonic charge asymmetry in $t\bar{t}W$ production in final states with three leptons at $\sqrt{s} = 13$ TeV. *JHEP*, 07:033, 2023.

[349] Georges Aad et al. Measurement of the total and differential cross-sections of $t\bar{t}W$ production in pp collisions at $\sqrt{s} = 13$ TeV with the ATLAS detector. *JHEP*, 05:131, 2024. [Erratum: JHEP 11, 127 (2025)].

[350] Aram Hayrapetyan et al. Measurements of $t\bar{t}W$ differential cross sections and the leptonic charge asymmetry at $\sqrt{s} = 13$ TeV. *JHEP*, 03:083, 2026.

[351] Albert M Sirunyan et al. Search for production of four top quarks in final states with same-sign or multiple leptons in proton-proton collisions at $\sqrt{s} =$ 13 TeV. *Eur. Phys. J. C*, 80(2):75, 2020.

[352] Armen Tumasyan et al. Evidence for four-top quark production in proton-proton collisions at $\sqrt{s}$=13TeV. *Phys. Lett. B*, 844:138076, 2023.

[353] Georges Aad et al. Observation of four-top-quark production in the multilepton final state with the ATLAS detector. *Eur. Phys. J. C*, 83(6):496, 2023. [Erratum: Eur.Phys.J.C 84, 156 (2024)].

[354] Georges Aad et al. Probing the Higgs-top Yukawa interaction in the $t\bar{t}H$ and tH processes using $H \to \gamma\gamma$ with the ATLAS detector, arXiv:2606.04855 [hep-ph]. 2026.

[355] Qing-Hong Cao, Shao-Long Chen, and Yandong Liu. Probing Higgs Width and Top Quark Yukawa Coupling from $t\bar{t}H$ and $t\bar{t}t\bar{t}$ Productions. *Phys. Rev. D*, 95(5):053004, 2017.

[356] Luc Darmé, Benjamin Fuks, and Fabio Maltoni. Top-philic heavy resonances in four-top final states and their EFT interpretation. *JHEP*, 09:143, 2021.

[357] P. S. Bhupal Dev and Apostolos Pilaftsis. Maximally Symmetric Two Higgs Doublet Model with Natural Standard Model Alignment. *JHEP*, 12:024, 2014. [Erratum: JHEP 11, 147 (2015)].

[358] Nathaniel Craig, Francesco D'Eramo, Patrick Draper, Scott Thomas, and Hao Zhang. The Hunt for the Rest of the Higgs Bosons. *JHEP*, 06:137, 2015.

[359] Stefania Gori, Ian-Woo Kim, Nausheen R. Shah, and Kathryn M. Zurek. Closing the Wedge: Search Strategies for Extended Higgs Sectors with Heavy Flavor Final States. *Phys. Rev. D*, 93(7):075038, 2016.

[360] Nathaniel Craig, Jan Hajer, Ying-Ying Li, Tao Liu, and Hao Zhang. Heavy Higgs bosons at low $\tan\beta$: from the LHC to 100 TeV. *JHEP*, 01:018, 2017.

[361] Ben Lillie, Jing Shu, and Timothy M. P. Tait. Top Compositeness at the Tevatron and LHC. *JHEP*, 04:087, 2008.

[362] Alex Pomarol and Javi Serra. Top Quark Compositeness: Feasibility and Implications. *Phys. Rev. D*, 78:074026, 2008.

[363] Kunal Kumar, Tim M. P. Tait, and Roberto Vega-Morales. Manifestations of Top Compositeness at Colliders. *JHEP*, 05:022, 2009.

[364] Giovanni Banelli, Ennio Salvioni, Javi Serra, Tobias Theil, and Andreas Weiler. The Present and Future of Four Top Operators. *JHEP*, 02:043, 2021.

[365] Giacomo Cacciapaglia, Roberto Chierici, Aldo Deandrea, Luca Panizzi, Stephane Perries, and Silvano Tosi. Four tops on the real projective plane at LHC. *JHEP*, 10:042, 2011.

[366] Tilman Plehn and Tim M. P. Tait. Seeking Sgluons. *J. Phys. G*, 36:075001, 2009.

[367] Samuel Calvet, Benjamin Fuks, Philippe Gris, and Loic Valery. Searching for sgluons in multitop events at a center-of-mass energy of 8 TeV. *JHEP*, 04:043, 2013.

[368] Cen Zhang. Constraining *qqtt* operators from four-top production: a case for enhanced EFT sensitivity. *Chin. Phys. C*, 42(2):023104, 2018.

[369] Jacob J. Ethier, Giacomo Magni, Fabio Maltoni, Luca Mantani, Emanuele R. Nocera, Juan Rojo, Emma Slade, Eleni Vryonidou, and Cen Zhang. Combined SMEFT interpretation of Higgs, diboson, and top quark data from the LHC. *JHEP*, 11:089, 2021.

[370] Rafael Aoude, Hesham El Faham, Fabio Maltoni, and Eleni Vryonidou. Complete SMEFT predictions for four top quark production at hadron colliders. *JHEP*, 10:163, 2022.

[371] Albert M Sirunyan et al. Search for standard model production of four top quarks with same-sign and multilepton final states in proton–proton collisions at $\sqrt{s} = 13\,\text{TeV}$. *Eur. Phys. J. C*, 78(2):140, 2018.

[372] Albert M Sirunyan et al. Search for physics beyond the standard model in events with two leptons of same sign, missing transverse momentum, and jets in proton–proton collisions at $\sqrt{s} = 13\,\text{TeV}$. *Eur. Phys. J. C*, 77(9):578, 2017.

[373] Morad Aaboud et al. Search for new phenomena in events with same-charge leptons and b-jets in pp collisions at $\sqrt{s} = 13$ TeV with the ATLAS detector. *JHEP*, 12:039, 2018.

[374] Morad Aaboud et al. Search for four-top-quark production in the single-lepton and opposite-sign dilepton final states in pp collisions at $\sqrt{s} = 13$ TeV with the ATLAS detector. *Phys. Rev. D*, 99(5):052009, 2019.

[375] Albert M Sirunyan et al. Search for the production of four top quarks in the single-lepton and opposite-sign dilepton final states in proton-proton collisions at $\sqrt{s} = 13$ TeV. *JHEP*, 11:082, 2019.

[376] Georges Aad et al. Evidence for $t\bar{t}t\bar{t}$ production in the multilepton final state in proton–proton collisions at $\sqrt{s} = 13$ TeV with the ATLAS detector. *Eur. Phys. J. C*, 80(11):1085, 2020.

[377] Georges Aad et al. Measurement of the $\mathrm{t\bar{t}t\bar{t}}$ production cross section in pp collisions at $\sqrt{s} = 13$ TeV with the ATLAS detector. *JHEP*, 11:118, 2021.

[378] Aram Hayrapetyan et al. Observation of four top quark production in proton-proton collisions at s=13TeV. *Phys. Lett. B*, 847:138290, 2023.

[379] G. Bevilacqua and M. Worek. Constraining BSM Physics at the LHC: Four top final states with NLO accuracy in perturbative QCD. *JHEP*, 07:111, 2012.

[380] Melissa van Beekveld, Anna Kulesza, and Laura Moreno Valero. Threshold Resummation for the Production of Four Top Quarks at the LHC. *Phys. Rev. Lett.*, 131(21):211901, 2023.

[381] Melissa van Beekveld, Anna Kulesza, Michele Lupattelli, and Tommaso Saracco. Invariant-mass threshold resummation for the production of four top quarks at the LHC. *JHEP*, 10:209, 2025.

[382] Tomáš Ježo and Manfred Kraus. Hadroproduction of four top quarks in the powheg box. *Phys. Rev. D*, 105(11):114024, 2022.

[383] Torbjörn Sjöstrand, Stefan Ask, Jesper R. Christiansen, Richard Corke, Nishita Desai, Philip Ilten, Stephen Mrenna, Stefan Prestel, Christine O. Rasmussen, and Peter Z. Skands. An introduction to PYTHIA 8.2. *Comput. Phys. Commun.*, 191:159–177, 2015.

[384] Stefano Frixione, Eric Laenen, Patrick Motylinski, and Bryan R. Webber. Angular correlations of lepton pairs from vector boson and top quark decays in Monte Carlo simulations. *JHEP*, 04:081, 2007.

[385] Nikolaos Dimitrakopoulos and Malgorzata Worek. Four top final states with NLO accuracy in perturbative QCD: 4 lepton channel. *JHEP*, 06:129, 2024.

[386] Nikolaos Dimitrakopoulos and Malgorzata Worek. Four top final states with NLO accuracy in perturbative QCD: 3 lepton channel. *JHEP*, 03:025, 2025.

[387] Manal Alsairafi, Nikolaos Dimitrakopoulos, and Malgorzata Worek. Modeling top-quark decays in $t\bar{t}t\bar{t}$ production at the LHC. *Phys. Rev. D*, 112(11):114002, 2025.

[388] G. Bevilacqua, M. Czakon, M. V. Garzelli, A. van Hameren, A. Kardos, C. G. Papadopoulos, R. Pittau, and M. Worek. HELAC-NLO. *Comput. Phys. Commun.*, 184:986–997, 2013.

[389] R. L. Workman et al. Review of Particle Physics. *PTEP*, 2022:083C01, 2022.

[390] Guido Altarelli and G. Parisi. Asymptotic Freedom in Parton Language. *Nucl. Phys. B*, 126:298–318, 1977.

[391] John C. Collins, Davison E. Soper, and George F. Sterman. Transverse Momentum Distribution in Drell-Yan Pair and W and Z Boson Production. *Nucl. Phys. B*, 250:199–224, 1985.

[392] John C. Collins, Davison E. Soper, and George F. Sterman. Factorization for Short Distance Hadron - Hadron Scattering. *Nucl. Phys. B*, 261:104–142, 1985.

[393] John C. Collins, Davison E. Soper, and George F. Sterman. Factorization of Hard Processes in QCD. *Adv. Ser. Direct. High Energy Phys.*, 5:1–91, 1989.

[394] Richard D. Ball et al. The PDF4LHC21 combination of global PDF fits for the LHC Run III. *J. Phys. G*, 49(8):080501, 2022.

[395] Yuri L. Dokshitzer. Calculation of structure functions for deep-inelastic scattering and e^+e^- annihilation by perturbation theory in quantum chromodynamics. *Sov. Phys. JETP*, 46:641–653, 1977.

[396] V. N. Gribov and L. N. Lipatov. Deep inelastic e p scattering in perturbation theory. *Sov. J. Nucl. Phys.*, 15:438–450, 1972.

[397] Andre van Hameren. PARNI for importance sampling and density estimation. *Acta Phys. Polon. B*, 40:259–272, 2009.

[398] A. van Hameren. Kaleu: A General-Purpose Parton-Level Phase Space Generator, arXiv:1003.4953 [hep-ph]. 2010.

[399] T. Kinoshita. Mass singularities of Feynman amplitudes. *J. Math. Phys.*, 3:650–677, 1962.

[400] T. D. Lee and M. Nauenberg. Degenerate Systems and Mass Singularities. *Phys. Rev.*, 133:B1549–B1562, 1964.

[401] S. Catani and M. H. Seymour. A General algorithm for calculating jet cross-sections in NLO QCD. *Nucl. Phys. B*, 485:291–419, 1997. [Erratum: Nucl.Phys.B 510, 503–504 (1998)].

[402] Stefano Catani, Stefan Dittmaier, Michael H. Seymour, and Zoltan Trocsanyi. The Dipole formalism for next-to-leading order QCD calculations with massive partons. *Nucl. Phys. B*, 627:189–265, 2002.

[403] G. Bevilacqua, M. Czakon, M. Kubocz, and M. Worek. Complete Nagy-Soper subtraction for next-to-leading order calculations in QCD. *JHEP*, 10:204, 2013.

[404] W. T. Giele and E. W. Nigel Glover. Higher Order Corrections to Jet Cross Sections in e+ e- Annihilation. *Phys. Rev. D*, 46:1980–2010, 1992.

[405] W. T. Giele, E. W. Nigel Glover, and David A. Kosower. Higher order corrections to jet cross-sections in hadron colliders. *Nucl. Phys. B*, 403:633–670, 1993.

[406] Andy Buckley et al. General-purpose event generators for LHC physics. *Phys. Rept.*, 504:145–233, 2011.

[407] M. Bahr et al. Herwig++ Physics and Manual. *Eur. Phys. J. C*, 58:639–707, 2008.

[408] Johannes Bellm et al. Herwig 7.0/Herwig++ 3.0 release note. *Eur. Phys. J. C*, 76(4):196, 2016.

[409] Torbjörn Sjöstrand, Stephen Mrenna, and Peter Z. Skands. PYTHIA 6.4 Physics and Manual. *JHEP*, 05:026, 2006.

[410] Tanju Gleisberg, Stefan Hoeche, Frank Krauss, Andreas Schalicke, Steffen Schumann, and Jan-Christopher Winter. SHERPA 1.α: A Proof of concept version. *JHEP*, 02:056, 2004.

[411] T. Gleisberg, Stefan. Hoeche, F. Krauss, M. Schonherr, S. Schumann, F. Siegert, and J. Winter. Event generation with SHERPA 1.1. *JHEP*, 02:007, 2009.

[412] Enrico Bothmann et al. Event Generation with Sherpa 2.2. *SciPost Phys.*, 7(3):034, 2019.

[413] Enrico Bothmann et al. Event generation with Sherpa 3. *JHEP*, 12:156, 2024.

[414] Stefan Hoeche, Frank Krauss, Marek Schonherr, and Frank Siegert. QCD matrix elements + parton showers: The NLO case. *JHEP*, 04:027, 2013.

[415] Thomas Gehrmann, Stefan Hoche, Frank Krauss, Marek Schonherr, and Frank Siegert. NLO QCD matrix elements + parton showers in $e^+e^- \to$ hadrons. *JHEP*, 01:144, 2013.

[416] Keith Hamilton, Paolo Nason, Carlo Oleari, and Giulia Zanderighi. Merging H/W/Z + 0 and 1 jet at NLO with no merging scale: a path to parton shower + NNLO matching. *JHEP*, 05:082, 2013.

[417] X. Artru and G. Mennessier. String model and multiproduction. *Nucl. Phys. B*, 70:93–115, 1974.

[418] Bo Andersson, G. Gustafson, G. Ingelman, and T. Sjostrand. Parton Fragmentation and String Dynamics. *Phys. Rept.*, 97:31–145, 1983.

[419] B. R. Webber. A QCD Model for Jet Fragmentation Including Soft Gluon Interference. *Nucl. Phys. B*, 238:492–528, 1984.

[420] Jan-Christopher Winter, Frank Krauss, and Gerhard Soff. A Modified cluster hadronization model. *Eur. Phys. J. C*, 36:381–395, 2004.

[421] R. V. Harlander, S. Y. Klein, and M. Lipp. FeynGame. *Comput. Phys. Commun.*, 256:107465, 2020.

[422] Robert Harlander, Sven Yannick Klein, and Magnus C. Schaaf. FeynGame-2.1 – Feynman diagrams made easy. *PoS*, EPS-HEP2023:657, 2024.

[423] Lars Bündgen, Robert V. Harlander, Sven Yannick Klein, and Magnus C. Schaaf. FeynGame 3.0. *Comput. Phys. Commun.*, 314:109662, 2025.

[424] Stefano Frixione, Eric Laenen, Patrick Motylinski, Bryan R. Webber, and Chris D. White. Single-top hadroproduction in association with a W boson. *JHEP*, 07:029, 2008.

[425] Emanuele Re. Single-top Wt-channel production matched with parton showers using the POWHEG method. *Eur. Phys. J. C*, 71:1547, 2011.

[426] Morad Aaboud et al. Probing the quantum interference between singly and doubly resonant top-quark production in pp collisions at $\sqrt{s} = 13$ TeV with the ATLAS detector. *Phys. Rev. Lett.*, 121(15):152002, 2018.

[427] Ernestos N. Argyres, Wim Beenakker, Geert Jan van Oldenborgh, Ansgar Denner, Stefan Dittmaier, Jiri Hoogland, Ronald Kleiss, Costas G. Papadopoulos, and Giampiero Passarino. Stable calculations for unstable particles: Restoring gauge invariance. *Phys. Lett. B*, 358:339–346, 1995.

[428] Wim Beenakker, Geert Jan van Oldenborgh, Ansgar Denner, Stefan Dittmaier, Jiri Hoogland, Ronald Kleiss, Costas G. Papadopoulos, and Giampiero Passarino. The Fermion loop scheme for finite width effects in e^+e^- annihilation into four fermions. *Nucl. Phys. B*, 500:255–298, 1997.

[429] Ansgar Denner, S. Dittmaier, M. Roth, and D. Wackeroth. Predictions for all processes $e^+e^- \to$ fermions + γ. *Nucl. Phys. B*, 560:33–65, 1999.

[430] Ansgar Denner, S. Dittmaier, M. Roth, and L. H. Wieders. Electroweak corrections to charged-current $e^+e^- \to 4$ fermion processes: Technical details and further results. *Nucl. Phys. B*, 724:247–294, 2005. [Erratum: Nucl.Phys.B 854, 504–507 (2012)].

[431] Ansgar Denner and S. Dittmaier. The Complex-mass scheme for perturbative calculations with unstable particles. *Nucl. Phys. B Proc. Suppl.*, 160:22–26, 2006.

[432] C. F. Uhlemann and N. Kauer. Narrow-width approximation accuracy. *Nucl. Phys. B*, 814:195–211, 2009.

[433] Victor S. Fadin, Valery A. Khoze, and Alan D. Martin. How suppressed are the radiative interference effects in heavy instable particle production? *Phys. Lett. B*, 320:141–144, 1994.

[434] John M. Campbell and R. Keith Ellis. Top-Quark Processes at NLO in Production and Decay. *J. Phys. G*, 42(1):015005, 2015.

[435] Kirill Melnikov and Markus Schulze. NLO QCD corrections to top quark pair production and decay at hadron colliders. *JHEP*, 08:049, 2009.

[436] Aggeliki Kanaki and Costas G. Papadopoulos. HELAC: A Package to compute electroweak helicity amplitudes. *Comput. Phys. Commun.*, 132:306–315, 2000.

[437] M. Czakon, C. G. Papadopoulos, and M. Worek. Polarizing the Dipoles. *JHEP*, 08:085, 2009.

[438] A. van Hameren, C. G. Papadopoulos, and R. Pittau. Automated one-loop calculations: A Proof of concept. *JHEP*, 09:106, 2009.

[439] J. Alwall et al. A Standard format for Les Houches event files. *Comput. Phys. Commun.*, 176:300–304, 2007.

[440] I. Antcheva et al. ROOT: A C++ framework for petabyte data storage, statistical analysis and visualization. *Comput. Phys. Commun.*, 180:2499–2512, 2009.

[441] Z. Bern, L. J. Dixon, F. Febres Cordero, S. Höche, H. Ita, D. A. Kosower, and D. Maitre. Ntuples for NLO Events at Hadron Colliders. *Comput. Phys. Commun.*, 185:1443–1460, 2014.

[442] G. Bevilacqua. unpublished. 2019.

[443] Alessandro Cafarella, Costas G. Papadopoulos, and Malgorzata Worek. HelacPhegas: A Generator for all parton level processes. *Comput. Phys. Commun.*, 180:1941–1955, 2009.

[444] Costas G. Papadopoulos. PHEGAS: A Phase space generator for automatic cross-section computation. *Comput. Phys. Commun.*, 137:247–254, 2001.

[445] Jonathan Hermann. *Signal and background modeling in BSM studies in the top-quark sector at the LHC*. PhD thesis, RWTH Aachen University, 2023.

[446] Petros Draggiotis, Ronald H. P. Kleiss, and Costas G. Papadopoulos. On the computation of multigluon amplitudes. *Phys. Lett. B*, 439:157–164, 1998.

[447] Petros D. Draggiotis, Ronald H. P. Kleiss, and Costas G. Papadopoulos. Multijet production in hadron collisions. *Eur. Phys. J. C*, 24:447–458, 2002.

[448] Gerard 't Hooft. A Planar Diagram Theory for Strong Interactions. *Nucl. Phys. B*, 72:461, 1974.

[449] F. Maltoni, K. Paul, T. Stelzer, and S. Willenbrock. Color Flow Decomposition of QCD Amplitudes. *Phys. Rev. D*, 67:014026, 2003.

[450] Costas G. Papadopoulos and Malgorzata Worek. Multi-parton cross sections at hadron colliders. *Eur. Phys. J. C*, 50:843–856, 2007.

[451] W. Kilian, T. Ohl, J. Reuter, and C. Speckner. QCD in the Color-Flow Representation. *JHEP*, 10:022, 2012.

[452] Michelangelo L. Mangano and Stephen J. Parke. Multiparton Amplitudes in Gauge Theories. *Phys. Rept.*, 200:301–367, 1991.

[453] Daniel Stremmer. *Precise modeling of prompt photons in associated top-quark pair production*. PhD thesis, RWTH Aachen University, 2024.

[454] Giovanni Ossola, Costas G. Papadopoulos, and Roberto Pittau. Reducing full one-loop amplitudes to scalar integrals at the integrand level. *Nucl. Phys. B*, 763:147–169, 2007.

[455] Giovanni Ossola, Costas G. Papadopoulos, and Roberto Pittau. CutTools: A Program implementing the OPP reduction method to compute one-loop amplitudes. *JHEP*, 03:042, 2008.

[456] A. van Hameren. OneLOop: For the evaluation of one-loop scalar functions. *Comput. Phys. Commun.*, 182:2427–2438, 2011.

[457] F. del Aguila and R. Pittau. Recursive numerical calculus of one-loop tensor integrals. *JHEP*, 07:017, 2004.

[458] W. L. van Neerven and J. A. M. Vermaseren. Large loop integrals. *Phys. Lett. B*, 137:241–244, 1984.

[459] Giovanni Ossola, Costas G. Papadopoulos, and Roberto Pittau. On the Rational Terms of the one-loop amplitudes. *JHEP*, 05:004, 2008.

[460] R. Keith Ellis, Zoltan Kunszt, Kirill Melnikov, and Giulia Zanderighi. One-loop calculations in quantum field theory: from Feynman diagrams to unitarity cuts. *Phys. Rept.*, 518:141–250, 2012.

[461] Achilleas Lazopoulos, Kirill Melnikov, and Frank Petriello. QCD corrections to tri-boson production. *Phys. Rev. D*, 76:014001, 2007.

[462] T. Binoth, G. Ossola, C. G. Papadopoulos, and R. Pittau. NLO QCD corrections to tri-boson production. *JHEP*, 06:082, 2008.

[463] R. Pittau. Testing and improving the numerical accuracy of the NLO predictions. *Comput. Phys. Commun.*, 181:1941–1946, 2010.

[464] Simon Badger, Benedikt Biedermann, and Peter Uwer. NGluon: A Package to Calculate One-loop Multi-gluon Amplitudes. *Comput. Phys. Commun.*, 182:1674–1692, 2011.

[465] Zoltan Nagy and Zoltan Trocsanyi. Next-to-leading order calculation of four jet observables in electron positron annihilation. *Phys. Rev. D*, 59:014020, 1999. [Erratum: Phys.Rev.D 62, 099902 (2000)].

[466] Zoltan Nagy. Next-to-leading order calculation of three jet observables in hadron hadron collision. *Phys. Rev. D*, 68:094002, 2003.

[467] Zoltan Nagy and Davison E. Soper. Ordering variable for parton showers. *JHEP*, 06:178, 2014.

[468] Stefano Actis, Ansgar Denner, Lars Hofer, Jean-Nicolas Lang, Andreas Scharf, and Sandro Uccirati. RECOLA: REcursive Computation of One-Loop Amplitudes. *Comput. Phys. Commun.*, 214:140–173, 2017.

[469] Ansgar Denner, S. Dittmaier, M. Roth, and D. Wackeroth. Electroweak radiative corrections to $e^+e^- \to WW \to 4$ fermions in double-pole approximation: The RacoonWW approach. *Nucl. Phys. B*, 587:67–117, 2000.

[470] E. Accomando, Ansgar Denner, and A. Kaiser. Logarithmic electroweak corrections to gauge-boson pair production at the LHC. *Nucl. Phys. B*, 706:325–371, 2005.

[471] Sayipjamal Dulat, Tie-Jiun Hou, Jun Gao, Marco Guzzi, Joey Huston, Pavel Nadolsky, Jon Pumplin, Carl Schmidt, Daniel Stump, and C. P. Yuan. New parton distribution functions from a global analysis of quantum chromodynamics. *Phys. Rev. D*, 93(3):033006, 2016.

[472] S. Bailey, T. Cridge, L. A. Harland-Lang, A. D. Martin, and R. S. Thorne. Parton distributions from LHC, HERA, Tevatron and fixed target data: MSHT20 PDFs. *Eur. Phys. J. C*, 81(4):341, 2021.

[473] Jon Butterworth et al. PDF4LHC recommendations for LHC Run II. *J. Phys. G*, 43:023001, 2016.

[474] Richard D. Ball et al. Parton distributions from high-precision collider data. *Eur. Phys. J. C*, 77(10):663, 2017.

[475] Tie-Jiun Hou et al. New CTEQ global analysis of quantum chromodynamics with high-precision data from the LHC. *Phys. Rev. D*, 103(1):014013, 2021.

[476] Andy Buckley, James Ferrando, Stephen Lloyd, Karl Nordström, Ben Page, Martin Rüfenacht, Marek Schönherr, and Graeme Watt. LHAPDF6: parton density access in the LHC precision era. *Eur. Phys. J. C*, 75:132, 2015.

[477] Matteo Cacciari, Gavin P. Salam, and Gregory Soyez. The anti-k_t jet clustering algorithm. *JHEP*, 04:063, 2008.

[478] Carola F. Berger, Claudio Marcantonini, Iain W. Stewart, Frank J. Tackmann, and Wouter J. Waalewijn. Higgs Production with a Central Jet Veto at NNLL+NNLO. *JHEP*, 04:092, 2011.

[479] Iain W. Stewart, Frank J. Tackmann, and Wouter J. Waalewijn. N-Jettiness: An Inclusive Event Shape to Veto Jets. *Phys. Rev. Lett.*, 105:092002, 2010.

[480] Thomas Becher and Matthias Neubert. Factorization and NNLL Resummation for Higgs Production with a Jet Veto. *JHEP*, 07:108, 2012.

[481] Andrea Banfi, Gavin P. Salam, and Giulia Zanderighi. NLL+NNLO predictions for jet-veto efficiencies in Higgs-boson and Drell-Yan production. *JHEP*, 06:159, 2012.

[482] Andrea Banfi, Pier Francesco Monni, Gavin P. Salam, and Giulia Zanderighi. Higgs and Z-boson production with a jet veto. *Phys. Rev. Lett.*, 109:202001, 2012.

[483] Johannes K. L. Michel, Piotr Pietrulewicz, and Frank J. Tackmann. Jet Veto Resummation with Jet Rapidity Cuts. *JHEP*, 04:142, 2019.

[484] John M. Campbell, R. Keith Ellis, Tobias Neumann, and Satyajit Seth. Jet-veto resummation at $\mathrm{N^3LL}_p$ + NNLO in boson production processes. *JHEP*, 04:106, 2023.

[485] Gregory Mahlon and Stephen J. Parke. Angular correlations in top quark pair production and decay at hadron colliders. *Phys. Rev. D*, 53:4886–4896, 1996.

[486] Gregory Mahlon and Stephen J. Parke. Maximizing spin correlations in top quark pair production at the Tevatron. *Phys. Lett. B*, 411:173–179, 1997.

[487] Gregory Mahlon and Stephen J. Parke. Spin Correlation Effects in Top Quark Pair Production at the LHC. *Phys. Rev. D*, 81:074024, 2010.

[488] Werner Bernreuther and Zong-Guo Si. Distributions and correlations for top quark pair production and decay at the Tevatron and LHC. *Nucl. Phys. B*, 837:90–121, 2010.

[489] Georges Aad et al. Observation of spin correlation in $t\bar{t}$ events from pp collisions at $\sqrt{s} = 7$ TeV using the ATLAS detector. *Phys. Rev. Lett.*, 108:212001, 2012.

[490] CMS collaboration. Measurement of Spin Correlations in $t\bar{t}$ events in the dilepton channels in pp collisions at $\sqrt{s} = 7$ TeV, CMS PAS TOP-12-004. 2012.

[491] D. Yu. Bardin, A. Leike, T. Riemann, and M. Sachwitz. Energy Dependent Width Effects in e^+e^- Annihilation Near the Z-Boson Pole. *Phys. Lett. B*, 206:539–542, 1988.

[492] Ansgar Denner and Jean-Nicolas Lang. The Complex-Mass Scheme and Unitarity in perturbative Quantum Field Theory. *Eur. Phys. J. C*, 75(8):377, 2015.

[493] Morad Aaboud et al. Measurement of the top quark mass in the $t\bar{t} \to$ dilepton channel from $\sqrt{s} = 8$ TeV ATLAS data. *Phys. Lett. B*, 761:350–371, 2016.

[494] Albert M Sirunyan et al. Measurement of the top quark mass in the dileptonic $t\bar{t}$ decay channel using the mass observables $M_{b\ell}$, M_{T2}, and $M_{b\ell\nu}$ in pp collisions at $\sqrt{s} = 8$ TeV. *Phys. Rev. D*, 96(3):032002, 2017.

[495] C. G. Lester and D. J. Summers. Measuring masses of semiinvisibly decaying particles pair produced at hadron colliders. *Phys. Lett. B*, 463:99–103, 1999.

[496] Alan Barr, Christopher Lester, and P. Stephens. m(T2): The Truth behind the glamour. *J. Phys. G*, 29:2343–2363, 2003.

[497] S. Catani, F. Krauss, R. Kuhn, and B. R. Webber. QCD matrix elements + parton showers. *JHEP*, 11:063, 2001.

[498] F. Krauss. Matrix elements and parton showers in hadronic interactions. *JHEP*, 08:015, 2002.

[499] S. Catani, Yuri L. Dokshitzer, M. H. Seymour, and B. R. Webber. Longitudinally invariant K_t clustering algorithms for hadron hadron collisions. *Nucl. Phys. B*, 406:187–224, 1993.

[500] F. R. Anger, F. Febres Cordero, S. Höche, and D. Maître. Weak vector boson production with many jets at the LHC $\sqrt{s} = 13$ TeV. *Phys. Rev. D*, 97(9):096010, 2018.

[501] Niccolo Moretti. *Precise Predictions for Top-quark Pair Production in Association with Multiple Jets*. PhD thesis, Zurich U., 2016.

[502] S. Catani, B. R. Webber, and G. Marchesini. QCD coherent branching and semiinclusive processes at large x. *Nucl. Phys. B*, 349:635–654, 1991.

[503] Keith Hamilton, Tom Melia, Pier Francesco Monni, Emanuele Re, and Giulia Zanderighi. Merging WW and WW+jet with MINLO. *JHEP*, 09:057, 2016.